IMPROVED UNDERSTANDING OF FIREBRAND PROCESSES DURING LARGE SCALE FIRE DISASTERS

EDITED BY: Samuel L. Manzello, Sayaka Suzuki, Domingos Xavier Viegas and Naian Liu

PUBLISHED IN: Frontiers in Mechanical Engineering

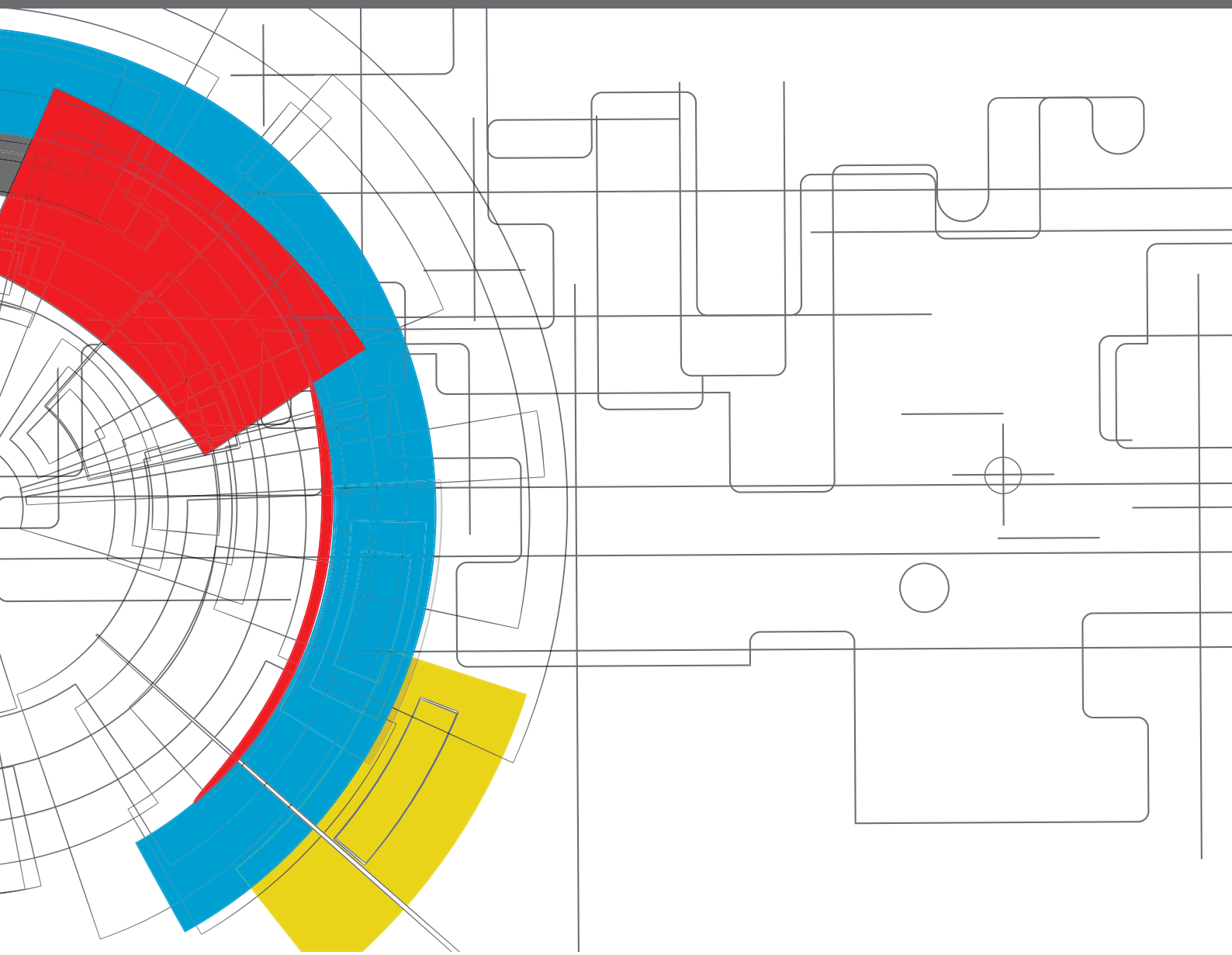

frontiers Research Topics

ISSN 1664-8714
ISBN 978-2-88974-688-0
DOI 10.3389/978-2-88974-688-0

About Frontiers

Frontiers is more than just an open-access publisher of scholarly articles: it is a pioneering approach to the world of academia, radically improving the way scholarly research is managed. The grand vision of Frontiers is a world where all people have an equal opportunity to seek, share and generate knowledge. Frontiers provides immediate and permanent online open access to all its publications, but this alone is not enough to realize our grand goals.

Frontiers Journal Series

The Frontiers Journal Series is a multi-tier and interdisciplinary set of open-access, online journals, promising a paradigm shift from the current review, selection and dissemination processes in academic publishing. All Frontiers journals are driven by researchers for researchers; therefore, they constitute a service to the scholarly community. At the same time, the Frontiers Journal Series operates on a revolutionary invention, the tiered publishing system, initially addressing specific communities of scholars, and gradually climbing up to broader public understanding, thus serving the interests of the lay society, too.

Dedication to Quality

Each Frontiers article is a landmark of the highest quality, thanks to genuinely collaborative interactions between authors and review editors, who include some of the world's best academicians. Research must be certified by peers before entering a stream of knowledge that may eventually reach the public - and shape society; therefore, Frontiers only applies the most rigorous and unbiased reviews.
Frontiers revolutionizes research publishing by freely delivering the most outstanding research, evaluated with no bias from both the academic and social point of view. By applying the most advanced information technologies, Frontiers is catapulting scholarly publishing into a new generation.

What are Frontiers Research Topics?

Frontiers Research Topics are very popular trademarks of the Frontiers Journals Series: they are collections of at least ten articles, all centered on a particular subject. With their unique mix of varied contributions from Original Research to Review Articles, Frontiers Research Topics unify the most influential researchers, the latest key findings and historical advances in a hot research area! Find out more on how to host your own Frontiers Research Topic or contribute to one as an author by contacting the Frontiers Editorial Office: frontiersin.org/about/contact

IMPROVED UNDERSTANDING OF FIREBRAND PROCESSES DURING LARGE SCALE FIRE DISASTERS

Topic Editors:
Samuel L. Manzello, Reax Engineering, United States
Sayaka Suzuki, National Research Institute for Fire and Disaster, Japan
Domingos Xavier Viegas, University of Coimbra, Portugal
Naian Liu, University of Science and Technology of China, China

Citation: Manzello, S. L., Suzuki, S., Viegas, D. X., Liu, N., eds. (2022). Improved Understanding of Firebrand Processes During Large Scale Fire Disasters. Lausanne: Frontiers Media SA. doi: 10.3389/978-2-88974-688-0

Table of Contents

frontiers in Mechanical Engineering

EDITORIAL
published: 23 February 2022
doi: 10.3389/fmech.2022.819633

Editorial: Improved Understanding of Firebrand Processes During Large Scale Fire Disasters

Samuel L. Manzello[1]*, *Sayaka Suzuki*[2], *Domingos Xavier Viegas*[3] and *Naian Liu*[4]

[1]Reax Engineering, Berkeley, CA, United States, [2]National Research Institute of Fire and Disaster, Chofu, Japan, [3]University of Coimbra, Coimbra, Portugal, [4]State Key Laboratory of Fire Science, University of Science and Technology of China, Hefei, China

Keywords: large outdoor fires and the built environment, firebrands, embers, WUI fires, ignition

Editorial on the Research Topic

Improved Understanding of Firebrand Processes During Large Scale Fire Disasters

All across the globe, large outdoor fires have been responsible for destruction of infrastructure. Wildland fires that spread into urban areas, often called wildland-urban interface (WUI) fires, are capable of massive destruction. The rise of densely populated urban areas has also seen the development of large urban fires. In China and Japan, such urban fires have occurred for hundreds of years. Similarly, the United States has also experienced several major urban fires, such as the Great Chicago Fire in 1872 and the Baltimore Fire in 1904. In some cases, earthquakes have served to initiate these fires but it is not a necessary condition for these urban fires to develop. In addition, the rise of informal settlement communities in Southeast Asia and Africa continues to result in large outdoor fires capable of great destruction.

A common feature in the rapid spread of large outdoor fires are the generation of smaller combustible fragments from the original fire source, referred to as firebrands. In the case of WUI fires, the production of firebrands occurs from the combustion dynamics of vegetative, such as trees and shrubs, and human-made fuel elements, such as homes and other structures. For urban fires and informal settlement fires, firebrands are produced primarily from human-made fuel elements.

Firebrand combustion has a series of important aspects: initial generation or formation from the combustion of both vegetative and structural fuel types, transport, deposition, and ignition of fuel sources generally far removed the original fire source. Post-fire investigations, for WUI fires, have reported that firebrand processes are responsible for a majority of structure losses in these fires (https://link.springer.com/referenceworkentry/10.1007/978-3-319-51727-8_46-1).

As part of this Research Topic in *Frontiers in Mechanical Engineering*, nine papers were ultimately accepted for publication. Several studies in this Research Topic are focused on firebrand generation characteristics from burning vegetation. In the studies by Adusumilli et al. and Almeida et al., experiments were undertaken to better understand firebrand generation characteristics at the individual tree and shrub level. Noteworthy is the use of advanced diagnostics, such as particle image velocimetry (PIV), to investigate these generation processes (Almeida et al.). In the work of Thomas et al., field experiments were undertaken to attempt to couple the fire dynamics to the firebrand processes.

Two of the contributed papers investigated the complex process of firebrand deposition. Mankame and Shotorban conducted numerical simulations around simplified flow obstacles and Suzuki and Manzello conducted real-scale experiments, in an effort to shed light on the physics of firebrand deposition. Firebrand deposition processes within communities remain an area that has been largely unexplored.

Lastly, four of the contributed papers all focused on the processes of ignition by firebrands. Salehizadeh et al., attempt to determine critical conditions for wood ignition by simulated firebrand

Edited and reviewed by:
Xinyan Huang,
Hong Kong Polytechnic University,
Hong Kong SAR, China

***Correspondence:**
Samuel L. Manzello
manzello@reaxengineering.com

Specialty section:
This article was submitted to Thermal and Mass Transport, a section of the journal Frontiers in Mechanical Engineering

Received: *22 November 2021*
Accepted: *04 February 2022*
Published: *23 February 2022*

Citation:
Manzello SL, Suzuki S, Viegas DX and Liu N (2022) Editorial: Improved Understanding of Firebrand Processes During Large Scale Fire Disasters. Front. Mech. Eng 8:819633. doi: 10.3389/fmech.2022.819633

piles using small-scale experiments. Wang et al., considered fundamental experiments of wood discs to better understand combustion processes need to understand firebrand ignition. In the work of Bean and Blunck, ignition of both solid and porous surfaces was considered. Bearinger et al., tried to look at various parameters to determine what are the key sensitivities to ignition from firebrands.

AUTHOR CONTRIBUTIONS

SM was invited to develop and lead this Research Topic by Frontiers in Mechanical Engineering. He invited and assembled the team of guest editors. SS, NL, and DV each served as editor for various papers in the Research Topic.

Conflict of Interest: The authors declare that the research was conducted in the absence of any commercial or financial relationships that could be construed as a potential conflict of interest.

frontiers in Mechanical Engineering

ORIGINAL RESEARCH
published: 28 January 2021
doi: 10.3389/fmech.2020.628510

Investigating the Effect of Structure to Structure Separation Distance on Firebrand Accumulation

Sayaka Suzuki[1] *and Samuel L. Manzello*[2]*

[1]National Research Institute of Fire and Disaster, Tokyo, Japan, [2]National Institute of Standards and Technology (NIST), Gaithersburg, MD, United States

Wind plays an important role in the built environment. Large outdoor fires in the built environment are no exception. Under strong wind, firebrands fly far, which leads to quick fire spread. In this study, the effect of structure to structure separation distance on firebrand accumulation was investigated by using a custom designed firebrand generator installed in a real scale wind tunnel. Firebrands accumulated at 4 and 6 m s^{-1}, but no firebrand accumulation zone was observed at 8 and 10 m s^{-1}, regardless of separation distance (SD). Experimental results were compared with a simple CFD flow simulation (no firebrands included). The size of firebrand accumulation zone as well as distance from the structure front was compared with SD in the cases of 4 and 6 m s^{-1} wind speeds. It was found that firebrands behave differently from SD = 1 to 2 m, to that of SD = 2 to 3 m. The results of this study are the first to explore these important interactions between firebrands and structure separation distances. The results of this work will help develop and design sustainable communities that may better resist the destruction of increasing large outdoor fire outbreaks worldwide, as well as help develop the next generation of CFD models needed to grasp the important large outdoor fire problem and associated firebrand processes.

Keywords: large outdoor fires and the built environment, firebrands, accumulation, separation distance, firebrand generator

OPEN ACCESS

Edited by:
Myeongsub Kim,
Florida Atlantic University,
United States

Reviewed by:
Xinyan Huang,
Hong Kong Polytechnic University,
Hong Kong
Gianni Pagnini,
Basque Center for Applied Mathematics, Spain

***Correspondence:**
Samuel L. Manzello
samuelm@nist.gov

Specialty section:
This article was submitted to Thermal and Mass Transport, a section of the journal Frontiers in Mechanical Engineering

Received: *12 November 2020*
Accepted: *15 December 2020*
Published: *28 January 2021*

Citation:
Suzuki S and Manzello SL (2021) Investigating the Effect of Structure to Structure Separation Distance on Firebrand Accumulation. Front. Mech. Eng 6:628510. doi: 10.3389/fmech.2020.628510

INTRODUCTION

Wind plays an important role in the built environment, from ventilation within buildings, wind force on buildings, effects on rain, to pollution dispersion (Shah and Ferziger, 1997; Blocken and Carmeliet, 2004; Quyang et al., 2006; Chaves et al., 2011; Yuan and Ng, 2012; Razak et al., 2013). The importance of wind applies to fire safety, where an increasing number of large outdoor fires, such as urban fires, informal settlement fires, wildland-urban interface (WUI) fires and wildland fires, are a major concern (Manzello et al., 2018).

Outdoor fires spread via three paths; direct flame contact, radiative heat, and firebrands. Wind largely influences outdoor fire spread behavior. Especially in the presence of strong wind, fires spread quickly, endangering people in vast areas. Stronger wind enhances flame spread processes; heat transfer processes are augmented (Albini 1985; Weber 1989; Pitts, 1991; Weber 1991; Potter, 1996; Morandini et al., 2001; Hu et al., 2009; Morandini and Silvani, 2010; Sharples et al., 2012).

Firebrand processes are also affected by winds (Tarifa et al., 1965; Lee and Hellman 1969; Albini 1983; Ellis 2000; Albini et al., 2012; Koo et al., 2012; Suzuki et al., 2013; Tohidi et al., 2015; Suzuki and Manzello, 2017a; Tohidi and Kaye, 2017a; Tohidi and Kaye, 2017b; Fernandez-Pello, 2017; Song

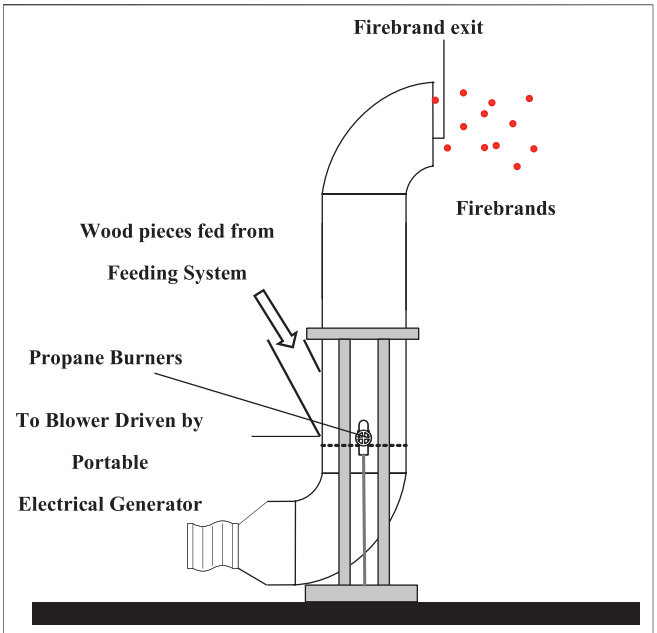

FIGURE 1 | The continuous-feed firebrand generator (the continuous-feed NIST Dragon).

firebrand deposition is the least studied to the authors' knowledge. While many research studies that model the wildland fire behavior have been undertaken (Rothermel, 1972; Koo et al., 2005; Alexander and Cruz, 2006; Cheney and Sullivan, 2008; Sullivan, 2009; Martin and Hillen, 2016; Trucchia et al., 2019), including firebrands in these models is a great challenge. Modeling firebrands is complex in nature, such as change in mass, size, and combustion state during transport. More experimental studies are needed to understand the flow dynamics of firebrands near and around structures. In a past, first attempt (Suzuki and Manzello, 2017a), firebrand accumulation behavior in front of a simple wall under different wind speeds was investigated and compared with simple wind flow modeling.

One of important measures in areas prone to large outdoor fires are home ignition zones (HIZ) (Cohen, 2000; Syphard et al., 2012; Biswas et al., 2013). It is important to remove all the combustibles including sheds or mulches, in case of any combustibles being ignited by firebrands, which will lead to ignition of homes. Unfortunately, it is difficult to implement in practice (Mell and Maranghides, 2009). More understanding on firebrand behavior around structures is needed. To this end, experiments were performed to investigate the firebrand behavior around structures, with a special emphasis on the separation distance between structures.

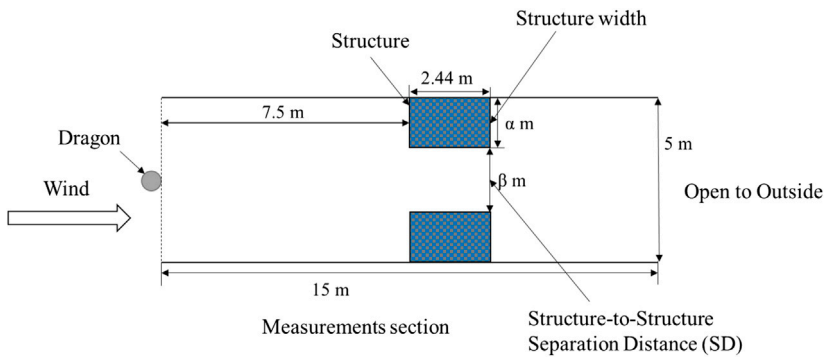

FIGURE 2 | Schematics of structure locations in wind tunnel.

et al., 2017; Suzuki and Manzello, 2019; Suzuki and Manzello 2020a; Manzello et al., 2020; Manzello and Suzuki, 2020; Suzuki and Manzello 2021). Wind influences all aspects of firebrand behavior; firebrand generation from fuels (Suzuki et al., 2013; Tohidi et al., 2015; Suzuki and Manzello, 2019; Manzello and Suzuki, 2020; Suzuki and Manzello 2020; Suzuki and Manzello 2021), transport distance (Tarifa et al., 1965; Lee and Hellman 1969; Albini 1983; Ellis 2000; Albini et al., 2012; Koo et al., 2012; Tohidi and Kaye, 2017a; Tohidi and Kaye, 2017b; Song et al., 2017), firebrand deposition patterns (Suzuki and Manzello, 2017a), and ignition behavior induced by firebrands (Ganteaume 2009; Manzello et al., 2012; Manzello and Suzuki 2012; Manzello, 2014; Suzuki et al., 2015; Suzuki and Manzello, 2017b; Manzello et al., 2017; Wang et al., 2017; Suzuki and Manzello, 2020b). Out of four firebrand behaviors, the

EXPERIMENTS

Experimental Description

The continuous-feed firebrand generator (NIST Dragon) was used for all the experiments. The details of this apparatus are described in (Manzello and Suzuki, 2014), so a brief overview is provided here. The continuous-feed NIST Dragon was made of a continuous-feed part connected to the firebrand generator (**Figure 1**). The continuous-feed part has the storage of wood pieces (for firebrands) connected with a pipe to the NIST Dragon, with two gates to mitigate fire spread from the apparatus to the feeding system. The firebrand generator has a blower that was set to 3 m s^{-1} at the exit of firebrand generator in order to loft the generated firebrands. This blower velocity is selected to be able to produce smoldering firebrands. The feeding rate was 800 g/min,

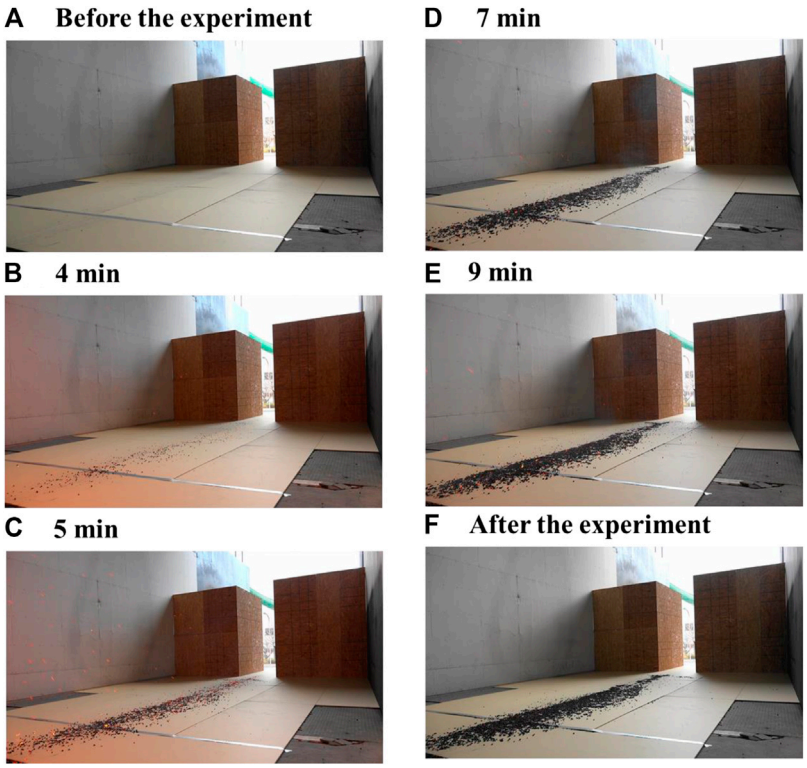

FIGURE 3 | Firebrand Accumulation Pattern via Time under SD = 1 m and 4 m s^{-1} wind **(A)** before the experiment, **(B)** 4 min, **(C)** 5 min, **(D)** 7 min, **(E)** 9 min and **(F)** after the experiment.

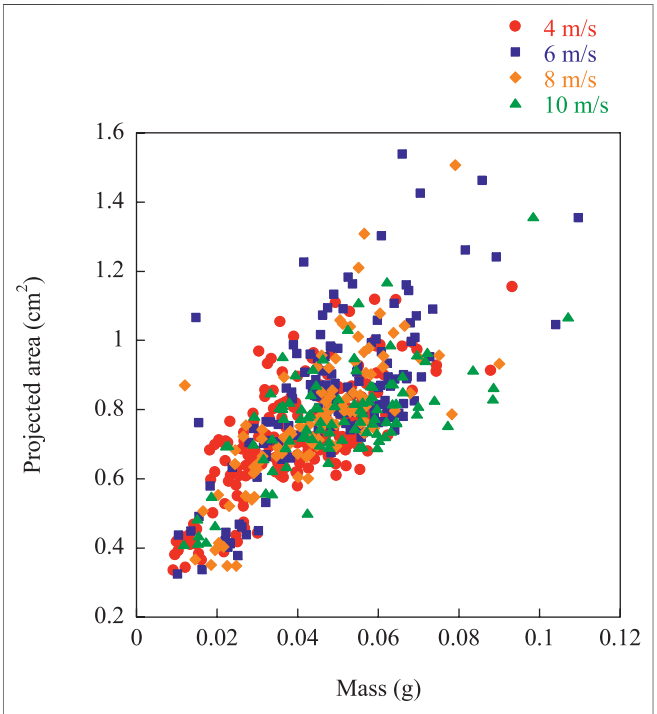

FIGURE 4 | Characteristics of firebrands under 4, 6, 8 and 10 m s^{-1}.

or approximately 16,000/min of wood pieces (1 piece of wood piece weighs approximately 0.5 g before the combustion). With this feeding rate, the firebrand flux at the exit of the NIST Dragon is 17 g/m^2 s (mass flux) or approximately 342/m^2 s (number flux). Experiments were performed in the Fire Research Wind Tunnel Facility (FRWTF) in Building Research Institute (BRI), Tsukuba, Japan as the wind is an important parameter in large outdoor fires. FRWTF has a 4 m fan and provides a wind profile up to 10 m s^{-1} (±10%) in a measurement section of 5 m width × 15 m length × 20 m height with both sides being wall.

Structures were symmetrically placed at 7.5 m downwind (to the leading edge of structures) from the NIST Dragon (Suzuki and Manzello, 2017a). This distance was far enough to investigate the firebrand behavior around a wall (Suzuki and Manzello, 2017a). The dimensions of the structures were 1, 1.5 or 2 m wide (shown as α in **Figure 2**) × 2.44 m long × 2.44 m high depending on the selected separation distance (SD) = either 3, 2, and 1 m (shown as β in **Figure 2**). The SD considered in this study were 1, 2, and 3 m as the SD of approximately 2 m is allowed in USA (Maranghides and Johnsson, 2008). Schematics of experimental settings are provided in **Figure 2A** feeding time of 10 min was selected for most cases as it was reported that (Suzuki and Manzello, 2017a) the firebrand deposition reached a peak and remain the same after a certain time. For 10 m s^{-1} wind speed cases with SD = 1 and 2 m, 5 min feeding time was selected for safety, since it was

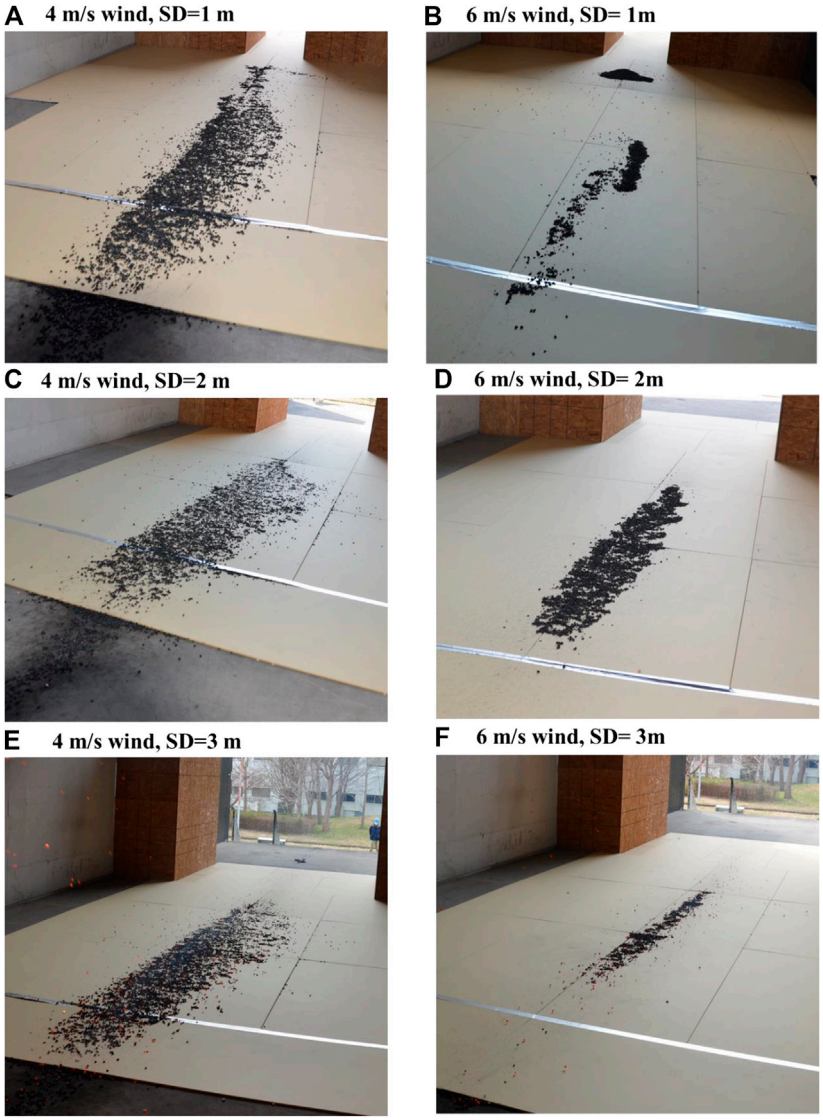

FIGURE 5 | Firebrand Accumulation pattern under different wind speeds and SD **(A)** 4 m s^{-1} and SD = 1 m **(B)** 6 m s^{-1} and SD = 1 m, **(C)** 4 m s^{-1} and SD = 2 m, **(D)** 6 m s^{-1} and SD = 2 m, **(E)** 4 m s^{-1} and SD = 3 m and **(F)** 6 m s^{-1} and SD = 3 m. Images under 8 and 10 m s^{-1} are not provided as accumulation was not observed.

possible to produce outside fires due to the large effluent of firebrands outside the wind facility. **Figure 3** shows the images of firebrand deposition process in the experiments under 4 m s^{-1} and SD = 1 m. The firebrand accumulation zone was not completely symmetric.

Separate experiments were performed to verify the characteristics of firebrands produced under different wind speeds, specifically, 4, 6, 8 and 10 m s^{-1}. Firebrands were produced under a desired wind and collected in water pans. After the collection, firebrands were dried at 104 °C in the oven. The mass of each firebrand was measured with a scale, and a picture of each firebrand was taken. The image analysis was performed to measure the projected area. Characteristics of firebrands produced under different wind speeds is shown in **Figure 4**.

Experimental Results and Discussion

Experiments showed a clear firebrand accumulation zone in front of the separation zone (upwind side) at lower wind speeds, 4 and 6 m s^{-1} while no accumulation zones were observed at higher wind speeds, 8 and 10 m s^{-1} (**Figure 5**). In **Figure 5**, no images are provided for experiments with 8 or 10 m s^{-1}, due to the absence of accumulation zones. **Figure 5** shows that the firebrand accumulation zone was not completely symmetric. In the case of SD = 3 m under 4 m s^{-1}, the firebrand accumulation was observed between structures, also on the downwind side (**Figure 5E**). Under 6 m s^{-1} wind with SD = 1 m, firebrands accumulated into two zones (**Figure 5D**). Under 8 m s^{-1} wind with SD = 1 m, a small number of firebrands showed a tendency to accumulate, rolling on the floor together, however those accumulations were not sustained at the end. This behavior is shown in **Figure 6**.

FIGURE 6 | Firebrand behavior under SD = 1 m and 8 m s^{-1}.

measured after each experiment (**Figure 7**). The accumulation distance in front of a structure is plotted against SD in **Figure 8A**, as well as the maximum length and width of firebrand accumulation zone in **Figures 8B and 8C**, respectively. **Figure 8A** showed that the D_f had a peak at SD = 2 m for experiments at 4 m s^{-1}, while the effect of SD is less clear in experiments at 6 m s^{-1}, due to two firebrand accumulation zones observed at SD = 1 m. In **Figure 8B**, the length of firebrand accumulation zone was longer at 4 than 6 m s^{-1}.

The length of the accumulation zone varies depending on SD, and that behavior for experiments at 4 m s^{-1} was the opposite to those at 6 m s^{-1} wind speed. The similarity between the two was a peak at 2 m SD, which was the same as the case for D_f under 4 m s^{-1} wind shown in **Figure 8A**.

Figure 8C shows that the width of firebrand accumulation zone was wider at 4 than 6 m s^{-1}, which is the same for length shown in **Figure 8B**. The total area of the accumulation zone was plotted in **Figure 8D**. It was observed that the higher wind speed led to a smaller accumulation zone. This is similar behavior to very simple wall experiments (Suzuki and Manzello, 2017a). Under 4 m s^{-1} wind speed, the size of the firebrand accumulation zone was similar, regardless of SD, yet it changed significantly under a 6 m s^{-1} wind. This, in some sense, is similar to the accumulation distance, as it indicated that wind profile changes more significantly between SD 1 and 2 m than between 2 and 3 m. This effect needs to be more carefully investigated as the minimum SD between buildings is 2 m. The firebrand accumulation behind the separation (downstream) under SD = 3 m and 4 m s^{-1} wind was located (**Figure 7**) between 1.4 and 2.1 m (L = 0.7 m) with the width 0.25 m and the area of 0.0829 m^2.

SIMULATIONS

The Fire Dynamic Simulator (FDS) was used to simulate the wind field of these experiments (McGrattan et al., 2013). FDS does not

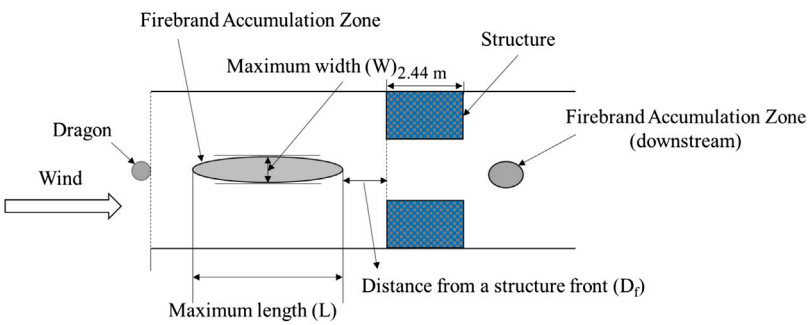

FIGURE 7 | Schematic of firebrand accumulation patterns and their dimensions.

The distance from the front of the structure (D_f), the maximum length (L), width (W) of firebrand accumulated area, and the total area of firebrand accumulation were contain firebrands; however, it was used to describe the firebrand accumulation behavior based on predicted wind profiles (Suzuki and Manzello, 2017a). Firebrands follow the wind as they are

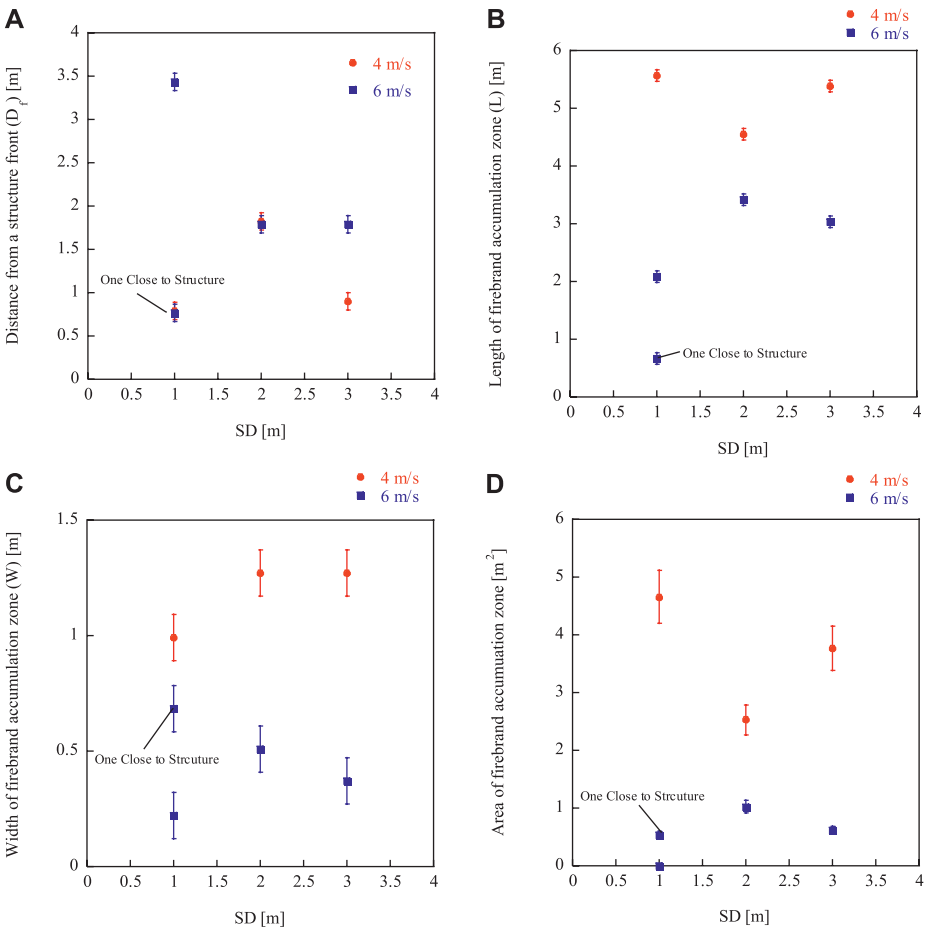

FIGURE 8 | Measurements of firebrand accumulation zone under 4 and 6 m s^{-1} wind experiments **(A)** Distance from a structure front D_f and SD **(B)** Length of firebrand accumulation zone (L) and SD **(C)** Width of firebrand accumulation zone (W) and SD **(D)** Area of firebrand accumulation zone and SD.

TABLE 1 | Conditions for FDS simulation.

Mesh size	**10 cm × 10 cm × 10 cm**
Simulation domain	5 m (W) × 16 m (L) × 20 m (H)
Simulation time	20 s
Wind speed	4, 6, 8, 10 m s^{-1}
Separation distance (SD) between structures	1, 2, 3 m

Wood pieces fed from Feeding System.

relatively light but not completely due to their mass. FRWTF was simulated with experimental structures and the NIST Dragon as an obstacle with the dimension of 5 m (W) × 16 m (L) × 20 m (H). The mesh size was 10 cm × 10 cm × 10 cm. The conditions of simulation are summarized in **Table 1**. After 10 s, modeling shows that the wind has stabilized. The simulation was performed up to 20 s for all cases in order to observe the repeated wind behavior.

In a simple calculation performed in (Suzuki and Manzello, 2017a), the wind speed of 2.3 m s^{-1} was the lowest wind speed for firebrands to move on the floor where the surface was relatively smooth considering the balance between friction force between a firebrand and the floor (gypsum board) and the wind force:

$$F_{friction} = F_{wind} \tag{1}$$

And

$$F_{friction} = \mu m_{firebrand} g \tag{2}$$

$$F_{wind} = \frac{1}{2}\rho_{air} v^2 \times A \tag{3}$$

Therefore, μ is the friction coefficient between a gypsum board and smoldering firebrands, $m_{firebrand}$ is the average mass of a firebrand, ρ_{air} is the density of the air, g is gravitation acceleration, v is wind speed on a firebrand and A is the average projected area of a firebrand. As seen in **Figure 4**, the mass and the size of firebrands under 4, 6, 8 and 10 m s^{-1} can be considered within the range of uncertainties (±10%), average of mass (0.05 g) and projected area (0.78 cm^2) was used for calculation. The

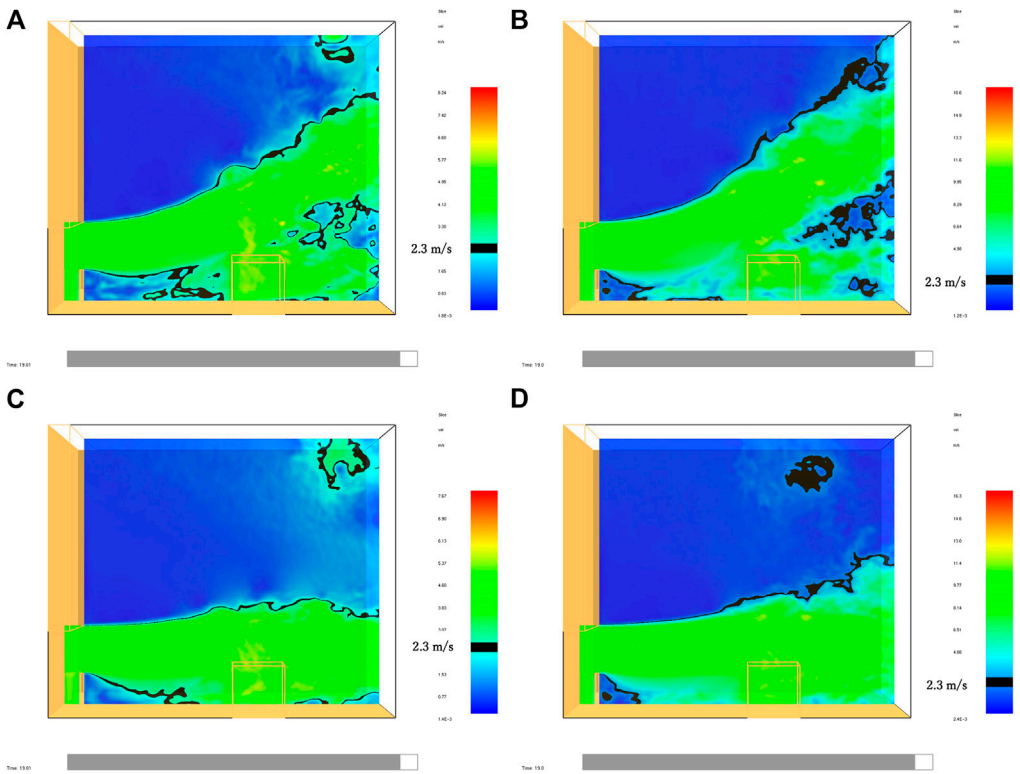

FIGURE 9 | FDS simulation results with different SD and wind speeds. Wind profile at centerline. Black line in the images shows wind speed of around 2.3 m s^{-1} **(A)** 4 m s^{-1} wind, SD = 1 m, **(B)** 8 m s^{-1} wind speed, SD = 1 m, **(C)** 4 m s^{-1} wind speed, SD = 3 m and **(D)** 8 m s^{-1} wind speed, SD = 3 m.

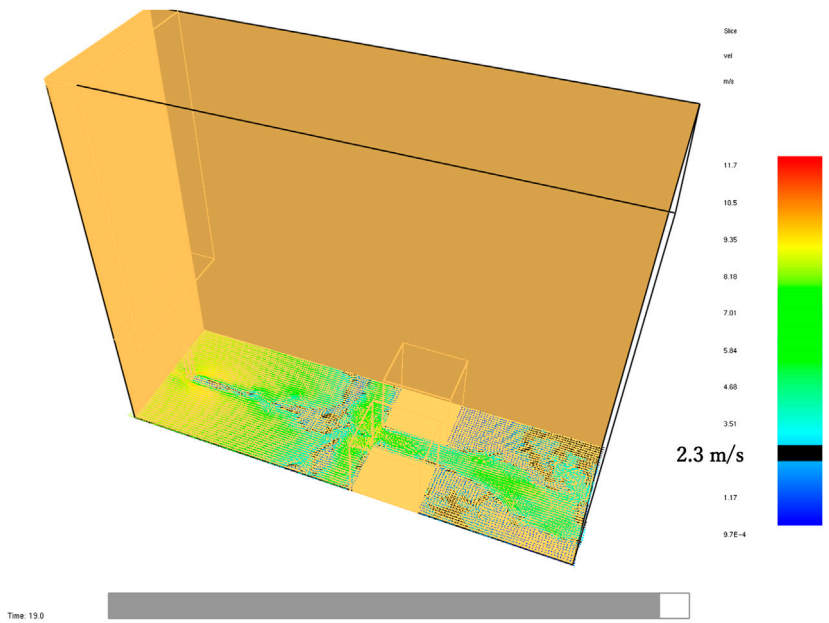

FIGURE 10 | FDS simulation results with 8 m s^{-1} wind speed and SD = 1 m. Wind profile at ground level.

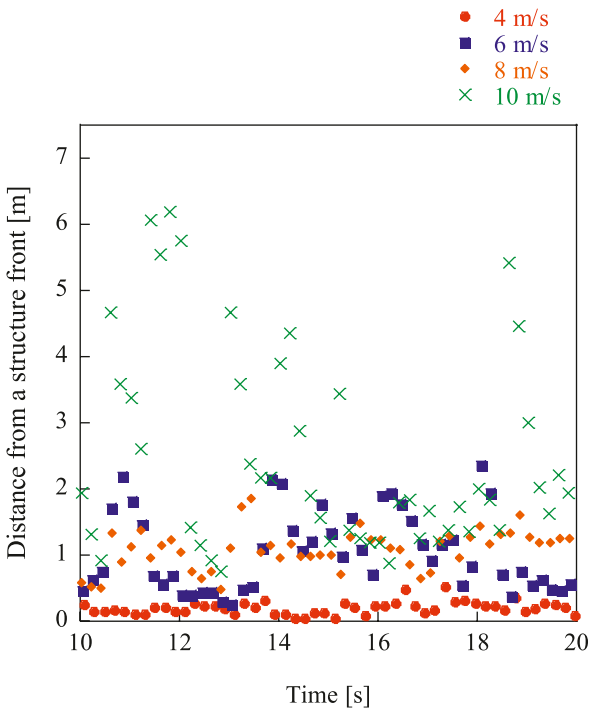

FIGURE 11 | Time varying distance from a stagnation zone (wind speed 2.3 m s^{-1}) from a structure front in FDS simulation under 1 m s^{-1} wind.

unknown parameter was μ, as there is no data available for a smoldering firebrand and a gypsum board. Therefore μ = 0.5 was used based on data for wood on wood (Japanese Society of Mechanical Engineers, 2004). Applying 2.3 m s^{-1} for the lowest wind speed for firebrands to move, we consider the stagnation zone (wind speed less than 2.3 m s^{-1}) as the firebrand accumulation zone.

An FDS simulation was performed using the conditions shown in **Table 1**. The FWTRF was simulated. **Figures 9** and **10** show the FDS simulation results under 4 and 8 m s^{-1} in the cases of SD = 1 m and 3 m. **Figures 9** and **10** shows the wind speed 2.3 m s^{-1} being marked in black. As shown in **Figure 9**, as the wind speed increases, the distance to the stagnation zone from the front of structures, D_f, decreases, and as SD become larger, wind between structures become less turbulent. **Figure 11** shows the distance to the stagnation zone from the front of structures, D_f, vs. time (10–20 s) in the case of 1 m SD for example. Overall, the D_f increases as the wind speed increases. Data from 4 m s^{-1} is relatively stable, while those from 10 m s^{-1} is changing a lot. Those from 6 m s^{-1} are fluctuating. It is assumed the two firebrand accumulation zones observed in experiments are due to this behavior. **Figure 12** shows the 10 s average, D_f, against wind speeds along with experimental results. Results from FDS shows that D_f increases as the wind speed increases. D_f also increases as SD increases with the exception of SD = 1 and 2 m under 6 m s^{-1} wind. This is interesting as experiments showed the wind profile around the structures may change between SD from 1 to 2 m, and SD from 2 to 3 m. Experimental data with SD = 1 m has similar D_f to FDS results while experimental results does not match well when SD = 2 or 3 m. For the same SD, as the wind speed increases the wind flow around structures becomes complicated, and it is expected firebrands may not follow the wind completely; the calculation deduced from simple analysis no longer works.

SUMMARY

Wind has an impact on the built environment. For large outdoor fire safety, wind plays a critical role, from enhancing flame spread processes to firebrand spotting. Firebrands fly far under high wind, which presents risks to many houses. This study focused on understanding firebrand behavior between two structures by varying the separation distances and wind speeds experimentally and by simulation. No significant accumulation was observed under 8 and 10 m s^{-1}, regardless of structure separation distance. The size of firebrand accumulation as well as distance from structure front was compared with separation distance in the cases of 4 and 6 m s^{-1} wind speeds. It was found that firebrands behave differently from SD = 1–2 m, to that of SD = 2–3 m. The results of this study are the first to explore these important interactions between firebrands and structure separation distances.

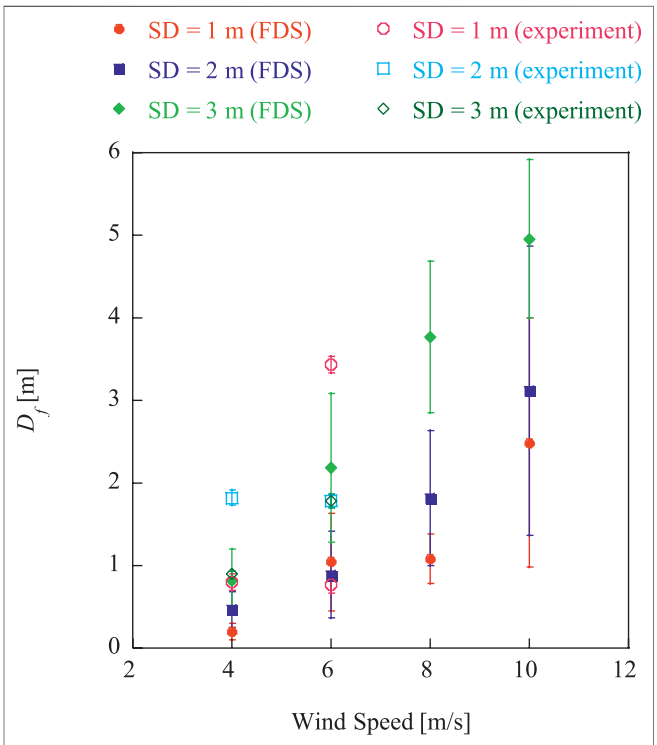

FIGURE 12 | Comparison between average distance from a stagnation zone (wind speed 2.3 m s^{-1}) from a structure front in FDS simulation and those in experiments.

DATA AVAILABILITY STATEMENT

The raw data supporting the conclusions of this article will be made available by the authors, upon request.

AUTHOR CONTRIBUTIONS

SS: Conceptualization, Investigation, Formal analysis, Writing - original draft. SM: Conceptualization, Investigation, Formal analysis, Writing - original draft.

REFERENCES

Albini, F. A. (1983). Transport of firebrands by line thermals. *Combust. Sci. Technol.* 32 (5–6), 277–288.

Albini, F. A. (1985). A model for fire spread in wildland fuels by-radiation†. *Combust. Sci. Technol.* 42, 229–258. doi:10.1080/00102208508960381

Albini, F. A., Alexander, M. E., and Cruz, M. G. (2012). A mathematical model for predicting the maximum potential spotting distance from a crown fire. *Int. J. Wildland Fire* 21, 609–627. doi:10.1071/wf11020

Alexander, M. E., and Cruz, M. G. (2006). Evaluating a model for predicting active crown fire rate of spread using wildfire observations. *Can. J. For. Res.* 36, 3015–3028. doi:10.1139/x06-174

Biswas, K., Werth, D., and Gupta, N. (2013). A home ignition assessment model applied to structures in the wildland-urban interface. Available at: https://web.ornl.gov/sci/buildings/conf-archive/2013%20B12%20papers/085_Biswas.pdf.

Blocken, B., and Carmeliet, J. (2004). A review of wind-driven rain research in building science. *J. Wind Eng. Ind. Aerod.* 92 (13), 1079–1130. doi:10.1016/j.jweia.2004.06.003

Chaves, M., Hajra, B., Stathopoulos, T., and Bahloul, A. (2011). Near-field pollutant dispersion in the built environment by CFD and wind tunnel simulations. *J. Wind Eng. Ind. Aerod.* 99 (4), 330–339. doi:10.1016/j.jweia.2011.01.003

Cheney, P., and Sullivan, A. (2008). *Grassfires: fuel, weather and fire behaviour*. 6th Edn. Melbourne, Australia: CSIRO Publishing.

Cohen, J. D. (2000). Preventing disaster: home ignitability in the wildland-urban Interface *J. For.* 98, 15–21.

Ellis, P. F. (2000). *The aerodynamic and combustion characteristics of eucalypt bark – a firebrand study*. Canberra, Australia: Australian National University.

Fernandez-Pello, A. C. (2017). Wildland fire spot ignition by sparks and firebrands. *Fire Saf. J.* 91, 2–10. doi:10.1016/j.firesaf.2017.04.040

Ganteaume, A., Hernando, C., Jappiot, M., and Fonturbel, T. (2009). Spot fires: fuel bed flammability and capability of firebrands to ignite fuel beds. *Int. J. Wildland Fire* 18 (8), 951–969. doi:10.1071/wf07111

Guijarro, L. H., Huo, R., and Yang, D. (2009). Large eddy simulation of fire-induced buoyancy driven plume dispersion in an urban street canyon under perpendicular wind flow. *J. Hazard Mater.* 166 (1), 394–406. doi:10.1016/j.jhazmat.2008.11.105

Japanese Society of Mechanical Engineers (2004). *JSME mechanical Engineers' handbook Alpha 2*. Maruzen (in Japanese).

Koo, E., Linn, R. R., Pagni, P. J., and Edminster, C. B. (2012). Modelling firebrand transport in wildfires using HIGRAD/FIRETEC. *Int. J. Wildland Fire* 21, 396–417. doi:10.1071/wf09146

Koo, E., Pagni, P., Stephens, S., Huff, J., Woycheese, J., and Weise, D. (2005). A simple physical model for forest fire spread rate. *Fire Saf. Sci.* 8, 851–862. doi:10.3801/iafss.fss.8-851

Lee, S.-L., and Hellman, J. M. (1969). Study of firebrand trajectories in a turbulent swirling natural convection plume. *Combust. Flame* 13 (6), 645–655. doi:10.1016/0010-2180(69)90072-8

Manzello, S. L. (2014). Enabling the investigation of structure vulnerabilities to wind- driven firebrand showers in wildland-urban interface (WUI) fires. *Fire Saf. Sci.* 11, 83–96. doi:10.3801/iafss.fss.11-83

Manzello, S. L., Suzuki, S., and Nii, D., Full-scale experimental investigation to quantify building component ignition vulnerability from mulch beds attacked by firebrand showers. *Fire Technol.* 53, 535–551. doi:10.1007/s10694-015-0537-3

Manzello, S. L., Blanchi, R., Gollner, M. J., Gorham, D., McAllister, S., Pastor, E., et al. (2018). Summary of workshop large outdoor fires and the built environment. *Fire Saf. J.* 100, 76–92. doi:10.1016/j.firesaf.2018.07.002

Manzello, S. L., Suzuki, S., Gollner, M. J., and Fernandez-Pello, A. C. (2020). Role of firebrand combustion in large outdoor fire spread. *Prog. Energy Combust. Sci.* 76, 100801. doi:10.1016/j.pecs.2019.100801

Manzello, S. L., Suzuki, S., and Hayashi, Y. (2012). Enabling the study of structure vulnerabilities to ignition from wind driven firebrand showers: a summary of experimental results. *Fire Saf. J.* 54, 181–196. doi:10.1016/j.firesaf.2012.06.012

Manzello, S. L., and Suzuki, S. (2020). Influence of angle orientation on firebrand production from the combustion of surrogate photovoltaic (PV) panel assemblies exposed to applied wind fields. *Fuel* 279, 118507. doi:10.1016/j.fuel.2020.118507

Manzello, S. L., and Suzuki, S. (2012). 'The new and improved NIST dragon's LAIR (lofting and ignition research) facility: coupling the reduced scale continuous feed firebrand generator to bench scale wind tunnel'. *Fire Mater.* 36 (8), 623–635. doi:10.1002/fam.1123

Manzello, S., and Suzuki, S. (2014). Exposing decking assemblies to continuous wind-driven firebrand showers. *Fire Saf. Sci.* 11, 1339–1352. doi:10.3801/iafss.fss.11-1339

Maranghides, A., and Johnsson, E. (2008). *Residential structure separation fire experiments*. Gaithersburg, ML: NIST TN, TN1600.

Martin, J., and Hillen, T. (2016). The spotting distribution of wildfires. *Appl. Sci.* 6, 177. doi:10.3390/app6060177

McGrattan, K., Hostikka, S., Floyd, J., McDermott, R., and Vanella, M. (2013). in *Fire dynamics simulator, User's Guide*. 6th Edn. Finland, United Kingdom: National Institute of Standards and Technology, and VTT Technical Research Centre of Finland.

Mell, W., and Maranghides, M. (2009). A case study of a community affected by the Witch and Guejito Fires. NIST Technical Note 1635.

Morandini, F., Santoni, P. A., and Balbi, J. H. (2001). The contribution of radiant heat transfer to laboratory-scale fire spread under the influences of wind and slope. *Fire Saf. J.* 36 (6), 519–543. doi:10.1016/s0379-7112(00)00064-3

Morandini, F., and Silvani, X. (2010). Experimental investigation of the physical mechanisms governing the spread of wildfires. *Int. J. Wildland Fire* 19, 570–582.

Pitts, W. M. (1991). Wind effects on fires. *Prog. Energy Combust. Sci.* 17 (2), 83–134. doi:10.1016/0360-1285(91)90017-h

Potter, B. (1996). Atmospheric properties associated with large wildfires. *Int. J. Wildland Fire* 6, 71–76. doi:10.1071/wf9960071

Quyang, Q., Dai, W., Li, H., and Zhu, Y. (2006). Study on dynamic characteristics of natural and mechanical wind in built environment using spectral analysis. *Build. Environ.* 41 (4), 418–426.

Razak, A., Hagishima, A., Ikegaya, N., and Tanimoto, J. (2013). Analysis of airflow over building arrays for assessment of urban wind environment. *Build. Environ.* 59, 56–65. doi:10.1016/j.buildenv.2012.08.007

Rothermel, R. (1972). A mathematical model for predicting fire spread in wildland fuels. Ogden, UT: U.S. Department of Agriculture, Intermountain Forest and Range Experiment Station.

Shah, K. B., and Ferziger, J. H. (1997). A fluid mechanicians view of wind engineering: large eddy simulation of flow past a cubic obstacle. *J. Wind Eng. Ind. Aerod.* 67-68, 211–224. doi:10.1016/s0167-6105(97)00074-3

Sharples, J., McRae, R. H. D., and Wilkes, S. R. (2012). Wind - terrain effects on the propagation of wildfires in rugged terrain: fire channelling. *Int. J. Wildland Fire* 21, 282–296. doi:10.1071/wf10055

Song, J., Huang, X., Liu, N., Li, H., and Zhang, L. (2017). The wind effect on the transport and burning of firebrands. *Fire Technol.* 53, 1555–1568. doi:10.1007/s10694-017-0647-1

Sullivan, A. L. (2009). Wildland surface fire spread modelling, 1990 - 2007. 1: physical and quasi-physical models. *Int. J. Wildland Fire* 18, 349–368. doi:10.1071/wf06143

Suzuki, S., and Manzello, S. L. (2017a). Experimental investigation of firebrand accumulation zones in front of obstacles. *Fire Saf. J.* 94, 1–7. doi:10.1016/j.firesaf.2017.08.007

Suzuki, S., and Manzello, S. L. (2017b). Experiments to provide the scientific-basis for laboratory standard test methods for firebrand exposure. *Fire Saf. J.* 91, 784–790. doi:10.1016/j.firesaf.2017.03.055

Suzuki, S., and Manzello, S. L. (2020a). Garnering understanding into complex firebrand generation processes from large outdoor fires using simplistic laboratory-scale experimental methodologies. *Fuel* 267, 117154. doi:10.1016/j.fuel.2020.117154

Suzuki, S., and Manzello, S. L. (2020b). Role of accumulation for ignition of fuel beds by firebrands. *App. Energy Comb. Sci.* 1-4, 100002. doi:10.1016/j.jaecs.2020.100002

Suzuki, S., Manzello, S. L., and Hayashi, Y. (2013). The size and mass distribution of firebrands collected from ignited building components exposed to wind. *Proc. Combust. Inst.* 34 (2), 2479–2485. doi:10.1016/j.proci.2012.06.061

Suzuki, S., and Manzello, S. L. (2019). Investigating effect of wind speeds on structural firebrand generation in laboratory scale experiments. *Int. J. Heat Mass Tran.* 130, 135–140. doi:10.1016/j.ijheatmasstransfer.2018.10.045

Suzuki, S., Manzello, S. L., Kagiya, K., Suzuki, J., and Hayashi, Y., (2015). Ignition of mulch beds exposed to continuous wind-driven firebrand showers, *Fire Technol.*, 51:905–922. doi:10.1007/s10694-014-0425-2

Suzuki, S., and Manzello, S. L. (2021). Towards understanding the effect of cedar roof covering application on firebrand production in large outdoor fires. *J. Clean. Prod.* 278, 123243. doi:10.1016/j.jclepro.2020.123243

Syphard, A. D., Keeley, J. E., Massada, A. B., Brennan, T. J., and Radeloff, V. C. (2012). Housing arrangement and location determine the likelihood of housing loss due to wildfire. *PLoS One* 7 (3), e33954. doi:10.1371/journal.pone.0033954

Tarifa, C. S., Notario, P. P. d., and Moreno, F. G. (1965). On the flight paths and lifetimes of burning particles of wood. *Symp. Int. Comb.* 10, 1021–1037. doi:10.1016/s0082-0784(65)80244-2

Tohidi, A., and Kaye, N. B. (2017a). Comprehensive wind tunnel experiments of lofting and downwind transport of non-combusting rod-like model firebrands during firebrand shower scenarios. *Fire Saf. J.* 90, 95–111. doi:10.1016/j.firesaf.2017.04.032

Tohidi, A., and Kaye, N. B. (2017b). Stochastic modeling of firebrand shower scenarios. *Fire Saf. J.* 91, 91–102. doi:10.1016/j.firesaf.2017.04.039

Tohidi, A., Kaye, N., and Bridges, W. (2015). Statistical description of firebrand size and shape distribution from coniferous trees for use in Metropolis Monte Carlo simulations of firebrand flight distance. *Fire Saf. J.* 77, 21–35. doi:10.1016/j.firesaf.2015.07.008

Trucchia, A., Egorova, V., Butenko, A., Kaur, I., and Pagnini, G. (2019). RandomFront 2.3: a physical parameterisation of fire spotting for operational fire spread models - implementation in WRF-SFIRE and response analysis with LSFire+. *Geosci. Model Dev.* 12, 69–87. doi:10.5194/gmd-12-69-2019

Wang, S., Huang, X., Chen, H., and Liu, N. (2017). Interaction between flaming and smouldering in hot-particle ignition of forest fuels and effects of moisture and wind. *Int. J. Wildland Fire* 26 (1), 71–81. doi:10.1071/wf16096

Weber, R. O. (1989). Analytical models for fire spread due to radiation. *Combust. Flame* 78, 398–408. doi:10.1016/0010-2180(89)90027-8

Weber, R. O. (1991). Modelling fire spread through fuel beds. *Prog. Energy Combust. Sci.* 17 (1), 67–82. doi:10.1016/0360-1285(91)90003-6

Yuan, C., and Ng, E. (2012). Building porosity for better urban ventilation in high-density cities - a computational parametric study. *Build. Environ.* 50, 176–189. doi:10.1016/j.buildenv.2011.10.023

Conflict of Interest: The authors declare that the research was conducted in the absence of any commercial or financial relationships that could be construed as a potential conflict of interest.

frontiers in Mechanical Engineering

ORIGINAL RESEARCH
published: 16 March 2021
doi: 10.3389/fmech.2021.630324

Critical Ignition Conditions of Wood by Cylindrical Firebrands

Hamed Salehizadeh[1†], *Raquel S. P. Hakes*[1†] *and Michael J. Gollner*[1,2*]

[1] *Department of Fire Protection Engineering, University of Maryland, College Park, MD, United States,* [2] *Department of Mechanical Engineering, University of California, Berkeley, Berkeley, CA, United States*

This study investigated the thermal conditions preceding ignition of three dense woody fuels often found on structures by firebrands, a major cause of home ignition during wildland-urban interface (WUI) fires. Piles of smoldering cylindrical firebrands, fabricated from wooden dowels, were deposited either on a flat inert surface instrumented with temperature and heat flux sensors or on a target fuel (marine-grade plywood, oriented-strand board, or cedar shingles) to investigate critical conditions at ignition. The former provided thermal data to characterize the time before and at ignition, while the latter provided smoldering and flaming ignition times. Tests were conducted in a small-scale wind tunnel. Larger firebrand piles produced higher temperatures at the center of the pile, thought to be due to re-radiation within the pile. Ignition was found to be dependent on target fuel density; flaming ignition was additionally found to be dependent on wind speed. Higher wind speeds increased the rate of oxidation and led to higher temperatures and heat fluxes measured on the test surface. The heat flux at ignition was determined by combining results of inert and ignition tests, showing that ignition occurred while transient heating from the firebrand pile was increasing. Ultimately, critical ignition conditions from firebrand pile exposure are needed to design appropriate fire safety standards and WUI fire modeling.

Keywords: critical ignition conditions, WUI fuels, wildland fire, firebrand ignition, embers

OPEN ACCESS

Edited by:
Domingos Xavier Viegas, University of Coimbra, Portugal

Reviewed by:
Xinyan Huang, Hong Kong Polytechnic University, Hong Kong
Wei Tang, National Institute for Occupational Safety and Health (NIOSH), United States
Albert Simeoni, Worcester Polytechnic Institute, United States

***Correspondence:**
Michael J. Gollner
mgollner@berkeley.edu

[†]These authors have contributed equally to this work

Specialty section:
This article was submitted to Thermal and Mass Transport, a section of the journal Frontiers in Mechanical Engineering

Received: *17 November 2020*
Accepted: *22 February 2021*
Published: *16 March 2021*

Citation:
Salehizadeh H, Hakes RSP and Gollner MJ (2021) Critical Ignition Conditions of Wood by Cylindrical Firebrands. Front. Mech. Eng. 7:630324. doi: 10.3389/fmech.2021.630324

1. INTRODUCTION

Over the past few decades, losses from fires at the wildland-urban interface (WUI) have increased dramatically (Caton et al., 2016). The WUI, the area where human development intermixes or borders undeveloped wildland (Radeloff et al., 2005), represents a confluence of structures and surrounding flammable vegetation. Previous investigations have shown that firebrands are a major cause of fire spread during WUI fires, igniting structures and secondary fires far away from the main fire front (Mell et al., 2010), thus complicating suppression efforts. While early works by Cohen (2008) and numerous investigations by Maranghides and Mell (2011), Maranghides et al. (2013), Maranghides et al. (2015), and Maranghides and McNamara (2016) have shown that firebrands are a major source of structural losses, our understanding of the physical mechanisms by which firebrands generate, loft, and eventually ignite structures is still in its early stages (Caton et al., 2016; Manzello et al., 2020).

To better understand potential metrics to quantify critical ignition conditions for structural fuels exposed to firebrand piles, this study investigates the heating from and ignition by firebrand piles under wind on a small-scale, building on initial work by Hakes et al. (2019). The goal of this study is to quantify heat flux conditions at ignition of dense fuels representative of WUI fuels.

This work applies the methodology developed by Hakes et al. (2019) and later used by Tao et al. (2020) to measure heat fluxes from piles of firebrands under various wind conditions and understand how these conditions relate to those which cause flaming and smoldering ignition of various WUI materials. Measurements are conducted over both an inert substrate and with representative WUI fuels, allowing for the influence of a target material to be separated from firebrand pile heating. The effect of wind, both on the heat flux and on the time to ignition, has been investigated.

2. LITERATURE REVIEW

There have been a number of studies on firebrand ignition, which can loosely be split into small-scale studies on ignition by individual firebrands or of vegetative fuels (Manzello et al., 2006; Ellis, 2015; Fernandez-Pello et al., 2015; Wang et al., 2017; Urban et al., 2018) and large-scale studies on structural components exposed to firebrand showers. Previous studies and post-fire investigations of ignition by firebrands in the WUI (Manzello et al., 2009; Maranghides et al., 2013) have found that firebrands frequently form piles on structural fuels prior to ignition, especially in crevices or corners around the exterior of structures. As a result, ignition of structural elements in WUI fires is expected to occur differently than ignition by a single firebrand, since individual firebrands exhibit different thermal characteristics than piles of firebrands (Hakes et al., 2019). Additionally, vegetative fuels ignite differently than dense materials, such as wooden structural elements used on residential homes, necessitating the study of solid fuels. Larger-scale studies have mostly focused on the generation of firebrand "showers" and large wind-driven depositions of and ignition by firebrands in a wind tunnel setting (Manzello et al., 2012; Manzello and Suzuki, 2017). Investigations of accumulated firebrand piles under wind are more realistic; however, they are difficult to reproduce on a small-scale in the laboratory and require extensive characterization.

A recent small-scale study by Hakes et al. (2019) investigated heat fluxes from piles of firebrands, finding that larger pile sizes increased rates of heating while the effect of firebrand diameter was relatively negligible for all cylindrical firebrands. Most tests were performed under ambient conditions; however, one test was performed at a higher wind speed. This wind test presented a dramatic increase in heating and reduction in the time to flaming ignition of the tested target fuel. Another recent study led by the senior author investigated the effect of firebrand size and shape on heating under different wind speeds (Tao et al., 2020). They found that piles from real firebrand fuels, such as barks and sticks, achieved higher peak heat fluxes at higher wind speeds than firebrand piles produced from artificial birch fuels, which exhibited little change with firebrand geometry. This effect was mostly attributed to the porosity of the firebrand pile; however, the effect of the mass of the firebrand pile and ignition of recipient WUI fuels were not studied. Bearinger et al. (2020) recently used IR thermography and inverse heat transfer analysis to measure localized heat transfer from firebrands to an inert surface. They found relatively high localized heat fluxes ($80-105\ kW/m^2$) from individual firebrands under a $1-2$ m/s wind speed; however, when these heat fluxes were averaged over an area the size of the heat flux gauge used in Hakes et al. (2019), heat fluxes were in a similar range (7–25 kW/m^2). Hakes et al. (2019) also hypothesized that structural fuels ignite in a smoldering state and then transition to flaming. Numerous previous studies have investigated the transition from smoldering to flaming; however, work on transition to flaming has primarily focused on less dense fuels such as foams (Ohlemiller, 1990; Tse et al., 1996) and remains challenging to model and predict (Dodd et al., 2012).

In summary, there is a need for improved physical understanding of firebrand ignition behavior, especially for structural fuels. In particular, previous studies on firebrand ignition have not described the thermal conditions at ignition of dense WUI fuels, conditions which are needed to determine critical ignition criteria for firebrand exposure. Minimum conditions that can cause ignition are unknown, although the importance of wind in contributing to ignition has been highlighted extensively. Additionally, it is necessary to understand the heating expected under worst-case firebrand loading scenarios. Ultimately, quantification of critical ignition criteria for firebrand exposure is necessary to design appropriate fire safety standards and to model propagation of wildland fires through WUI areas.

3. MATERIALS AND METHODS

Two series of tests were performed in this experimental study. First, inert tests were performed to characterize thermal conditions of a pile of smoldering firebrands over an inert sample, using an array of thin-skin calorimeters (TSCs), a water-cooled heat flux gauge (WC-HFG), and K-type thermocouples (TCs). Second, for ignition tests, a pile of smoldering firebrands was deposited over a target fuel, and ignition time was recorded. Both inert thermal characterization tests and ignition tests were performed in a small, enclosed wind tunnel that produced wind speeds in the range of 0.5–3.5 m/s. The wind tunnel had a 30 × 30 cm inlet which reduced into a 25 × 7.5 cm test section made of stainless steel. Gases were exhausted through a high-temperature variable fan. The interior of the wind tunnel was painted matte black to reduce re-radiation, and a 20 × 6 cm window of borosilicate glass provided visual access to the experiments. At the bottom of the wind tunnel, experiments were placed in a 15 × 12 cm hole, as shown in **Figures 1**, **2**. An additional 1.5 cm diameter hole located past the reducing section and before the test sample allowed for wind speed measurements with a hot-wire anemometer. Wind speeds were measured as a function of height, revealing a relatively flat profile at the inlet (Salehizadeh, 2019). The firebrand pile blocked a relatively large portion of the wind tunnel, which caused the wind speed over the firebrand pile to actually be lower than the wind speed setting. This effect was measured for several different pile sizes to calibrate the wind speed setting with the "corrected" wind speed that the firebrands actually experience. Wind speeds given throughout this paper are for this corrected wind speed.

Firebrands were fabricated from 1.27 cm diameter and 2.54 cm long cylindrical birch wooden dowels. All dowels were cut and fully dried in an oven at 103°C before testing. Dowels were measured to have an initial density of $527 \pm 16\ kg/m^3$ based on

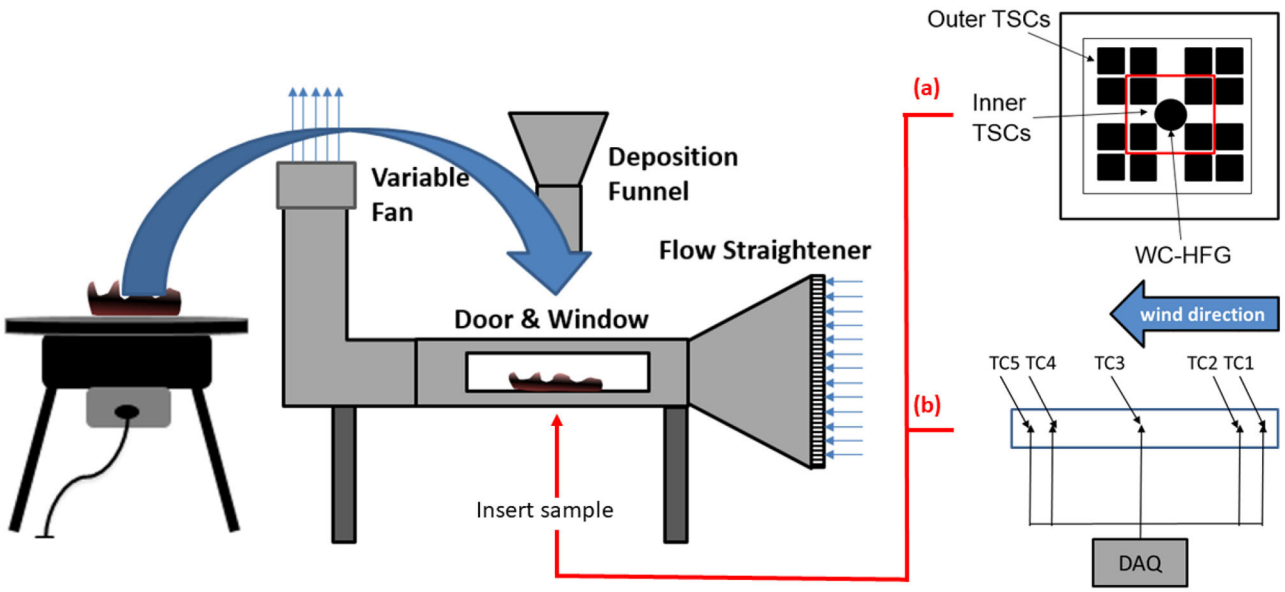

FIGURE 1 | Schematic of the experimental setup, from left to right: burner used to ignite firebrands (modified figure from Caton, 2016), enclosed wind tunnel, **(a)** sensor array for inert tests with thin-skin calorimeters (TSC) and a water-cooled heat flux gauge (WC-HFG), and **(b)** thermocouple (TC) array for ignition tests, and data acquisition (DAQ) system.

FIGURE 2 | Photograph of the experimental setup **(left)** with an inert sensor array mounted and **(right)** a photograph showing cylindrical brands just before flames die out and firebrands are deposited on the test surface.

mass and geometry measurements of a sampling of cut dowels. The density of birch is slightly higher than those wood species, such as pine, typically found in WUI fires; however, it was not possible to source the desired quantity of the lower density materials for the firebrand diameter and shape considered here. We chose to use birch as a surrogate which could be readily supplied for the experiments and was used in previous firebrand ignition experiments (Hakes et al., 2019). Smoldering firebrands were fabricated following the method described in Hakes et al. (2019) by placing the dowels in a mesh basket over a large propane burner, shown on the left in **Figure 1** and on the right in **Figure 2**. Once all firebrands achieved flaming (after 10–15 s

depending on the pile size), the propane burner was turned off and the firebrands were allowed to burn until all flaming combustion ceased.

Firebrands were deposited on the experimental setup in a smoldering state using a funnel-like dumper. This dumper was used so that the firebrand pile was ensured of being deposited on the sensor array; both dumper outlet area and array area were approximately 10 × 10 cm. There was some natural variation in the deposition of the pile, meaning that there was variation in the contact area between the firebrands and the sensors. While this deposition method is anticipated to slightly increase variability between tests, the time-dependent deformation of smoldering wood as it transitions to ash adds inherent variability to this physical process, even for individual firebrand placement. Despite the associated uncertainty, clear and repeatable trends are still extracted by repeating experiments multiple times. Fully depositing the firebrand pile also allows for simulation of a worst-case heating scenario, capturing the initial high heat fluxes, conditions that could not be captured by placing each firebrand individually.

Three firebrand loading conditions were used for both inert and ignition tests. Initial mass of the wood was measured and resulted in smoldering piles about 16% the mass of the original wooden dowels, as shown in **Table 1**. For simplicity, the three piles will be referred to as 16, 8, and 4 g piles in the rest of the paper. As an indicator of the porosity, the bulk density of the resulting piles was also examined using volume measurements from side-view photographs of the pile and mass measurements from a load cell. Three tests for each deposited mass of 4, 8, and 16 g were chosen and pictures from a side and front view of the pile were analyzed with the software ImageJ. The volume of the pile was calculated based on the average height of the pile and the contact area between the pile and inert sample, approximately 10 × 10 cm, the area of the funnel-like dumper used. The bulk density of the pile, also shown in **Table 1**, was found to increase—indicating a decrease in porosity—with increasing deposited mass of firebrands. Bulk density is recorded for reference, but not varied in these experiments (i.e., the firebrand pile was never compacted).

3.1. Inert Tests

Inert tests for thermal characterization were conducted by depositing a firebrand pile on a 1.27 cm thick sheet of ceramic insulation board (SuperWool 607), which was used to simulate a relatively adiabatic surface. Three types of sensors were inserted into the insulation board, flush with its surface, to take thermal measurements beneath the pile. These sensors included a single WC-HFG, which was inserted in the center of an array of sixteen TSCs, as shown in **Figure 1a**. Five K-type TCs, fabricated in-house, were used for temperature measurement. The number of repetitions for each condition was determined based on the variability of the results and will be discussed with the heat flux results. These tests were conducted under wind speeds varying from 0.5 to 2.0 m/s. This range was selected because wind speeds greater than 2 m/s moved and eventually blew away firebrands in 4 and 8 g piles. While these wind speeds are much lower than free-stream wind speeds expected in a WUI fire, speeds will reduce close to the surface due to boundary-layer effects, potential obstructions, and re-circulation zones adjacent to buildings.

First, a 1.27 cm diameter Medtherm Schmidt-Boelter WC-HFG (model GTW-7-32-485A, range: 0–70 kW/m^2, maximum non-linearity ±2% of range, repeatability ±0.5%) was used to precisely measure the time-resolved heat flux beneath the center of the array. This type of WC-HFG is typically used for incident radiant heat flux measurement, but is used here following the methodology of Hakes et al. (2019). Although the WC-HFG is exposed to conductive heat fluxes, these conductive fluxes are negligible, as firebrands are rarely fully in contact with the gauge surface. Instead, ash and air pockets may block the firebrand from being fully in contact with the surface (Bearinger et al., 2020). Additionally, previous work (Hakes et al., 2019) presenting spatial maps of heat flux from individual firebrands shows radiation measured by sensors near the firebrand, but not in contact with it, indicating that even individual firebrands produce radiative heat fluxes. A firebrand pile is a non-contiguous heat source and, thus, expected to be dominated by radiation (Babrauskas, 2003). In order to account for the effect of ash on the surface of the WC-HFG, the gauge was regularly re-painted and re-calibrated. The WC-HFG was inspected visually after each test and was painted and calibrated with a frequency based on visual inspection of the surface paint on the gauge and heat fluxes reached during the test. Calibration was performed using a radiant cone heater, comparing measured heat flux values against a NIST-traceable calibration gauge. For smaller firebrand loading conditions (at lower wind speeds), the gauge was calibrated and re-painted at least every ten tests; for larger firebrand loading conditions (and higher wind speeds), the gauge was calibrated at least every five tests.

One concern with the use of a WC-HFG is whether the cooling of the gauge will also provide cooling to the firebrand pile. Previous work by Hakes (2017) compared the cooling to a firebrand pile from two WC-HFGs of different diameters, a 2.54 cm diameter gauge and a 1.27 cm diameter gauge. The latter is the size of the gauge used in the present study. That study found clear effects of cooling from the 2.54 cm gauge: tests on 8 g firebrand piles using the 2.54 cm gauge were 250–750 s shorter than those using the 1.27 cm gauge. Additionally, heat fluxes measured were on average lower when measured with the 2.54 cm gauge as opposed to the 1.27 cm gauge, indicating a cooling effect from the larger gauge. A comparison between heat fluxes measured by the 1.27 cm WC-HFG and an array of 16 TSCs found that heat fluxes measured by the WC-HFG were slightly lower than those measured by the TSCs (Hakes, 2017). It is unclear whether

TABLE 1 | Firebrand loading conditions for three pile sizes used in inert and ignition tests.

Wood pile mass (g)	Deposited firebrand pile mass (g)	Bulk pile density (kg/m^3)
100	16.4 ± 0.68	54.0 ± 8.1
50	8.14 ± 0.38	46.8 ± 4.1
25	4.18 ± 0.65	38.3 ± 2.8

these results indicate cooling from the 1.27 cm WC-HFG or a heating time-lag associated with the TSCs. In the present study, the uncertainty due to potential cooling from the WC-HFG is estimated to be on the order of ∼10% at most. The potential cooling was estimated for a firebrand pile at a temperature of 800°C, an average based on Urbas et al. (2004), Caton et al. (2016), and Urban et al. (2019), with a gauge held at the water temperature of 20°C, assuming radiative heat transfer between the firebrands and the WC-HFG. Given the difference in size between the pile and the gauge, cooling by the WC-HFG is ∼10% for the worst case scenario (i.e., the lowest longtime heat fluxes measured). For the larger pile and highest wind cases, this loss is expected to be much lower.

To provide a spatial representation of temperature, 16 TSCs were fabricated in-house by spot welding a 30 gauge Chromel-Alumel K-Type thermocouple to the back of a 1 × 1 cm Inconel alloy 625 plate, of thickness 0.1 cm. The top surface of the TSC was painted matte black using high temperature Zynolyte paint in order to reduce the reflectively of the alloy plate and, subsequently, the re-radiation from the TSCs to the firebrands. The TSC array was split into two regions, as shown in **Figure 1a**: a set of inner TSCs to determine the temperature at the center of the firebrand pile, and a set of outer TSCs to indicate the temperature at the edges of the firebrand pile. While originally designed for heat flux measurements, TSCs have been found to provide a reliable, spatially-resolved surface temperature measurement, albeit with a slow time response. The viability of using TSCs for temperature measurements at the surface was verified by using five fine-wire, 30 gauge K-type thermocouples, placed adjacent to the surface of five TSCs, which provided relative measurements of temperature on the inert surface during the test. Further details on the construction and selection of TSCs can be found in Hakes (2017) and Hakes et al. (2019).

3.2. Ignition Tests

Ignition tests were performed by depositing firebrand piles over target fuels which represented WUI materials. Three target fuels were tested: marine-grade plywood, oriented-strand board (OSB) and cedar shingles, all of which were chosen based on availability, uniformity, and a range of densities which are expected to produce varying ignition behavior. The density of each target fuel was calculated using mass and volume measurements for five samples of each fuel type after the samples had been fully dried to 0% moisture content (MC). The target fuel densities measured were 565.4 ± 12.5, 662.6 ± 11.1, and 305.2 ± 5.0 kg/m^3 for plywood, OSB and cedar, respectively. Sample thickness ranged from 0.7 to 1 cm for cedar samples and 1–1.2 cm for OSB and plywood samples. For OSB and plywood, variation in thickness was due to manufacturer error. For cedar samples, cedar shingles decreased in thickness from one side to the opposite one. Ignition tests were performed under a narrower band of wind speeds from 0.5 to 1.4 m/s. Higher wind speeds resulted in a rapid transition to flaming that was not sustainable in the test apparatus. A minimum of five test repetitions were conducted for each fuel/wind speed condition.

The ignition test setup was instrumented with a side-view video camera and TCs embedded in the target fuel to measure both flaming and smoldering ignition times, shown in **Figure 3**. Ignition time was measured from the time of firebrand deposition on the target fuel. The flaming ignition time was determined using a video camera to observe when flames anchored to the fuel surface, rather than to firebrands in the pile. The smoldering ignition time was determined using five K-type thermocouples pinned inside the target fuel, 0.5 cm below the top surface, as shown schematically in **Figure 1b**. Smoldering ignition time was determined as the time it took for one of the five TCs to reach a threshold temperature. Preliminary tests were conducted with a range of firebrand loading conditions to determine a representative threshold temperature for smoldering. Target fuel samples were extinguished and cut at various times to expose the smoldering front, denoted visually as the blackened section of the wood. For samples where this front reached the embedded thermocouples, a threshold temperature of 200°C was determined, above which the fuel sample blackened completely. This threshold temperature is thought to be lower than realistic smoldering temperatures because thermocouples, initially in contact with the sample, became detached from the wood when the front approached. It is also possible that this blackened region

FIGURE 3 | (Left) Photograph of a sample of plywood instrumented with thermocouples and attached to the DAQ card used in the experiment and **(right)** a representative smoldering firebrand pile with wind flowing from right to left.

represented pyrolysis of the fuel; however, the fuel samples were observed to be in a glowing condition at least at the surface for the majority of tests where smoldering was indicated by the temperature threshold. The thermal wave appears to move linearly through the sample making the trends observed valid regardless of the choice. This definition was still useful as it helped to segregate a point of self-propagating smoldering; at lower temperatures, smoldering was only maintained by the heating of the firebrand pile. For all experiments, this threshold temperature was reached first by TC3, the thermocouple below the center of the pile, as shown in **Figure 1b**.

4. RESULTS

Results are presented first for inert thermal characterization tests and second for ignition tests. Heat fluxes and temperatures from the inert tests are compared with time to smoldering or flaming ignition in the ignition tests to shed light on the phenomena leading to ignition of different materials.

4.1. Inert Thermal Characterization

Both time-resolved single-point heat flux measurements and time-resolved spatial temperature measurements were taken for varying firebrand deposited pile mass and wind speed conditions.

4.1.1. Heat Flux Results

For each test, heat flux over time was recorded from the WC-HFG. Subsequently, the heat fluxes from individual tests under the same conditions were averaged to provide an average heat flux curve for each pile size and wind speed test condition. **Figure 4** shows both the individual test heat flux curves as well as the averaged heat flux curve for two test conditions: 16 g of smoldering birch dowels deposited on the inert sensor array for wind speeds of 1.2 and 1.4 m/s. For all tests, there is an initial heat flux spike at the beginning of the test which is not sustained. This spike occurs when the firebrand pile is first placed on the WC-HFG and is not considered as part of the analysis here. After the firebrand pile is deposited, the heat flux increases to a peak, between 500 and 1,000 s on average in the tests shown here, then decays gradually as the firebrand pile cools.

Included in **Figure 4** is the standard deviation for the averaged curve. The standard deviation between tests increases as the variability of tests increases. The number of tests performed at each condition was determined based on the variability of the heat flux measurements from test to test. At 1.2 and 1.4 m/s, which both lie at the transition point between smoldering and flaming, 11 and 7 test repetitions, respectively, were performed. A lower wind speed of 0.5 m/s exhibited repeatable behavior and only three tests were performed. The large standard deviations shown for 1.2 and 1.4 m/s are indicative of the stochastic nature of transition between flaming and smoldering. Indeed, even for experiments over an inert substrate, piles of firebrands sometimes transitioned to flaming under high enough wind speeds, dramatically affecting the heat fluxes measured. The probability of transition to flaming for a firebrand pile on the inert surface was determined from recorded videos of experiments for each wind speed and deposited mass condition. The transition from smoldering to flaming (using a probability threshold of 0.5) occurred at around 1.2 m/s for 16 g and 1.4 m/s for 8 g deposited mass piles. It is expected that the probability of transition to flaming may be responsible for some of the variability between the tests.

4.1.2. Temperature Results

For inert tests, temperatures beneath the firebrand pile were recorded using the TSC array. Averaged temperatures of the inner and outer group TSCs (shown in **Figure 1a**) provide representative temperatures for the center of the pile and perimeter of the pile, respectively. The averaged inner TSC temperature provides a representative temperature for the area around the WC-HFG. **Figure 5** shows averaged center and perimeter temperatures for two pile sizes under four different

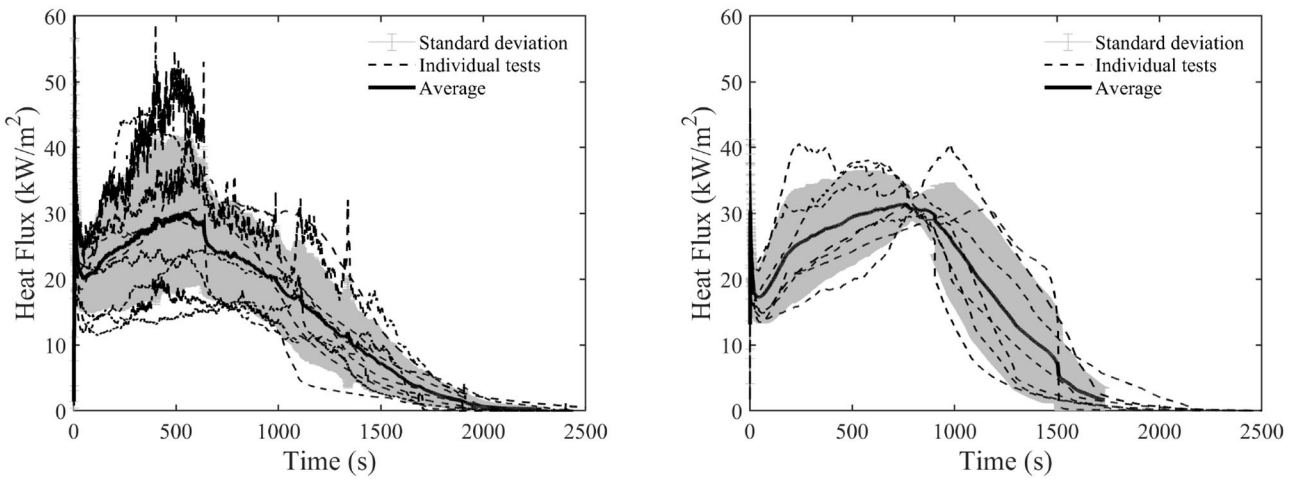

FIGURE 4 | Heat fluxes recorded from a WC-HFG are shown for 16 g of smoldering birch firebrands deposited over the sensor array for 1.2 m/s **(left)** and 1.4 m/s **(right)**. The shaded area represents the standard deviation between tests. Dashed lines represent all individual tests recorded.

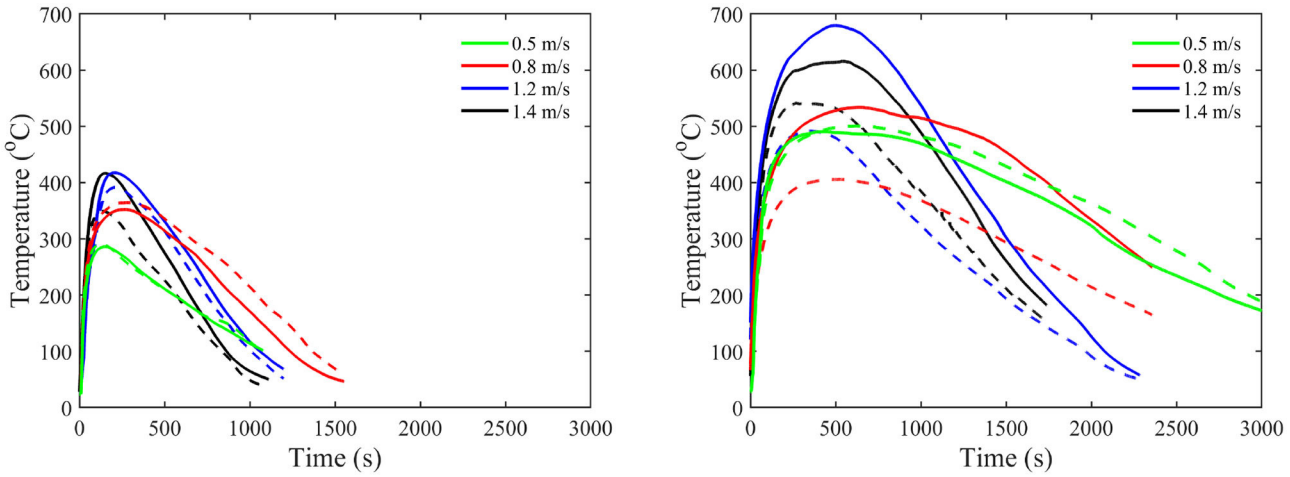

FIGURE 5 | Averaged TSC temperatures for **(left)** a 4 g deposited mass pile and **(right)** a 16 g deposited mass pile. Solid lines represent inner TSCs; dashed lines represent outer TSCs.

wind speeds. First, it is clear that temperatures increased as the deposited pile mass increased. Additionally, the heating duration also increased as the deposited pile mass increased, while the duration of heating slightly decreased with higher wind speeds owing to faster oxidation rates.

In larger piles the average temperature of the inner TSCs reached 500-700°C, close to expected values for smoldering ignition under wind, while the center temperatures for the 4 g pile only reached approximately 400°C, much lower than what would be expected for a smoldering reaction under wind. While averaged temperatures for the inner TSCs for the large pile reach about 700°C, the temperatures of individual TSCs reached well over 900°C instantaneously at higher wind speeds. These temperatures correspond well with previously measured temperatures by Urban et al. (2019) using color pyrometry.

A comparison between averaged temperatures at the center of the pile and the perimeter of the pile show that, for the most part, the center of the pile experiences higher average temperatures. This trend is the clearest for the large 16 g pile shown on the right in **Figure 5**; however, at lower wind speeds, there is little difference between central and perimeter temperatures. For 0.5 m/s, neither the small nor the large pile experienced higher center temperatures than perimeter temperatures. At 0.8 m/s, the 4 g pile shows perimeter temperatures that are slightly higher than center temperatures. The difference between center and perimeter temperature reached 200°C for the 16 g pile under a 1.2 m/s wind.

The differences between the 4 and 16 g pile, both in terms of temperatures reached and trends between the center and perimeter of the pile, are expected to be the result of two phenomena. First, sensors were more completely surrounded for the large pile, while the small pile was sparse in nature, resulting in poor coverage of the sensors. Second, visually, the larger piles of smoldering firebrands reached a glowing state as the wind speed was increased. It is expected that the higher temperatures from the 16 g pile resulted in a firebrand pile dominated by re-radiation. Additionally, the size of the large pile, in comparison to the small one, served to better insulate the firebrands from some of the convective cooling effects from the surrounding wind. On the other hand, for the 4 g pile, it is expected that conduction may still play a significant role in heating. The sparse nature of the 4 g pile more closely resembles contact from individual firebrands rather than a pile structure which insulates, suspends firebrands, and encourages re-radiation.

4.1.3. Peak Heating and Heating Duration

The above investigation of averaged temperatures indicated that both pile size and wind speed have a considerable effect on heating duration and maximum temperatures. Similar results can be seen when comparing the averaged heat fluxes for different pile size and wind speed configurations. The effect of pile size and wind speed on averaged heat flux is shown in **Figure 6**. As shown for temperature in **Figure 5**, higher wind speeds are shown to yield higher maximum heat fluxes and result in a shorter heating duration. In **Figure 6**, it is clear that there is a large uptick in the maximum heat flux as the mass of the pile increases from 4 to 8 g; however, there is little difference between 8 and 16 g, except that the duration of heating generally lasts longer for the larger pile.

The influence of wind speed and deposited pile mass on heat flux and temperature can also be observed by investigating the point values of peak heat flux and peak temperature, as shown in **Figure 7**. Peak heat flux is seen to be highly dependent on wind speed with a relatively linear increase in peak heat flux as wind speed is increased. The differences in peak heat flux resulting from pile size are mostly small and within the standard deviation of other pile sizes, though 8 g piles experienced high peak heat fluxes on average for wind speeds from 0.7 to 1.4 m/s.

The effect of wind speed on peak heat flux is anticipated as higher wind speeds produce higher temperatures as a result of increased surface oxidation. Increased oxidation will invariably increase heat fluxes to the surface. As heat is released at a higher

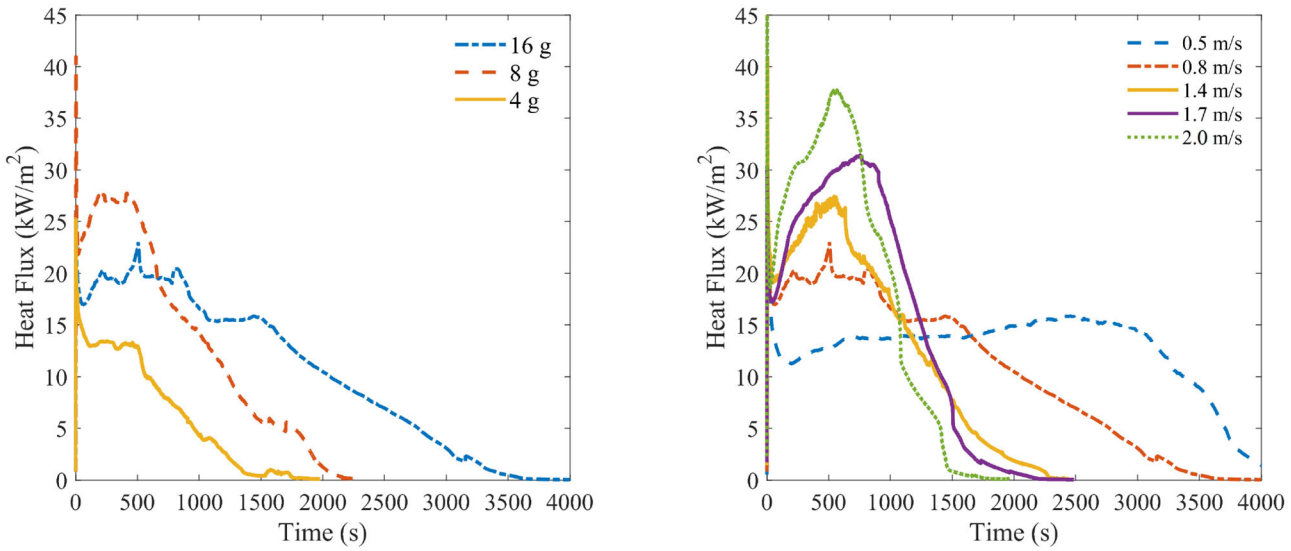

FIGURE 6 | (Left) Time-resolved heat flux for three deposited mass piles at 0.8 m/s wind. **(Right)** Time-resolved heat flux for a 16 g deposited mass pile under five different wind speeds.

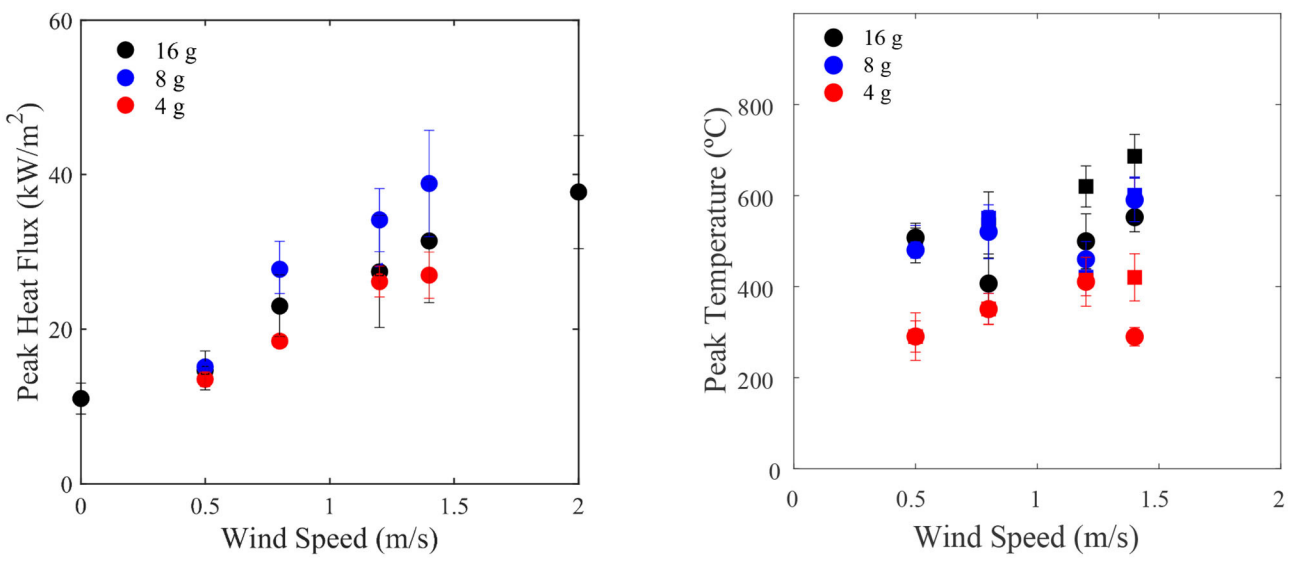

FIGURE 7 | Peak heat flux **(left)** and peak temperature **(right)** as a function of wind speed for three pile sizes. For most pile sizes, peak heat flux and temperature increases with increasing wind speed. Peak temperatures are shown for inner TSCs (squares) and outer TSCs (circles).

rate, firebrands burn out faster, resulting in a reduced duration of heating. While increased wind speeds may increase the cooling rate from firebrands, it appears that the effect of increased rates of oxidation is considerably larger than any cooling effects within the regimes tested here.

Peak temperature shows somewhat different trends from peak heat flux. While peak heat flux depended mostly on wind speed, peak temperature is dependent on both pile size and wind speed. While the two larger piles experience similar peak temperatures, the 4 g pile reaches much lower peak temperatures. This is due to the smaller bulk density in the 4 g piles, which results in decreased interaction between firebrands and a larger cooling effect from the wind. Although there is generally an increase of peak temperature with wind speed, there are more variations for sensors along the perimeter (outer TSCs). This variation is likely due to the fact that the sensors on the edges of the pile were sometimes more sparsely covered than those at the center of the pile and subject to more convective cooling effects from the wind. An effect concealed here is the area that receives this heat flux. A larger pile will heat a larger area, which is indicated by the large peak temperature differences for the outer TSCs.

4.2. Ignition Results

In order to understand ignition behavior, smoldering and flaming observations and times were compared over a range of wind speeds for the three different target fuels tested. All samples experienced smoldering on the surface. Some samples also experienced in-depth smoldering or flaming ignition. In intermediate regimes where conditions could cause either smoldering or flaming, tests were repeated above the minimum five repetitions per scenario. Surface smoldering occurred early in the test for almost all conditions studied, and eventually propagated in-depth in the target fuel for some conditions. In some cases, especially those with high wind speeds and a low target fuel density, transition to flaming occurred and flames appeared on the surface of the fuel.

In order to determine which tests experienced flaming of the target fuel, it was necessary to distinguish between flaming of the firebrands (which occurred even in some inert tests) and flaming ignition of the target fuel. **Figure 8** shows the difference between flaming of the firebrand pile and flaming ignition of the target fuel. The flames over the glowing firebrands appear higher in the photograph, while the flame anchored to the target fuel surface is visually lower down, indicating the location of the top surface of the target fuel. Flames over the firebrand pile usually started at the top of the pile and moved to the left of the pile (downwind). On the other hand, flaming ignition of the target fuel typically started at the boundary of the fuel and pile of firebrands, at the right side of the pile (upwind). These flames were typically anchored to the target fuel surface.

A representative time to smoldering and time to flaming ignition was determined in each case and used to quantify ignition conditions for different materials. Self-sustained smoldering of the target fuel was quantified with a time to smoldering, defined as the time when smoldering propagated to a 0.5 cm depth in the target fuel. Therefore, the smoldering times shown do not represent surface smoldering but in-depth smoldering. Time to flaming ignition is the time when smoldering at the surface of the fuel transitioned to flaming ignition at the surface of target fuels. After observing a flame at the surface of the fuel, the test was ended and the time to flaming was recorded. Time to smoldering was only collected from samples without flames observed at the surface of the fuel, i.e., flaming ignition. This was due to the fact that flaming, if it occurred, happened quickly, whereas in-depth smoldering would be observed at later times. Therefore, tests with flaming on the surface of the fuel were ended before smoldering was measured in-depth. If flaming samples were allowed to continue to burn, which was allowed to occur in limited cases, they would eventually burn through the entire sample.

Figure 9 shows the time to ignition for both in-depth smoldering and flaming as a function of wind speed for the three fuels tested. The ignition times presented here represent cases where either smoldering or flaming occurred, not a transition from one to the other. Under certain wind speed and firebrand loading conditions not all tests transitioned to flaming, as indicated by the flaming propensity. In order to explore this transition region, additional ignition tests were conducted in the 0.8–1.4 m/s wind speed range.

The density of the fuel bed was found to be a critical parameter related to propensity of smoldering ignition. A higher fuel density resulted in generally longer times to smoldering ignition. This

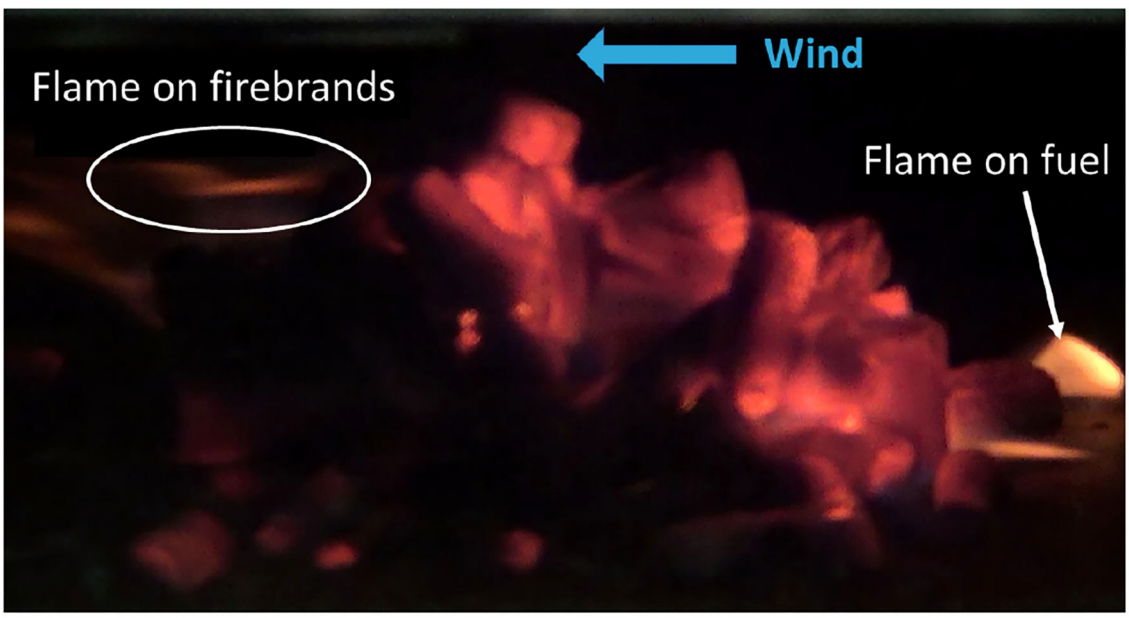

FIGURE 8 | Photograph showing flames present both over the pile of firebrands, downwind and attached to the glowing firebrands, and over the fuel surface, upwind and anchored to the fuel surface.

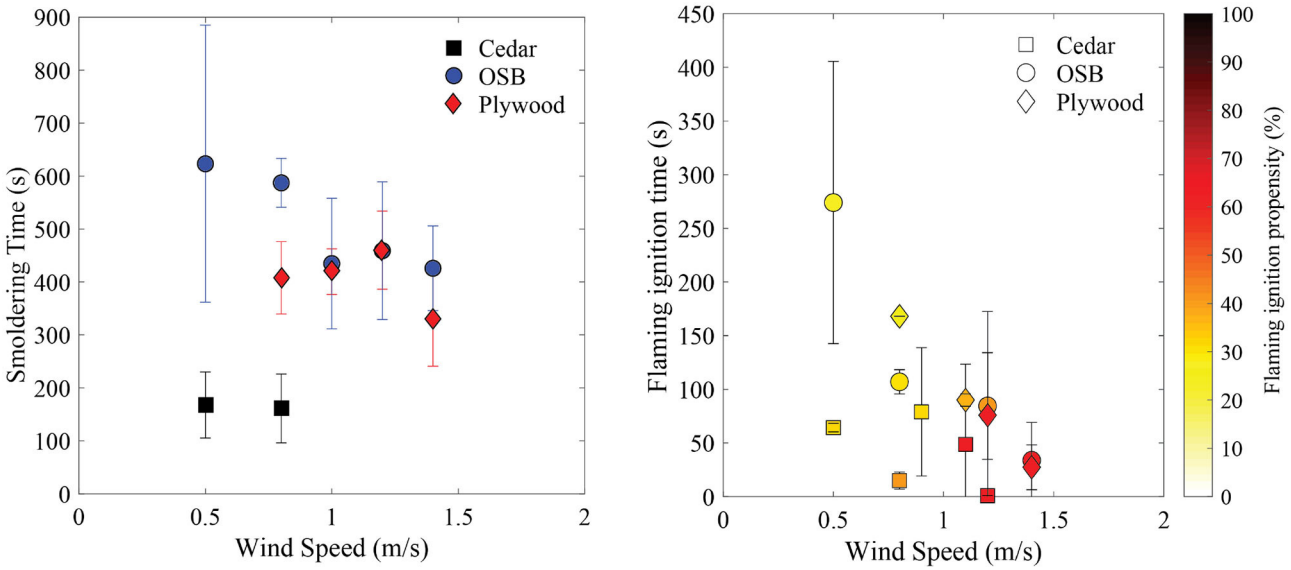

FIGURE 9 | Time to smoldering ignition **(left)** and time to flaming ignition **(right)** as a function of wind speed for three fuels and 16 g firebrand piles. Each point is averaged with error bars representing the standard deviation between values from individual tests. The flaming propensity is the ratio of tests that transitioned to flaming over those that did not; darker colors indicate a higher likelihood of transition to flaming.

effect is clearly seen for the lowest density material, cedar, which experienced the shortest ignition times and the greatest propensity for flaming. Smoldering ignition times decreased slightly and became more repeatable at higher wind speeds, while lower wind speeds exhibited more stochastic behavior. Many factors, including wind speed, firebrand pile mass, and target fuel density, influenced transition to flaming. Ultimately, higher wind speeds were more likely to transition to flaming. For low wind speeds, ignition behavior was found to be more variable and the probability of flaming on the fuel surface was low, especially for high fuel density.

4.3. Heat Flux at Ignition

While ignition times are important for a particular set of experiments, ultimately criteria are needed to fully describe ignition conditions. There are several different types of ignition criteria–critical temperature at ignition, critical mass flux, and critical heat flux at ignition–for each material. For radiation-based steady heating, it is possible to define a critical heat flux which, when sustained for a certain period of time, will result in ignition. Quantifying critical heat fluxes from firebrand piles is more complicated as heat fluxes change as a function of time. In some situations, values of instantaneous heat flux at ignition may be higher than the steady critical heat flux value (Santamaria and Hadden, 2019). Studies on transient heat flux (Bilbao et al., 2002; Lizhong et al., 2007; Zhai et al., 2017; Gong et al., 2018; Santamaria and Hadden, 2019) have investigated time to ignition for transient as opposed to constant heat flux, including investigating the ignition criteria of critical temperature, critical heat flux, and critical mass flux; however, these studies have focused on incident radiative heating. Studies by Vermesi et al. (2016, 2017, 2020) have investigated ignition of various materials exposed to transient heat fluxes and found that dual-criteria may be more accurate to describe ignition rather than a single criterion.

Most previous studies on transient heating focus either on increasing or decreasing heating. The heat flux from the firebrand pile provides both increasing and decreasing heating, depending on the portion of the test. As described previously, the heat flux profiles in these tests increase to a peak heat flux and then gradually decay. As the wind speed is increased, the peak heat flux achieved also increases, but the heating occurs over a shorter duration. In order to look at whether ignition occurs under the increasing or the decreasing part of the test, flaming and smoldering ignition times for target fuels were plotted on the averaged time-resolved heat flux curves, as shown in **Figure 10**. These results are shown for three wind speeds and all three target fuels. For all fuels and wind speeds, both smoldering and flaming ignition occur under a region of increasing heat flux.

Although the value of the heat flux at ignition may not be able to provide in itself a critical ignition criterion, the heat flux at the time of ignition may still be useful to assess and compare the relative conditions occurring at the point of ignition for different fuels. For smoldering ignition, there is a clear increase in the value of heat flux at ignition as wind speed is increased. For flaming ignition, a similar increase occurs from 0.5 to 0.8 m/s, but not for higher wind speeds. It is interesting to note that differences between the heat flux at ignition for smoldering and flaming ignition are minimal. Note that smoldering ignition here is again the in-depth smoldering propagation measured at 0.5 cm below the fuel surface.

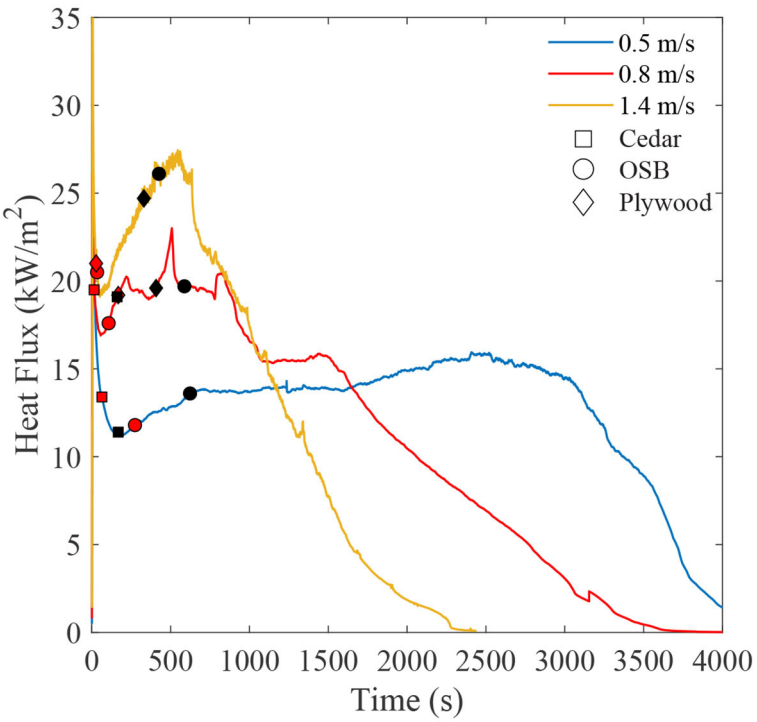

FIGURE 10 | Averaged heat flux curves for inert tests under three wind speeds and a 16 g firebrand pile. Time of flaming (red) or smoldering (black) ignition is marked on the heat flux curves for three fuels, cedar, OSB, and plywood.

The heat flux at ignition shown here illuminates some trends in smoldering and flaming ignition for different target fuels, but it does not fully describe the ignition process. It only provides a point value to describe an ignition condition and so is unable to account for the changing heat flux leading up to ignition or the duration over which this heat flux occurs. In determining ignition criteria, it is notable that ignition occurs during the increasing heating phase. Previous work on ignition under increasing radiant heat flux suggests defining the critical ignition criteria using a ratio between the surface losses and the incident heat flux (Santamaria and Hadden, 2019). For radiant heating, it is possible to develop a simplified one-dimensional model; however, the energy balance for the firebrand pile is more complicated and may require numerical simulations to provide further insight.

5. DISCUSSION AND CONCLUSIONS

Several factors were found to be critically important to the ignition of fuels, namely, the ambient wind speed, the firebrand pile mass, and the density of the target fuel. A large number of repetitions of several experimental conditions were conducted due to the stochastic nature of the transition from smoldering to flaming and natural variability in wood samples. Despite the high variability, some key trends were extracted from these experiments. Both the temperature beneath the firebrand pile and the heat flux from firebrands over an inert sample increased with increased wind speeds as a result of more rapid oxidation in firebrands. For ignition tests, these increases in temperature and heat flux were reflected in the decreased time to ignition and increased likelihood of flaming ignition of the target fuel under higher wind speeds. For both smoldering and flaming ignition, density of the target fuel was found to be the most important factor.

Results point to interesting interactions between firebrands once they are deposited in bulk over a surface. In particular, firebrands at the center of a pile have higher temperatures than surrounding firebrands, which are losing heat to the surrounding environment. Interactions between firebrands in the pile and enhanced oxidation driven by the wind overcomes some cooling effects and results in increased temperatures and heat fluxes with higher wind speeds. The role of re-radiation within the pile was not explicitly explored, but may be important here. Wind speeds were varied from 0.5 to 2.0 m/s for inert tests, and heat flux trends for those wind conditions were illustrated. In particular, tests at higher wind speeds resulted in higher peak heat fluxes and shorter test duration. While not possible in this work, it is important to consider conducting experiments with higher wind speeds in the future, as higher wind speeds may provide increasing rates of cooling to the firebrand pile and affect the trends found.

The ignition of a target fuel is complex and influenced by a number of factors. In this study, a number of simplifications were made to isolate the effects of wind speed, pile size, and target

fuel type. The present work shows that ignition, at least for the configuration considered here, occurs under the increasing heat flux regime. Future work should consider expanding to more complex and realistic considerations, including fuel geometry, additional fuel types and fuel moisture content (MC). To simulate a worst-case scenario, the MC of the fuels remained zero in all experiments; however, MC may have a non-negligible effect on ignition and should be considered in future tests. A flat fuel surface presents a perfect configuration for this fundamental study, but future work will have to address more complex geometries. Other geometries, such as crevices, L-shaped walls, and corners, are more common accumulation points in real fires than the flat surfaces studied here. It will be important to understand how geometry influences ignition of a dense fuel on a small-scale.

DATA AVAILABILITY STATEMENT

The datasets presented in this study can be found in online repositories. The names of the repository/repositories and accession number(s) can be found below: https://doi.org/10.5281/zenodo.3964633.

AUTHOR CONTRIBUTIONS

MG conceived of the presented idea and supervised the project. HS conducted the experiments. HS and RH analyzed the data. RH took the lead in writing the manuscript. All authors discussed the results and contributed to the final manuscript.

FUNDING

This research was funded by the National Institute of Standards and Technology, Fire Research Grant Program under financial assistance awards 60NANB15D358, 70NANB16H284, and 70NANB17H288.

ACKNOWLEDGMENTS

The authors would like to thank Alison Davis, Alicea Fitzpatrick, Erin Griffith, Michael Jones, Seth Lattner, and Jessen Oey for their assistance with laboratory experiments, Hanyu Xiong for comments on the manuscript, and the NIST WUI group, especially Nelson Bryner, Jiann Yang, Kathryn Butler, and Erica Kuligowski for their advice and support.

REFERENCES

Babrauskas, V. (2003). *Ignition Handbook*. Issaquah, WA:Fire Science Publishers.

Bearinger, E., Lattimer, B., Hodges, J., and Rippe, C. (2020). "Measuring heat transfer from firebrands to surfaces," in *Proceedings of the ASME 2020 Heat Transfer Summer Conference*. Virtual doi: 10.1115/HT2020-9165

Bilbao, R., Mastral, J., Lana, J., Ceamanos, J., Aldea, M. E., and Betrán, M. (2002). A model for the prediction of the thermal degradation and ignition of wood under constant and variable heat flux. *J. Anal. Appl. Pyrol*. 62, 63–82. doi: 10.1016/S0165-2370(00)00214-X

Caton, S. (2016). *Laboratory studies on the generation of firebrands from cylindrical wooden dowels* (Masters thesis). University of Maryland, College Park, MD, United States

Caton, S., Hakes, R., Gorham, D., Zhou, A., and Gollner, M. (2016). Review of pathways for building fire spread in the wildland urban interface part I: exposure conditions. *Fire Technol*. 53, 429–473. doi: 10.1007/s10694-016-0589-z

Cohen, J. (2008). "The wildland-urban interface problem," in *Forest History Today*, Durham, NC, 20–26.

Dodd, A., Lautenberger, C., and Fernandez-Pello, C. (2012). Computational modeling of smolder combustion and spontaneous transition to flaming. *Combust. Flame* 159, 448–461. doi: 10.1016/j.combustflame.2011.06.004

Ellis, P. (2015). The likelihood of ignition of dry-eucalypt forest litter by firebrands. *Int. J. Wildland Fire* 24, 225–235. doi: 10.1071/WF14048

Fernandez-Pello, A., Lautenberger, C., Rich, D., Zak, C., Urban, J., Hadden, R., et al. (2015). Spot fire ignition of natural fuel beds by hot metal particles, embers, and sparks. *Combust. Sci. Technol*. 187, 269–295. doi: 10.1080/00102202.2014.973953

Gong, J., Li, Y., Chen, Y., Li, J., Wang, X., Jiang, J., et al. (2018). Approximate analytical solutions for transient mass flux and ignition time of solid combustibles exposed to time-varying heat flux. *Fuel* 211, 676–687. doi: 10.1016/j.fuel.2017.09.107

Hakes, R. (2017). *Thermal characterization of firebrand piles* (Masters thesis). University of Maryland, College Park, MD, United States.

Hakes, R., Salehizadeh, H., Weston-Dawkes, M., and Gollner, M. (2019). Thermal characterization of firebrand piles. *Fire Saf. J*. 104, 34–42. doi: 10.1016/j.firesaf.2018.10.002

Lizhong, Y., Zaifu, G., Yupeng, Z., and Weicheng, F. (2007). The influence of different external heating ways on pyrolysis and spontaneous ignition of some woods. *J. Anal. Appl. Pyrol*. 78, 40–45. doi: 10.1016/j.jaap.2006.04.001

Manzello, S., Cleary, T., Shields, J., and Yang, J. (2006). On the ignition of fuel beds by firebrands. *Fire Mater*. 30, 77–87. doi: 10.1002/fam.901

Manzello, S., Park, S., and Cleary, T. (2009). Investigation on the ability of glowing firebrands deposited within crevices to ignite common building materials. *Fire Saf. J*. 44, 894–900. doi: 10.1016/j.firesaf.2009.05.001

Manzello, S., and Suzuki, S. (2017). Experimental investigation of wood decking assemblies exposed to firebrand showers. *Fire Saf. J*. 92, 122–131. doi: 10.1016/j.firesaf.2017.05.019

Manzello, S., Suzuki, S., and Hayashi, Y. (2012). Enabling the study of structure vulnerabilities to ignition from wind driven firebrand showers: a summary of experimental results. *Fire Saf. J*. 54, 181–196. doi: 10.1016/j.firesaf.2012.06.012

Manzello, S. L., Suzuki, S., Gollner, M. J., and Fernandez-Pello, A. C. (2020). Role of firebrand combustion in large outdoor fire spread. *Prog. Energy Combust. Sci*. 76:100801. doi: 10.1016/j.pecs.2019.100801

Maranghides, A., and McNamara, D. (2016). *2011 Wildland Urban Interface Amarillo Fires Report #2-Assessment of Fire Behavior and WUI MEasurement Science, NIST TN 1909*. National Institute of Standards and Technology. doi: 10.6028/NIST.TN.1909

Maranghides, A., McNamara, D., Mell, W., Trook, J., and Toman, B. (2013). *A Case Study of a Community Affected by the Witch and Guejito Fires: Report 2 - Evaluating the Effects of Hazard Mitigation Actions on Structure Ignitions*. National Institute of Standards and Technology. doi: 10.6028/NIST.TN.1796

Maranghides, A., McNamara, D., Vihnanek, R., Restaino, J., and Leland, C. (2015). *A Case Study of a Community Affected by the Waldo Fire Event Timeline and Defensive Actions*. Technical Report. National Institute of Standards and Technology. doi: 10.6028/NIST.TN.1910

Maranghides, A., and Mell, W. (2011). A case study of a community affected by the witch and guejito wildland fires. *Fire Technol*. 47, 379–420. doi: 10.1007/s10694-010-0164-y

Mell, W., Manzello, S., Maranghides, A., Butry, D., and Rehm, R. (2010). The wildland-urban interface problem - current approaches and research needs. *Int. J. Wildland Fire* 19, 238–251. doi: 10.1071/WF07131

Ohlemiller, T. (1990). Forced smolder propagation and the transition to flaming in cellulosic insulation. *Combust. Flame* 81, 354–365. doi: 10.1016/0010-2180(90)90031-L

Radeloff, V., Hammer, R., Stewart, S., Fried, J., Holcomb, S., and McKeefry, J. (2005). The wildland-urban interface in the united states. *Ecol. Appl.* 15, 799–805. doi: 10.1890/04-1413

Salehizadeh, H. (2019). *Critical ignition conditions of structural materials by cylindrical firebrands* (thesis). University of Maryland, College Park, MD, United States.

Santamaria, S., and Hadden, R. M. (2019). Experimental analysis of the pyrolysis of solids exposed to transient irradiation. Applications to ignition criteria. *Proc. Combust. Inst*. 37, 4221–4229. doi: 10.1016/j.proci.2018.05.104

Tao, Z., Bathras, B., Kwon, B., Biallas, B., Gollner, M., and Yang, R. (2020). Effect of firebrand size and geometry on heating from a smoldering pile under wind. *Fire Saf. J*. 103031. doi: 10.1016/j.firesaf.2020.103031

Tse, S., Fernandez-Pello, A., and Miyasaka, K. (1996). "Controlling mechanisms in the transition from smoldering to flaming of flexible polyurethane foam," in *Symposium (International) on Combustion*, (Naples: Elsevier), 1505–1513. doi: 10.1016/S0082-0784(96)80372-9

Urban, J., Vicariotto, M., Dunn-Rankin, D., and Fernandez-Pello, A. (2019). Temperature measurement of glowing embers with color pyrometry. *Fire Technol.* 55, 1013–1026. doi: 10.1007/s10694-018-0810-3

Urban, J., Zak, C., and Fernandez-Pello, C. (2018). Spot fire ignition of natural fuels by hot aluminum particles. *Fire Technol.* 54, 797–808. doi: 10.1007/s10694-018-0712-4

Urbas, J., Parker, W., and Luebbers, G. (2004). Surface temperature measurements on burning materials using an infrared pyrometer: accounting for emissivity and reflection of external radiation. *Fire Mater*. 28, 33–53. doi: 10.1002/fam.844

Vermesi, I., DiDomizio, M., Richter, F., Weckman, E., and Rein, G. (2017). Pyrolysis and spontaneous ignition of wood under transient irradiation: experiments and a-priori predictions. *Fire Saf. J*. 91, 218–225. doi: 10.1016/j.firesaf.2017.03.081

Vermesi, I., Richter, F., Chaos, M., and Rein, G. (2020). Ignition and burning of fibreboard exposed to transient irradiation. *Fire Technol.* doi: 10.1007/s10694-020-01017-6. [Epub ahead of print].

Vermesi, I., Roenner, N., Pironi, P., Hadden, R., and Rein, G. (2016). Pyrolysis and ignition of a polymer by transient irradiation. *Combust. Flame* 163, 31–41. doi: 10.1016/j.combustflame.2015.08.006

Wang, S., Huang, X., Chen, H., and Liu, N. (2017). Interaction between flaming and smouldering in hot-particle ignition of forest fuels and effects of moisture and wind. *Int. J. Wildland Fire* 26, 71–81. doi: 10.1071/WF 16096

Zhai, C., Gong, J., Zhou, X., Peng, F., and Yang, L. (2017). Pyrolysis and spontaneous ignition of wood under time-dependent heat flux. *J. Anal. Appl. Pyrol.* 125, 100–108. doi: 10.1016/j.jaap.2017.04.013

Conflict of Interest: The authors declare that the research was conducted in the absence of any commercial or financial relationships that could be construed as a potential conflict of interest.

frontiers in Mechanical Engineering

ORIGINAL RESEARCH
published: 24 May 2021
doi: 10.3389/fmech.2021.651135

Characterization of Firebrands Released From Different Burning Tree Species

Miguel Almeida[1]*, *Leonardo Porto*[2] *and Domingos Viegas*[1,2]

[1] ADAI, Department of Mechanical Engineering, University of Coimbra, Coimbra, Portugal, [2] Department of Mechanical Engineering, University of Coimbra, Coimbra, Portugal

The number, dimensions, and initial velocity of the firebrands released from burning *Quercus suber*, *Eucalyptus globulus*, *Quercus robur*, and *Pinus pinaster* trees were analyzed in laboratory experiments using a particle image velocimetry system. Additionally, the flame height, tree mass decay, vertical flow velocity, and temperature at the top of the trees were measured during the experiments. The relationship between the various parameters was analyzed and a good connection was found. The specimens burnt were mostly young trees, so large particles (e.g., pine cones, thick trunk barks, branches) were not included in this study as they were not present. Actually, the firebrands produced in the laboratory tests, mainly burning leaves, had a cross-sectional area of $< 1{,}600$ mm^2, having the potential to cause short distance spotting (up to tens of meters). Quercus trees are often considered to have a lower fire risk than eucalyptus or pine trees. However, in this study, *Quercus suber* and *Quercus robur* were the species that produced more firebrands, both in terms of number and total volume. The tests with *Quercus suber* were the only ones using specimens from an adult tree, confirming the great importance of the age of trees in the propensity to release firebrands. The results obtained with *Quercus robur* confirmed the high tendency of this species to originate spot fires at a short distance. Thus, these results are of great relevance to afforestation plans and to evaluating the risk of the presence of these species in wildland–urban interface areas.

Keywords: spotting, spot fires, firebrands, wildfires, extreme fire behavior, fire modeling, fire spread, trees

OPEN ACCESS

Edited by:
Melanie C. Rochoux, Centre Europeen de Recherche et de Formation Avancee en Calcul Scientifique, France

Reviewed by:
Ali Tohidi, San Jose State University, United States
Wei Tang, National Institute for Occupational Safety and Health (NIOSH), United States

***Correspondence:**
Miguel Almeida
miguelalmeida@adai.pt

Specialty section:
This article was submitted to Thermal and Mass Transport, a section of the journal Frontiers in Mechanical Engineering

Received: *15 January 2021*
Accepted: *22 April 2021*
Published: *24 May 2021*

Citation:
Almeida M, Porto L and Viegas D (2021) Characterization of Firebrands Released From Different Burning Tree Species. Front. Mech. Eng. 7:651135. doi: 10.3389/fmech.2021.651135

INTRODUCTION

Spotting is one of the most relevant and common mechanisms of fire spread in wildfires, especially in extreme burning conditions. Its importance derives from the increased difficulty in firefighting caused by spotting; the serious consequences in terms of accidents, infrastructures, and other economic losses caused; and the great difficulty with regard to the prediction of this phenomenon. Moreover, spotting can dramatically increase the fire spread rate, being in some circumstances the main factor affecting it (Rothermel, 1983). Indeed, despite the several studies performed on this topic, the prediction of spotting is still very basic, which clearly jeopardizes the firefighting operations and threatens fire safety.

The analysis of the spot fires mechanism is frequently divided into four stages (Almeida et al., 2013): (1) release of firebrands, (2) lofting of the firebrands in the thermal plume, (3) downwind transport of the firebrands, and (4) ignition of the fuel recipient where the firebrands land. Most of

the work seeking the determination of the maximum spotting distance is carried out in the second and third phases (e.g., Tarifa et al., 1967; Albini, 1979; Ellis, 2000; Hall et al., 2015) considering that firebrands, after leaving the thermal plume, travel at a velocity defined by the terminal velocity and the wind speed. The determination of the probability of ignition of landing firebrands was also the focus of some experimental studies. Statistical analysis based on tests with different combinations of firebrand types and fuel bed recipients (e.g., Ganteaume et al., 2009; Viegas et al., 2014; Ellis, 2015) or in a shower of firebrands artificially generated that hit building façades or other relevant structures (e.g., Manzello et al., 2011; Manzello and Suzuki, 2014; Oliveira et al., 2014) was produced.

The work performed on the release of firebrands is less frequent, and consequently, there is a great lack of knowledge on this phase of the process. The release of firebrands depends on several factors, the most important ones being the fire intensity, the airflow direction, velocity and turbulence, the characteristics of the source of the firebrands (e.g., tree type, species, age, etc.), and the characteristics of the firebrands (type, shape and dimensions, terminal velocity, moisture content, rate of combustion, etc.). Research on the firebrand generation can be divided into two areas, namely (1) firebrands generated by burning structures, which was initially investigated by Waterman (1969), paving the way for more recent research such as Suzuki et al. (2012) or Foote et al. (2011); and (2) firebrands generated by vegetation, which is the main topic of this work and is an even less investigated problem.

Six relevant works addressing this topic are as follows:

(1) Gould et al. (2008) performed four field experiments in plots with the size of 200 × 200 m and, among other analyses, studied the firebrand generation and spotting behavior resulting from a fire front spreading in a eucalyptus forest. Besides the successful validation of the model developed by Ellis (2000) to predicting maximum spotting distance of fibrous firebrands, these authors confirmed the importance of the fire intensity, and consequently of the convection column, in the release of the firebrands. It was also stated that younger fuels, including young trees, produce fewer firebrands than mature specimens.

(2 and 3) Manzello et al. (2007) analyzed the size and mass distribution of firebrands generated from burning Douglas-fir (*Pseudotsuga menziesii*) trees with heights of 2.6 and 5.2 m by collecting the firebrands in pans methodically distributed on the ground. The average firebrand size reported was 3 and 4 mm in diameter and 40 and 53 mm in length for the 2.6-m tall and 5.2-m tall trees, respectively. Later, Manzello et al. (2008) carried out similar tests with 3.6-m high Korean pine trees, which did not result in a significant number of firebrands produced. However, the dominant firebrands collected had a cylindrical shape with a diameter of 5 mm and a length of 40 mm, on average.

(4) Almeida et al. (2014) used a methodology based on particle image velocimetry (PIV) to analyze the firebrands lofted during the burning of pieces of the bark of eucalyptus trees in several scenarios with different arrangements of the barks tested. The methodology then used was quite similar to the one described herein.

(5) Tohidi et al. (2015) presented a mechanical firebrand break-off model for determining the formation of cylindrical firebrands produced during the burning of coniferous trees, stating the importance of the limb break-off process on the release of the particles. For validation, the laboratory data presented in Manzello et al. (2007) and Manzello et al. (2008), previously mentioned, were used.

(6) Filkov et al. (2017) studied the firebrand production in a prescribed fire in a pine forest by following a methodology described in Houssaimi et al. (2015). Around 80% of the firebrands collected in pans distributed on the ground, mostly from bark fragments (≈70%) and twigs (≈30%), had a cross-sectional area between 50 and 200 mm^2.

The present work intends to contribute to mitigating these knowledge gaps. The main focus is studying the release of firebrands by typical tree species in the Mediterranean area, namely cork trees (*Quercus suber*), oak trees (*Quercus robur*), pine trees (*Pinus pinaster*), and eucalyptus trees (*Eucalyptus globulus*). These species were chosen among the other tree species with major representation in the Mediterranean forests (San-Miguel-Ayanz et al., 2016) for their role in the spotting mechanisms.

The eucalyptus species is by far the most associated one to spotting in several fire events such as the Black Saturday Australian Fires (Cruz et al., 2012) or the fires on October 15, 2017 that occurred in Central Portugal (Viegas et al., 2019). Spot fires driven from pine species also have some references, such as the 2010 Mount Carmel Forest Fire (Israel) described by Kutiel (2012). The role of the oak and cork trees is not as recognized. However, its potential has been well-established in several fire events, for example:

(a) Fire of Cicouro—Portugal (Viegas et al., 2013), in 2013, where an episode of oak leaves spotting drastically increased the rate of fire spread, surprising a group of firefighters, causing two fatalities;

(b) Fire of Pedrógão Grande of June 2017, in Central Portugal (Viegas et al., 2017), where the control of the fire in Regadas was lost due to spotting of cork oak leaves across a 10-m wide road.

The main aim of this work is to understand the relative role of the mentioned tree species in the short-distance spotting process. Spotting by large firebrands is not addressed in this work since the intense airflow convection column required to naturally produce such particles (Gould et al., 2008) was not achieved in the laboratory experiments. On the other hand, the trees tested did not have large particles such as thick barks or cones available to burn and potentially produce medium- to long-distance spotting, but, given the large number of particles produced, they have a great potential to produce a large number of spot fires.

The most common firebrands observed in the laboratory tests carried out were burning leaves released from the trees. Many reports (e.g., Viegas et al., 2013, 2019; Ribeiro et al., 2014) on large forest fires mention spotting by leaves as an essential mechanism

TABLE 1 | Main data related to the experimental conditions (m_0–initial mass of the trees; m_f–residual mass of the trees after the burning tests; H—tree height; FMC—fuel moisture content in wet basis; T—air temperature; RH—air relative humidity).

Test Reference	Fuel					Indoor environment	
	Specie	m_0 (kg)	m_f (kg)	H (m)	FMC (%)	T (°C)	RH (%)
CORK02	*Quercus suber*	3.360	1.576	1.3	13.9	30.3	33
CORK03	*Quercus suber*	3.072	1.586	1.0	13.9	30.4	33
EUC01	*Eucalyptus globulus*	2.424	1.356	1.8	47.6	35.0	29
EUC02	*Eucalyptus globulus*	2.436	0.954	1.8	47.6	28.6	36
OAK01	*Quercus robur*	2.412	1.288	1.8	47.3	31.9	31
OAK02	*Quercus robur*	2.464	1.088	1.2	47.3	33.0	29
PIN01	*Pinus pinaster*	4.110	2.420	1.3	51.5	28.2	37
PIN02	*Pinus pinaster*	4.090	2.800	1.8	51.5	27.9	39

of the fire spread. However, the majority of the research on spot fires addresses rigid artificial shapes (like spheres, cylinders, and disks) or natural shapes (cones, barks, and twigs) and usually neglect other potential firebrands like leaves. Clements (1977) is one of the rare exceptions where the terminal velocity of leaves from 17 different species were determined. This author found terminal velocities values of 1.54, 1.57, and 1.80 $m{\cdot}s^{-1}$ for the leaves of Quercus species (*Q. phellos, Q. nigra,* and *Q. falcata,* respectively) and 2.90, 4.00, and 4.14 $m{\cdot}s^{-1}$ for Pinus trees needles (*P. echinate, P. elliottii,* and *P. taeda*, respectively).

TABLE 2 | Representative mass distribution of the trees used in the tests.

Specie	Average mass fraction in wet basis (%)		
	Thick branches (diameter 5–30 mm)	Thin branches (diameter below 5 mm)	Leaves
Quercus suber	58.9	25.9	15.2
Eucalyptus globulus	32.5	13.6	53.9
Pinus pinaster	42.0	13.6	44.3
Quercus robur	66.3	13.0	20.7

METHODOLOGY

General Conditions and Characterization of Fuels

The experimental work presented herein was carried out at the Forest Fires Research Laboratory (LEIF: *Laboratório de Estudos sobre Incêndios Florestais*), located in Lousã (Coimbra—Portugal), of Association for the Development of Industrial Aerodynamics (ADAI: *Associação para o Desenvolvimento da Aerodinâmica Industrial*).

The young trees were collected from forests close to the LEIF in the early hours on the day of the experiments. The samples of *Quercus suber* were collected 2 days before the experiments. *Quercus suber* is a protected species in Portugal, but a license (reference 53521/2014/DCNF-C/DLAP) for cutting a mature specimen that was about to fall on a road was obtained. Due to the impossibility of cutting young specimens, the branches of this mature tree were used as samples of *Quercus suber*. For simplicity, the authors will mention each *Quercus suber* branch as a tree and use this differentiation during the discussion of results.

The tests were performed on a single day. The 10 previous days were normally sunny with an average temperature of 19.7°C (from 12 to 31°C), an average wind velocity of 6.2 $km{\cdot}h^{-1}$ (from 0 to 22 $km.h^{-1}$), and an accumulated precipitation of 1.0 mm (data from www.wunderground.com). So, the trees collected presented a moisture content value that allowed a sustained burning. On the day of the experiments, the fuels were stored in the laboratory and protected from the sun with the indoor environmental conditions mentioned in **Table 1**. The air temperature and relative humidity values are the average values registered at a portable weather station located inside the LEIF. **Table 1** shows the moisture content values of the different trees used. The moisture content was determined immediately before each burning test by using a moisture analyzer (AnD ML-50 0.1%) using samples composed of leaves and branches (<3 mm in diameter) in a percentage distribution representative of each species.

A brief characterization of the structure of the trees used is presented in **Table 2**. This determination was carried out by detaching the leaves and branches of one representative tree (i.e., roughly medium dimensions) from each species. The main trunk of the trees was not considered in the analysis. The images of the trees used in the experiments are presented in **Figure 1**.

Experimental Apparatus and Procedures

The experimental apparatus can be seen in **Figure 2**. The tests were carried out in a burning trees platform with an area of 1.5 × 1.5 m and a height of 0.15 m, supported by three load cells with 0.1 g of precision each, connected to a computer for automatic mass recording.

The burning of the trees was only sustainable through the addition of a complementary fuel under the canopy. Since the use of bushes or other wild fuels as an ignition fuel would produce firebrands that would disturb the final analysis, denatured alcohol (DA) was used as a complementary fuel.

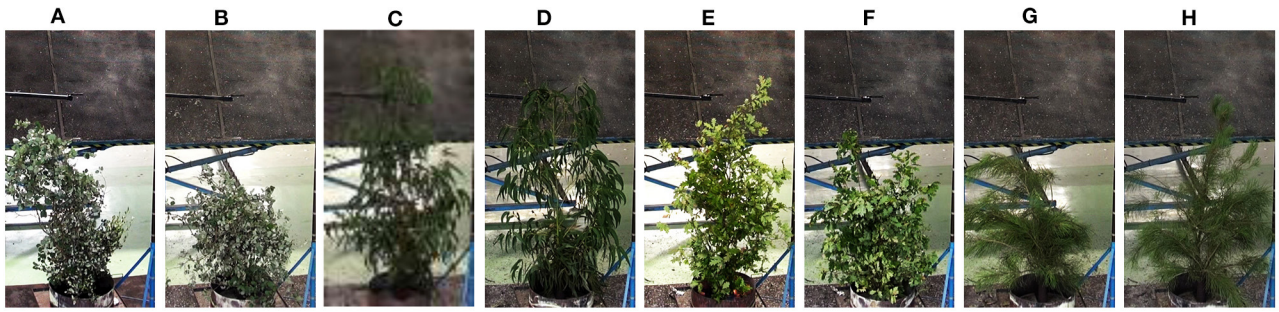

FIGURE 1 | Photography of the experimental set up: **(A)** CORK02; **(B)** CORK03; **(C)** EUC01; **(D)** EUC02; **(E)** OAK01; **(F)** OAK02; **(G)** PIN01; and **(H)** PIN02.

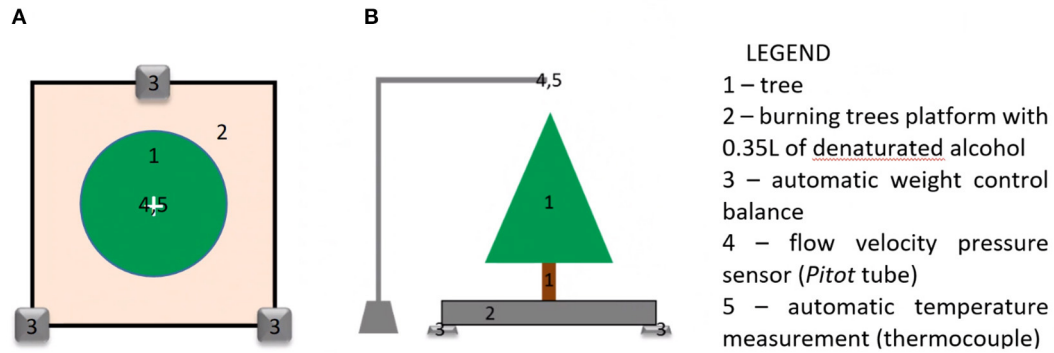

FIGURE 2 | Design of the experimental apparatus: **(A)** top view; **(B)** profile view.

Thus, in each burning test, a container with a diameter of 0.75 cm filled with 0.35 L of DA (ethanol 90% v/v) was placed under the tree. In order to check the eventual effect of the DA on the final results and to correct the mass loss, the authors carried out some experiments with a similar methodology but with no trees, thus exclusively burning 0.35 L of DA. As expected, these tests did not produce any firebrand and allowed for the determination of the constant mass-loss rate of the burning alcohol, which was found to be equal to 2.8 g/s.

Using a supporting structure, an S-Pitot tube (6 mm of internal diameter) and a thermocouple (1-mm thick) were placed over the platform, 1.8 m above the ground. This equipment was connected to a computer in order to record the vertical velocity and temperature of the convective airflow. Consistently, the mass, the temperature, and the pressure were registered at a frequency of 2 Hz during the experiments.

For each test, the tree specimen was placed vertically on the platform after measuring the fuel moisture content (FMC) of the samples of leaves and branches < 3 mm in diameter. Ignition was achieved by dropping a match on the DA, which immediately started to burn, spreading the flames to the tree canopy. The DA continued to burn with a constant intensity/flame height until after the test was over.

Characterization of the Particles Released Using the PIV System

For determining the particles released by the trees, a system of PIV was used. The software used was DynamicStudio, version 15, from Dantec. A Speedsense 1,040 camera and a Frame Grabber 1,031 from National Instruments (National Instruments Corp., Switzerland)[1] were used.

The PIV device was located 5.8 m away from the tree and the platform and 3.3 m above the ground, so as to minimize parallax errors, and horizontally oriented to the smoke plume. The image selected for analysis had an area of 0.7 × 0.7 m, thus capturing images in the height range of 2.95–3.65 m (**Figure 3**). The height of the PIV capturing area was chosen considering an expected maximum flame height of about 2.5 m, according to previous tests performed by Almeida et al. (2014), thus avoiding the interference of the flame in the analysis of the PIV images. Since there were no predominant horizontal airflows, the flames observed tended to be vertical. Therefore, the flame height coincided with the flame length and consisted of the vertical distance between the DA level and the top of the flame. Eventual detached flames were not considered.

As can be seen in **Figure 3**, the PIV image-capturing system targeted the central axis of the smoke column at a height of 3.3 m. In the middle of the smoke column, the firebrands have a strong

[1]https://www.ni.com/

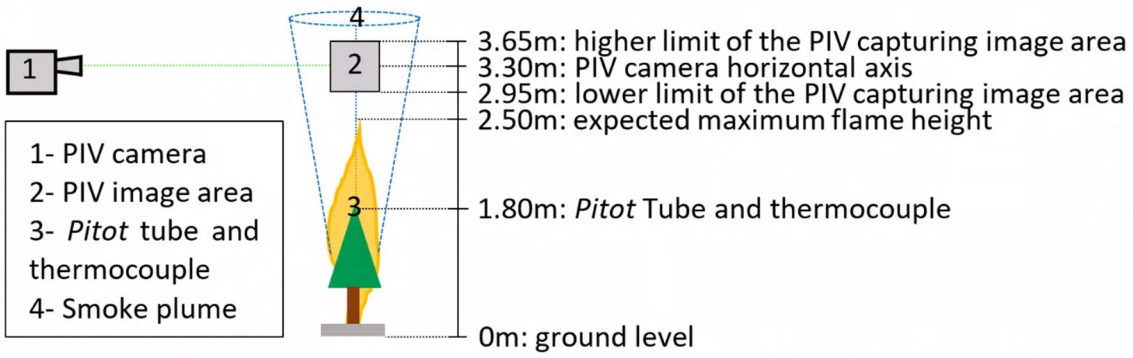

FIGURE 3 | Profile view of the experimental apparatus. For convenience, the figure is not to scale.

vertical upward component (**Figure 4**). After being lofted, the firebrands, commonly extinct or less glowing, start a descending movement out of the smoke column and thus were not able to be captured by the PIV system. Thus, almost all the particles captured in the PIV images are glowing and being lofted in the convective column of smoke.

The authors assumed a radial symmetry of the tree and of the characteristics of the smoke plume. The PIV images were acquired at a frequency of 143 Hz, in double frame, using the Shadow Processing tool to identify the firebrands (**Figure 4**). The domain of interest in the PIV images was the analysis area of size 0.7 × 0.7 m (square 2 of **Figure 3**). This methodology was previously tested with good results, allowing for an accurate particle velocity determination through the comparison of two consecutive frames, thus reducing the likelihood of firebrands being incorrectly identified. Since the brightness of the incandescent particles highlights them in the images taken, the process of tracking is facilitated without the need for complementary illumination systems (laser or other). Thus, not only the number and area of the firebrands but also their velocity can be accurately determined using the double frame in the Cross-Correlation tool.

Due to the limitation of the computer storage capacity, and because of the large number of images being captured, the PIV images were acquired during 44 s in each test. Thus, the capture of images by the PIV system was initiated only when the first release of firebrands was observed. This process was started typically by an initial increase in the release rate of the firebrands and, after reaching a maximum value at time t_M, the number of firebrands produced started to decrease. In order to increase the accuracy of the method, the authors used the data of the time interval $t_M \pm 5$ *s*, which was designated as the "10 s-peak period." Thus, the authors ensured that the comparison between the various burning tests was made at the same stage of the process around the maximum release period. Since the period of 10 s provided in this method is limited in duration and consequently in sample size, when appropriate, the entire PIV image acquisition period of 44 s was used in the analysis of the results.

In **Figure 5**, on the right of the burning tree, it is possible to see a vertical pole with 25-cm markers that were used as a scale to estimate the flame height, using frames captured from the video recordings. The same scale was used to calibrate the PIV images.

The firebrands released were divided into five classes based on average cross-sectional area A_{av}: $10 < A_{av} \leq 50$ mm^2; $50 < A_{av} \leq 100$ mm^2; $100 < A_{av} \leq 500$ mm^2; $500 < A_{av} \leq 1{,}000$ mm^2; $A_{av} > 1{,}000$ mm^2. Firebrands with $A_{av} \leq 10$ mm^2 were not considered in this analysis since their potential to cause new ignitions is very low.

It was observed that the majority of firebrands released were the leaves of the burning trees. Thus, since the authors did not find in the literature typical values of the terminal velocity for the leaves of the species used in these tests, a set of tests with that purpose was performed using a methodology very similar to that used by Clements (1977). Ten leaves of each species, randomly collected, were dropped from a height of 9 m in the absence of wind. The time t_{fall} that each leaf took to fall in the last 5 m, when the falling velocity is practically constant, was found using video footage. The terminal velocity V_t was determined by the quotient between the 5 m distance and the time t_{fall} elapsed on this final 5 m. The resulting V_t values (**Table 3**) were not significantly different from those found by Clements (1977) for the species of the same taxonomic genre.

RESULTS AND THEIR INTERPRETATION

Number and Cross-Sectional Area of the Firebrands Released

The total number of firebrands released during the capture period of the PIV images is presented in **Figure 6**. In order to allow for the extension of the use of these data in future works, the number of particles released is denoted as those released per unit of area (N·m^{-2}). Once again, due to data storage limitations of the system, the capture of PIV images was started after fire ignition, when the operators considered the burning process to already be in sustained development. Therefore, the first point

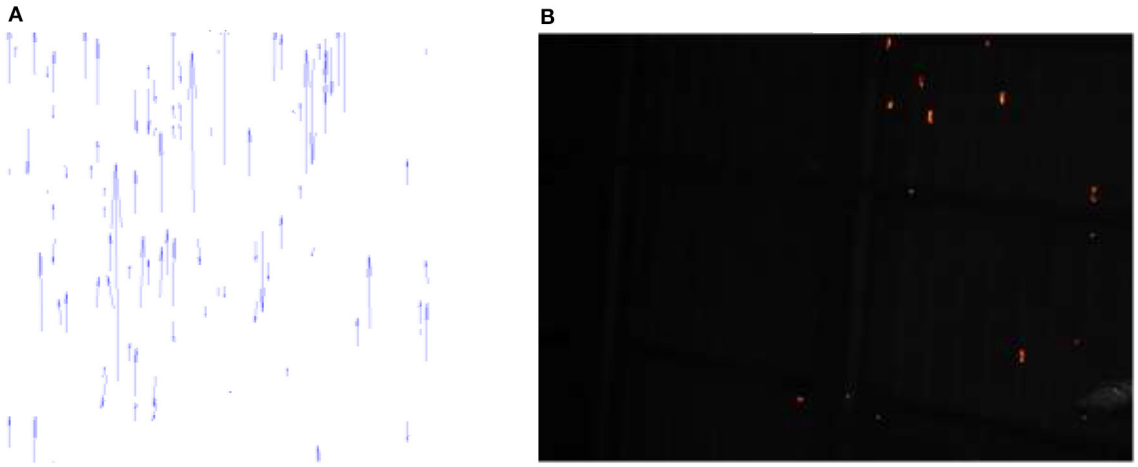

FIGURE 4 | Images from the PIV system: **(A)** velocity vectors of the firebrands; **(B)** firebrands identified using the shadow processing tool.

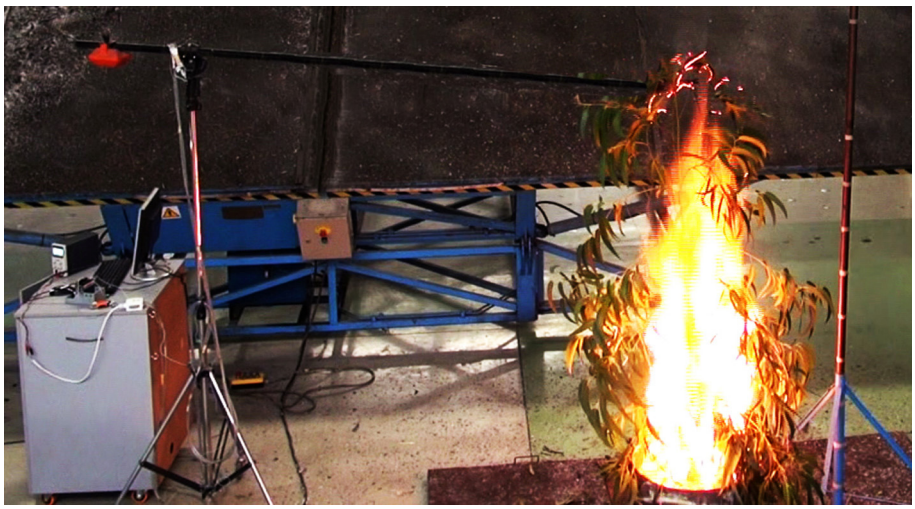

FIGURE 5 | Image of a burning test captured just before the start of the acquisition of the PIV images (test EUC02).

TABLE 3 | Terminal velocity results from the experimental tests.

	Cork leaves	Eucalyptus leaves	Oak leaves	Pine needles
Sample size	16	15	12	13
Average V_t value (m.s^{-1})	1.94	2.36	1.69	3.31
Standard deviation (m.s^{-1})	0.17	0.45	0.25	0.37
V_t Clements, 1977 (m.s^{-1})	1.3–1.9*	–	1.3–1.9*	2.9–4.1^{+}

**values found for Q. marilandica, Q. falcata, Q. nigra, and Q. phallus.*
$^{+}$values found for P. taeda, P. elliottii, and P. echinatta.

of the graph in **Figure 6** does not initiate at $t = 0$ *s*, when the ignition occurred.

The distribution of the total number of firebrands released during the capture period of the PIV images, grouped in classes based on their cross-sectional area A_{av}, is presented in **Figure 7**. As previously mentioned, the analysis was limited to the 10 s-peak period, allowing for a fair comparison among the different species used.

Each pair of tests on the same species showed a very similar tendency in terms of the number of firebrands released, except

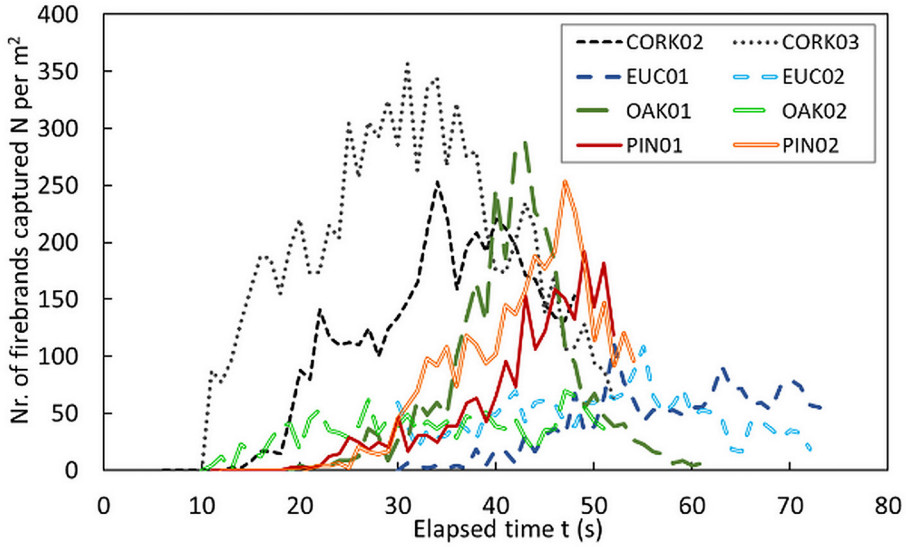

FIGURE 6 | Number of firebrands released per m^2 captured in the PIV images. Time "0 s" corresponds to the beginning of the burning test, which is different from the beginning of PIV image capture.

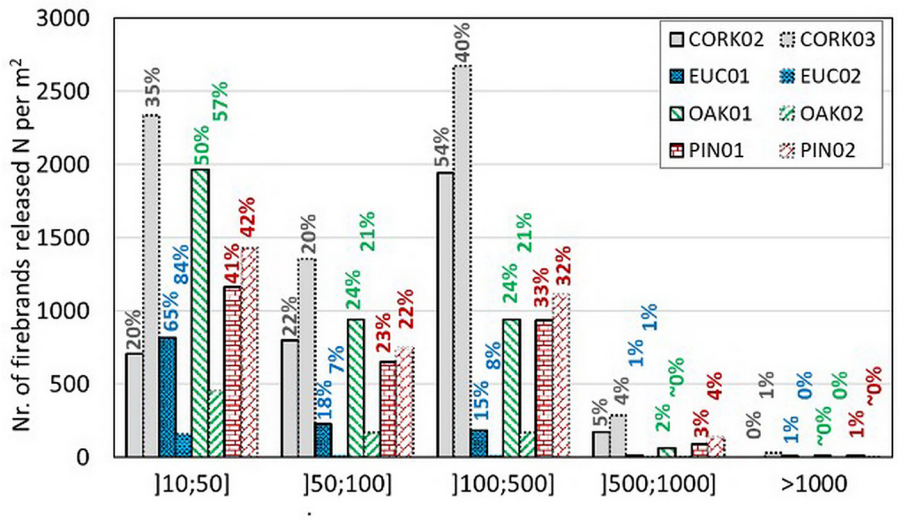

FIGURE 7 | Distribution of firebrands released per m^2, captured in the PIV images, by classes of cross-sectional area during the 10 s-peak period. Above the vertical bars is the percentage values of the firebrands for the respective classes.

in the oak trees tests, where, for test *OAK01*, the number of firebrands counted was much higher than that for *OAK02*. By observing the *OAK02* test video, it was possible to notice that during the capture period of the PIV images, this tree burned mostly on one side of the canopy unlike the other tests, where the burning was more comprehensive. Therefore, the release of firebrands in the *OAK02* test may have been affected. Regarding the distribution of firebrands by the classes based on the cross-sectional area A_{av}, the results show a satisfactory reproducibility in the tendency obtained for each pair of tests, even for both the oak trees tests.

It is possible to state that the maximum number of firebrands was released by the cork trees and by the oak trees (excluding *OAK02),* followed by the pine trees and finally the eucalyptus trees. On the other side, the most represented area classes A_{av} in terms of the number of firebrands released are [10, 50] mm^2 and [100, 500] mm^2. This figure also shows that Cork tree tests have a higher tendency to produce larger firebrands, while tests

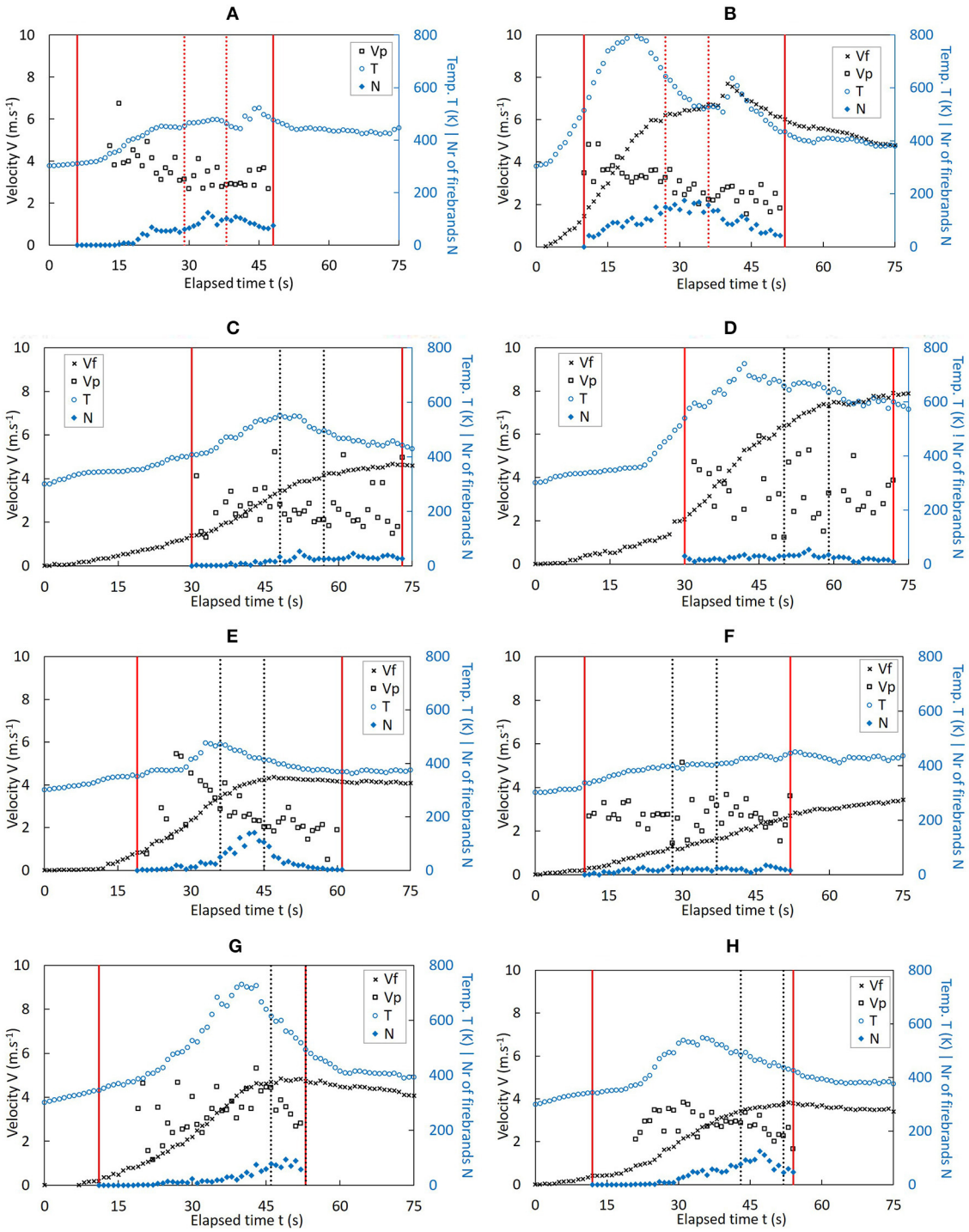

FIGURE 8 | Values of up-flow velocity Vf, velocity of the firebrands V_p, temperature T, and the number of firebrands N as a function of the elapsed time t for each test. The two vertical solid lines limit the period of PIV image acquisition. The two vertical dotted lines limit the 10 s-peak period. The color of the markers corresponds to the color of the axes to which they refer. **(A)** CORK02; **(B)** CORK03; **(C)** EUC01; **(D)** EUC02; **(E)** OAK01; **(F)** OAK02; **(G)** PIN01; and **(H)** PIN02.

with the other species drove mainly toward the production of smaller particles within the range of $10 < A_{av} \leq 50$ mm^2. It is worth noting that the cork trees were collected 2 days before the tests while the other trees were cut on the day of the experiments. Although the storage of the cork trees occurred under controlled conditions and these trees did not show visible degradation, the

decay of FMC (**Table 2**, above) may have affected the results, thus contributing to the change in the number and dimensions of the firebrands released.

Temperature and Vertical Airflow Velocity

In the graphs in **Figure 8**, the values of temperature T and vertical airflow velocity V_f, measured at a height of 1.8 m and the values of the velocity of the particles V_p determined using the PIV images at the heights of 2.95–3.65 m are represented as a function of the time elapsed since the ignition up to 75 saver. The number of firebrands released is represented in the same figure to facilitate the establishment of relationships. The velocity and temperature values of the *CORK02* test were not obtained as the Pitot tube did not work properly during this experiment. The sampling of the values of the velocity of the firebrands is limited to the 44-s acquisition time period for the PIV images for all tests. This period is marked in the figure by the two vertical solid lines. The dotted vertical lines in the graphs limit the 10 s-peak period of the particles released.

As can be verified, the values of the velocity of the firebrands do not differ considerably from the values of airflow velocity registered at the same time, following an approximate trend as the number of firebrands released. It would be expected that the V_p values were consistently smaller than the V_f values because of gravity and drag effects. It is worth noting that the values of V_f at a height of 1.8 m were not measured exactly at the same position as that of the firebrands (2.95–3.65 m high). Besides, the values of V_f correspond only to the vertical component of the flow velocity, while V_p is the modulus of the two-dimensional velocity of the particle and is limited to the PIV image-capturing area. This could be the reason why occasionally the values of V_p are larger than V_f.

The average velocity of the particles in the smoke plume should be given by the difference between the airflow velocity and the terminal velocity of the particle V_t (Equation 1).

$$V_p = V_f - V_t \tag{1}$$

During the burning tests, the authors observed that most of the firebrands released were leaves or parts of leaves. Some twigs were also released but in much smaller quantities. Therefore, the authors used the terminal velocity values measured for the leaves of each species (**Table 3**) to make a comparison with the results obtained with the PIV system. The results given in **Table 4** show that the values of V_t obtained in the PIV tests are of the same order of magnitude as those measured in the free fall tests. The small discrepancies can be justified by the differences in the relative measurement positions of V_f and V_f, as explained above. In the case of *OAK2* test, a negative value of V_t was obtained possibly because the tree did not burn with radial symmetry. Thus, the central axis of the smoke plume did not coincide with the central vertical axis of the tree where the Pitot tube was located. Therefore, the V_f value determined was not the highest flow value in the smoke plume, leading to apparent negative V_p values.

Mass Decay

In order to estimate the mass loss of each tree during the burning test, the authors considered the mass loss of the DA, which was also placed in a pan on the weighing platform. A reference test was made using only the alcohol container under the same conditions as those of the burning tests. Assuming that the burning conditions of the alcohol in the pan were not affected by the presence of the tree, in all tests, the authors estimated the mass m of the tree by subtracting to the total mass m_T the mass m_{DA} of the alcohol, which decreased linearly with a rate of $2.8 g{\cdot}s^{-1}$ ($r^2 = 0.99$).

In order to make a fair comparison of the mass loss among all tests, the mass values were normalized using the initial value of the tree mass m_0 and its value after the burning test m_f, as given in Equation (2) for the determination of the relative mass α. The relative mass α as a function of the elapsed time for all tests performed is presented in **Figure 9**.

$$\alpha = \frac{m - m_f}{m_0 - m_f} \tag{2}$$

During the 10 s-peak period presented in **Figure 9**, the relative mass decay curves can be fitted to an exponential function as indicated by Equation (3) and as shown in **Figure 10**.

$$\alpha = e^{-a \times t} \tag{3}$$

In Equation (4), the relative mass decay coefficient "*a*" allows for the comparison among the several tests. As can be seen in **Table 5**, the *OAK02* test, which was not a conventional one, and the eucalyptus trees tests were those in which the relative mass consumption was slower.

The relative mass loss rate $\breve{\alpha}$, which is used to estimate the relative mass decay per unit of time, is defined by Equation (4).

TABLE 4 | Terminal velocity V_t of the leaves of the species used in the tests.

	CORK02	CORK03	EUC01	EUC02	OAK01	OAK02	PIN01	PIN02
V_t (specific tests) ($m.s^{-1}$)	1.94		2.34		1.69		3.31	
V_f ($m.s^{-1}$)	N/D	6.3	3.7	7.3	3.8	1.4	4.7	3.6
V_p ($m.s^{-1}$)	3.2	2.8	2.5	2.7	2.8	2.6	3.6	2.7
$V_t \approx V_f - V_p$ ($m.s^{-1}$)	–	3.5	1.2	4.5	1.0	−1.2	0.9	0.9

The up-flow velocity V_f and the velocity of the firebrands V_p are average values determined for the 10 s-peak period with greater release of firebrands. The specific tests were previously described in ***Table 3****.*

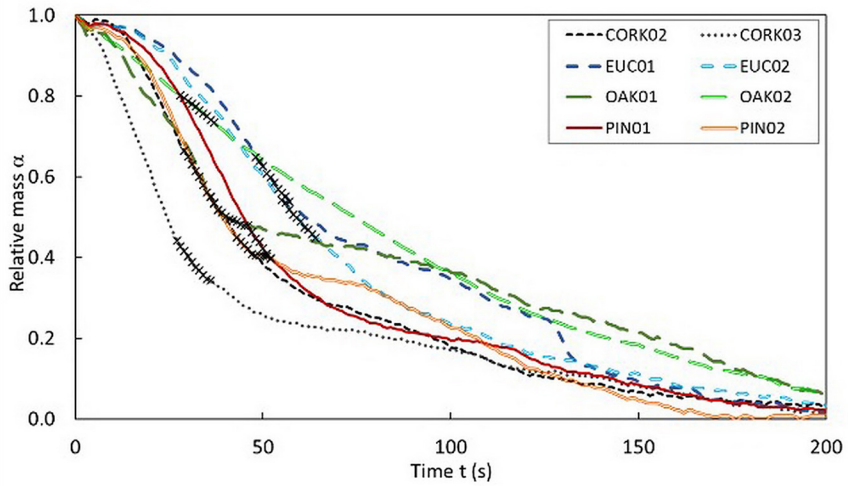

FIGURE 9 | Relative mass α as a function of the elapsed time t for each entire test. The cross marks (x) correspond to the values determined for the 10 s-peak period.

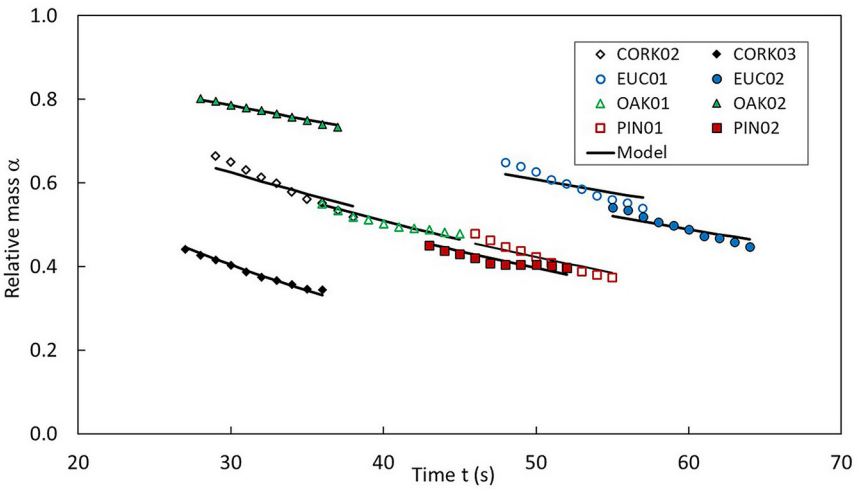

FIGURE 10 | Fractions of the curves presented in depicting the values of the 10 s-peak period to fit the model of Equation (4).

TABLE 5 | Exponential relative mass decay coefficient "a" (s^{-1}) and correlation coefficient achieved in the fitting of the relative mass α of the trees by the elapsed time t during the 10 s-peak period (**Figure 10**), according to Equation (4).

	CORK02	CORK03	EUC01	EUC02	OAK01	OAK02	PIN01	PIN02
$a^{*}10^{-5}$ (s^{-1})	1,592	3,030	1,005	1,192	1,687	814	1,698	1,847
r^2	0.82	0.99	0.72	0.80	0.91	0.96	0.80	0.72

The variation in relative mass loss rate $\breve{\alpha}$ during the 44 s of the capture period of the PIV images is shown in **Figure 11**. This representation of the relative mass loss rate $\breve{\alpha}$ indicates a faster mass consumption for cork tests, *OAK01,* and pine tests.

$$\breve{\alpha} = \left|\frac{d\alpha}{dt}\right| = \left|\frac{d}{dt}\left(\frac{m - m_f}{m_0 - m_f}\right)\right| \quad (4)$$

Correlation Between Parameters

The mass and the volume of the firebrands released were not determined since only one PIV camera was used and consequently only a two-dimensional analysis was carried out. However, a rough association between the cross-sectional area can be made with the volume and mass of the particles. The accumulated values of the total cross-sectional area A_{ac} (Equation 5) of the firebrands released since the beginning of image

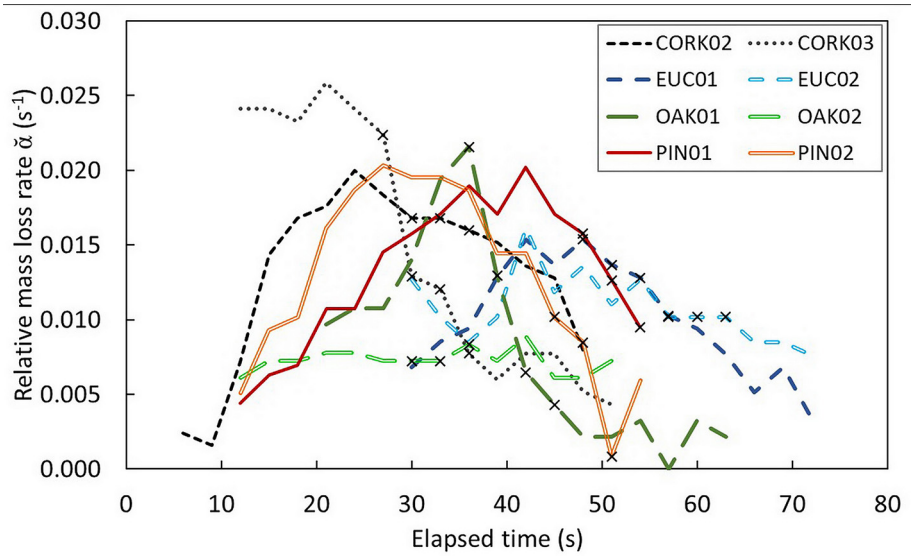

FIGURE 11 | Relative mass loss rate$\breve{\alpha}$ as a function of the elapsed time t for the period of PIV image acquisition in each test. The cross marks (x) correspond to the values determined for the 10 s-peak period.

acquisition up to a certain moment t were related with the relative mass α of the trees, as presented in **Figure 12**.

$$A_{ac} = \sum_{i=0}^{t} A_i \tag{5}$$

As expected, the accumulated total cross-sectional area A_{ac} of the firebrands released increases with the decrease in tree mass (**Figure 12**). The tree mass decay is dependent on three parameters: (1) the mass transferred to the firebrands released, (2) the mass lost in the water volatilization process, and (3) the mass lost to the formation of volatile gases. The relationship given in **Figure 12** deals with that between the mass transferred and the firebrands released.

Making the same relationship for the 10 s-peak period (**Figure 13**), the slope m of the tendency lines formed by each data set (**Table 6**) can be analyzed. Larger values of the slope m mean less mass reduction dependency on the mass associated with the A_{ac} of the firebrands released.

Using the same relationship in **Figure 13**, the exponential coefficient k obtained from Equation (6) was determined as presented in **Table 6**.

$$\alpha = e^{-k \times A_{ac}} \tag{6}$$

The results show that the mass loss of burning eucalyptus trees is less driven by the production of firebrands than for other trees. This is consistent with **Figure 7**, where it is shown that the small firebrands were the most represented in the *EUC* experiments. On the opposite side, the variation of α vs. Ac for the cork trees was very strong as denoted by the lowest k value, which is consistent with the larger number of firebrands released (**Figure 6**, above) and with the lowest values of moisture content (**Table 1**).

When equations 3 and 6 are combined using the common parameter α, Equation (7) is obtained.

$$\begin{aligned} \alpha &= e^{-k \times A_{ac}} \\ \alpha &= e^{-a \times t} = e^{-k \times A_{ac}} \Leftrightarrow a \times t = k \times A_{ac} \Leftrightarrow A_{ac} = \frac{a}{k} \times t \end{aligned} \tag{7}$$

In **Figure 14**, the evolution of A_{ac} as a function of t is represented using the data from all tests. The dotted line presented, characterized by the linear function shown in the figure, was achieved by the overall tendency of the values. The slope of this function is close to 1, showing the close similarity between both members of Equation (7). Therefore, the relationship between the parameters "a" and k, derived from the relative mass α, and the accumulated total area of the firebrands A_{ac} is well-established.

The flame height H_f variation was also analyzed and compared with the other parameters described above. As can be seen in **Figure 15**, the flame height follows a trend comparable to the relative mass loss decay$\breve{\alpha}$.

The variations in the flame height and in the total cross-sectional area of the firebrands released are presented in **Figure 16**. The total cross-sectional area A_t represents the sum of the areas of all the firebrands captured at each instant. It is possible to see that both parameters follow the same tendency; however, the A_t peaks show a delay of some seconds when compared with the H_f peaks. The time difference between A_t and H_f peaks is hereby denoted by "delay time."

In **Table 7**, the delay times determined for each test are presented. One of the factors affecting the delay time is the period required for the particles to take off from the tree by detachment as a consequence of fire; this time is hereby denoted by "reaction

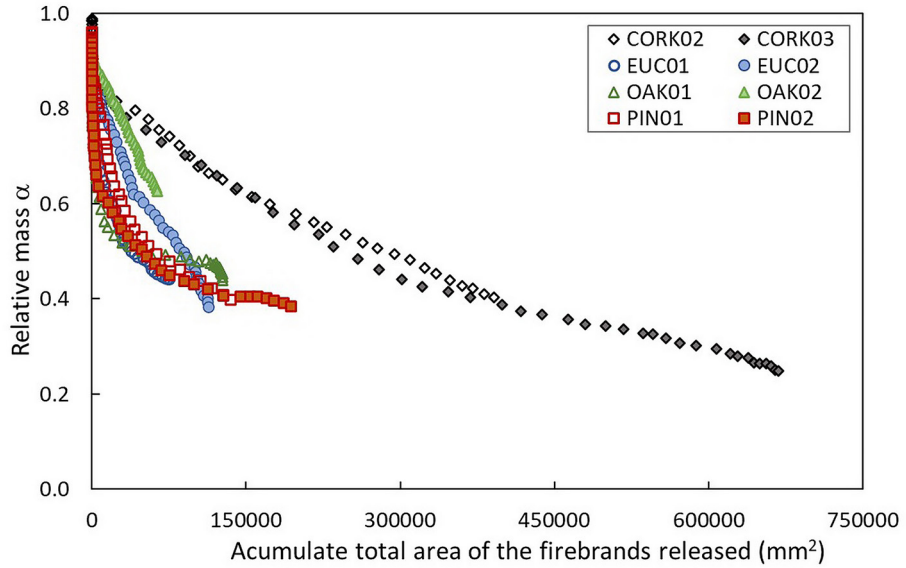

FIGURE 12 | Variation of the relative mass of the trees α as a function of the accumulated total cross-section area A_{ac} of the released firebrands captured in the PIV images.

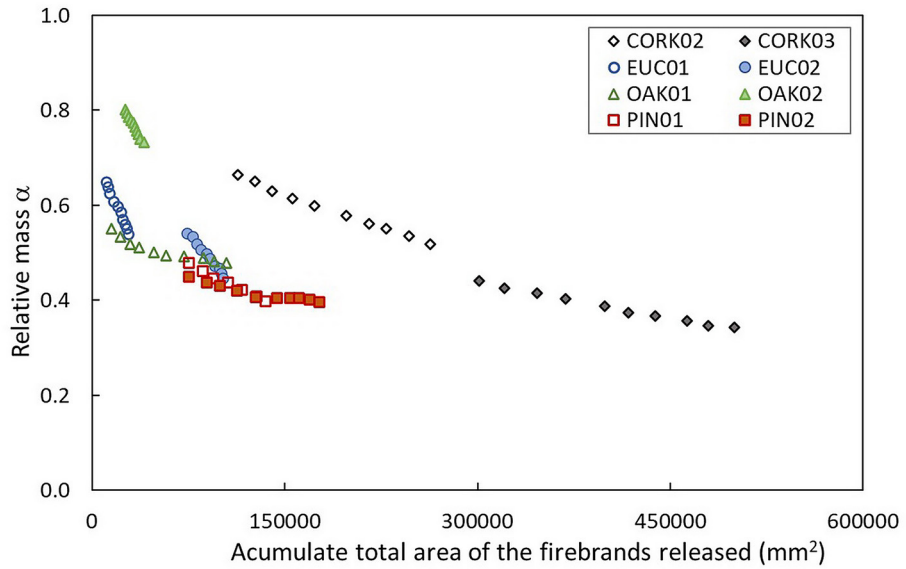

FIGURE 13 | Variation of the relative mass of the trees α as a function of the accumulated total cross-section area A_{ac} of the released firebrands captured in the PIV images during the 10 s-peak period.

TABLE 6 | Linear coefficient m (mm^{-2}) and exponential coefficient k (mm^{-2}) and respective correlation coefficients achieved in the fitting of the mass of the trees by the estimated values of firebrands released (**Figure 11**) using Equation (6).

	CORK02	CORK03	EUC01	EUC02	OAK01	OAK02	PIN01	PIN02
$m*10^{-9}$ (mm^{-2})	949	503	5,930	3,269	680	4,903	1,314	481
r^2	1.00	0.99	0.99	0.99	0.86	0.99	0.99	0.91
$k*10^{-9}$ (mm^{-2})	2,768	2,339	24,592	7,887	9,711	8,071	7,678	6,358
r^2	0.99	0.99	0.97	1.00	0.83	1.00	0.99	0.96

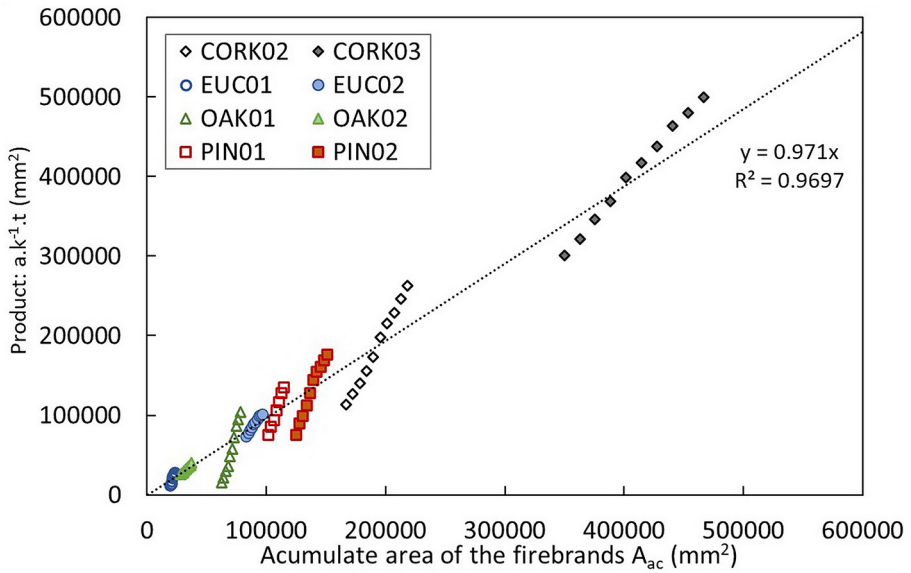

FIGURE 14 | Variation of A_{ac} as a function of the second term of Equation (7). The dotted line represents the linear tendency of all the values, which is characterized by the linear function presented in the graph.

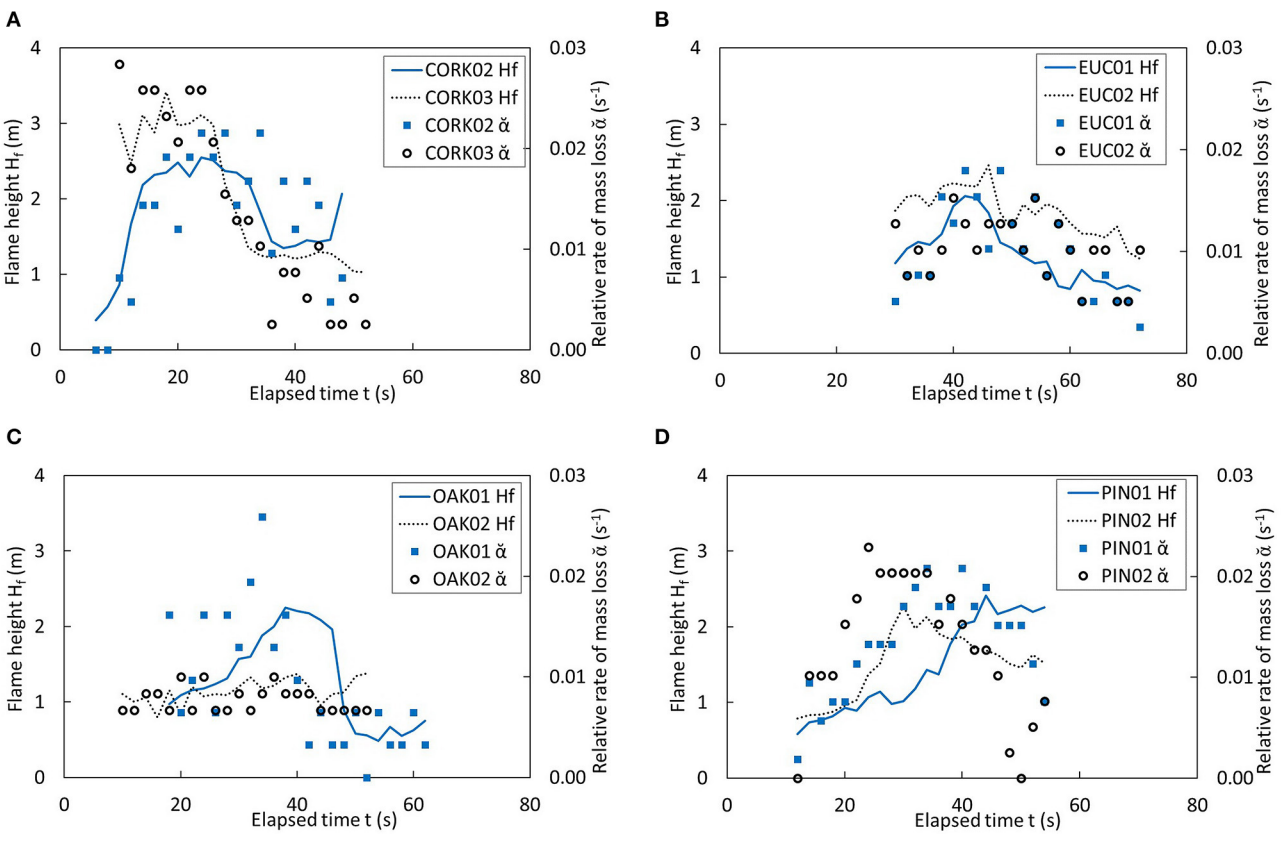

FIGURE 15 | Comparison between the flame height Hf and relative rate of mass loss$\dot{\alpha}$ variations during the PIV image-capturing period of the tests. **(A)** Tests on cork trees; **(B)** tests on eucalyptus trees; **(C)** tests on oak trees; **(D)** tests on pine trees.

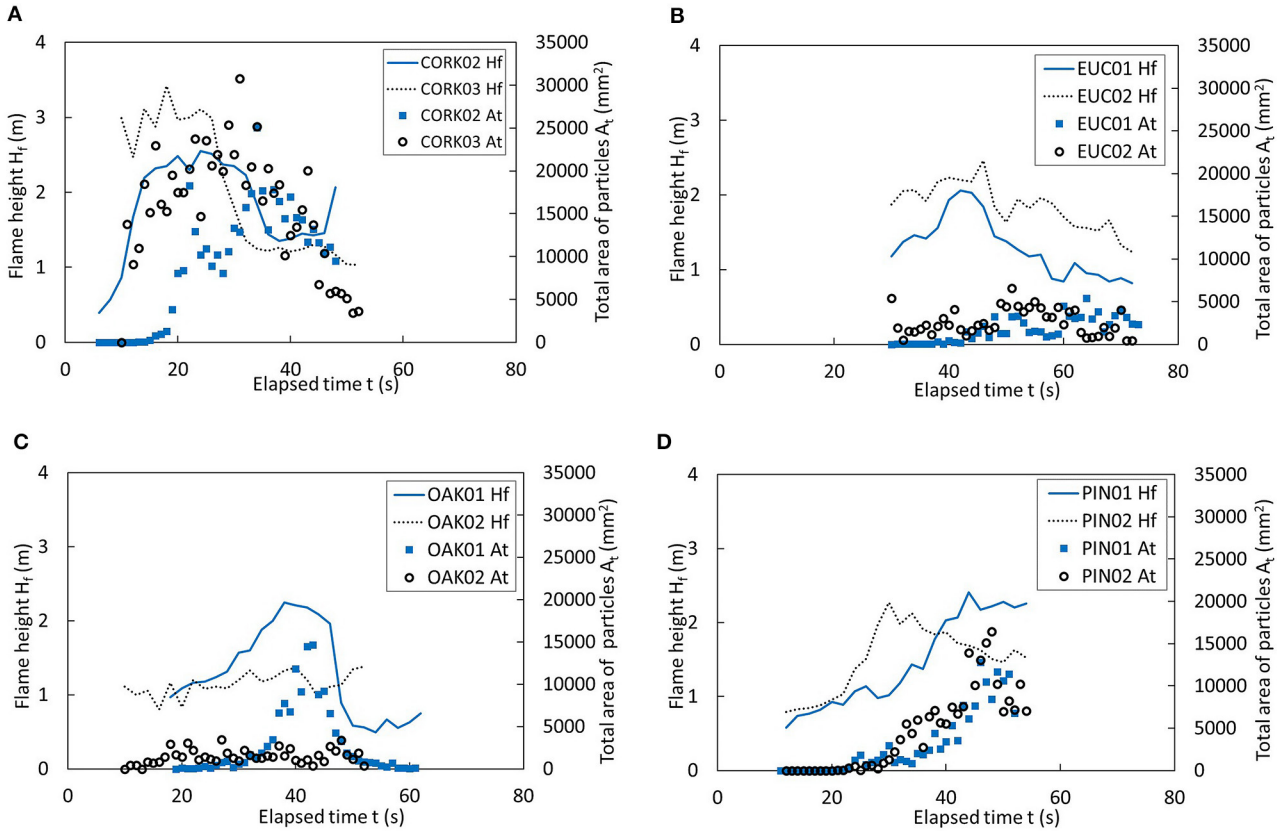

FIGURE 16 | Comparison between the flame height H_f variation and total cross-sectional area of the firebrands released A_t during the PIV image-capturing period of the tests. **(A)** Tests on cork trees; **(B)** tests on eucalyptus trees; **(C)** tests on oak trees; **(D)** tests on pine trees.

TABLE 7 | Values of the reaction times for the different experiments seen as the average time required to detach the particles from the tree as a consequence of the burning.

	CORK02	CORK03	EUC01	EUC02	OAK01	OAK02	PIN01	PIN02
Delay time (s)	5.0	7.0	10.0	15.0	3.0	4.0	3.0	6.0
Distance (m)	2.0	2.3	1.5	1.5	1.5	2.1	2	1.5
V_p ($m.s^{-1}$)*	3.2	2.8	2.5	2.7	2.8	2.6	3.6	2.7
Uplift time (s)	0.6	0.8	0.6	0.6	0.5	0.8	0.6	0.6
Reaction time (s)	4.4	6.2	9.4	14.4	2.5	3.2	2.4	5.4

Firebrands' velocity V_p from **Table 4.*

time." On the other hand, the firebrands were separated from the tree at approximately the height of its canopy (**Table 1**), but the particles were captured in the PIV images at an average height of 3.30 m (2.95–3.65 m). The time taken for uplifting firebrands from the canopy to the average height of the PIV image capture was determined by dividing the average velocity of the firebrands V_p (**Table 4**) and the vertical distance between the canopy and the PIV image center. The reaction time was determined by calculating the difference between the delay time and the uplift time (**Table 7**).

The reaction times found for the several species were very similar except for the eucalyptus trees, which require more time to release firebrands due to a change in the fire intensity. On the other hand, the reaction time of the oak trees and the pine trees was about four times lower than that of the eucalyptus trees, and about two times smaller than that of the cork trees (except for the *PIN02*). The authors believe that these differences are much related to the thickness and robustness of the petiole that links the leaves to the branches. However, specific tests are required to better explore these observations.

FINAL DISCUSSION OF RESULTS

The results of several tests aiming at the analysis of the firebrands released during the burning of different trees common in the Mediterranean forests were presented and preliminarily discussed. A compilation of the main results (**Table 8**) and an integrated discussion are carried out in this section.

TABLE 8 | Compilation of the main results previously presented and discussed.

Parameter | Specie	*Quercus suber* (CORK)	*Eucalyptus globulus* (EUC)	*Quercus robur* (OAK)	*Pinus pinaster* (PIN)
Maximum number of firebrands released counted in each 0.5 s frame	124 | 175	59 | 53	141 | 32*	89 | 124
% of firebrands larger than 100 mm^2	59 | 45	17 | 9	26 | 21	37 | 36
Terminal velocity of the firebrands V_t	– | 3.5	1.2 | 4.5	1.0 | –	0.9 | 0.9
Exponential relative mass decay coefficient a (s^{-1})	1,592 | 3,030	1,005 | 1,192	1,687 | 814	1,698 | 1,847
m^*10^{-9} (mm^{-2}): mass loss dependency on the firebrands released	949 | 503	5,930 | 3,269	680 | 4,903	1,314 | 481
Exponential coefficient k^*10^{-9} (mm^{-2})	2,768 | 2,339	24,592 | 7,887	9,711 | 8,071	7,678 | 6,358
Reaction time (s)—time for the particles to take-off from the tree	4.4 | 6.2	9.4 | 14.4	2.5 | 3.2	2.4 | 5.4

The values of each pair of experiments are separated by a vertical bar "|."
**test value considered as partially valid.*

Contrary to what is usually assumed, the eucalyptus trees were found to be the species releasing fewer firebrands, while cork and oak trees produced more firebrands. In many situations of fuel management in the wildland–urban interface, the oak and cork trees are used to reduce the fire risk propensity, but the results of these tests and other observations show that their predisposition to produce firebrands able to cause spot fires at a shorter distance (tens of meters) cannot be neglected. These results are corroborated by the analysis that was carried out in order to understand the dependence of the mass loss on the release of firebrands. Once again, the loss of mass recorded during the burning of the cork trees was the one that proved to be most influenced by the release of particles. Eucalyptus was the species in which this dependence was the lowest.

On the other hand, the terminal velocity of the firebrands released by the cork trees was shown to be higher than that of the trees in the OAK tests, and so a larger spotting distance is expected for the firebrands produced by oak trees.

It is worth highlighting that in these experiments, with the exception of the cork trees, only young trees were tested and these results are not extended to mature trees. For example, the thicker barks of eucalyptus trees or pine cones were not available in these tests, and their relevant role in the development of spot fires in real fire events was not addressed. On the other hand, these results must be interpreted considering the limited fire intensity achieved in these experiments. In real fire events, not only would several episodes with higher intensity and thus more convective airflow velocity be expected but also the existence of meteorological wind, which would lead to the production of more and larger firebrands, would be anticipated. Still, this study allows a comparative analysis of the species with higher potential to produce firebrands that are able to originate spot fires at a distance up to some tens of meters.

It was observed that most of the firebrands released were the leaves of the trees. Since the eucalyptus trees used were the species with a larger mass percentage of leaves (**Table 2**) and a lower mass percentage of thick branches, a greater release of firebrands would be expected in these trees. However, it was also noted that the eucalyptus leaves require a high energy value to release firebrands, which is shown by the larger reaction time (**Table 8**) and by a higher value (52 and 56%, respectively) of final mass m_f of fuel to burn after the tests (**Table 1**).

CONCLUSIONS

In this work, the number and characteristics of the firebrands produced during the burning of four different trees were analyzed. The authors observed that a young tree belonging to *Eucalyptus globulus* had a lower potential to produce spot fires, followed by *Pinus pinaster, Quercus robur,* and *Quercus suber*. These trees released mostly leaves and twigs capable of producing spot fires at a short distance.

The results presented are relevant when used in fire behavior prediction models that consider the mechanism of spotting. However, the results obtained for cork, oak, and pine trees are related to young specimens and cannot be directly transposed to adult trees.

The methodology based on PIV images proved to be useful in this analysis. However, since the analysis was made on a two-dimension basis, it is expected that the number and mass of firebrands determined are underestimated since firebrands can be hidden behind each other. Moreover, some firebrands may have had an early abandonment of the smoke plume and so might not have been captured by the PIV images and considered in the analysis. Thus, the previously mentioned sequence of the potential for those trees to cause spot fires is valid.

The authors of this study intend to perform additional tests with other species commonly found in the Mediterranean and non-Mediterranean forests of not only trees but also shrubs and herbaceous plants that have the potential to cause spot fires. Moreover, the authors aim to analyze the effect of the age of the tree and the effect of wind on the firebrands released during the burning of several forest species. The test results like the ones presented herein will be used as a reference to harmonize the results of tests performed in different conditions.

DATA AVAILABILITY STATEMENT

The original contributions presented in the study are included in the article/supplementary material, further inquiries can be directed to the corresponding author/s.

AUTHOR CONTRIBUTIONS

MA: coordinated the study, designed, supervised and participated in laboratory tests, analyzed data, led the writing of the manuscript. LP: participated in the laboratory tests, performed PIV data processing, revised the manuscript. DV: supervised the study, discussed the results, revised and contributed to the writing of the manuscript. All authors contributed to the article and approved the submitted version.

FUNDING

This research was funded by the Project Firestorm (www.adai.pt/firestorm) and House Refuge (www.adai.pt/houserefuge) with the references PCIF/GFC/0109/2017 and PCIF/AGT/0109/2018, respectively. Both projects are funded by the Portuguese Foundation for Science and Technology (http://www.fct.pt).

ACKNOWLEDGMENTS

The authors acknowledge the contributions in the laboratory tests of several members of the ADAI, namely Jorge Raposo, Cláudia Pinto, Joel Teixeira, Nuno Luís, and Ana Beatriz. The authors would also like to thank Ana Albuquerque and Millo Magnocavallo for their help in reviewing the English writing.

REFERENCES

Albini, F. A. (1979). *Spot Fire Distance From Burning Trees: A Predictive Model. USDA Forest Service, Intermountain Forest and Range Experiment Station, Technical Report INT-56*. (Ogden, UT). Available online at: https://www.frames.gov/catalog/8153

Almeida, M., Viegas, D., and X., Miranda, A. I. (2013). Combustion of eucalyptus bark firebrands in varying flow incidence and velocity conditions. *Int. J. Wildl. Fire* 22, 980–991. doi: 10.1071/WF12210

Almeida, M., Viegas, D. X., and Raposo, J. R. (2014). "Analysis of firebrand release on the spot fire mechanism," in *Advances in Forest Fire Research,* ed D. X. Viegas (Coimbra: Imprensa da Universidade de Coimbra). doi: 10.14195/978-989-26-0884-6_6

Clements, H. B. (1977). *Lift-Off of Forest Firebrands. USDA Forest Service South-Eastern Forest Experiment Station, SE-159* (Asheville, NC). Available online at: https://books.google.pt/books/about/Lift_off_of_Forest_Firebrands.html?id=jSnBMQEACAAJ&redir_esc=y

Cruz, M. G., Sullivan, A. L., Gould, J. S., Sims, N. C., Bannister,. A. J., Hollis, J. J., et al. (2012). Anatomy of a catastrophic wildfire: the black saturday kilmore east fire in Victoria, Australia. *For. Ecol. Manag.* 284, 269–285. doi: 10.1016/j.foreco.2012.02.035

Ellis, P. F. (2000). *The Aerodynamic and Combustion Characteristics of Eucalypt Bark – A Firebrand Study* (PhD thesis). Australian National University, Canberra, ACT. Available online at: https://openresearch-repository.anu.edu.au/handle/1885/49422

Ellis,. P. F. M. (2015). The likelihood of ignition of dry-eucalypt forest litter by firebrands. *Int. J. Wildl. Fire* 24, 225–235. doi: 10.1071/WF14048

Filkov, A. I., Prohanov, S., Mueller, E., Kasymov, D., Martynov, P., ElHoussami, M., et al. (2017). "Investigation of firebrand production during prescribed fires conducted in a pine forest," in *Proceedings of the Combustion Institute,* Vol. 36, 3263–3270. doi: 10.1016/j.proci.2016.06.125

Foote, E. I., Liu, J., and Manzello, S. L. (2011). "Characterizing firebrand exposure during wildland urban interface fires," in *Proceedings of Fire and Materials 2011 Conference, Interscience Communications* (London). Available online at: https://tsapps.nist.gov/publication/get_pdf.cfm?pub_id=907530

Ganteaume, A., Lampin-Maillet, C., Guijarro, M., Hernando, C., Jappiot, M., Fonturbel, T., et al. (2009). Spot fires: fuel bed flammability and capability of firebrands to ignite fuel beds. *Int. J. Wildl. Fire* 18, 951–969. doi: 10.1071/WF07111

Gould, J. S., McCaw, W. L., Cheney, N. P., Ellis, P. F., Knight, I. K., and Sullivan, A. L. (eds.). (2008). *Project Vesta - Fire in Dry Eucalypt Forest: Fuel Structure, Fuel Dynamics and Fire Behaviour*. Canberra, ACT; Perth, WA: CSIRO Publishing and Department of Environment and Conservation. doi: 10.1071/9780643101296

Hall, J., Ellis, P. F., Cary, G. J., Bishop, G., and Sullivan, A. L. (2015). Long-distance spotting potential of bark strips of a ribbon gum (*Eucalyptus viminalis*). *Int. J. Wildl. Fire* 24, 1109–1117. doi: 10.1071/WF15031

Houssaimi, E. M., Mueller,. E., Filkov, A. I., and Simeoni, A. (2015). Experimental procedures characterising firebrand generation in wildland fires. https://www.researchgate.net/journal/0015-2684_Fire_Technology Fire Technol. 52, 731–751. doi: 10.1007/s10694-015-0492-z

Kutiel, H. (2012). Weather conditions and forest fire propagation—The case of the carmel fire, december 2010. *Isr. J. Ecol. Evol.* 58, 113–122. doi: 10.1560/IJEE.58.2-3.113

Manzello, S. L., Maranghides, A., and Mell, W. E. (2007). Firebrand generation from burning vegetation. *Int. J. Wildl. Fire* 16, 458–462. doi: 10.1071/WF06079

Manzello, S. L., Maranghides, A., Shields, J. R., and Mell, W. E. (2008). Mass and size distribution of firebrands generated from burning Korean pine (*Pinus koraiensis*) trees. *Fire Mater*. 33, 21–31. doi: 10.1002/fam.977

Manzello, S. L., Park, S. H., Suzuki, S., Shields, J. R., and Hayashi, Y. (2011). Experimental investigation of structure vulnerabilities to firebrand showers. *Fire Saf. J.* 46, 568–578. doi: 10.1016/j.firesaf.2011.09.003

Manzello, S. L., and Suzuki, S. (2014). Exposing decking assemblies to continuous wind-driven firebrand showers. *Fire Saf. Sci.* 11, 1339–1352. doi: 10.3801/IAFSS.FSS.11-1339

Oliveira, R. F. S., Quesada-Fernández, C., Viegas, D. X., Freitas, E. I., and Raposo, J. R. N. (2014). "Firebrand generator system applied to wildland-urban interface research," in *Advances in Forest Fire Research*, ed D. X. Viegas (Coimbra: Imprensa da Universidade de Coimbra). doi: 10.14195/978-989-26-0884-6_84

Ribeiro, L. M., Oliveira, R., and Viegas, D. X. (2014). "The history of a large fire or how a series of events lead to 14000 Hectares burned in 3 days," in *Advances in Forest Fire Research*, ed D. X. Viegas (Coimbra: Imprensa da Universidade de Coimbra). doi: 10.14195/978-989-26-0884-6_109

Rothermel, R. C. (1983). *How to predict the spread and intensity of forest and range fires. USDA Forest Service, Intermountain Forest and Range Experiment Station, General Technical Report INT-143* (Ogden, UT). Available online at: http://www.fs.fed.us/rm/pubs_int/int_gtr143.pdf doi: 10.2737/INT-GTR-143

San-Miguel-Ayanz, J., de Rigo, D., Caudullo, G., Houston Durrant, T., and Mauri, A. (2016). *European Atlas of Forest Tree Species. Publication Office of the European Union, Luxembourg*. Available online at: http://forest.jrc.ec.europa.eu/european-atlas-of-forest-tree-species/atlas-download-page

Suzuki, S., Manzello, S. L., Lage, M., and Laing, G. (2012). Firebrand generation data obtained from a full-scale structure burn. *Int. J. Wildl. Fire* 21, 961–968. doi: 10.1071/WF11133

Tarifa, C. S., del Notario, P. P., Moreno, F. G., and Villa, A. R. (1967). *Transport and Combustion of Firebrands*. Instituto Nacional de Tecnica Aeroespacial, Report no. Grants FG-SP-114, FG-SP-146.

Tohidi, A., Kaye, N., and Bridges, W. (2015). Statistical description of firebrand size and shape distribution from coniferous trees for use in Metropolis

Monte Carlo simulations of firebrand flight distance. *Fire Saf. J.* 77, 21–35. doi: 10.1016/j.firesaf.2015.07.008

Viegas, D. X., Almeida, M., Raposo, J., Oliveira, R., and Viegas, C. X. (2014). Ignition of mediterranean fuel beds by several types of firebrands. *Fire Technol.* 50, 61–77. doi: 10.1007/s10694-012-0267-8

Viegas, D. X., Almeida, M. F., Ribeiro, L. M., et al. (2017). O *Complexo dos Incêndios de Pedrógão Grande e Concelhos Limítrofes, iniciado a 17 de Junho de 2017 [The Pedrógão Grande and Border Councils Fire Complex, started on June 17, 2017]*. Available online at: https://www.portugal.gov.pt/download-ficheiros/ficheiro.aspx?v=3bb9773b-59fb-4099-9de5-a22fdcad1e3b

Viegas, D. X., Almeida, M. F., Ribeiro, L. M., et al. (2019). *Análise dos Incêndios Florestais Ocorridos a 15 de Outubro de 2017 [Analysis of Forest Fires Occurring on October 15, 2017]*. Available online at: https://www.portugal.gov.pt/download-ficheiros/ficheiro.aspx?v=c2da3d7e-dcdb-41cb-b6ae-f72123a1c47d

Viegas, D. X., Ribeiro, L. M., Almeida, M. A., et al. (2013). *Relatório sobre os Dois Grandes Incêndios Florestais e os Acidentes Mortais ocorridos em 2013 [Report on the two major forest fires and fatal accidents in 2013]*. Available online at: https://www.portugal.gov.pt/media/1281135/Relatório_IF2013_parte1.pdf

Waterman, T. E. (1969). *Experimental Study of Firebrand Generation. IIT Research Institute, Project J6130* (Chicago, IL). Available online at: https://apps.dtic.mil/dtic/tr/fulltext/u2/695640.pdf

Conflict of Interest: The authors declare that the research was conducted in the absence of any commercial or financial relationships that could be construed as a potential conflict of interest.

frontiers in Mechanical Engineering

ORIGINAL RESEARCH
published: 10 June 2021
doi: 10.3389/fmech.2021.640979

Deposition Characteristics of Firebrands on and Around Rectangular Cubic Structures

*Aditya Mankame and Babak Shotorban**

Department of Mechanical and Aerospace Engineering, The University of Alabama in Huntsville, Huntsville, AL, United States

The focus of the present work is on the deposition of firebrands in a flow over a rectangular cubic block representative of a structure in wildland-urban interface (WUI). The study was carried out by physics based modeling where the wind flow turbulence was dealt with by large eddy simulation (LES) and firebrands were treated by Lagrangian tracking. The Lagrangian equations coupled with the flow solver, accounted for both translational and rotational motions as well as thermochemical degradation of firebrands, assumed to be cylindrical. The dimensions of the structure were varied from 3 to 9 m in the simulations for a parametric study. The simulations were carried out by tracking many firebrands randomly released with a uniform distribution from a horizontal plane 35 m above the ground into the computational domain. The coordinates of the deposited firebrands were used to calculate their normalized number density (number of landed firebrands per unit surface area) to quantify their deposition pattern. On the leewardside of the block, an area, referred to as the safe zone, was identified right behind the structure where firebrands never deposit. The size of the safe zone in the direction perpendicular to the wind was nearly identical to the width of the structure. The length of the safe zone in the wind direction was proportional to the height of the structure. The leeward face of the blocks was never hit by a firebrand. The windward face was hit by many more firebrands than the lateral faces but much less than the top face. The distribution of the number density of the deposited firebrands on the top face was found to be correlated with the flow separation and reattachment on this face.

Keywords: firebrands, flow over a block, large eddy simulation, firebrand deposition, WUI fire, Lagrangian tracking

OPEN ACCESS

Edited by:
Naian Liu,
University of Science and Technology of China, China

Reviewed by:
Wei Tang,
National Institute for Occupational Safety and Health (NIOSH), United States
Xinyan Huang,
Hong Kong Polytechnic University, Hong Kong

****Correspondence:***
Babak Shotorban
babak.shotorban@uah.edu

Specialty section:
This article was submitted to Thermal and Mass Transport, a section of the journal Frontiers in Mechanical Engineering

Received: *12 December 2020*
Accepted: *17 May 2021*
Published: *10 June 2021*

Citation:
Mankame A and Shotorban B (2021) Deposition Characteristics of Firebrands on and Around Rectangular Cubic Structures. Front. Mech. Eng 7:640979. doi: 10.3389/fmech.2021.640979

1 INTRODUCTION

A critical mechanism for the spread of large outdoor fires, e.g., wildland-urban interface (WUI) fires is spotting. Spotting is the creation of the secondary (spot) fires by firebrands that are generated by the primary fires. Firebrands can be lofted up into the atmosphere and carried away by the ambient wind to short/long distances (Tarifa et al., 1967; Sardoy et al., 2008). In the presence of strong ambient winds, firebrands can cross distances from a few 100 m to a few kilometers, thus capable of spreading fires over barriers such as rivers, lakes, hills, etc. Spotting is seen frequently in WUI fires and can burn down many WUI structures under extreme conditions such as an ember shower (Manzello, 2014). This motivated the present computational study with a focus on characterizing the deposition pattern of firebrands carried by the wind on top and in the vicinity of a structure shaped as a rectangular cuboid mounted on the ground. The computational configuration here can be considered as a simplified representation of a single isolated WUI structure.

There have been several studies on the role of firebrands in the spread of wildland and WUI fires. Manzello et al. (2007) performed experiments by burning two Douglas-fir trees with 2.6 and 5.2 m heights. They found that the generated firebrands were predominately cylindrical in shape with an average diameter of 3 mm and length of 40 mm for the shorter tree and 4 and 53 mm for the taller tree. Manzello et al. (2008) constructed an apparatus capable of generating glowing firebrands and used it to release firebrand in a wind tunnel. The firebrands released in the wind-tunnel at 9 m/s experienced a mass loss of 20–40% when compared to firebrands released in no wind condition. Tohidi and Kaye (2017b), Tohidi and Kaye (2017a) experimentally and computationally studied the lofting of firebrands in a wind tunnel where in addition to wind, a convective plume was included. They observed that for higher wind speeds, the change in the initial vertical velocity of the convective column did not affect the mean or standard deviation of the heights where the firebrands lofted or the distances they traveled to land. Yin et al. (2003), Oliveira et al. (2014) developed numerical models for the firebrand transport accounting for the drag, lift and gravitational forces and their effect on the rotation of firebrands to model both translational and rotational motions of cylindrical firebrands. To validate their model, Oliveira et al. (2014) performed computations and experiments for a cylindrical firebrand (balsa wood) falling from an elevated point under a no ambient flow condition. The influence of different formulations for the distance between center of pressure and center of mass of a cylindrical object in motion was explored in the modeling by Rayleigh (1876), Marchildon et al. (1964), Rosendahl (2000), Yin et al. (2003).

Anand et al. (2018) preformed simulations to investigate the deposition of cylindrical firebrands released in a turbulent wind environment from a fixed elevated point. They assumed for firebrands to retain their mass from release to landing. They reported a bivariate Gaussian function like distribution for the landed firebrand position with a larger variance in the streamwise direction, compared to the spanwise direction. Anand (2018) performed similar simulations while allowing firebrands to experience mass loss due to thermal degradation, taking into account the effect of burning. They observed that, firebrands with a higher mass density (570 kg/m^3) experienced a higher mass loss, as compared to lower density (230 kg/m^3) firebrands. The lower density firebrands cooled rapidly and reached ambient temperature before landing. On the other hand, the higher density firebrands retained more thermal energy while flying, thus had higher temperatures at landing. Song et al. (2017) performed wind tunnel experiments with disc-shape firebrands and showed the deposited firebrands had uni-modal distribution except for certain wind speed and firebrand conditions where they displayed a bimodal distribution.

Properties of the flow over a cubic obstacle mounted on the ground have been studied in the past (Murakami et al., 1987; Werner and Wengle, 1993; Lee and Bienkiewicz, 1997; Rodi, 1998). One of the earliest works is due to Murakami et al. (1987) who simulated a cube submerged in a boundary layer using large-eddy simulation (LES). Werner and Wengle (1993), Rodi (1998) computationally studied a cube mounted on a surface in a channel flow with a Reynolds number of $O(10^4)$ based on the velocity at the height of the cube. Werner and Wengle (1993), Rodi (1998) showed the existence of a horse-shoe vortex on the windward side of the cube and flow separation and reattachment on the top face of the cube. Rodi (1998), using different turbulence models, reported two counter rotating re-circulation region on the leeward side of the cube. Vortex shedding was observed originating from the lateral faces with a pair of re-circulation region closer to these faces. More recently, Richards et al. (2001) claimed the pressure coefficient on the surface of the cube is independent of the Reynolds number *via* a field test. Later in wind-tunnel experiments (Richards et al., 2007), they observed a drop in the pressure coefficient on the windward and leeward faces of the cube as the wind direction changed from 90° to 45° with respect to the windward face of the cube. Lim et al. (2009) performed experiments and simulations for a flow around a cube submerged in a turbulent atmospheric surface layer (ASL) and showed that the mean profiles of pressure coefficient and velocity components are independent of the Reynolds number.

The present work is a modeling study focused on deposition of firebrands in a flow over a cubic block representative of a structure in WUI. The flow is dealt with by LES while the deposition of firebrands is treated in the Lagrangian framework. In **Section 2**, modeling approaches are illustrated for both firebrands and the flow. In **Section 3**, results are presented with the model validation results included. Concluding remarks are made in **Section 4**.

2 MODELING APPROACHES

2.1 Firebrand Equations

The firebrand equations are expressed and solved in the Lagrangian framework. Firebrands are assumed to be cylinders with a large ratio of length to diameter, undergoing both translational and rotational motions (Yin et al., 2003; Oliveira et al., 2014; Anand et al., 2018) and thermal degradation as a result of pyrolysis and charring (Morvan and Dupuy, 2004; Anand, 2018).

2.1.1 Translational Motion

The position and velocity of the center of mass of the firebrand are denoted by $\vec{x}_\mathrm{p}$ and $\vec{V}_\mathrm{p}$, respectively, which are governed by

$$\frac{d\vec{x}_\mathrm{p}}{dt} = \vec{V}_\mathrm{p}, \tag{1}$$

$$m_\mathrm{p}\frac{d\vec{V}_\mathrm{p}}{dt} = \vec{F}_\mathrm{G} + \vec{F}_\mathrm{D} + \vec{F}_\mathrm{L}, \tag{2}$$

where d/dt is the time derivative calculated in the Lagrangian framework. **Eq. 2** is an expression of Newton's second law where the forces are due to gravity combined with buoyancy $\vec{F}_\mathrm{G}$, drag $\vec{F}_\mathrm{D}$ and lift $\vec{F}_\mathrm{L}$, which are calculated (Hoerner, 1965) by:

$$\vec{F}_\mathrm{G} = \left(\rho_\mathrm{p} - \rho_\mathrm{gas}\right)\mathcal{V}\vec{g}, \tag{3}$$

$$\vec{F}_{\mathrm{D}} = \frac{1}{2} C_{\mathrm{D}} \rho_{\mathrm{gas}} D_{\mathrm{p}} l \left| \vec{V}_{\mathrm{rel}} \right| \left| \sin\alpha \right|^{3} \vec{V}_{\mathrm{rel}}, \tag{4}$$

$$\vec{F}_{\mathrm{L}} = \frac{1}{2} C_{\mathrm{D}} \rho_{\mathrm{gas}} D_{\mathrm{p}} l \left(\left| \vec{V}_{\mathrm{rel}} \right| \sin\alpha \right)^{2} \cos\alpha \, \frac{\hat{z}_{\mathrm{r}} \times \vec{V}_{\mathrm{rel}} \times \vec{V}_{\mathrm{rel}}}{\left| \hat{z}_{\mathrm{r}} \times \vec{V}_{\mathrm{rel}} \times \vec{V}_{\mathrm{rel}} \right|}, \tag{5}$$

$$C_{\mathrm{D}} = \begin{cases} \dfrac{10}{\mathrm{Re}_{\alpha}^{0.778}} & \text{for } \mathrm{Re}_{\alpha} \leq 0.1, \\ \dfrac{10}{\mathrm{Re}_{\alpha}^{0.778}} \left(1 + 0.1076 \mathrm{Re}_{\alpha}^{0.778} \right) & \text{for } 0.1 < \mathrm{Re}_{\alpha} \leq 6 \times 10^{3}, \\ 1.1 & \text{for } 6 \times 10^{3} < \mathrm{Re}_{\alpha} \leq 2 \times 10^{5}. \end{cases} \tag{6}$$

Here, $\rho_{\mathrm{p}}, D_{\mathrm{p}}, l, \mathcal{V}, m_{\mathrm{p}}$ and $\vec{V}_{\mathrm{rel}}$ are the firebrand density, diameter, length, volume, mass and velocity relative to the flow at the center of mass of the particle, respectively. It is calculated by $\vec{V}_{\mathrm{rel}}(t) = \vec{U}[\vec{x}_{\mathrm{p}}(t), t] - \vec{V}_{\mathrm{p}}(t)$ where the first term indicates the flow velocity at the position of the center of mass of the firebrand. The drag coefficient C_{D} is calculated, using the particle Reynolds number $\mathrm{Re}_{\alpha} = D_{\mathrm{p}} \rho \left| \vec{V}_{\mathrm{rel}} \right| \sin\alpha / \mu$ (Kelbaliyev, 2011), where ρ_{gas} is the density of air and α is the incidence angle between the relative velocity and the major axis of the cylindrical firebrand $\hat{z}_{\mathrm{r}}$.

2.1.2 Rotational Motion

The rotational motion is described by the Euler rotation equation:

$$I_{x'} \frac{d\omega_{x'}}{dt} - \omega_{y'} \omega_{z'} \left(I_{y'} - I_{z'} \right) = T'_{x'}, \tag{7}$$

$$I_{y'} \frac{d\omega_{y'}}{dt} - \omega_{z'} \omega_{x'} \left(I_{z'} - I_{x'} \right) = T'_{y'}, \tag{8}$$

$$I_{z'} \frac{d\omega_{z'}}{dt} - \omega_{x'} \omega_{y'} \left(I_{x'} - I_{y'} \right) = T'_{z'}, \tag{9}$$

where $I_{x'}, I_{y'}$ and $I_{z'}$ are the moments of inertia with respect to the Cartesian frame of reference x'-y'-z' attached to the cylindrical firebrand with the origin at the cylinder center and the z' axis constituting the cylinder axis. The total torque is the addition of the torque $\vec{T}'_{\mathrm{hydro}}$ due to the hydrodynamic forces and the torque $\vec{T}'_{\mathrm{resist}}$ (Oliveira et al., 2014) due to the frictional air resistance experienced by the firebrand

$$\vec{T}' = \vec{T}'_{\mathrm{hydro}} + \vec{T}'_{\mathrm{resist}}, \tag{10}$$

$$\vec{T}'_{\mathrm{resist}} = \sqrt{\left(T^{x'}_{\mathrm{resist}} \right)^{2} + \left(T^{y'}_{\mathrm{resist}} \right)^{2}}, \tag{11}$$

$$T^{x'}_{\mathrm{resist}} = -\rho_{\mathrm{gas}} \left| \omega_{x'} \right| a b^{4} \left[0.538 + 3.62 \left(\frac{\rho_{\mathrm{gas}} a \left| \omega_{x'} \right| b}{\mu} \right)^{-0.778} \right] \omega_{x'}, \tag{12}$$

$$T^{y'}_{\mathrm{resist}} = -\rho_{\mathrm{gas}} \left| \omega_{y'} \right| a b^{4} \left[0.538 + 3.62 \left(\frac{\rho_{\mathrm{gas}} a \left| \omega_{y'} \right| b}{\mu} \right)^{-0.778} \right] \omega_{y'}, \tag{13}$$

$$\vec{T}'_{\mathrm{hydro}} = x_{\mathrm{cp}} \mathbf{A} \cdot \left[\hat{z}_{\mathrm{r}} \times \left(\vec{F}_{\mathrm{D}} + \vec{F}_{\mathrm{L}} \right) \right], \tag{14}$$

$$x_{\mathrm{cp}} = l(90 - \alpha) / 480. \tag{15}$$

Here, $a = D_{\mathrm{p}}/2$ is the radius of the firebrand, $b = l/2$ is the half length and x_{cp} is the distance between the center of pressure and the center of mass (Marchildon et al., 1964), and $\mathbf{A}$ is the transformation matrix expressed in terms of quaternions $\epsilon_1, \epsilon_2, \epsilon_3$ and η (Yin et al., 2003):

$$\mathbf{A} = \begin{bmatrix} 1 - 2\left(\epsilon_2^2 + \epsilon_3^2\right) & 2\left(\epsilon_1\epsilon_2 + \epsilon_3\eta\right) & 2\left(\epsilon_1\epsilon_3 - \epsilon_2\eta\right) \\ 2\left(\epsilon_2\epsilon_1 - \epsilon_3\eta\right) & 1 - 2\left(\epsilon_3^2 + \epsilon_1^2\right) & 2\left(\epsilon_2\epsilon_3 + \epsilon_1\eta\right) \\ 2\left(\epsilon_1\epsilon_3 + \epsilon_2\eta\right) & 2\left(\epsilon_3\epsilon_2 - \epsilon_1\eta\right) & 1 - 2\left(\epsilon_1^2 + \epsilon_2^2\right) \end{bmatrix}. \tag{16}$$

Quaternions are governed by

$$\frac{d}{dt} \begin{bmatrix} \epsilon_1 \\ \epsilon_2 \\ \epsilon_3 \\ \eta \end{bmatrix} = \frac{1}{2} \begin{bmatrix} \eta\omega_{x'} - \epsilon_3\omega_{y'} + \epsilon_2\omega_{z'} \\ \epsilon_3\omega_{x'} + \eta\omega_{y'} - \epsilon_1\omega_{z'} \\ -\epsilon_2\omega_{x'} + \epsilon_1\omega_{y'} + \eta\omega_{z'} \\ -\epsilon_1\omega_{x'} - \epsilon_2\omega_{y'} - \epsilon_3\omega_{z'} \end{bmatrix}. \tag{17}$$

The quaternions are correlated with Euler angles (ϕ, ψ, θ) through the following equations, which are used here to find initial values of the quaternions:

$$\epsilon_1 = \cos\left(\frac{\phi - \psi}{2}\right) \sin\left(\frac{\theta}{2}\right), \tag{18}$$

$$\epsilon_2 = \sin\left(\frac{\phi - \psi}{2}\right) \sin\left(\frac{\theta}{2}\right), \tag{19}$$

$$\epsilon_3 = \sin\left(\frac{\phi + \psi}{2}\right) \cos\left(\frac{\theta}{2}\right), \tag{20}$$

$$\eta = \cos\left(\frac{\phi + \psi}{2}\right) \cos\left(\frac{\theta}{2}\right). \tag{21}$$

2.1.3 Mass and Temperature

Heat is transfered from the firebrand to the surrounding gas through thermal radiation and convection. The firebrand undergoes thermal degradation and loses mass as a result of pyrolysis and char oxidation. To take this effect into account, the firebrand model assumes for the firebrand to be thermally thin (i.e. temperature throughout the firebrand is spatially uniform) with a mass governed by:

$$\frac{dm_{\mathrm{p}}}{dt} = -\dot{m}_{\mathrm{pyr}} - \dot{m}_{\mathrm{char}}, \tag{22}$$

where $\dot{m}_{\mathrm{pyr}}$ and $\dot{m}_{\mathrm{char}}$ are the mass loss rates due to pyrolysis and char oxidation, respectively, which are modeled by the Arrhenius equation:

$$\dot{m}_i = -m_i A_i \exp\left(-\frac{T_i}{T_{\mathrm{p}}} \right), \tag{23}$$

where m_i represents the mass of the solid constituent, namely i = pyr for the charring of the fuel and char for char oxidation, A_i is the pre-exponential factor, T_{p} is the temperature of the firebrand and $T_i = E_i/R$ is the activation temperature where E_i is the activation energy. The pre-exponential factor and activation temperature for pyrolysis are $A_{\mathrm{pyr}} = 725\ \mathrm{s}^{-1}$, $T_{\mathrm{pyr}} = 6899$ K (for *Pinus*) and for char oxidation are $A_{\mathrm{char}} = 430$ m/s, $T_{\mathrm{char}} = 9000$ K (Morvan and Dupuy, 2004; Sardoy et al., 2007; Anand, 2018).

The firebrand temperature is governed by

$$m_{\mathrm{p}} c_{\mathrm{p}} \frac{dT_{\mathrm{p}}}{dt} = -\Delta h_{\mathrm{pyr}} \dot{m}_{\mathrm{pyr}} - \Delta h_{\mathrm{char}} \dot{m}_{\mathrm{char}} - \dot{q}_{\mathrm{c}} - \dot{q}_{\mathrm{r}}, \tag{24}$$

where $\Delta h_{\mathrm{pyr}} = 418$ kJ/kg and $\Delta h_{\mathrm{char}} = 12 \times 10^{3}$ kJ/kg are the enthalpy of pyrolysis and char oxidation, respectively (Sardoy

et al., 2007; Mell et al., 2009; Anand, 2018). Here, $\dot{q}_c$ and $\dot{q}_r$ are the rates of the convective and radiative heat transfer, respectively:

$$\dot{q}_c = h_c A\left(T_p - T_\infty\right), \tag{25}$$

$$\dot{q}_r = \sigma\epsilon A\left(T_p^4 - T_\infty^4\right), \tag{26}$$

where A is the surface area of the firebrand, T_∞ is the ambient temperature, h is the heat transfer coefficient, σ is the Stefan-Boltzmann constant and ϵ is the emmisitivity of the firebrand set to 0.9. It is noted that for improved modeling of the mass loss and thermal energy, combustion models are needed in addition to the char oxidation representation here to more accurately represent the burning effect.

2.2 Computational Approach

Our group developed a model that handles the transport and burning of firebrands, according to **Eqs. 1–26**, in the framework of Fire Dynamic Simulator (FDS, version 6.7.0) (McGrattan et al., 2018). FDS is computational fluid dynamics (CFD) based software capable of modeling the fire dynamics while representing significant thermal, chemical and physical processes such as combustion, turbulence, radiation, etc. In the present study, only the fluid dynamical features of FDS are relevant. Turbulence is dealt with by LES in FDS with the default option of Deardoff model (Deardorff, 1980) set to represent the subgrid-scale (SGS) terms here. FDS uses Wall-Adapting Local Eddy-viscosity model (WALE) (Nicoud and Ducros, 1999) as the near-wall model by default. The firebrand equations are solved by a second-order Admas-Bashforth time integration method, as described by Anand et al. (2018) and Anand (2018). In computations, $\vec{U}[\vec{x}_p(t), t]$ defined in **Section 2.1.1** is calculated *via* a trilinear interpolation of the flow velocities at cell faces to the location of center of mass of the firebrand. The coupling of firebrands to the flow solver is one-way, as the influence of firebrands on the flow is assumed negligible. The firebrands deposited on the solid surfaces, i.e., ground and faces of the block, are removed from the simulation after their deposition coordinates are recorded.

3 RESULTS AND DISCUSSION

3.1 Firebrand Model Validation

To validate the firebrand model, first, a firebrand drop test previously investigated both experimentally and computationally (Oliveira et al., 2014) was considered. The exercise involved a non-burning cylindrical firebrand made from balsa wood with diameter 10 mm and length 80 mm, which was released from the height 8.7 m in a no-wind condition. At the release point, the firebrand had zero velocities and made an angle of 60° with the vertical axis. The firebrand mass density was reported $\rho_p = 215.5\ \mathrm{kg/m^3}$. Using the firebrand model illustrated in **Section 2.1.1** and **Section 2.1.2**, the drop test was simulated here in a computational domain $1.5 \times 1.5 \times 9$ m (length × width × height). In lieu of **Eq. 15** (Marchildon et al., 1964), other formulas (**Table 1**) have been also reported in the literature (Rayleigh, 1876; Rosendahl, 2000; Yin et al., 2003) for calculation of x_{cp}. This motivated a sensitivity study of the model to these formulas to be a part of this validation exercise.

Table 1 tabulates the landing times calculated in the current study using various x_{cp} formulas and compares them against those obtained in the modeling and measurement of Oliveira et al. (2014). Corresponding trajectories of the firebrand from release to landing are shown in **Figure 1**. Both table and figure suggest the significance of the x_{cp} formula in the firebrand landing time and trajectory. Discussed by Oliveira et al. (2014) was the notable difference between the amplitudes of the trajectory oscillation in their model (panel E in **Figure 1**) and their measurement (panel F). They additionally argued that this difference was correlated with the difference between their corresponding calculated and measured landing times, as tabulated in **Table 1**. On the other hand, **Figure 1** suggests that the amplitude obtained in the current simulations, regardless of the formula used x_{cp}, was significantly more consistent with the experimental data of Oliveira et al. (2014). When the x_{cp} formulas of Rayleigh (1876) (panel A) and Marchildon et al. (1964) (panel B) were used, the amplitudes of the trajectories were slightly larger than those observed in the experiment and accordingly, the calculated landing times were slightly smaller than the measured landing time. When the formula of Rosendahl (2000) (panel C) was used, the calculated amplitude seemed to be more consistent with the amplitude in the experiment. However, the calculated landing time was greater than the measured landing time by a larger amount. When the formula of Yin et al. (2003) (panel D) was used in the calculations, the resulting amplitude was larger than both the measured amplitude and the amplitude measured by other formals. However, the landing time was closer to the measured landing time.

3.2 Flow Model Validation

The flow model used here was first validated against the previous experimental and modeling data obtained in a wind tunnel for a flow over a cubic block (Lim et al., 2009). The test section of the wind tunnel had dimensions of $4.5 \times 0.9 \times 0.6$ m (length, width and height, respectively) with a cube of height of 0.08 m situated 2.36 m from the inlet of the tunnel. **Figure 2** displays the computational domain $0.8 \times 0.4 \times 0.4$ m with a gird resolution of $320 \times 160 \times 160$ and the cube with height 0.08 m. The computational configuration and resolution here are consistent with the simulation of Lim et al. (2009). A power law profile was set as the inlet boundary condition with a power law exponent of 0.18. Consistent with the simulation of Lim et al. (2009), a Reynolds number of $\mathrm{Re}_h = U_h h/\nu = 20,000$, where h is a reference length identical to the cube height and $U_h = 4.5$ m/s is the reference velocity at the inlet at the vertical location $z = h$. It is noted that Lim et al. (2009) reported that they conducted their experiments for Reynolds numbers in the range between 18, 600 and 73, 100 but did not find the mean and variance of measured velocities to significantly change at this range of Reynolds numbers. The lateral and top boundaries were set to be free slip and the outflow boundary condition was set to be open. At the inlet, turbulence with the intensity of 5% was introduced.

TABLE 1 | Landing time of a cylindrical firebrand released in a still air in the previous experiment and simulation (Oliveira et al., 2014), and present simulations using different formula for the center of pressure x_{cp} (Rayleigh, 1876; Marchildon et al., 1964; Rosendahl, 2000; Yin et al., 2003).

	Landing time (s)	Formula of x_{cp}/l	References
A	1.5312 (present)	$0.75\sin\alpha/(4+\pi\cos\alpha)$	Rayleigh (1876)
B	1.5246 (present)	$(90-\alpha)/480$	Marchildon et al. (1964)
C	1.9397 (present)	$0.25(1-\sin^3\alpha)$	Rosendahl (2000)
D	1.6564 (present)	$0.125\cos^3\alpha$	Yin et al. (2003)
E	2.06 (previous)	$(90-\alpha)/480$	Oliveira et al. (2014) (simulation)
F	1.70 ± 0.05 (previous)	—	Oliveira et al. (2014) (experiment)

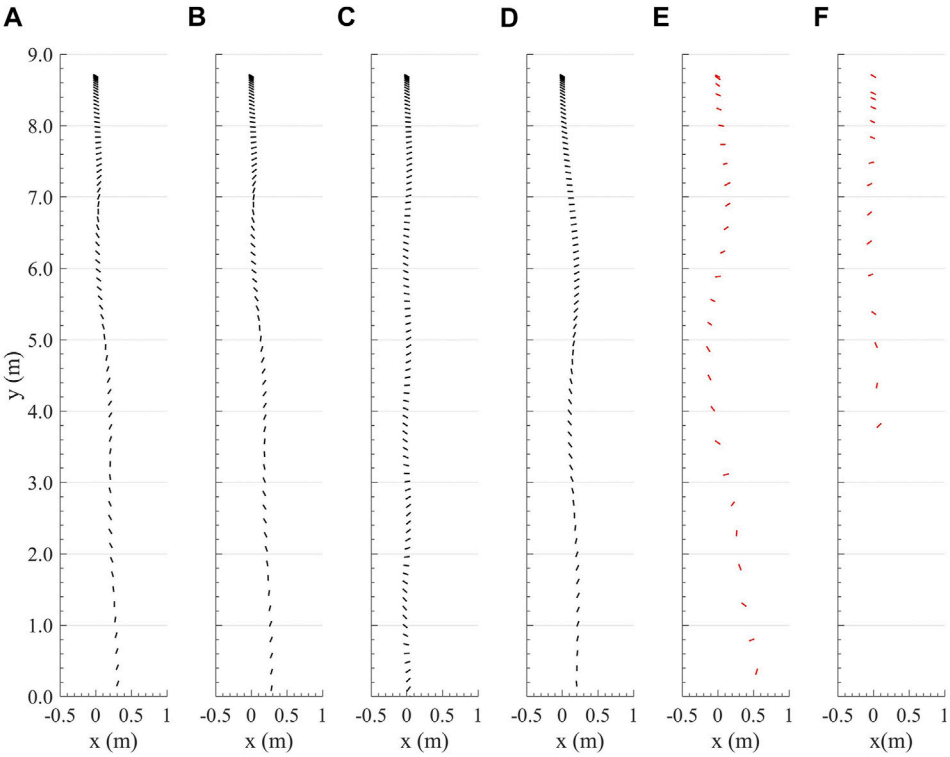

FIGURE 1 | Trajectory of a cylindrical particle released in still air condition in the present simulations using center of pressure formulation of **(A)** Rayleigh (1876); **(B)** Marchildon et al. (1964); **(C)** Rosendahl (2000); **(D)** Yin et al. (2003); **(E)** Oliveira et al. (2014); and **(F)** the experiment of Oliveira et al. (2014).

Flow turbulence was dealt with by LES with the Deardoff SGS (Deardorff, 1980) and near-wall models, as discussed in **Section 2.2**. However, the simulations were repeated with other SGS models including constant Smagorinsky (Smagorinsky, 1963), dynamic Smagorinsky (Germano et al., 1991; Moin et al., 1991), Vreman (Vreman, 2004) and RNG (Yakhot et al., 1989) available in FDS. It was determined that the results were negligibly sensitive to the SGS models. Hence, only the results of the Deardoff model are presented here.

Figure 3 shows the mean velocity streamlines at a slice $y = 0$ and $z = 0.5h$ obtained from present simulations. This figure shows the key flow structures around the cube, viz. the center of the horseshoe vortex, the flow separation and reattachment on the top and lateral faces, flow reattachment on the leeward side of the cube, the two counter rotating re-circulation region and the stagnation point of the windward face of the cube. **Table 2** compares the locations of these points of interest obtained in the current study with those obtained in the simulation of Lim et al. (2009). The center of the horseshoe vortex obtained here is a little further away from the windward face of the cube when compared to the previous simulation (Lim et al., 2009). On the other hand, the locations of the stagnation point on the windward face of the cube, the reattachment length on the top face of the cube and the reattachment length on the leeward side of the cube obtained here closely match those in the simulation of Lim et al. (2009), as seen in **Table 2**.

Figure 4 shows the pressure coefficient C_p on the axial (i.e. $y/h = 0$) and transverse (i.e. $x/h = 0.5$) center-lines on the faces of the block as indicated in **Figure 2**. As could be seen **Figure 4**, the pressure coefficient calculated here for the top

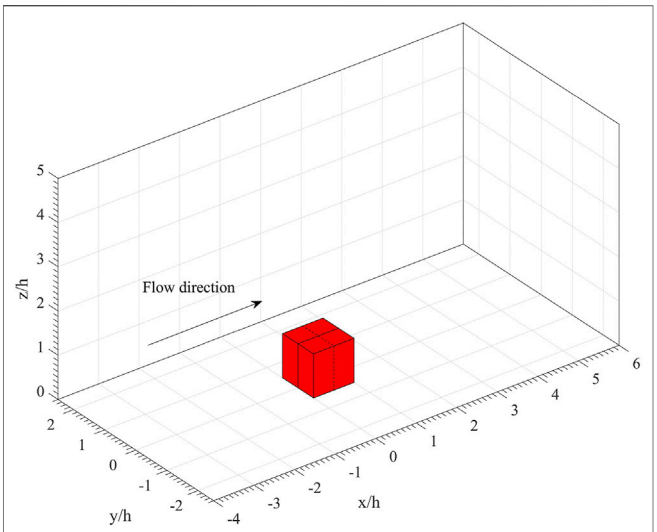

FIGURE 2 | Computational domain $10h \times 5h \times 5h$ for the cube height, $h = 0.08$ m with a grid resolution of $320 \times 160 \times 160$ used in the model validation against the experimental data of Lim et al. (2009). The axial centerline (solid line) at $y/h = 0$ and the transverse centerline (dashed line) at $x/h = 0.5$ are shown.

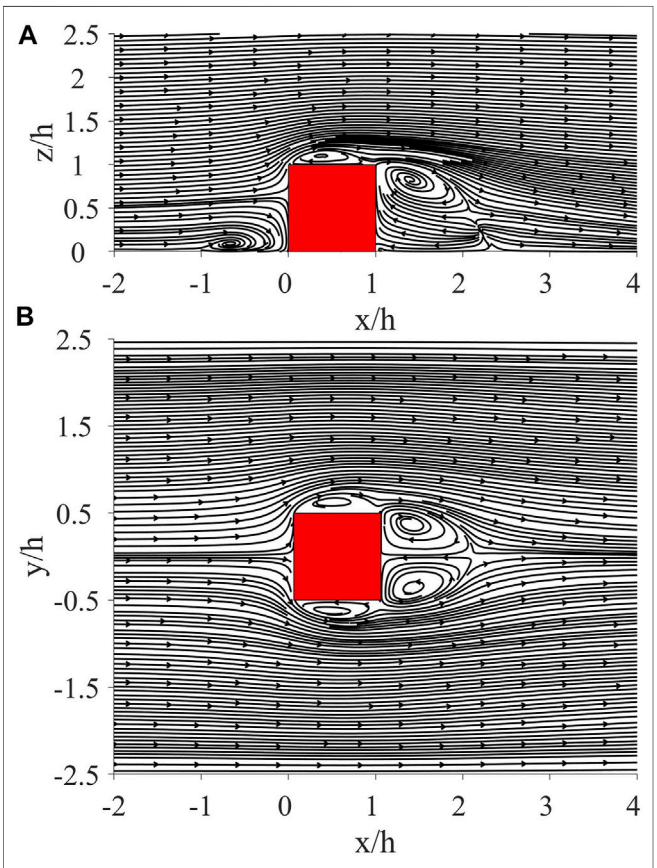

FIGURE 3 | Mean velocity streamlines at **(A)** slice $y = 0$; and **(B)** slice $z = 0.5h$ of the flow over $8 \times 8 \times 8$ cm cube at $Re_h = 2 \times 10^4$ in the flow model validation study.

TABLE 2 | The locations of the center of the horseshoe vortex (HSV) (x_{HVC}, y_{HVC}); the stagnation point on the windward face y_{stag}; the flow reattachment point on the top face x_{top} and the flow reattachment point on the leeward side of the structure x_{lee} in the previous (Lim et al., 2009) and current simulations in the flow model validation study.

	(x_{HVC}, y_{HVC})	y_{stag}	x_{top}	x_{lee}
Simulation of Lim et al. (2009)	(–0.50, 0.10 *h*)	0.73 *h*	0.75 *h*	1.56 *h*
Present simulation	(–0.74, 0.08 *h*)	0.66 *h*	0.83 *h*	1.51 *h*

face of the cube compares very well against the experimental and simulation data of Lim et al. (2009). The agreement between the current simulation and the previous works for this coefficient is reasonable for the rest of the faces. The experimental data of Richards et al. (2001) is also shown here for a comparison albeit they were obtained for a different Reynolds number of 4.1×10^6. The profile in **Figure 4A** shows the largest positive pressure on the windward face of the cube closer to the leading edge which is a result of the cube blocking the flow. On the top face, the largest negative pressure right after the leading edge is associated with the flow separation at the leading edge which is followed pressure recovery corresponding to the flow reattachment.

In **Figure 5**, the mean streamwise and vertical velocities are plotted vs. z on the axial centerline of the top face of the block at various x's. The agreement between the current simulation and the previous experiment and simulation (Lim et al., 2009) is very good. The change of the velocity profile in the x direction is attributed to the flow separation on the top face.

Figure 6 shows the profiles of the root mean square (rms) of the streamwise and vertical velocities as well as the Reynolds shear stress at various x's on the axial center-line of the top face of the block. As could be seen in **Figures 6A,B**, the current simulation substantially over-predicts the rms values obtained in the previous experiments and the simulation (Lim et al., 2009). On the other hand, the Reynolds shear stress in the simulation is in reasonably good agreement with the previous experimental and simulation data.

3.3 Firebrand Deposition in the Flow Over a Single Structure

Figure 7 shows the computational configuration used in the simulation of firebrand deposition in a flow over a single cubic structure. The length, width and height of the structure are indicated by L, W and H, which are its dimensions in the x, y and z directions, respectively. Simulations were carried out for structures with various lengths, widths and heights. The domain size is $75 \times 36 \times 36$ m in the x, y and z directions, respectively. The domain is divided into two sub-domains with a finer gird ($0.15 \times 0.15 \times 0.15$ m) between heights 0–12 m and a coarse grid ($0.3 \times 0.3 \times 0.3$ m) between heights 12–36 m. The inlet flow velocity was specified by a power law with an exponent of 0.18 with a velocity of 6 m/s at a reference height $h = 3$ m which resulted in $Re_h = 1 \times 10^6$. The turbulent intensity at the inlet was set to 20%. This inlet boundary condition is an approximate

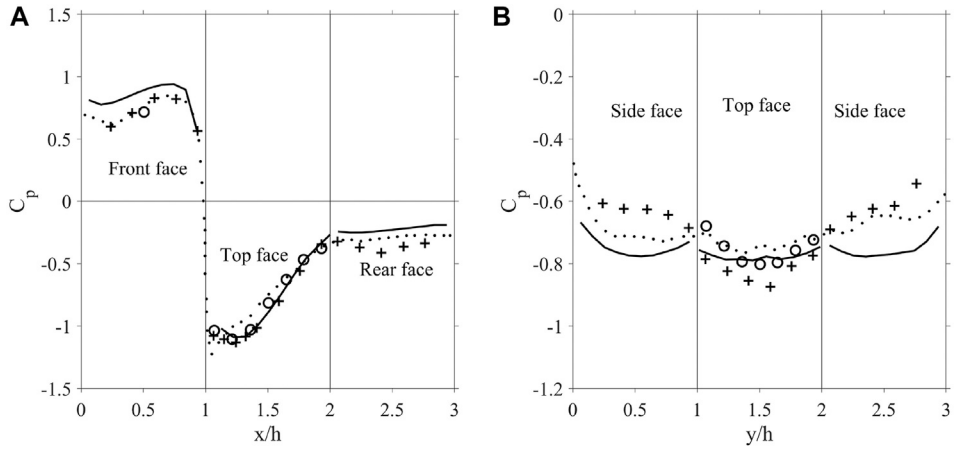

FIGURE 4 | Pressure coefficient on the surface of the cube in the flow validation study; **(A)** the axial centerline where $y/h = 0$; and **(B)** the transverse centreline where $x/h = 0.5$ in the experiments of Lim et al. (2009) (∘) and Richards et al. (2001) (+), the simulations of Lim et al. (2009) (dotted line) and the present computational study (solid line).

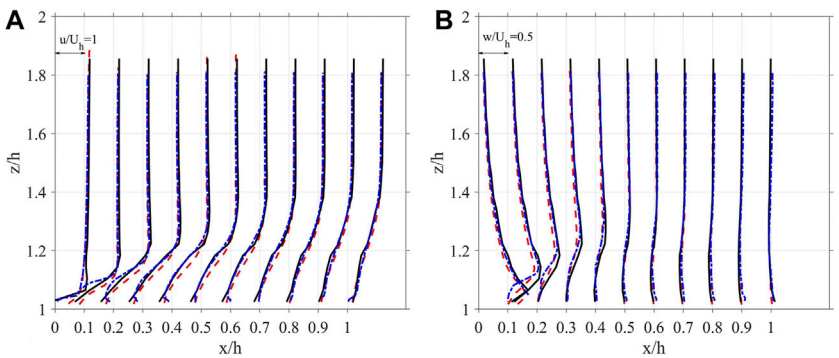

FIGURE 5 | Profiles of **(A)** the streamwise mean velocity; and **(B)** the vertical mean velocity in the flow model validation study; the experiment (blue dashed-dotted line), and simulation (red dashed line) of Lim et al. (2009) and the present simulation (solid line).

representation of a neutrally stable ASL. The modeling approaches such as SGS turbulent closure model and the near-wall models are the same described in **Section 3.2**. The dimension and velocity scales the structures are selected here to be relevant to WUI.

The firebrands were released every second from positions with coordinates randomly selected with a uniform distribution from a horizontal plane passing $z = 35$ m, as shown in **Figure 7**, after the flow reached a statistically stationary state. At the release points, firebrands had a zero velocity with the orientation of 60° with respect to the vertical axis and the initial firebrand temperature $T_p = 773$ K. The initial firebrand mass density was 570 kg/m^3, and the firebrand diameter and length of 3 mm and 40 mm, respectively (Manzello et al., 2007). Considering the flow and firebrand release conditions, the simulations here will be relevant to long range spotting. The random initial distribution of firebrands is to account for the uncertainty of the firebrand release point.

To quantify the spatial distribution of the firebrands deposited on the ground and the top face of the block, a criterion proposed by Anand et al. (2018) with the following function, was used:

$$\widehat{f}(x,y) = \frac{1}{nB^2}\sum_{i=1}^{n}\kappa\left(\frac{x-x_i}{B},\frac{y-y_i}{B}\right) \tag{27}$$

where n is the total number of the deposited firebrands, and $\kappa(\cdot,\cdot)$ is the kernel function with $\widehat{f}$ satisfying the normalization condition $\int\int \widehat{f}\,dxdy = 1$. Here, B is the bandwidth, which set to 0.25 m in this study, and x_i and y_i are the landing coordinates of the firebrand number i. In the simulation, $n \sim 3.8 \times 10^6$ firebrands were deposited. The reason for release of many firebrands is to generate enough samples for the statistical description of the deposition location of firebrands. A Gaussian function was selected as the kernel function MathWorks (2019a) here. It is noted that $\widehat{f}(x,y)$

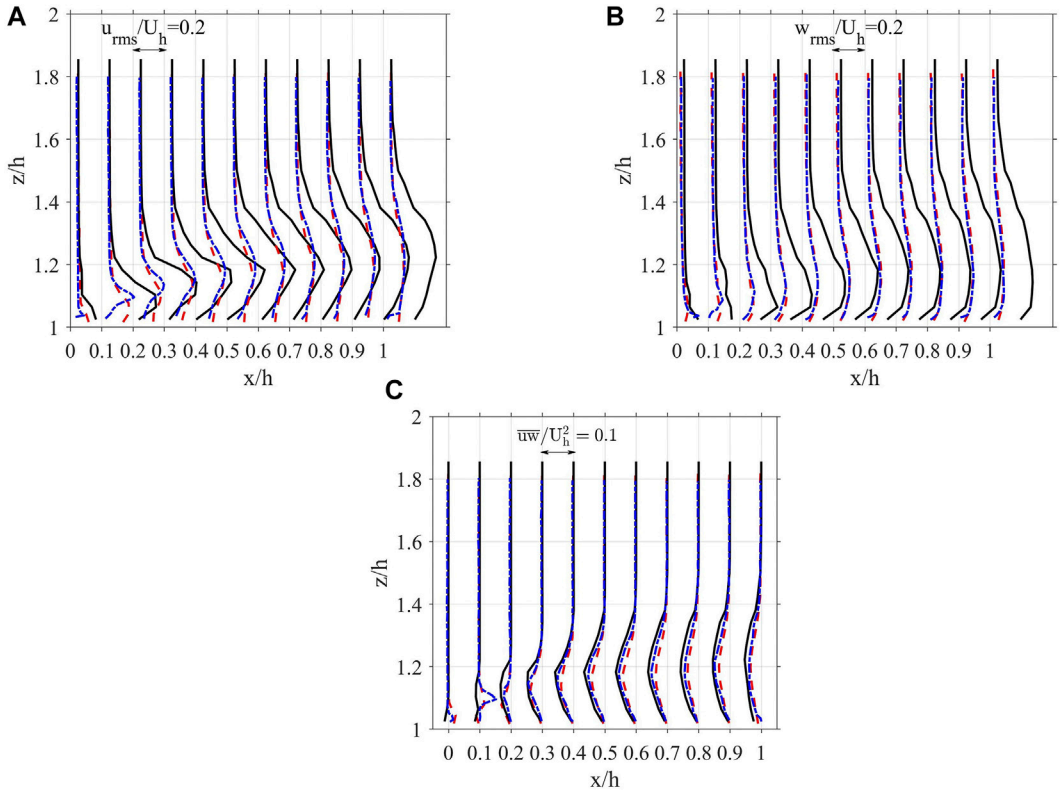

FIGURE 6 | Profiles of **(A)** the streamwise velocity rms; **(B)** the vertical velocity rms; and **(C)** Reynolds shear stress $\overline{uw}$ in flow model validation study; the experiment (blue dashed-dotted line) and simulation (red dashed line) of Lim et al. (2009), and the present simulation (solid line).

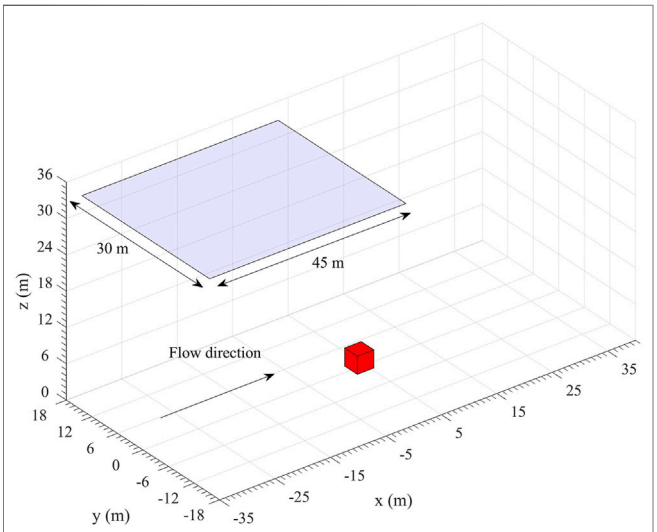

FIGURE 7 | Computational configuration in the firebrand deposition study with a structure 3 × 3 × 3 m. The horizontal plane located at z = 35 m is where the firebrands are released from.

defined in **Eq. 27** indicates the normalized number density (NND) of deposited firebrands, where the number density is defined as the number of firebrands deposited per unit area.

Figure 8 shows the mean velocity streamlines superimposed on the contour plots of mean velocity magnitude on the slice $y = 0$ for varying structure sizes (panels B–H) and no structure (panel A). The streamline features here, when there is a structure, overall resemble the ones seen in **Figure 3A**, which is for a low Reynolds number. However, the details of these features are different for various displayed cases. In the group of structures (panels C, E, F) with fixed lengths and heights but varying widths, the horseshoe vortex and the length of the wake on the leeward side of the structure increases in size with the increase of the width. It can also be seen that the flow accelerates above the leading edge of the structure. This acceleration in the flow is more prominent for a group of structures (panels B,C,D) with fixed lengths and widths but varying heights, as the height of the structure increases. The length of the wake on the leeward side of the structure decreases slightly as the length of the structure increases as seen in the group of structures (panels C,G,H).

Figure 9 shows a top view of the contour plots of NND of the deposited firebrands for cases displayed in **Figure 8**. As seen in this figure, there is a region of very low NND on the leeward side in panels with structures. Examining the scattered deposited particle data revealed that no firebrands were deposited on this region. This region is hereby referred to as the safe zone. The safe zone is approximately shaped like a rectangle with a

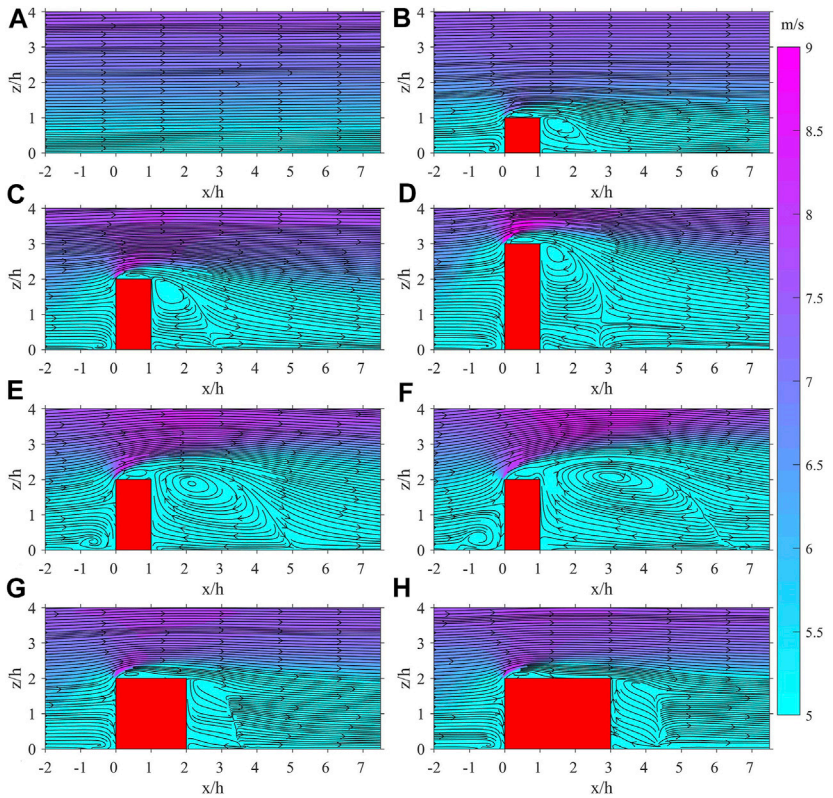

FIGURE 8 | Mean velocity streamlines superimposed on the contour plots of mean velocity magnitude at slice $y = 0$ **(A)** with no structure; and with structure with **(B)** $L = W = H = 3$ m; **(C)** $L = W = 3$ m, $H = 6$ m; **(D)** $L = W = 3$ m, $H = 9$ m; **(E)** $L = 3$ m, $W = H = 6$ m; **(F)** $L = 3$ m, $W = 9$ m, $H = 6$ m; **(G)** $L = H = 6$ m, $W = 3$ m; **(H)** $L = 9$ m, $W = 3$ m, $H = 6$ m.

length l_r and a width w_r (in the spanwise direction), which is almost identical to the width of the structure W. The length l_r is calculated as the distance from the leeward face of the structure to where the NND is 3.85×10^{-4}. As seen in **Figure 9**, the safe zone length is larger for the structures with larger heights. **Figure 10** displays l_r vs. H and indicates that for every 3 m increase of the structure height, the safe zone length increases roughly by one meter. The change in width W or length L of the structure barely affected the length of the safe zone. The simulation of the structure size $L = W = H = 3$ m was repeated with a grid size twice larger in each direction and it was found that l_r decreased less than 6%.

Figures 11A–C shows the NND of deposited firebrands vs. x at $y = 0$ and **Figures 11E,F** plots it against y at $x = 0$ for various structure sizes and the case with no structure. Seen in **Figures 11A–C**, are distinct troughs in cases with a structure, which correspond to the safe zones. It is also seen in these panels that NND overall decreases from the leading to the trailing edge on top of the structures. This feature is associated with the flow separation that occurs on top faces of the block, which is visible in **Figure 8**. It is seen in **Figures 8G,H**, which are for the blocks with longer lengths, this separated flow reattaches. It is believed that this reattachment gives rise to the local peaks of NND on the top face of the structure which are more pronounced for $L = 6$ and 9 m in **Figure 11C**. This could be a result of some firebrands gaining momentum from the accelerated flow above the leading edge of the structure (**Figure 8**) and depositing closer to its trailing edge. The curves of the cases with structures in **Figures 11D–F** show that the NND on top faces overall has smaller values compared to the neighboring areas on the ground. **Figures 11A,D** shows that an increase in the height of the structure results in a slightly higher NND on the top face of the structure.

Table 3 shows the number of firebrands deposited and their temperatures on the top, front and lateral faces of the structure. In none of the cases, a firebrand was deposited on the back face of the structure. This table shows that in the cases with varying height but the same width and length, the number of firebrands deposited on the top face and their average temperature increase with an increasing height. The reason for this average temperature increase is that overall as firebrands descend, their temperatures drop. **Figure 12** shows the exact location and temperature of each deposited firebrand on all faces of one of the considered structures but the leeward face. As noted earlier, the leeward face did not receive any firebrands in any of the cases. As evident in this figure, the temperature of the

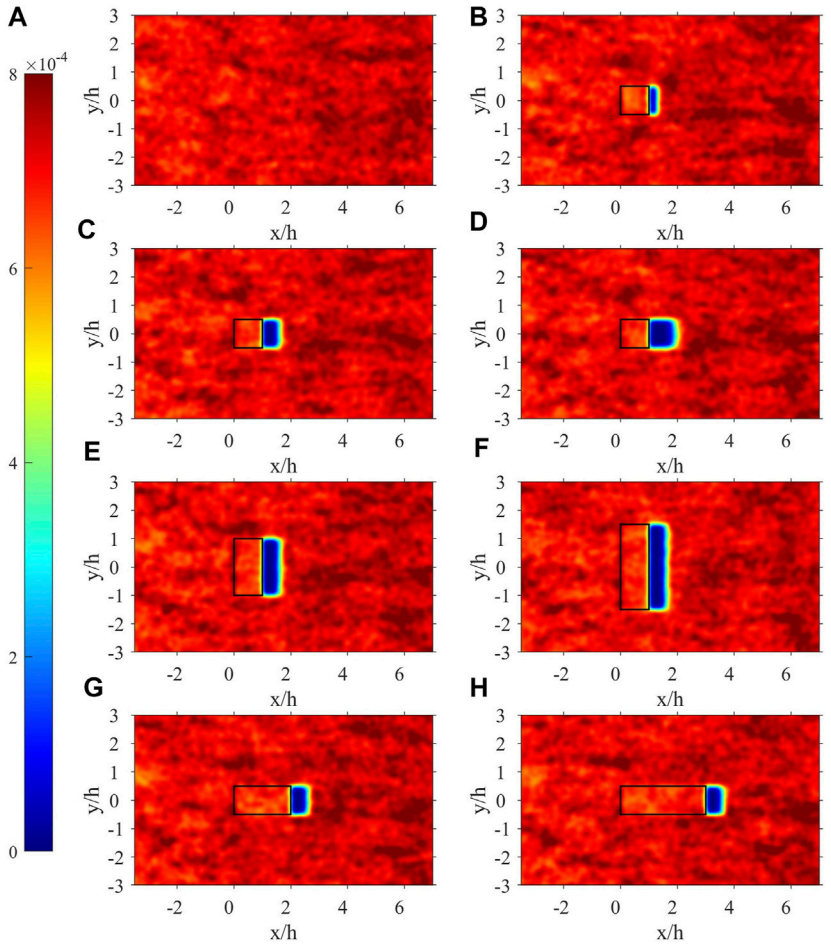

FIGURE 9 | Contour plots of normalized number density of the deposited firebrands on the ground **(A)** with no structure; top face and the ground around single structures with **(B)** $L = W = H = 3$ m; **(C)** $L = W = 3$ m, $H = 6$ m; **(D)** $L = W = 3$ m, $H = 9$ m; **(E)** $L = 3$ m, $W = H = 6$ m; **(F)** $L = 3$ m, $W = 9$ m, $H = 6$ m; **(G)** $L = H = 6$ m, $W = 3$ m; **(H)** $L = 9$ m, $W = 3$ m, $H = 6$ m.

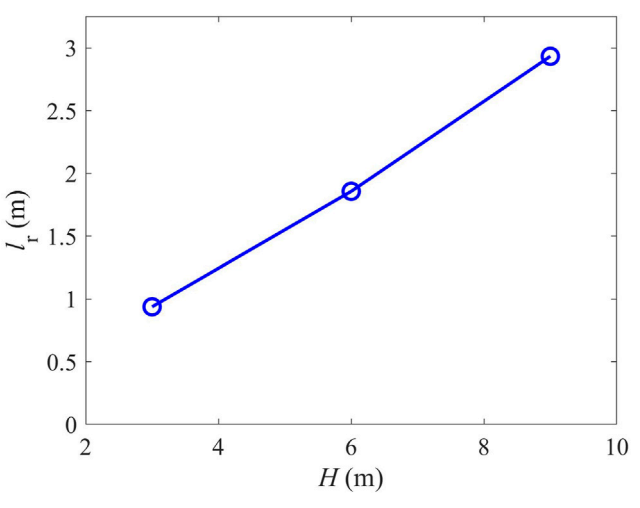

FIGURE 10 | Length of the region with no deposited firebrands vs. structure height for $L = W = 3$ m.

firebrands deposited on the windward face decrease with the decrease of z. A triangular like region with no firebrands on either lateral face of the block is noticeable.

4 SUMMARY AND CONCLUSION

A model was developed for simulation of cylindrical firebrand motion and burning in the FDS computational framework. The model was validated against the previous experimental and computational data (Oliveira et al., 2014) for a firebrand falling in a no-wind condition. The current model showed better agreement with the experimental data than the previous computational model. In addition, the previous experimental and CFD data (Lim et al., 2009) for a flow over a mounted 0.08 m height cube in a wind tunnel was used to validate FDS for simulation of flows over obstacles. The pressure coefficients in the simulation was in relatively good agreement with the experimental data. The mean velocity profiles in the streamwise

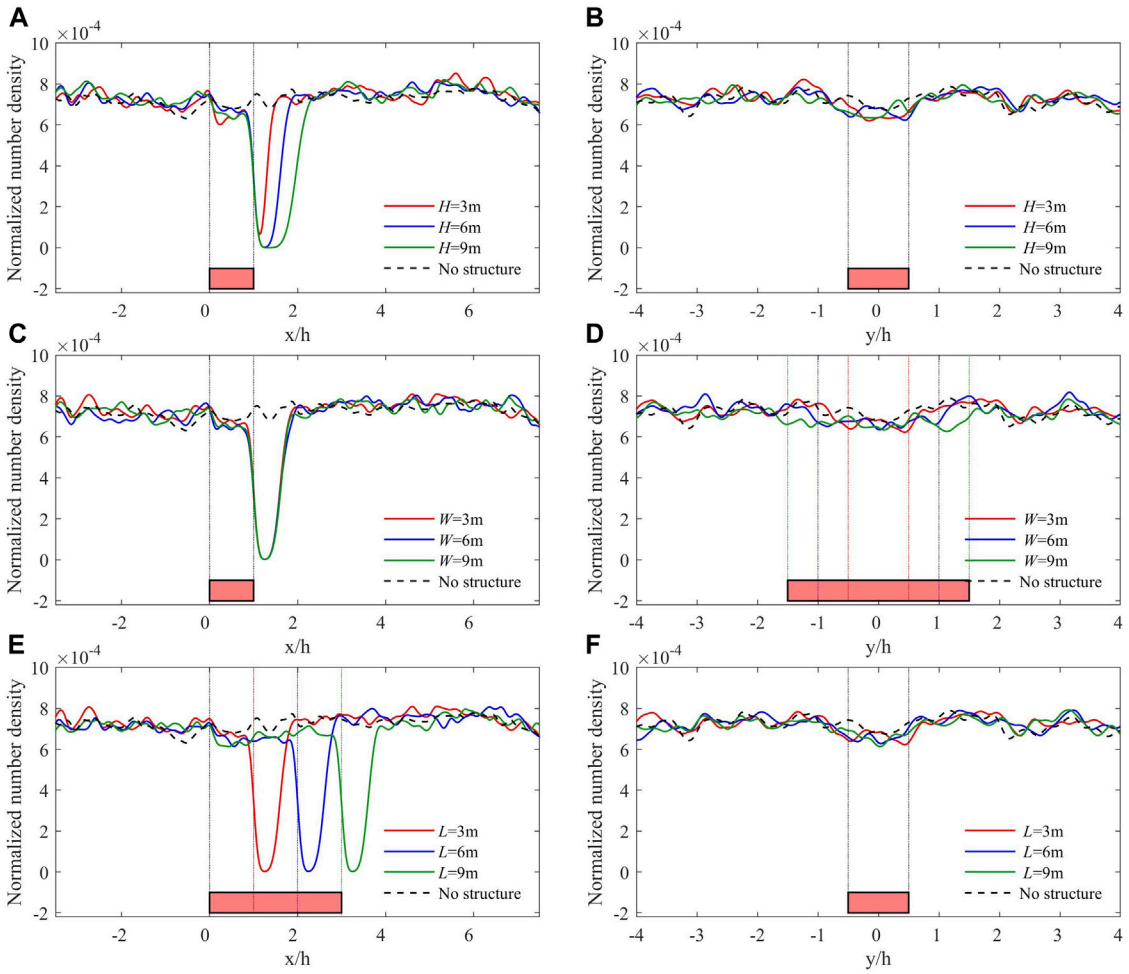

FIGURE 11 | Normalized number density of deposited firebrands vs. x at $y = 0$ on the left panels and vs. y at $x = 0$ on the right panels for **(A,D)** $L = W = 3$ m; **(B,E)** $H = 6$ m and $L = 3$ m; and **(C,F)** $H = 6$ m and $W = 3$ m.

TABLE 3 | Number and average temperature (K) of firebrands deposited on the top, front and lateral faces of the structure.

Cases	Top face		Front face		Lateral faces	
$L \times W \times H$	No	Avg. temp	No	Avg. temp	No	Avg. temp
3 m × 3 m × 3 m	22,949	424.92	6,820	418.77	244	419.17
3 m × 3 m × 6 m	23,428	436.24	14,112	424.06	428	424.22
3 m × 3 m × 9 m	23,670	448.82	21,959	430.33	494	435.97
3 m × 6 m × 6 m	46,927	435.49	28,425	423.69	351	426.71
3 m × 9 m × 6 m	70,412	435.06	43,367	423.34	443	424.94
6 m × 3 m × 6 m	46,737	436.19	14,154	424.15	1,006	425.17
9 m × 3 m × 6 m	71,267	436.17	14,192	424.09	1,516	424.73

and vertical directions as well as the Reynolds shear stress in the simulation closely matched the experimental data. On the other hand, the simulation substantially over-predicted the measured rms of the velocities in the streamwise and vertical directions. The developed firebrand model then used with FDS to simulate the deposition of firebrands carried by a flow over a rectangular cubic structure, as a representative of a single structure in an open domain. The Reynolds number in the deposition study was an order of magnitude larger than that in the validation study. A parametric study was conducted where heights, widths and lengths were varied from 3 to 9 m. It revealed an area on the leeward side of the structure on the ground where no firebrands

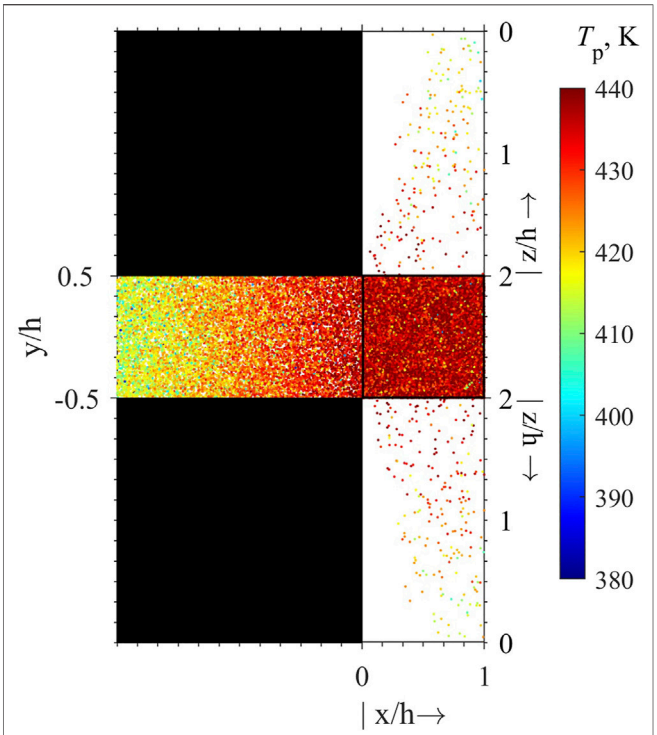

FIGURE 12 | Location and temperature of the firebrands deposited on the faces of the structure with length and width of 3 m and height of 6 m. Dots indicate the positions of the deposited firebrands on the block faces. The leeward face is not shown since no firebrands are deposited on it. The rectangles with the smallest number of dots are the lateral faces. The square between these two faces is the top face. The rectangle on the left of the top face is the windward face.

were deposited. This area was refereed to as the safe zone. The width of the zone was the same as the width of the structure (the dimension of the structure in the spanwise direction). The length of this zone in the streamwise direction was proportional to the height of the structure. No firebrand was deposited on the leeward face of the structure regardless of the size of the structure. The NND on the top face of the structure increases slightly with its height. For structures with longer lengths, the NND dropped near the leading edge and rose back again toward the trailing edge of the structure. This effect was attributed to the flow accelerating above the leading edge of the structure thus imparting extra momentum onto the firebrands and carrying them farther away.

Shapes of the structures considered here were simple but fundamental. Understanding the problem in fundamental setups seems an essential first step but considerations should be given to shapes representing more realistic structures. Realistic structures can significantly change from one to another in shape while involving additional geometric parameters, which can hinder the interpretation of the results. It is noted that the dimensions chosen for the structures here ranged from 3 to 9 m which are relevant to the overall dimensions of realistic small structures, e.g., houses. Future work should include sensitivity studies of the wind speed and direction. It should also include heat flux transferred from the deposited firebrands because of its consequence on ignition of the recipient fuel. Calculations of this flux require additional models to represent this phenomenon.

DATA AVAILABILITY STATEMENT

The data that support the findings of this study are available from the corresponding author upon reasonable request.

AUTHOR CONTRIBUTIONS

AM made changes to the code, ran the simulation and post processed the acquired data for this study under the supervision of BS. Both authors contributed to the development of the manuscript.

FUNDING

This work was performed under the following financial assistance award 70NANB17H281 from United States Department of Commerce, National Institute of Standards and Technology.

ACKNOWLEDGMENTS

The authors acknowledge the work by Chandanda Anand on integration of the firebrand model with the FDS version used in this study. The authors acknowledge the help received from Randall J. McDermott of NIST for the flow model validation study. High performance computing resources and technical support from the Alabama Supercomputer Authority are appreciated.

REFERENCES

Anand, C. (2018). "Computational Investigations of Ignition Characteristics of Live Fuels and Deposition of Firebrands in a Turbulent Boundary Layer,". Ph.D. thesis (The University of Alabama in Huntsville).

Anand, C., Shotorban, B., and Mahalingam, S. (2018). Dispersion and Deposition of Firebrands in a Turbulent Boundary Layer. *Int. J. Multiphase Flow* 109, 98–113. doi:10.1016/j.ijmultiphaseflow.2018.07.012

Deardorff, J. W. (1980). Stratocumulus-capped Mixed Layers Derived from a Three-Dimensional Model. *Boundary-layer Meteorol.* 18, 495–527. doi:10.1007/bf00119502

Germano, M., Piomelli, U., Moin, P., and Cabot, W. H. (1991). A Dynamic Subgrid-scale Eddy Viscosity Model. *Phys. Fluids A: Fluid Dyn.* 3, 1760–1765. doi:10.1063/1.857955

Hoerner, S. F. (1965). Fluid-dynamic Drag. *Hoerner Fluid Dyn.*

Kelbaliyev, G. I. (2011). Drag Coefficients of Variously Shaped Solid Particles, Drops, and Bubbles. *Theor. Found. Chem. Eng.* 45, 248–266. doi:10.1134/s0040579511020084

Lee, S., and Bienkiewicz, B. (1997). Large-eddy Simulation of Wind Effects on bluff Bodies Using the Finite Element Method. *J. wind Eng. Ind. aerodynamics* 67-68, 601–609. doi:10.1016/s0167-6105(97)00103-7

Lim, H. C., Thomas, T. G., and Castro, I. P. (2009). Flow Around a Cube in a Turbulent Boundary Layer: LES and experiment. *J. Wind Eng. Ind. Aerodynamics* 97, 96–109. doi:10.1016/j.jweia.2009.01.001

Manzello, S. (2014). Enabling the Investigation of Structure Vulnerabilities to Wind- Driven Firebrand Showers in Wildland-Urban Interface (WUI) Fires. *Fire Saf. Sci.* 11, 83–96. doi:10.3801/iafss.fss.11-83

Manzello, S. L., Maranghides, A., and Mell, W. E. (2007). Firebrand Generation from Burning Vegetation. *Int. J. Wildland Fire* 16, 458–462. doi:10.1071/wf06079

Manzello, S. L., Shields, J. R., Cleary, T. G., Maranghides, A., Mell, W. E., Yang, J. C., et al. (2008). On the Development and Characterization of a Firebrand Generator. *Fire Saf. J.* 43, 258–268. doi:10.1016/j.firesaf.2007.10.001

Marchildon, E. K., Clamen, A., and Gauvin, W. H. (1964). Drag and Oscillatory Motion of Freely Falling Cylindrical Particles. *Can. J. Chem. Eng.* 42, 178–182. doi:10.1002/cjce.5450420410

MathWorks (2019a). Multivariant Kernel Smoothing Density.

McGrattan, K., Hostikka, S., Floyd, J., McDermott, R., and Vanella, M. (2018). *Fire Dynamics Simulator Technical Reference Guide Volume 1: Mathematical Model. NIST Special Publication*. Sixth Edition. U.S. Department of Commerce, National Institute of Standards and Technology, 1018–1026.

Mell, W., Maranghides, A., McDermott, R., and Manzello, S. L. (2009). Numerical Simulation and Experiments of Burning douglas Fir Trees. *Combustion and Flame* 156, 2023–2041. doi:10.1016/j.combustflame.2009.06.015

Moin, P., Squires, K., Cabot, W., and Lee, S. (1991). A Dynamic Subgrid-scale Model for Compressible Turbulence and Scalar Transport. *Phys. Fluids A: Fluid Dyn.* 3, 2746–2757. doi:10.1063/1.858164

Morvan, D., and Dupuy, J. L. (2004). Modeling the Propagation of a Wildfire through a Mediterranean Shrub Using a Multiphase Formulation. *Combustion and flame* 138, 199–210. doi:10.1016/j.combustflame.2004.05.001

Murakami, S., Mochida, A., and Hibi, K. (1987). Three-dimensional Numerical Simulation of Air Flow Around a Cubic Model by Means of Large Eddy Simulation. *J. Wind Eng. Ind. Aerodynamics* 25, 291–305. doi:10.1016/0167-6105(87)90023-7

Nicoud, F., and Ducros, F. (1999). Subgrid-scale Stress Modelling Based on the Square of the Velocity Gradient Tensor. *Flow, turbulence and Combustion* 62, 183–200. doi:10.1023/a:1009995426001

Oliveira, L. A., Lopes, A. G., Baliga, B. R., Almeida, M., and Viegas, D. X. (2014). Numerical Prediction of Size, Mass, Temperature and Trajectory of Cylindrical Wind-Driven Firebrands. *Int. J. Wildland Fire* 23, 698–708. doi:10.1071/wf13080

Rayleigh, L. (1876). LIII. On the Resistance of Fluids. *Lond. Edinb. Dublin Phil. Mag. J. Sci.* 2, 430–441. doi:10.1080/14786447608639132

Richards, P. J., Hoxey, R. P., Connell, B. D., and Lander, D. P. (2007). Wind-tunnel Modelling of the Silsoe Cube. *J. Wind Eng. Ind. Aerodynamics* 95, 1384–1399. doi:10.1016/j.jweia.2007.02.005

Richards, P. J., Hoxey, R. P., and Short, L. J. (2001). Wind Pressures on a 6m Cube. *J. Wind Eng. Ind. Aerodynamics* 89, 1553–1564. doi:10.1016/s0167-6105(01)00139-8

Rodi, W. (1998). Large-eddy Simulations of the Flow Past bluff Bodies: State-Of-The Art. *JSME International Journal. Ser. B, Fluids Thermal Engineering* 41, 361–374. doi:10.1299/jsmeb.41.361

Rosendahl, L. (2000). Using a Multi-Parameter Particle Shape Description to Predict the Motion of Non-spherical Particle Shapes in Swirling Flow. *Appl. Math. Model.* 24, 11–25. doi:10.1016/s0307-904x(99)00023-2

Sardoy, N., Consalvi, J. L., Kaiss, A., Fernandez-Pello, A. C., and Porterie, B. (2008). Numerical Study of Ground-Level Distribution of Firebrands Generated by Line Fires. *Combustion and Flame* 154, 478–488. doi:10.1016/j.combustflame.2008.05.006

Sardoy, N., Consalvi, J., Porterie, B., and Fernandezpello, A. (2007). Modeling Transport and Combustion of Firebrands from Burning Trees. *Combustion and Flame* 150, 151–169. doi:10.1016/j.combustflame.2007.04.008

Smagorinsky, J. (1963). General Circulation Experiments with the Primitive Equations. *Mon. Wea. Rev.* 91, 99–164. doi:10.1175/1520-0493(1963)091<0099:gcewtp>2.3.co;2

Song, J., Huang, X., Liu, N., Li, H., and Zhang, L. (2017). The Wind Effect on the Transport and Burning of Firebrands. *Fire Technol.* 53, 1555–1568. doi:10.1007/s10694-017-0647-1

Tarifa, C. S., del Notario, P. P., and Moreno, F. G. (1967). "Transport and Combustion of Fire Brands,".

Tohidi, A., and Kaye, N. B. (2017a). Comprehensive Wind Tunnel Experiments of Lofting and Downwind Transport of Non-combusting Rod-like Model Firebrands during Firebrand Shower Scenarios. *Fire Saf. J.* 90, 95–111. doi:10.1016/j.firesaf.2017.04.032

Tohidi, A., and Kaye, N. B. (2017b). Stochastic Modeling of Firebrand Shower Scenarios. *Fire Saf. J.* 91, 91–102. doi:10.1016/j.firesaf.2017.04.039

Vreman, A. W. (2004). An Eddy-Viscosity Subgrid-Scale Model for Turbulent Shear Flow: Algebraic Theory and Applications. *Phys. Fluids* 16, 3670–3681. doi:10.1063/1.1785131

Werner, H., and Wengle, H. (1993). "Large-eddy Simulation of Turbulent Flow over and Around a Cube in a Plate Channel," in *Turbulent Shear Flows* (Springer), 8, 155–168. doi:10.1007/978-3-642-77674-8_12

Yakhot, A., Orszag, S. A., Yakhot, V., and Israeli, M. (1989). Renormalization Group Formulation of Large-Eddy Simulations. *J. Sci. Comput.* 4, 139–158. doi:10.1007/bf01061499

Yin, C., Rosendahl, L., Knudsen Kær, S., and Sørensen, H. (2003). Modelling the Motion of Cylindrical Particles in a Nonuniform Flow. *Chem. Eng. Sci.* 58, 3489–3498. doi:10.1016/s0009-2509(03)00214-8

Conflict of Interest: The authors declare that the research was conducted in the absence of any commercial or financial relationships that could be construed as a potential conflict of interest.

NOMENCALTURE

α	Angle of incidence
Δh_{char}	Enthalpy of charring
Δh_{pyr}	Enthalpy of pyrolysis
$\dot{m}_{\text{char}}$	Mass loss rate due to charring
$\dot{m}_{\text{pyr}}$	Mass loss rate due to pyrolysis
$\dot{q}_c$	Rate of convective heat transfer
$\dot{q}_r$	Rate of Radiative heat transfer
ϵ	emmisitivity of the firebrand
$\varepsilon_1, \varepsilon_2, \varepsilon_3, \eta$	Quaternions
$\widehat{f}(x, y)$	The normalized number density, NND
$\widehat{z}_r$	Major axis of the cylindrical firebrand
$\kappa(\cdot, \cdot)$	The kernel function
$\mathcal{V}$	Volume of the firebrand
Re_h	Reynolds number at the reference height h
Re_α	Reynolds number of the particle in motion
ω	Rotational velocity of the firebrand;
ϕ, ψ, θ	Euler angels
ρ_{gas}	Density of the air
ρ_p	Density of the firebrand
σ	Stefan-Boltzmann constant
$\overrightarrow{F}_D$	Drag force
$\overrightarrow{F}_G$	Force due to gravity
$\overrightarrow{F}_L$	Lift force
$\overrightarrow{T}'$	Total torque
$\overrightarrow{T}'_{\text{hydro}}$	Torque due to hydrodynamic forces
$\overrightarrow{T}'_{\text{resist}}$	Torque due to frictional air resistance
$\overrightarrow{V}_p$	Velocity vector of the centre of mass of the firebrand
$\overrightarrow{V}_{\text{rel}}$	Velocity relative to the flow at the centre of mass of the firebrand
$\overrightarrow{x}_p$	Position vector of the centre of mass of the firebrand
A	Surface area of the firebrand
$\mathbf{A}$	Transformation matrix
a	radius of a firebrand
A_{char}	Pre-exponential factor for charring
A_{pyr}	Pre-exponential factor for pyrolysis
B	Bandwidth
b	half length of the firebrand
C_D	Drag coefficient
D_p	Diameter of the firebrand
h	Reference height
h_c	Heat transfer coefficient
$I_{x'}, I_{y'}, I_{z'}$	Moment of inertia in the principal axes
l	Length of the firebrand
m_p	mass of the firebrand
n	Total number of firebrands deposited
T_∞	Ambient air temperature
T_{char}	Activation temperature for charring
T_{pyr}	Activation temperature for pyrolysis
T_p	Temperature of the firebrand
U_h	Inlet velocity at the reference height h
x_{cp}	Distance between centre of mass and centre of pressure

frontiers in Mechanical Engineering

ORIGINAL RESEARCH
published: 15 June 2021
doi: 10.3389/fmech.2021.655593

Firebrand Generation Rates at the Source for Trees and a Shrub

Sampath Adusumilli, James E. Chaplen and David L. Blunck*

School of Mechanical, Industrial and Manufacturing Engineering, Oregon State University, Corvallis, OR, United States

Source terms of the number of firebrands released as trees/shrubs torch are essential for helping to more accurately implement detailed physics-based models of wildfire propagation, particularly when torching occurs. A key challenge in estimating these source terms is the difficulty in measuring firebrand generation rates from the source. Typical studies have reported generation characteristics (firebrands/m^2), but enumeration of the total number of firebrands released has remained elusive. Recently, a fire-resistant fabric was successfully employed to quantify "hot" firebrands (i.e., can potentially lead to further fire spread) generated during tree-scale burns. In this paper, a total of 71 tree/shrubs were burned to quantify hot firebrand production statistics for Douglas-fir, ponderosa pine, and sagebrush. A network of 65 fire-resistant fabric stations were deployed during the burns to measure the "hot" firebrands that are released. These stations are placed strategically at several radii and angles in the prominent wind direction. Using the number of firebrands determined from the fabric, a first-order extrapolation method was developed and evaluated to estimate the source terms (i.e., total number of hot firebrands released). Variation in the firebrand production with the height of the trees and for three species is reported. The total number of hot firebrands produced typically increased with the height of the tree/shrub burned as expected. The specific hot firebrand production (firebrands produced per kg dry mass burned) is exponentially dependent on the moisture content of the tree and had an inconclusive correlation with the height of the trees. Overall, for trees of comparable moisture content, sagebrush produced higher specific hot firebrands when compared to ponderosa pine and Douglas-fir species.

Keywords: firebrand, generation, Douglas-fir, spot fires, wildfire, sagebrush, ponderosa pine, wildland urban interface

OPEN ACCESS

Edited by:
Sayaka Suzuki, National Research Institute for Fire and Disaster, Japan

Reviewed by:
Miguel Almeida, Associação para o Desenvolvimento da Aerodinâmica Industrial, Portugal
Michael John Gollner, University of California, Berkeley, United States

****Correspondence:***
Sampath Adusumilli
adusumis@oregonstate.edu

Specialty section:
This article was submitted to Thermal and Mass Transport, a section of the journal Frontiers in Mechanical Engineering

Received: *19 January 2021*
Accepted: *12 April 2021*
Published: *15 June 2021*

Citation:
Adusumilli S, Chaplen JE and Blunck DL (2021) Firebrand Generation Rates at the Source for Trees and a Shrub. Front. Mech. Eng. 7:655593. doi: 10.3389/fmech.2021.655593

INTRODUCTION

A major cause of the spread of wildfires into the wildland urban interface (WUI) are spot fires caused by firebrands. Firebrands are pieces of burning material (e.g., cones, branches, structural components) that are released from the main fire. One study estimated that, in some situations, 75% of structures burn because of exposure to firebrands and radiative heat transfer (Fernandez-Pello, 2017). The threat of fires caused by firebrands can be a particularly challenging because firebrands can be transported a long distance (e.g., kilometers), thus bypassing barriers that may stop the main fire front (e.g., rivers, roads, and green spaces).

Four processes lead to spot fires: generation of firebrands, transport and deposition of firebrands, and subsequent ignition of recipient fuel bed (Manzello et al., 2020). Understanding characteristics associated with each of these processes is important for developing strategies or tools to help

reduce the risk of spot fires, near the WUI. Knowledge gained regarding the processes leading to spot fires can be used to improve reduced-order and detailed physics models [e.g., FDS, WFDS, and FIRETEC (Linn et al., 2002; Jolly et al., 2016; Anand et al., 2017; Shotorban et al., 2018)]. In turn these models can be applied to better understand how to apply resources (Monedero et al., 2019), or to develop codes and standards which reduce the risk of spread of fire to the WUI.

Several studies, across multiple-scales have considered firebrand generation characteristics for building materials (Suzuki et al., 2012, 2013, 2014, 2015; Suzuki and Manzello, 2016; Hedayati, 2018) and vegetation (Manzello et al., 2006, 2007a, 2009; Benkoussas et al., 2007; Filkov et al., 2017) as part of efforts to understand processes that lead to spot fires. For example, Thomas et al. (2017) measured the time-resolved flux of firebrands onto pans of water during prescribed burns. The higher the heat release the greater the firebrand flux, in general. Studies by Manzello et al. (2007a) and Hudson et al. (2020) have shown sensitivities of firebrand characteristics to the species of tree or burning conditions. The firebrands with the largest mass from vegetation typically came from larger trees, showing a sensitivity of generation characteristics to the size and/or age of the tree (Manzello et al., 2007a). In related studies, the sizes of firebrands generated have been reported for two species of trees with similar heights. Korean pine provided firebrands that were shorter, but with a larger diameter than corresponding firebrands generated from Douglas-fir trees with similar heights (Manzello et al., 2007a,b).

Additionally, differentiating between firebrands which can cause ignition (i.e., have sufficient temperature and mass) and those which do not has been a problem of interest. The water tray method provides an estimation of the total number of firebrands, both those which can and cannot lead to spot fires. Several researchers have tried to quantify the number of "hot" firebrands that are produced from a fire. To this end, researchers have used the sizes and number of holes in trampoline mats near fires to evaluate the characteristics of "hot" firebrands (Rissel and Ridenour, 2013; Manzello and Foote, 2014). Recently, "hot" firebrands produced during tree-scale burns were estimated using char marks on a fire-resistant fabric and compared with the total number of firebrands produced using the water tray method (Hudson et al., 2020). A characterization of the fire-resistant fabric carried out by Adusumilli et al. (2020) indicated that the firebrands leaving char marks on the fabric would have a temperature of at least 300°C. The characteristics of the "hot" firebrands were found to be quite different compared to the total number of firebrands collected during experiments (Manzello et al., 2007a, 2020; Hudson et al., 2020). Since "hot" firebrands have a higher probability of causing spot fires, enumerating the production of these specific firebrands is of high priority.

One of the challenges to the fire community has been understanding how to link results from studies of firebrand generation characteristics, like those described above, to support models and/or fire decision makers. For example, firebrand generation characteristics have been measured based on firebrand fluxes or distributions at particular locations (Filkov et al., 2017; Thomas et al., 2017; Hudson et al., 2020). Yet a method for applying measured firebrand fluxes as boundary conditions in models is not clear, nor is it clear how the knowledge about the number of firebrands generated can be used to inform fire responders. To aid in such understanding, measurements or estimates of the total number of firebrands released are needed.

With this background, the objectives of this work are 3-fold. First, establish and evaluate a methodology for estimating the total number of "hot" firebrands that are released as trees/shrubs are burned. In turn, scale the results to provide specific source terms (i.e., "hot" firebrands released/kg of fuel consumed) that could potentially be used as source terms in models (Linn et al., 2002; Jolly et al., 2016; Anand et al., 2017; Shotorban et al., 2018). Second, apply this methodology to characterize how firebrand generation characteristics change as different species of trees burn. Third, assess the limitations in scaling of the source terms as the size of the tree/fuel are varied. By addressing these objectives, the following specific contributions can be derived of this work.

1) Source terms for firebrand generation (i.e., firebrands produced/kg-fuel consumed) can be used in both reduced-order and detailed physics based models examining wildfire propagation.
2) Sensitivities of measured source terms to fuel conditions (e.g., size of trees) are assessed. This information can be used to better understand how measured source terms are expected to scale as the number and size of trees are varied.
3) Establishing a methodology that can be used by the wider research community to further identity source terms for varying fuels and fire conditions relevant to wildfires and WUI communities.

To help achieve these objectives a total of 71 trees/shrubs were burned to understand "hot" firebrand production rates for 3 species of trees/shrubs. To measure the hot firebrand generation rates, a network of 65 fire-resistant fabric stations were deployed during the burns. These stations are placed strategically at several radii and angles in the prominent wind direction. Hot firebrands leave char marks on the fabric, as discussed later. Prior work has shown notable differences in the total number of firebrands released and hot firebrands (Hudson et al., 2020); only the results for hot firebrands are reported because of their potential to cause ignition during fires. For the remainder of this paper "hot" firebrands are described as firebrands.

APPROACH

The approach to quantify the firebrands generated from tree-scale burns expands upon the approach detailed by Hudson et al. (2020). In this effort, tree-scale burns of three species (Douglas-fir, ponderosa pine and sagebrush) of varying heights between 1.4 and 6.2 m were conducted. The measurement approach along with details regarding processes used to characterize the experiment (i.e., moisture content, wind speed measurements etc.) are provided in this section.

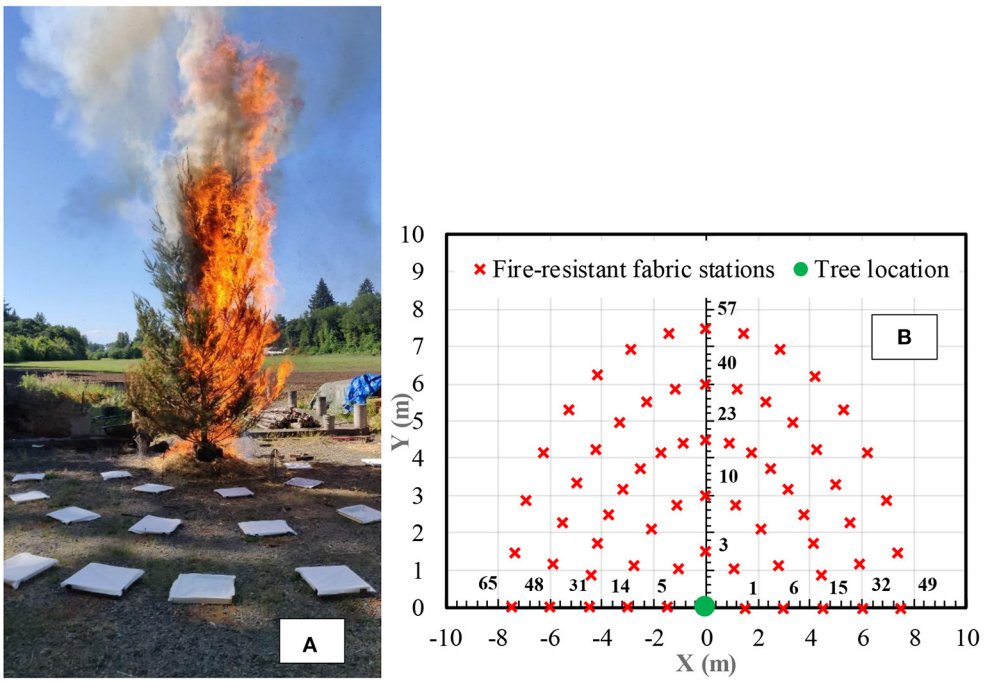

FIGURE 1 | (A) Torching ~6 m tall Douglas-fir tree (details about this particular burn are given in Table A.1, test number 17) with fire-resistant fabric stations setup to collect "hot" firebrands. **(B)** Location map of the 65 fire-resistant fabric stations, with the tree location at (0, 0). Shown are selected station numbers to indicate the numbering scheme.

Experimental Arrangement

Figure 1A shows the experimental arrangement, with a 6 m tall Douglas-fir tree being torched. The torching of the tree is achieved by lighting a 10 kg wheat straw bed at one end and allowing the flames to progress toward the tree. The typical dimensions of the fuel bed were on average 2.2 m in length, 1.3 m in width, and 0.3 m in depth. The straw bed was arranged at an inclination to provide a ladder fuel effect resulting in taller flames that could better ignite the trees. In the foreground of **Figure 1A** several fire-resistant fabric stations can be observed. The fire-resistant fabrics were arranged in a semi-circle format in the prominent wind-direction. The fabric was used to collect firebrands; the resulting char marks were used to quantify the number of hot firebrands. Prior work suggests that only firebrands with surface temperatures >300°C leave char marks (Adusumilli et al., 2020). **Figure 1B** shows a map of the locations of the fabric. Each firebrand collection station consisted of a sheet of fabric, typically 40 by 41 cm squares, mounted to a wooden frame. The stations were in five concentric semicircle bands. The first band contained five stations positioned 45° apart along a 1.5 m radius arc. The second contained nine stations positioned 22.5° apart along a 3 m radius arc. The third, fourth, and fifth bands each contained seventeen stations positioned 11.25° apart and had radii of 4.5, 6, and 7.5 m, respectively. A key improvement of this work compared to the work of Hudson et al. (2020) was the expansion of the number of fabric stations from 15 to 65. The number of fabric stations at a radius was increased as the distance from the tree was increased in an effort better to capture the spread of the firebrands. All firebrands generated from a burn are assumed to fall in this semicircular region; while some firebrands might fall beyond this region their number is considered minimal based on where firebrands are observed (i.e., relatively few along the edges). The fabric was collected as needed after the completion of a burn and subsequently analyzed, as discussed later. Wind speeds and directions were recorded using an anemometer (OnSet S-WSA-M003) and are reported.

Typically, seven or more trees were burned for each species at a particular height. Burning of the trees was influenced by the flammability of the tree, the spacing of the branches, and the proximity of the flames from the ladder fuel to the foliage. As a result of all these factors, some of the trees torched completely while others did not. Similar variations in the torching characteristics are expected during wildfires. Variability in the burning of the trees/shrubs is considered by normalizing the results by the mass of fuel consumed by the fires. The tree's height along the trunk, maximum width, and diameter at breast height (DBH measured at 1.4 m from base) were measured and reported. As sagebrush lacked a defined trunk, the maximum discernable height is measured rather than height along the trunk. For similar reasons the DBH for these trees was also not measured. The tree's pre-burn and post-burn mass was measured using a scale. Average measurements characterizing the trees/shrub are provided in **Tables 1–3** for Douglas-fir, ponderosa pine, and sagebrush (respectively). The ladder fuel was burned three times without a tree to evaluate the char mark production from the ladder fuel. No char marks were observed on the

fire-resistant fabric from these tests, indicating that all char marks observed during tree burns come from the firebrands produced by the trees.

Data Collection and Analysis

The firebrand collection stations were inspected and potentially replaced following each test. Initially, a station was replaced after a burn if char marks were present. In the second phase of testing, only stations with sufficient char marks to warrant concern about overlap between marks were removed. Pictures of the sheets of fabric were collected using a Canon EOS Rebel T3i camera (18-megapixel). The images were subsequently used to determine the number of firebrands. An exposure time of 0.008 s and an 18–55 mm lens were used. A studio lighting arrangement was used to ensure that the fabric was illuminated uniformly and that the contrast between the fabric and char marks can be clearly observed. **Figure 2A** shows the example of a fire-resistant fabric with char marks from firebrands. The spatial resolution for these images was 0.016 cm/pixel.

A computer algorithm written in MATLAB R2019b (MathWorks Inc., Natick, MA) (The MathWorks Inc., 2018) was used to process the images and extract firebrand characteristics. First, the zone outside the data collection region was cropped out and converted into a separate greyscale image. The greyscale image was converted to a binary image with the *imbinarize* function at a threshold of 0.4. This designated sufficiently dark pixels (i.e., the char marks) as one and left the rest as zero (example shown **Figure 2B**). Finally, the script used the distance to pixel ratio to measure the cropped image area and counted the number of char marks. Once the number of char marks was counted, the char mark area density was determined as the number of char marks divided by the area of the fabric. This process was repeated for fabric collected at every station, and an example representation of the processed data is shown in **Figure 3**. The data shown here is for a single tree burn; note that firebrands do not reach all the stations due to the transport characteristics. The number of firebrands at locations near the tree are significantly higher than the firebrands at locations farthest from the tree, consistent with the work by Hudson et al. (2020).

Fabric Characterization

To characterize the temperature response of the fire-resistant fabric used in these experiments, the experimental approach described by Adusumilli et al. (2020) was employed. Briefly, a cartridge heater at a known temperature was used to form a char mark on a sample of the fire-resistant fabric. The heater and fabric were in contact for several durations of time. Once the char marks were formed, the samples were imaged and analyzed using the same algorithm described before. There were two different fire-resistant fabrics employed during these tests. For Douglas-fir trees material A (Roc-Lon Cotton Lining Fabric, from Jo-Ann Fabrics, item no. 1144484) was used, whereas for ponderosa pine and sagebrush material B (Roc-Lon Cotton Lining Fabric, from Jo-Ann Fabrics, item no. 1144492) was employed. Ideally, the material would remain constant between species of trees but due to a shortage of material A, material B was chosen. Both materials conform to the National Fire Protection Association 701 standard for fire-resistant fabrics, are 100% cotton, and are ∼1 mm thick. The characterization of these fabrics became even more prudent with the need to change materials during testing.

Figure 4 shows the normalized char mark area variation with the cartridge heater power, temperature, and exposure time. This information is useful for understanding how the materials char when exposed to elevated temperatures (e.g., firebrand or heater). The exponential curve-fit for the data of both materials overlap, indicating that the char mark response of both materials is the same. This is expected as both these materials are made of 100% cotton and use the same fire retardant. **Table 4** shows a comparison of coefficients of the curve fit when compared to values for material A tested using similar apparatus by Adusumilli et al. (2020). The maximum difference between the coefficient values is ∼11%, which could be attributed to differences in experimental conditions. Adusumilli et al. (2020) established that material A would only form char marks if a firebrand had a temperature greater than roughly 300°C. Since both the materials have similar responses to heat exposure the minimum char mark formation temperature would also be 300°C for material B. As a result of the analysis just described, both types of fabric are considered to have equivalent responses to firebrands.

Moisture Content Measurement

Moisture content (MC) of the tree was measured using samples collected from the trees before a burn. The samples were collected from random locations of the tree to provide an accurate representation of the tree. In general, the firebrands observed on the fabric were needles or leaves from the trees. Certainly branches, bark, and cones can be firebrands during wildfires, however they were not observed in this study. The MC of the trees was estimated from the fine foliage (i.e., what formed firebrands). These samples were dried in an oven at ∼105°C (Matthews, 2010) until the mass of the samples did not change, this drying method typically took 4 days to complete. The temperature of the oven was chosen to vaporize the moisture in the samples, but not cause pyrolysis. The MC percentage on a dry basis in the sample was calculated using the following relation (MacLean, 1952; Eckelman, 1997):

$$\text{Moisture Content } (MC) = \left(\frac{\text{Initial Mass } (M_i)}{\text{Final Mass } (M_f)} - 1 \right) 100 \quad (1)$$

$$\text{Dry mass } (M_d) = \frac{\text{Initial Mass } (M_i)}{1 + \frac{MC}{100}} \quad (2)$$

In general, the MC value was below 100% for all the trees burned. Trees were allowed to dry before burning to increase their propensity for torching, making the trees under consideration to be drier than those that would be found in forests (live trees). This step was necessary as the current ladder fuel's heat is insufficient to torch live trees. The results from this work are expected to be conservative in the number of hot firebrands produced (i.e., a larger number) than live fuels because of the lower moisture content. This assumption requires further investigation. Since

TABLE 1 | Measurements corresponding to representative average trees for Douglas-fir species.

Average tree number	Number Of Trees Used For Average	Mass before burn (kg)	Mass after burn (kg)	% Tree burned	Height (m)	DBH (mm)	Max. width (m)	Moisture content (dry basis), *MC* (%)	Average wind speed (m/s)	Gust speed (m/s)	Average wind direction (°)
1	9	6.8	5.0	25.4	3.8	50.5	1.1	30.2	0.3	2.8	117.7
2	7	4.3	3.5	26.9	2.9	26.2	0.8	26.8	0.9	3.8	164.5
3	8	21.4	16.5	18.3	5.7	72.9	1.3	43.8	0.4	3.0	90.0

The wind direction is the angle from x-axis in counter clockwise direction. Moisture content is calculated using oven drying method and Equation (1). Details of each individual test can be found in Table A.1.

TABLE 2 | Measurements corresponding to representative average trees for ponderosa pine species.

Average tree number	Number of trees used for average	Mass before burn (kg)	Mass after burn (kg)	% Tree burned	Height (m)	DBH (mm)	Max. width (m)	Moisture content (dry basis), *MC* (%)	Average wind speed (m/s)	Gust speed (m/s)	Average wind direction (°)
1	8	14.7	12.8	12.7	3.6	69.3	0.9	45.5	0.6	4.3	111.5
2	8	5.2	4.0	20.1	2.7	37.3	0.5	41.9	0.6	3.3	126.0
3	7	40.8	37.5	7.6	5.7	106.8	1.2	58.3	0.1	1.8	124.7

The wind direction is the angle from x-axis in counter clockwise direction. Moisture content is calculated using oven drying method and Equation (1). Details of each individual test can be found in Table A.2.

TABLE 3 | Measurements corresponding to representative average trees for sagebrush species.

Average tree number	Number of trees used for average	Mass before burn (kg)	Mass after burn (kg)	% Tree burned	Height (m)	DBH (mm)	Max. width (m)	Moisture content (dry basis), *MC* (%)	Average wind speed (m/s)	Gust speed (m/s)	Average wind direction (°)
1	8	4.1	2.7	33.9	2.1	-	0.8	58.7	0.9	4.3	165.5
2	8	2.5	1.9	25.5	1.6	-	0.5	50.7	0.5	4.3	98.1
3	8	11.5	9.2	19.3	2.5	-	1.0	54.1	0.8	4.8	175.1

The wind direction is the angle from x-axis in counter clockwise direction. Moisture content is calculated using oven drying method and Equation (1). Details of each individual test can be found in Table A.3.

this drying is natural and happens over a few days, we can assume that the dehydration occurs due to loss of moisture. Any loss in volatility of the trees is minimal and is not measured in this study. The amount of moisture in trees varied from species to species as the duration the trees were left out to dry differed. **Figure 5** shows the measured MC for all the trees burned during the current tests. The average MC values for representative trees (using 7–8 trees of similar height) are given in **Tables 1**–**3** for Douglas-fir, ponderosa pine, and sagebrush, respectively. On average the Douglas-fir trees were the driest followed by ponderosa pine trees. The sagebrush had the highest moisture content despite being left out to dry for a similar number of days to the Douglas-fir trees (14–20 days). The Douglas-fir trees were tested during a drier climate (May to June) when compared to the sagebrush tests (October to November). The dry mass (M_d) was measured using the relationship given in Equation (2). All mass values reported in the table are of the actual mass measured, and M_d was calculated from the MC value reported as needed.

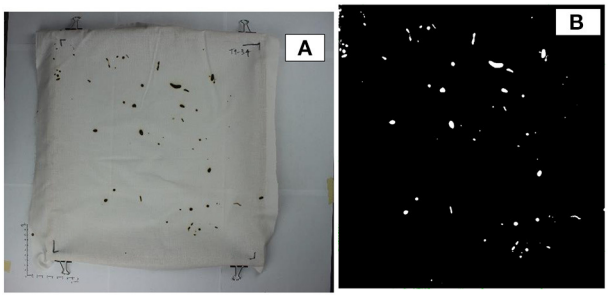

FIGURE 2 | (A) Raw image of a fire-resistant fabric showing char marks captured from a tree burn. **(B)** Corresponding binarized image to enumerate the number of char marks on the fabric.

Wind Speed and Direction Measurements

The burns were conducted at an outdoor testing site because of the size of the trees and fires. To monitor the wind conditions a wind speed and direction smart sensor (OnSet S-WSA-M003) was deployed. This sensor works in association with a HOBO® Station logger to record the wind speed and direction. The accuracy of this sensor is ±1.1 m/s and ±5° for speed and direction, respectively. The resolution is 0.38 m/s and 1.4° for speed and direction, respectively. The starting threshold for

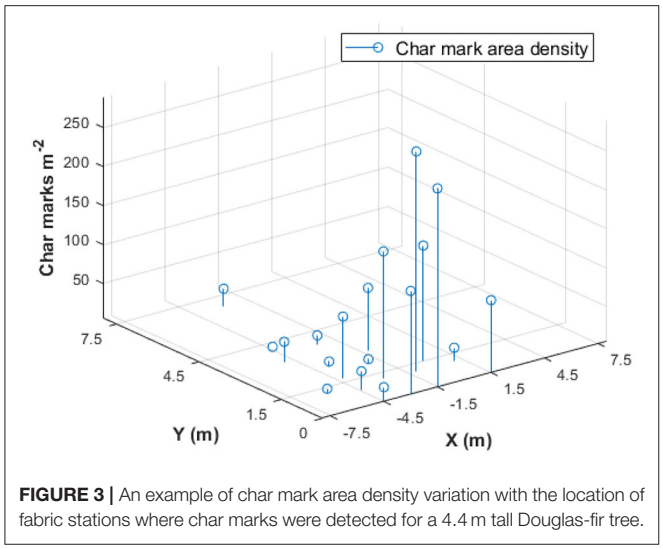

FIGURE 3 | An example of char mark area density variation with the location of fabric stations where char marks were detected for a 4.4 m tall Douglas-fir tree.

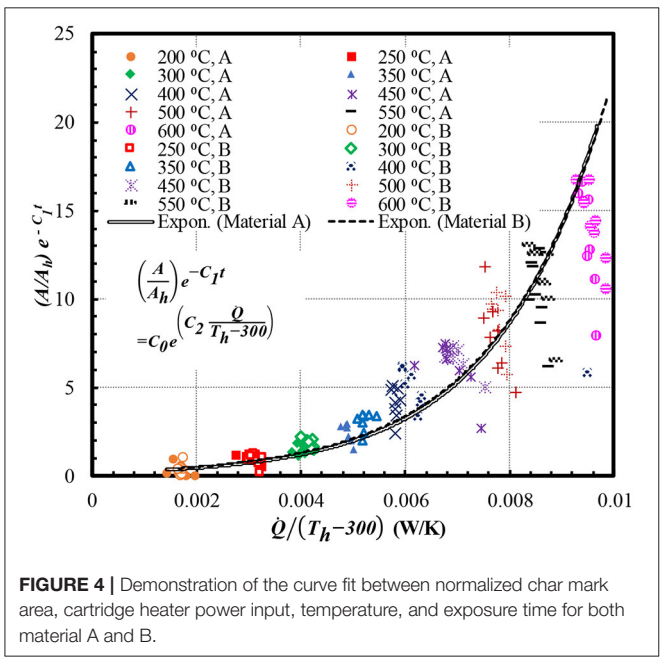

FIGURE 4 | Demonstration of the curve fit between normalized char mark area, cartridge heater power input, temperature, and exposure time for both material A and B.

TABLE 4 | Coefficients of the curve fit between normalized char mark area, heater power, temperature of the heater, and the time of exposure.

Material	Coefficients			
	C_0	C_1	C_2	R^2
A Adusumilli et al., 2020	0.1903	0.0001	491.83	0.77
A	0.1689	0.0001	492.13	0.76
B	0.1935	0.0001	477.09	0.83

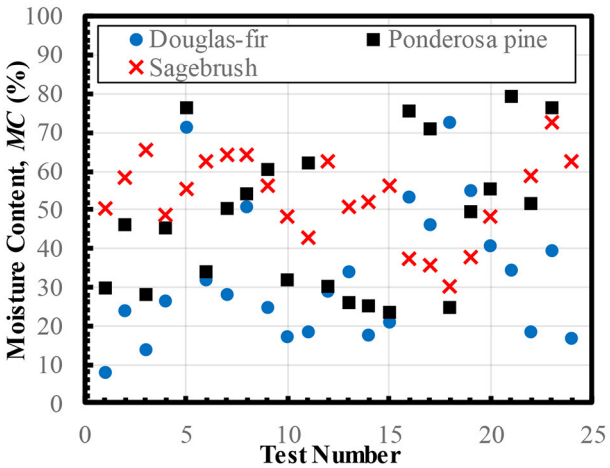

FIGURE 5 | Moisture content of three different species of trees/shrubs burned during this study.

the instrument is 1 m/s and the logging interval is 30 s. The wind speed reported is the average wind speed over the logging interval measured at a rate of 1 Hz, the gust speed is reported as the highest 3-s gust during the logging interval and the wind direction is logged as the vector average of wind direction measured every 3 s of the logging interval. The average wind speed and direction measurements (using 7–9 trees of similar height) are given in **Tables 1**–**3** for Douglas-fir, ponderosa pine, and sagebrush, respectively. For measurements of each individual test, refer to the tables provided in the **Appendix**.

In general, the average wind speed was <1 m/s; these relatively low values were deliberate as burns were not conducted when it was windier. The maximum wind gust recorded was 4.8 m/s (for sagebrush), but the median value was 2.3 m/s. Anecdotally, the sagebrush measurements were gustier than the tests for Douglas-fir and ponderosa pine due to the difference in the season (i.e., fall instead of spring).

The wind direction provided here is the angle from the x-axis in the counterclockwise direction. **Figure 6** shows the average wind direction of average trees for all the species under consideration. The average wind direction was between 0 and 180° which was the region where fire-resistant fabric stations were located. Although the average lies in this region, individual tests did sometimes have wind direction away from the region of interest indicating some of the firebrands might have been carried away from the region of interest. This would bias the measurements low. The error bars shown in **Figure 6** display this possibility as the boundary of one standard deviation values lies beyond 180° for some of the tests. But the wind direction measurements have a drawback in that the sensor starting threshold was 1 m/s and the average wind speed was <1 m/s so sometimes the logger could record a false wind direction for the lowest wind speeds. Considering the relatively low wind speeds, and the number of tests conducted for each tree/shrub condition, the influence of wind on the average results is expected to be relatively minor. Despite the inability to control the wind due to outdoor testing, current work contributes toward the understanding of physics governing firebrand generation, particularly in low wind conditions (i.e., <1 m/s). Other research

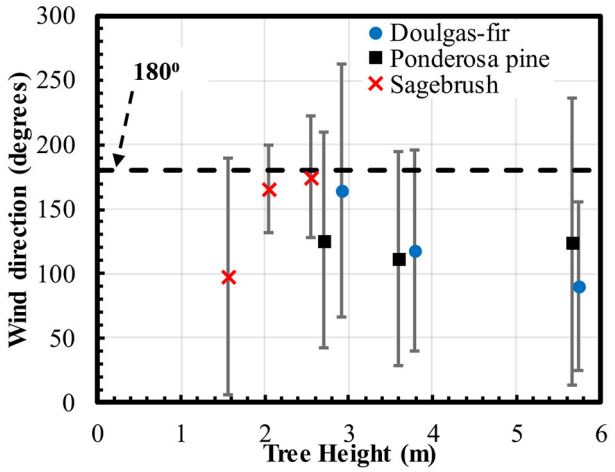

FIGURE 6 | Average wind direction for an average tree. The error bars indicate the boundary of one standard deviation values.

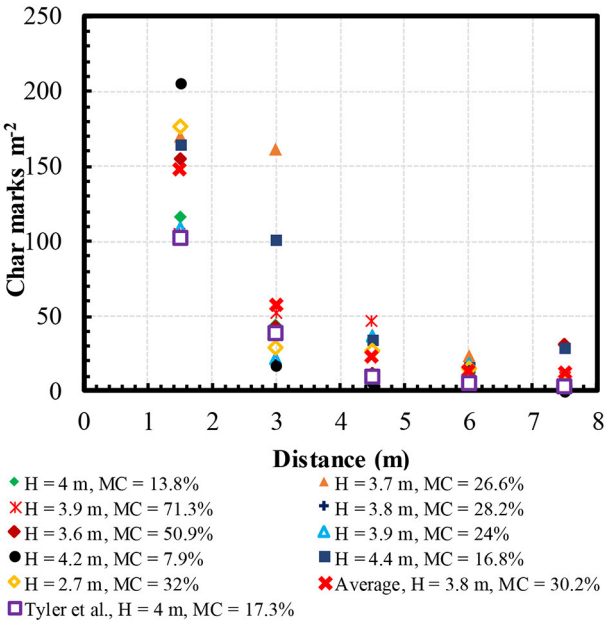

FIGURE 7 | Char marks generated with distance from the tree for Douglas-fir trees, compared to measurements by Hudson et al. (2020).

groups can obtain similar results for experiments conducted in low ambient wind speeds.

RESULTS

In this section, first, current measurements are compared with measurements from literature. Second, methodologies that can be used to estimate the total number of firebrands are discussed and evaluated. Third, the total weight and specific number of firebrands released are reported for Douglas-fir, ponderosa pine, and sagebrush. The sensitivity of the number of firebrands released to the height and MC of the tree/shrub are discussed.

Validation Results

Figure 7 reports the average char mark area density (i.e., number of char marks per m^2) with respect to distance from the Douglas-fir trees. The average is based on the results from all the fabric stations where firebrands are collected at a given radii. The char mark area density decreases as the distance increases, as expected because of the increasing surface area with increasing radii for firebrands to be deposited. On average, the char mark area density at a radius of 1.5 m is 15 times larger than the value at a radius of 7.5 m. For reference, measurements collected by Hudson et al. (2020) are included on **Figure 7**. They conducted similar experiments but with fewer number of fabric stations (i.e., 15). In general, the overall trends of the current and former data are similar. It is noted that current char mark area density measurement are typically higher (e.g., 50% higher at 1.5 m radius) than the values measured by Hudson et al. (2020). The difference between measurements is attributed to the higher number of fire-resistant fabric stations used in the current study. Specifically, the larger number of stations assists with more accurately capturing the number of firebrands that are released. With fewer stations, it is more likely for firebrands to not land on fabric, hence biasing the measurements lower.

Estimation of Total Number of Firebrands

Several methods were developed and evaluated for extrapolating from the number of measured char marks to estimate the total number of firebrands released by the tree/shrub during a burn. In particular, care was taken to ensure that the extrapolated values were not skewed by the data closest to the source. Currently, the assumption is that all the firebrands released fall in the semicircular region of interest. Since the fire-resistant fabric stations are in the wind's direction, the number of firebrands traveling in the opposite direction is minimal. Further, the data shown in **Figure 7** indicates that the number of firebrands beyond the last semicircle (at 7.5 m) will be low when compared to the total number of firebrands within the semicircular region of interest. Further, the data shown in **Figure 7** indicates that the number of firebrands beyond the last semicircle (at 7.5 m) will be low when compared to the total number of firebrands within the semicircular region of interest. The five extrapolation approaches considered are described and evaluated.

Node Method

With the node method to estimate the total number of hot firebrands released, the measured char mark/m^2 information was used directly to estimate the total number of firebrands released. The semi-circle in front of the tree was divided into 65 spatial regions, with each region including a fabric station (i.e., a node). The measured char mark area density for a node was multiplied by the corresponding area of the region to calculate the firebrands in that region. In turn, the estimated number of firebrands from all the regions were cumulated to determine the overall number of hot firebrands released. If a node had no char marks, then that corresponding node area was assumed

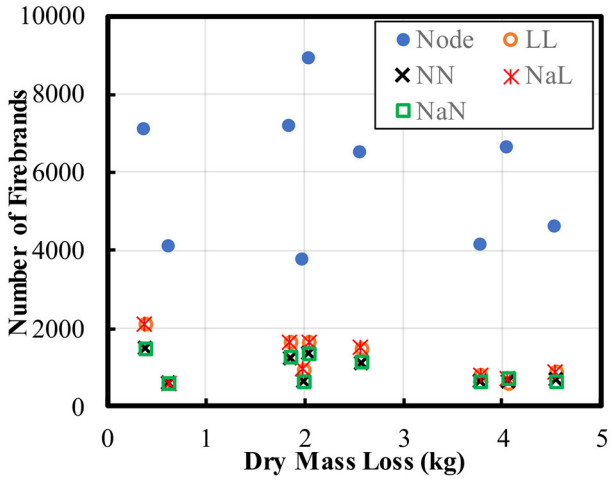

FIGURE 8 | Variation of total number of firebrands measured using the node method and several interpolation and extrapolation methods. The trees used for these tests are Douglas-fir with heights between 2.7 and 4.2 m. The captions represent: LL, Linear interpolation and extrapolation; NN, Nearest neighbor interpolation and extrapolation; NaL, Natural neighbor interpolation and linear extrapolation; NaN, Natural neighbor interpolation and nearest neighbor extrapolation.

to not have any firebrands. The advantage of the node method was its ease of implementation. However, the method suffers from disproportional area weight given to the nodes at the farther end of the area of interest (i.e., the area increases as the node location is farther away from the tree). As a result, the total number of firebrands estimated by this methodology tends to be an overestimate. **Figure 8** shows the estimated total number of firebrands released from Douglas-fir trees using the node method. The node method overestimates the number by a minimum of 100% when compared to other extrapolation and interpolation techniques.

Interpolation and Extrapolation Methods

Arguably, a more accurate method to estimate the total number of firebrands is to interpolate data between nodes (i.e., $1.5 < r < 7.5$ m) and extrapolate data for locations between center of the tree and nodes at 1.5 m radius (i.e., where not fabric could be placed). Once the char mark area density is interpolated and extrapolated, the char mark area density is integrated over the semicircular area of interest to estimate the total firebrand number. Four different interpolation/extrapolation combinations were used to estimate the total number of firebrands:

1. Linear interpolation and linear extrapolation (LL)
2. Nearest neighbor interpolation and extrapolation (NN)
3. Natural neighbor interpolation and linear extrapolation (NaL), and
4. Natural neighbor interpolation and nearest neighbor extrapolation (NaN)

These methods were implemented using functions already built into MATLAB software (The MathWorks Inc., 2018). Nodes that did not have char marks were specified as 0 when applying these methodologies. **Figure 8** shows the estimated number of hot firebrands released using the four interpolation/extrapolation approaches. The total number of estimated firebrands from all these methods produce similar values (i.e., usually agree within 10%) indicating no significant differences in the results when the different methodologies are used, at least for the conditions from this study. For all methodologies, the total number of firebrands released was 2000 or less for Douglas-fir trees 2.7–4.2 m tall, as shown in **Figure 8**.

The results from the 4 interpolation/extrapolation techniques were further explored to evaluate the physical accuracy. **Figure 9** shows the measurements (magenta) and the interpolated/extrapolated values (surface distribution) for the various methodologies. It is noted that both linear extrapolation methods resulted in a negative char mark area density at locations between 0 and 1.5 m radius (see **Figures 9A,C**). This occurred because linear extrapolation means extending data to unknown regions based on data at the last given point. A negative value for char mark area density is possible depending on the data at 1.5 m radius boundary. It was decided to not use either method employing linear extrapolation because of the unphysical aspect of extrapolation.

The nearest neighbor extrapolation method was used in conjunction with the nearest neighbor interpolation and natural neighbor interpolation methods (see **Figures 9B,D**). In the nearest neighbor interpolation method, the char mark area density between stations is calculated as the value of the nearest point leading to a piecewise constant value between data points (Amidror, 2002), as can be seen in **Figure 9B**. The natural neighbor interpolation method improves on the nearest neighbor interpolation method by applying a weighted value to neighboring known data points based on the distance between the point of interest and the neighbors (Amidror, 2002). This leads to a better estimation of the char mark area density at unknown locations as the approximation is smoother and close to the "true" function. This smoother approximation is evident in **Figure 9D** when compared to the nearest neighbor interpolation method shown in **Figure 9B**. The combination of natural neighbor interpolation and nearest neighbor extrapolation was used for the remainder of the work because linear extrapolation method is unphysical and natural neighbor interpolation method proved to be superior.

Single Tree vs. Accumulation Method

Two different approaches were evaluated for determining the total number of firebrands released. The first method was to collect the sheets of fabric after burning each tree [i.e., single tree method (STM)]. The results from each burn were added to provide the total number of firebrands produced for a type of tree for with a particular average height (using 7–9 trees). The second approach was the accumulation method (AM), where a total of 7–9 trees were burned separately and the fire-resistant fabric was changed between tests only if the fabric had enough char marks to warrant concern about marks merging together. If a station had to be replaced after a test, the char mark area density at that station is calculated as the

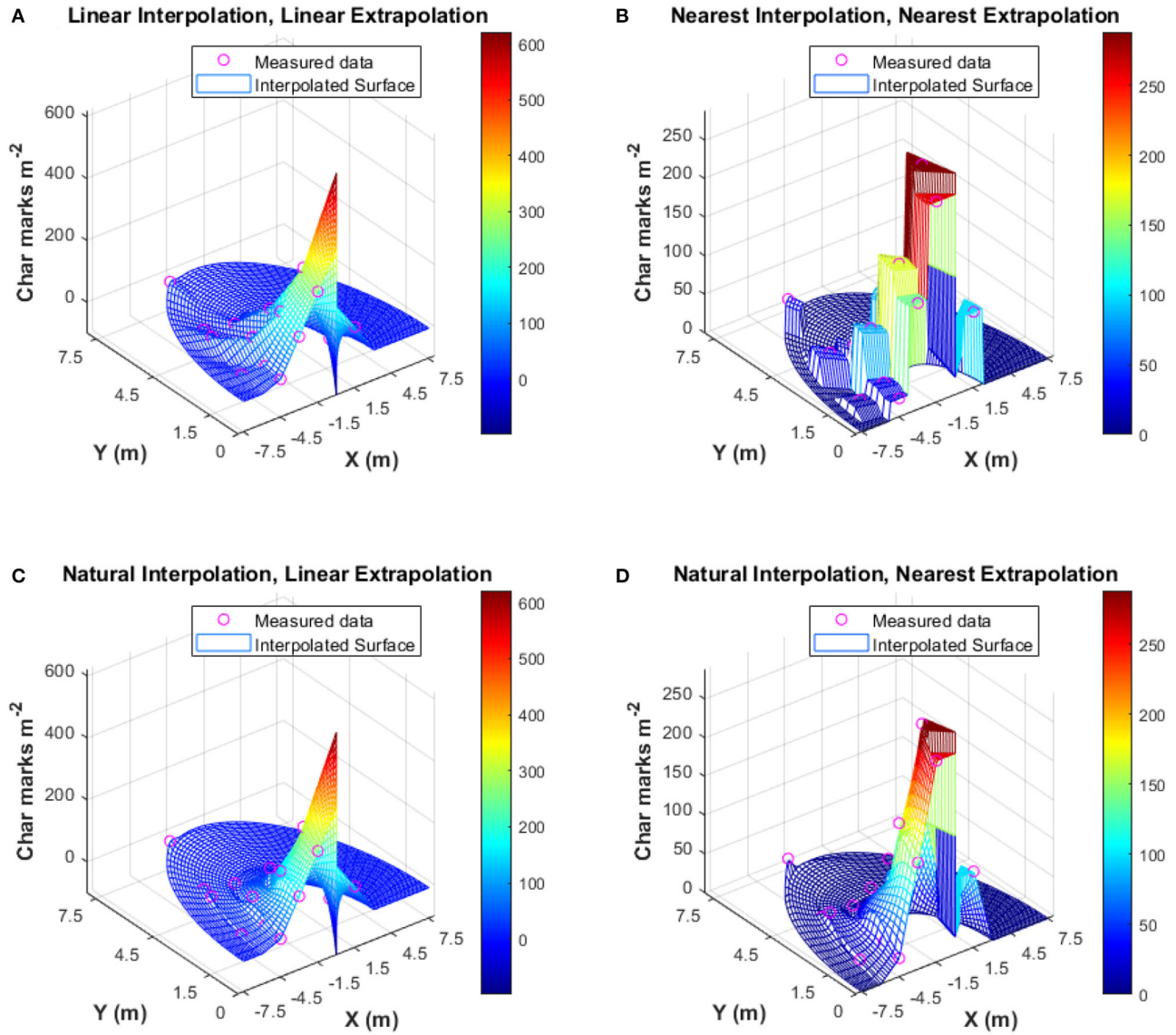

FIGURE 9 | Performance of various interpolation and extrapolation methods for a Douglas-fir tree of height 4.4 m and MC = 16.8%. **(A)** Linear interpolation and extrapolation, **(B)** Nearest neighbor interpolation and extrapolation, **(C)** Natural neighbor interpolation and linear extrapolation, and **(D)** Natural neighbor interpolation and nearest neighbor extrapolation.

sum of char mark area density of the fabrics at that station. The total number of firebrands was then estimated using the interpolation method. Each method has certain advantages, the STM provides resolution of the firebrands released for each tree whereas the AM method's data has char marks at more stations increasing the confidence in the interpolated data. The main advantage of the AM method is the ability to conduct tests with fewer resources (i.e., time and fabric) as the need to change fabric after every test is eliminated. Changing fabric typically consumes the longest amount of time to complete a test.

Figure 10 shows a comparison of the estimated number of firebrands produced per kg dry mass loss using the STM and AM for several Douglas-fir trees. Normalizing the total number of firebrands by the mass loss is important for allowing comparison between tests, and the values can potentially be used as source terms for models. Note that the AM provides a single data point (i.e., an accumulation for multiple trees) whereas the STM provides data points for individual trees. The data generated using STM was directly compared to the AM results by aggregating the former results for multiple trees [i.e., Accumulated Single tree method (ASTM)]. Considering both AM and ASTM data, as the average height of the tree increases the firebrands produced per dry mass loss decreases (i.e., **Figure 10a**). The trees studied using the STM measurements have an average height of 3.8 m, but a relatively large variation

in firebrands produced per kg dry mass loss is evident; no discernable trend can be observed indicating that other physical parameter(s) are key for firebrand production.

Comparison of firebrands produced relative to the MC of trees is shown in **Figure 10b**. As trees become drier their ability to produce firebrands increases roughly exponentially. This was expected, as the trees dry, they have less moisture which makes them burn with higher intensity and thus can produce more firebrands. The average MC of the trees measured using STM is 30.2% as shown by the ASTM data point. The AM data points in this comparison fall in trend with the STM data points, indicating that MC is a factor that determines the firebrands produced per kg dry mass loss. Admittedly, the moisture content evaluated in this study is lower than for live fuel. Hence caution should be exercised in extrapolating the sensitivity found in this study to live fuels.

Species Dependence

The AM was applied to measure the sensitivity of the production of firebrands as the species of tree/shrub was varied. The AM was used because the reduced resources needed for the method allowed a greater number of trees/shrubs to be evaluated. Additionally, the AM and STM methods provide similar results (see **Figure 10**). **Figure 11a** shows the total number of firebrands produced for trees/shrubs of different heights for various species. Sagebrush typically produces larger numbers of firebrands when compared to the other two trees. Anecdotally, the burning intensity of sagebrush tended to be the highest of all the trees/shrubs. As the tree height increases the total number of firebrands being produced increases for Douglas-fir trees and nearly remains constant for ponderosa pine trees. The different sensitivities for the two species of trees is attributed to differences in the burning behavior of the trees. Ponderosa pine trees were less prone to complete torching, in particular with increasing height, because of the spacing of the branches and needles.

The number of firebrands produced for sagebrush increases as the height of the tree increases but decreases for the tallest trees. The cause of the reduction is not clear but may have happened because the prevailing winds may have caused firebrands to not be deposited on the fabric. However, as discussed before, the average wind conditions are expected to have a minor impact on burning of the trees/shrubs. Recall that the average wind speed was always <1 m/s and the average wind direction was toward the region of interest. Perhaps a more likely reason for the reduction in firebrands is that the ground fire has a disproportionate impact on the shorter trees/shrubs. Shorter sagebrush, tended to torch completely, thus producing more firebrands. For the taller trees/shrubs the starter fire burns the leaves closer to the ground, but not always propagate throughout the trees/shrubs. In particular, the tallest sagebrush do not have foliage near the ground and hence could experience a reduction the total number of firebrands. The effect of this anecdotal observation needs to be examined further in future studies.

As discussed before, MC could be used as the physical parameter indicative of firebrand production instead of tree height. **Figure 11b** shows the total number of firebrands produced with varying MC measured using AM. The total number of firebrands increases as the MC increases for Douglas-fir and sagebrush species but remains roughly constant for ponderosa pine trees. This trend is counter intuitive and may require further investigation, specifically to identify if the moisture content couples with other physical parameters.

Figure 11c shows the variation of the number of firebrands produced per kg of fuel consumed (specific number of firebrands) relative to the height of the tree/shrub. As the tree height increases the specific number of firebrands decreases for Douglas-fir and ponderosa pine trees. The cause of this sensitivity is not clear, but it is plausible that the greater number of branches with larger diameters for the taller trees reduces the relative number of firebrands that are produced. Hudson and Blunck (2019) found that the diameter of dowels was one of the most significant parameters that influences the propensity to generate firebrands. Hence, the larger the tree the greater the number of branches that may burn (and consume mass), but not produce firebrands. For sagebrush the specific number of firebrands increases initially with height of the shrub and then decreases for the tallest bushes. It is also plausible that the upper branches of bigger trees block the movement or generation of firebrands. The specific cause of the sensitivity identified in **Figure 11c** requires further investigation.

Figure 11d shows the specific number of firebrands relative to the MC of the tree/shrub. The specific number of firebrands decreases as the MC of the trees increases for Douglas-fir and ponderosa pine trees. These trees produce similar specific numbers of firebrands, but ponderosa pine trees had higher moisture content than Douglas-fir trees even though they were left out to dry for a longer time period. Since these trees are less susceptible to drying, it is expected that they could produce a smaller number of firebrands during wildfires compared to Douglas-fir. In contrast, sagebrush produces approximately six times more specific number of firebrands when compared to ponderosa pine trees for similar amount of MC. This is consistent with a visible greater burning intensity of the sagebrush and greater consumption of the foliage.

SUMMARY AND CONCLUSIONS

In this work, a total of 71 individual trees/shrubs of varying heights (1.4–6.2 m) were burned to enumerate the total number of firebrands produced. Two tree species (Douglas-fir and ponderosa pine) and one shrub species (sagebrush) were evaluated. A total of 65 fire-resistant fabric stations were deployed for each tree/shrub; the enumeration was carried out by counting the total number of char marks firebrands left on the fabric. The number of char marks was equated to be the number of firebrands captured whose temperatures were $>300^{\circ}$C. A novel interpolation/extrapolation methodology was established to measure the total number of firebrands generated using the char mark information at individual stations.

The specific conclusions from this work are as follows:

1. Overall, sagebrush trees tend to produce a greater total number of firebrands and firebrands per kg of fuel consumed

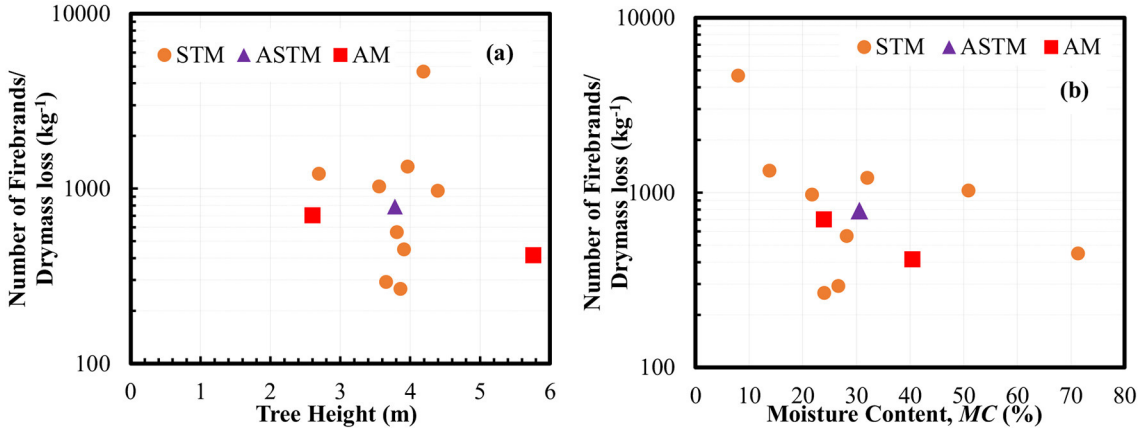

FIGURE 10 | Number of firebrands measured per dry mass loss for Douglas-fir trees using both single tree method (STM) and accumulation method (AM). **(a)** Shows generation characteristics with respect to the height of the trees. **(b)** Shows results with respect to the moisture content of the trees.

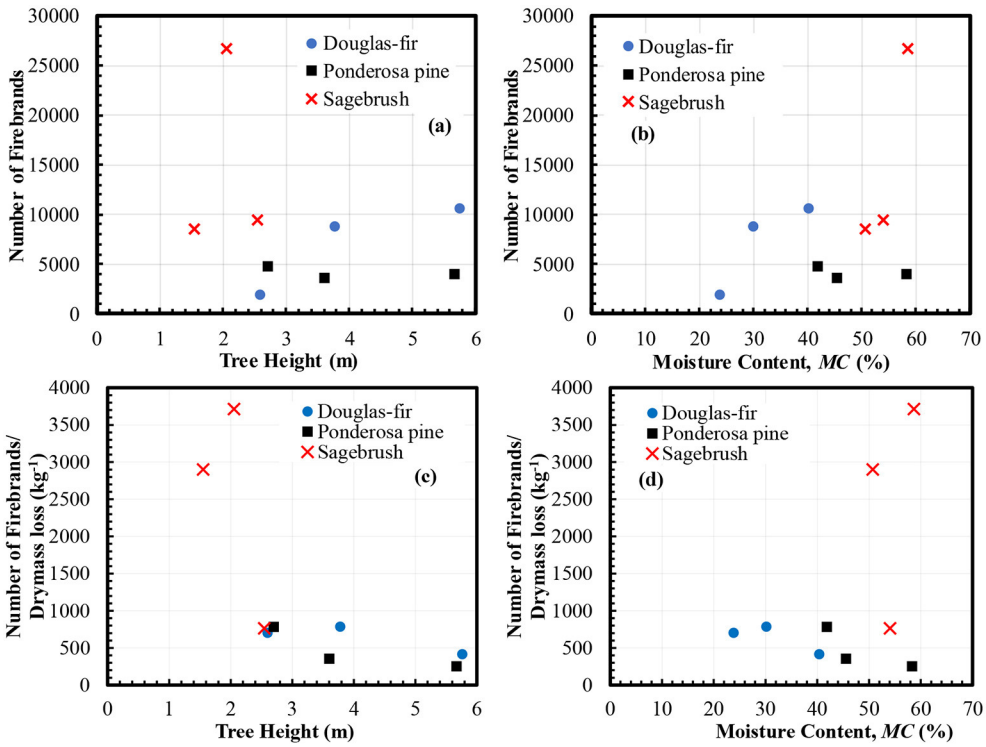

FIGURE 11 | (a) Variation of total number of firebrands with the height of trees, **(b)** variation of total number of firebrands with the MC of trees, **(c)** variation of number of firebrands per kg dry mass loss with the height of trees, **(d)** variation of number of firebrands per kg dry mass loss with the MC of trees.

(~6 times higher for trees of similar moisture content) when compared to the Douglas-fir and ponderosa pine trees. This is attributed to the relatively small diameters of the foliage/branches and the visibly greater burning intensity of sagebrush.

2. The total number of firebrands tends to increase with the increase in the height of the tree/shrub. The specific number of firebrands produced tends to decrease with increasing height of the tree/shrub. It is plausible that the greater number of branches with larger diameters for the taller trees reduces the relative number of firebrands that are produced.
3. The total number of firebrands tends to increase or remain similar as the moisture content of the tree varies. The specific firebrand production increased exponentially with decreasing moisture content in the trees for Douglas-fir and ponderosa pine trees. This is supported by the anecdotally observed increase in the intensity of burns for trees with lower moisture content irrespective of the species. The definite cause of

this sensitivity is unclear, but it is plausible that this trend results from a coupling of the moisture content with another physical parameter.

It is expected that the methodology established here can be used by other researchers to determine the total number of firebrands generated for other fuels of interest during fires. Moreover, the firebrand production terms reported here can be used within detailed physics-models to improve the fidelity of simulations of firebrand transport and ignition. Further, current measurements show that other experimental parameters, such as heat release rate from the burns, the size of tree branches and needles/leaves, and velocity within a tree during a burn need to be evaluated. Plans are in place to measure a few of these parameters in future experiments.

DATA AVAILABILITY STATEMENT

The raw data supporting the conclusions of this article will be made available by the authors, without undue reservation.

AUTHOR CONTRIBUTIONS

SA led the research, analyzed the results, and wrote the manuscript. JC contributed to the data collection and helped to write the manuscript. DB conceived of the research idea, helped with analysis, and contributed to the manuscript. All authors contributed to the article and approved the submitted version.

FUNDING

This research was supported by a NIST grant (grant number, 70NANB19H164).

ACKNOWLEDGMENTS

The authors would like to thank Andrew Ross, Nathan Gardner, Benjamin Smucker, Derek Bean, Harley Glad, and Kaz Teope for their support in conducting these experiments. The authors would also like to acknowledge the USDA-Forest service for lending their anemometer.

SUPPLEMENTARY MATERIAL

The Supplementary Material for this article can be found online at: https://www.frontiersin.org/articles/10.3389/fmech.2021.655593/full#supplementary-material

REFERENCES

Adusumilli, S., Hudson, T., Gardner, N., and Blunck, D. L. (2020). Quantifying production of hot firebrands using a fire-resistant fabric. *Int. J. Wildl. Fire*. 30, 154–159. doi: 10.1071/WF20051

Amidror, I. (2002). Scattered data interpolation methods for electronic imaging systems: a survey. *J. Electron. Imaging* 11:157. doi: 10.1117/1.1455013

Anand, C., Shotorban, B., Mahalingam, S., McAllister, S., and Weise, D. R. (2017). Physics-based modeling of live wildland fuel ignition experiments in the forced ignition and flame spread test apparatus. *Combust. Sci. Technol.* 189, 1551–1570. doi: 10.1080/00102202.2017.1308357

Benkoussas, B., Consalvi, J. L., Porterie, B., Sardoy, N., and Loraud, J. C. (2007). Modelling thermal degradation of woody fuel particles. *Int. J. Therm. Sci.* 46, 319–327. doi: 10.1016/j.ijthermalsci.2006.06.016

Eckelman, C. A. (1997). *Wood Moisture Calculations*. West Lafayette, IN: Purdue University, Department of Forestry & Natural Resources.

Fernandez-Pello, A. C. (2017). Wildland fire spot ignition by sparks and firebrands. *Fire Saf. J.* 91, 2–10. doi: 10.1016/j.firesaf.2017.04.040

Filkov, A., Prohanov, S., Mueller, E., Kasymov, D., Martynov, P., Houssami, M. El, et al. (2017). Investigation of firebrand production during prescribed fires conducted in a pine forest. *Proc. Combust. Inst.* 36, 3263–3270. doi: 10.1016/j.proci.2016.06.125

Hedayati, F. (2018). *Generation and Characterization of Firebrands From Selected Structural Fuels*. Charlotte, NC: University of North Carolina.

Hudson, T. R., and Blunck, D. L. (2019). Effects of fuel characteristics on ember generation characteristics at branch-scales. *Int. J. Wildl. Fire* 28, 941–950. doi: 10.1071/WF19075

Hudson, T. R., Bray, R. B., Blunck, D. L., Page, W., and Butler, B. (2020). Effects of fuel morphology on ember generation characteristics at the tree scale. *Int. J. Wildl. Fire*. 29, 1042–1051. doi: 10.1071/WF19182

Jolly, M. W., Hintz, J., Linn, R. L., Kropp, R. C., Conrad, E. T., Parsons, R. A., et al. (2016). Seasonal variations in red pine (*Pinus resinosa*) and jack pine (*Pinus banksiana*) foliar physio-chemistry and their potential influence on stand-scale wildland fire behavior. *For. Ecol. Manage.* 373, 167–178. doi: 10.1016/j.foreco.2016.04.005

Linn, R., Reisner, J., Colman, J., and Winterkamp, J. (2002). Studying wildfire behavior using FIRETEC. *Int. J. Wildl. Fire* 11, 233–246. doi: 10.1071/wf02007

MacLean, J. D. (1952). *Preservative Treatment of Wood by Pressure Methods*. Washington, DC: US Department of Agriculture, Forest Service.

Manzello, S. L., and Foote, E. I. D. (2014). Characterizing firebrand exposure from wildland-urban interface (WUI) fires: results from the 2007 Angora fire. *Fire Technol.* 50, 105–124. doi: 10.1007/s10694-012-0295-4

Manzello, S. L., Maranghides, A., and Mell, W. E. (2007a). Firebrand generation from burning vegetation. *Int. J. Wildl. Fire* 16:458. doi: 10.1071/WF06079

Manzello, S. L., Maranghides, A., Mell, W. E., Cleary, T. G., and Yang, J. C. (2006). Firebrand production from burning vegetation. *For. Ecol. Manage.* 234:S119. doi: 10.1016/j.foreco.2006.08.160

Manzello, S. L., Maranghides, A., Shields, J. R., Mell, W. E., Hayashi, Y., and Nii, D. (2007b). Measurement of firebrand production and heat release rate (HRR) from burning Korean pine trees. *Fire Saf. Sci*. 7, 108–116.

Manzello, S. L., Maranghides, A., Shields, J. R., Mell, W. E., Hayashi, Y., and Nii, D. (2009). Mass and size distribution of firebrands generated from burning Korean pine (*Pinus koraiensis*) trees. *Fire Mater.* 33, 21–31. doi: 10.1002/fam.977

Manzello, S. L., Suzuki, S., Gollner, M. J., and Fernandez-Pello, A. C. (2020). Role of firebrand combustion in large outdoor fire spread. *Prog. Energy Combust. Sci.* 76:100801. doi: 10.1016/j.pecs.2019.100801

Matthews, S. (2010). Effect of drying temperature on fuel moisture content measurements. *Int. J. Wildl. Fire* 19:800. doi: 10.1071/WF08188

Monedero, S., Ramirez, J., and Cardil, A. (2019). Predicting fi re spread and behaviour on the fi reline. Wild fire analyst pocket: a mobile app for wildland fire prediction. *Ecol. Modell.* 392, 103–107. doi: 10.1016/j.ecolmodel.2018.11.016

Rissel, S., and Ridenour, K. (2013). Ember production during the bastrop complex fire. *Fire Manag. Today* 72, 7–13. Available online at: https://www.fs.usda.gov/sites/default/files/legacy_files/fire-management-today/72-4.pdf

Shotorban, B., Yashwanth, B. L., Mahalingam, S., and Haring, D. J. (2018). An investigation of pyrolysis and ignition of moist leaf-like fuel subject to convective heating. *Combust. Flame* 190, 25–35. doi: 10.1016/j.combustflame.2017.11.008

Suzuki, S., Brown, A., Manzello, S. L., Suzuki, J., and Hayashi, Y. (2014). Firebrands generated from a full-scale structure burning under well-controlled laboratory conditions. *Fire Saf. J.* 63, 43–51. doi: 10.1016/j.firesaf.2013.11.008

Suzuki, S., and Manzello, S. L. (2016). Firebrand production from building components fitted with siding treatments. *Fire Saf. J.* 80, 64–70. doi: 10.1016/j.firesaf.2016.01.004

Suzuki, S., Manzello, S. L., and Hayashi, Y. (2013). The size and mass distribution of firebrands collected from ignited building components exposed to wind. *Proc. Combust. Inst.* 34, 2479–2485. doi: 10.1016/j.proci.2012.06.061

Suzuki, S., Manzello, S. L., Kagiya, K., Suzuki, J., and Hayashi, Y. (2015). Ignition of Mulch beds exposed to continuous wind-driven firebrand showers. *Fire Technol.* 51, 905–922. doi: 10.1007/s10694-014-0425-2

Suzuki, S., Manzello, S. L., Lage, M., and Laing, G. (2012). Firebrand generation data obtained from a full-scale structure burn. *Int. J. Wildl. Fire* 21, 961–968. doi: 10.1071/WF11133

The MathWorks Inc. (2018). *MATLAB: 2018, 9.7.0.1190202 (R2019b)*. Natick, MA: The MathWorks Inc.

Thomas, J. C., Mueller, E. V., Santamaria, S., Gallagher, M., El Houssami, M., Filkov, A., et al. (2017). Investigation of firebrand generation from an experimental fire: development of a reliable data collection methodology. *Fire Saf. J.* 91, 864–871. doi: 10.1016/j.firesaf.2017.04.002

Conflict of Interest: The authors declare that the research was conducted in the absence of any commercial or financial relationships that could be construed as a potential conflict of interest.

frontiers in Mechanical Engineering

ORIGINAL RESEARCH
published: 07 July 2021
doi: 10.3389/fmech.2021.702181

Statistical Assessment of Parameters Affecting Firebrand Pile Heat Transfer to Surfaces

Elias Bearinger[1], *Brian Y. Lattimer*[1]*, *Jonathan L. Hodges*[2], *Christian Rippe*[2] *and Anil Kapahi*[2]

[1]Virginia Tech, Blacksburg, VA, United States, [2]Jensen Hughes, Blacksburg, VA, United States

Firebrands are known to cause ignition of structures far from the primary fire front, resulting in significant damage to structures before firefighting can be attempted. To make structures more resilient to firebrand ignition, a better understanding of the heat transfer from firebrands to surfaces is needed. This paper provides a statistical assessment of different factors expected to have an impact on the heat flux from firebrand piles to a flat surface. The factors included in the study were wood moisture content, wood type (hardwood or softwood), wood density, wood state (live, dead, or artificial), wind speed, pile mass, firebrand diameter, and firebrand length. Using design of experiments, test matrices were developed that permitted a statistical analysis to be performed on the data. This statistical analysis was used to quantify which factors had a statistically significant impact on the heat flux from the pile as well as ranking the importance of the different factors. Artificial firebrands were found to have statistically higher heat fluxes compared with natural firebrands. Other factors that had a statistically significant impact on the heat flux were wind speed, firebrand length, and firebrand length-diameter interaction. Firebrand aspect ratio (related to the firebrand length-diameter interaction) is directly related to the pile porosity, which is a measure of the volume of air in the pile. Increasing the aspect ratio (which increases the pile porosity) results in higher heat fluxes across a larger region of the pile and was found to be an important factor. Firebrand diameter and pile mass were found to affect the burning duration but not as significantly as other parameters. The number of firebrands in the pile was also observed to potentially affect the heat flux, with a critical number required to reach the highest heat flux for a given firebrand geometry.

Keywords: firebrand, piles, heat transfer, statistics, experiments

OPEN ACCESS

Edited by:
Domingos Xavier Viegas, University of Coimbra, Portugal

Reviewed by:
Xinyan Huang, Hong Kong Polytechnic University, China
Michael John Gollner, University of California, Berkeley, United States

***Correspondence:**
Brian Y. Lattimer
lattimer@vt.edu

Specialty section:
This article was submitted to Thermal and Mass Transport, a section of the journal Frontiers in Mechanical Engineering

Received: *29 April 2021*
Accepted: *22 June 2021*
Published: *07 July 2021*

Citation:
Bearinger E, Lattimer BY, Hodges JL, Rippe C and Kapahi A (2021) Statistical Assessment of Parameters Affecting Firebrand Pile Heat Transfer to Surfaces. Front. Mech. Eng 7:702181. doi: 10.3389/fmech.2021.702181

INTRODUCTION

For much of the world, wildland fires present a serious and reoccurring threat to life, property, and the environment. The recent 2019–2020 fire season in Australia for example was so severe that it was named the Black Summer (Deb et al., 2020), with a cumulative 97,000 km^2 of vegetation burned (Ward et al., 2020). Tragically, Australia's Black Summer resulted in the destruction of 3,000 homes and 33 direct fatalities (Filkov et al., 2020). This type of destruction from wildland fires has been increasingly seen around the world. The 2017 fires in Portugal killed 112 people (Turco et al., 2019). In 2018, fires in Greece burned 3,000 houses (Lagouvardos et al., 2019). In the United States, the 2018 Camp Fire alone killed 85 people and destroyed 19,000 structures (Brown et al., 2020). Much of the

human toll from these fires occurred in the wildland urban interface (WUI), the confluence of rural and developed environments. As the wildland urban interface continues to expand (Theobald and Romme, 2007), there is a pressing need to design structures to withstand the potential destruction caused by wildfires.

Wildfires produce airborne pieces of burning vegetation and debris known as firebrands, which have been shown to be a prominent mode of home ignition (Mell and Alexander, 2009). Firebrands are particularly dangerous due to their lofting potential. The high winds associated with wildland fires can transport these firebrands 1–2 km from the fire front (Koo et al., 2010), where they have been witnessed to cause home ignition without direct flame contact. Experimental work has shown that during wind-driven firebrand showers, firebrands can accumulate in piles and easily ignite common building materials (Manzello and Suzuki, 2014). Understanding heat transfer from piles of firebrands is an important step in engineering fire-resistant structures.

One of the difficulties in identifying the risk of a structure igniting due to firebrand piles is the uncertainty and variability in the heat transfer from firebrand piles to surfaces. Early work in the field conducted by McArthur and Lutton investigated the ignition of mock building assemblies by radiata pine wood cribs at 3–5% moisture content. Crib masses from 0.8–12.0 g were tested in the absence of wind and it was found that burning damage to the structure increased with crib mass (Mcarthur and Lutton, 1991). Dowling collected embers from burned wood cribs which were then used to test the ignition of timber bridges. It was found that 7.0 g of firebrands deposited in a 10 mm gap was sufficient to cause ignition with no wind applied (Dowling, 1994).

Tests were conducted by Manzello et al. (2008) using machined Douglas fir firebrands to assess ignition in various fuel beds. The firebrands were cylindrical and came in two sizes. The first size had a diameter of 5 mm and a length of 51 mm, while second size had diameter of 10 mm and length of 76 mm. The study included tests with single and groups of four firebrands. It was found that increasing the number of deposited glowing firebrands led to an increased likelihood of ignition when all other factors were held constant. Increasing firebrand size and wind speed also led to increased ignition (Manzello et al., 2008). In another similar study, also by Manzello et al. (2006) ponderosa pine disks were used for firebrands. The authors point out that compared with disks, approximately half the mass of cylindrical Douglas fir firebrands are required to cause ignition under identical conditions (Manzello et al., 2008).

Filkov et al. (2016) investigated the effects of firebrand size, firebrand quantity, and wind speed on the ignition of pine needle beds at 9.3% moisture content. The firebrands were made from pine bark 5 mm thick with lengths and width dimensions of 10 × 10, 15 × 15, 20 × 20, 25 × 25, and 30 × 30 mm depending on the test. Firebrand quantity ranged from 1 to 10, and wind speed was varied between 0 and 3 m/s. It was found that the ignition of the fuel beds depended on the size and quantity of firebrands, with ignition being more likely with a greater quantity of large firebrands. For a given firebrand size and quantity, the likelihood of ignition increased with wind speed (Filkov et al., 2016).

Two separate studies investigated the ignition of recipient fuels by firebrand piles based on the geometric configuration of the piles and the substrate. Santamaria et al. (2015) used slices of bark to assess ignition on flat and angled (120°) configurations and concluded that ignition depends on pile mass. Manzello et al. (2009) also looked at the effect of configuration using plywood and oriented strand board with ponderosa pine firebrands. The size of a crevice between two boards was varied by changing the crevice angle. Results show that there was an interplay between configuration, wind, and mass/number of firebrands. Generally, the likelihood of ignition increased with increasing wind speed and decreasing crevice angle (Manzello et al., 2009).

The studies mentioned so far have mainly relied on binary observation data to assess heat transfer from firebrand piles (i.e., the pile did or did not cause ignition under certain conditions). Hakes et al. (2018) were some of the first to characterize the heat transfer from firebrand piles. Heat flux data was taken with both a 1.27 cm water-cooled heat flux gauge (WC-HFG) and an array of thin-skin calorimeters (TSC). The TSC's were used to resolve the distribution of heat flux across the surface area but suffered from poor spatial resolution (1.5 cm). All firebrands used in this study were 25 mm long, with diameters of 6.35, 9.5, and 12.7 mm. Deposited piles masses ranged from 0.1 to 9.6 g, and cases with and without wind were tested. It was found that for a given firebrand diameter, increasing the pile mass resulted in increased heat flux and duration. Additionally, it was found that if two piles had the same mass, the diameter of the firebrands within the piles made little difference on the recorded heat flux, a finding at odds with previous studies which point to firebrand geometry as an important parameter (Manzello et al., 2008). It was also found that wind substantially increased the heat flux from the firebrand pile but shortened the burning duration (Hakes et al., 2018). Bearinger et al. (2020) conducted a similar study where heat fluxes were measured at a high resolution (0.4 mm × 0.4 mm) using inverse heat transfer with infrared thermography. The authors observed local heat fluxes significantly higher than the critical heat fluxes for many building materials in single firebrand configurations which were not expected to cause ignition from previous studies.

Tao et al. (2020) further investigated the effects of firebrand size and geometry on heat transfer from piles of firebrands. In this study, a combination of firebrands collected from natural vegetation and those made from commercially available materials such as dowel rods were used. Piles were subjected to 0.5–1.4 m/s winds in a wind tunnel and heat flux measurements were again taken using a water-cooled heat flux gauge and TSC array. It was noted that based on the type of firebrand, piles exhibited differing bulk densities (i.e., mass divided by pile volume). The bulk density was found to have a significant impact on the measured heat transfer, but there are likely competing effects between oxygen availability and reradiation within the pile. There also appeared to be a difference in the heat transfer from piles made with natural firebrands compared with those made from dowel rods. As found in all previous studies, increasing wind led to increased heat flux (Tao et al., 2020).

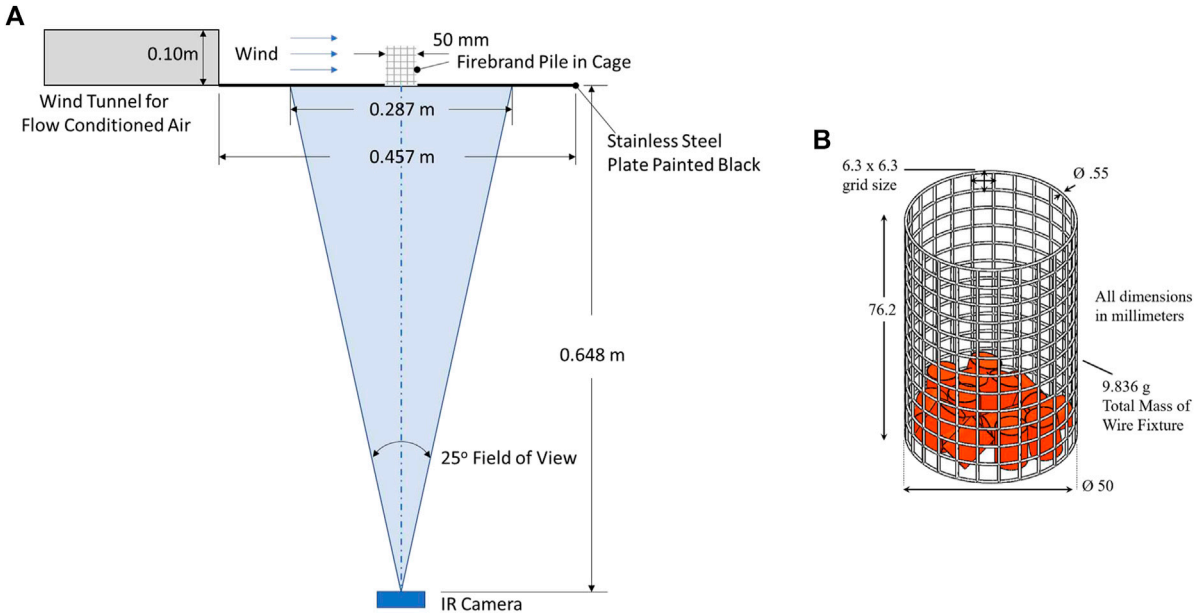

FIGURE 1 | Overview of test details including **(A)** test setup and **(B)** metal mesh cage used to contain firebrand piles.

It is apparent that there are many factors that could potentially affect the heat transfer from firebrand piles. Some of these factors such as pile mass, wind speed, firebrand size, and whether the firebrand was made from natural or processed wood have been at least partially explored in previous work. Other factors such as wood moisture content and density have received little attention. The goal of this work was to test the effect of as many independent factors as possible and statistically evaluate their importance. This work explored the impact of eight factors including wood moisture content, wood type (hardwood or softwood), wood density, wood state (live, dead, or artificial), wind speed, pile mass, firebrand diameter, and firebrand length on the heat flux from firebrand piles to a flat surface. Design of experiments was used to develop tests that would permit a statistical analysis of this data to determine the statistically significance of the factors as well as rank their importance on the heat flux from a firebrand pile. The data was then further analyzed to examine the impact of the important factors on the heat flux distributions.

EXPERIMENTAL METHODS

A series of tests were conducted using a custom testing apparatus to investigate the impact of the different factors on the heat flux from firebrand piles. High resolution heat transfer measurements from the firebrand piles were collected through time by a method of inverse heat transfer (IHT) using thermographs from an infrared (IR) camera. The test details were developed using design of experiments through the methodologies described below. In addition, analysis methods are described highlighting how the statistical analysis was used to analyze the test data and determine the significance of the various factors.

Experimental Setup

Apparatus

A custom experimental apparatus was developed for this testing (shown in **Figure 1**) consisting of a wind tunnel, support structure, an infrared (IR) camera, a wire mesh cage, and a black 304 stainless steel plate. The wind tunnel was 2.4 m long by 0.31 m wide with a flow-conditioning section in the middle. The wind tunnel exit was 0.31 m wide and 0.10 m high with a uniform flow across 90% of the opening. The flow through the tunnel was driven by an American Fan Company AF-8 blower, controlled by a 1 hp, 3-phase AC motor and a Reliance Electric SP500 variable speed drive. The maximum flow rate for the tunnel was 3.5 m/s corresponding to volumetric flow rate of 0.106 m^3/s (225 cfm).

The firebrand piles were supported on a 304 stainless steel plate having dimensions 457 mm × 457 mm x 0.762 mm. The plate was painted black on both sides using Rust-oleum™ High Heat black enamel paint. The paint thickness was approximately 20 μm and has been shown by Cholewa et al. (2016) to have an emissivity of $\varepsilon = 0.97$. The plate was clamped to the support structure and carefully leveled such that the top face of the plate aligned with lower edge of the wind tunnel exit. A thin piece of aluminum tape (not pictured in **Figure 1**) connected the inside of the wind tunnel exit to the top side of the plate, ensuring no wind reached the underside of the plate.

A FLIR A655sc IR camera was used in the testing and controlled by ResearchIR™ acquisition software. The A655sc camera records in the longwave infrared spectrum (7.5–14.0 μm), have 640 × 480 pixel resolution, and used a 25°lens. The camera recorded at 3.13 Hz with the data being down-sampled to 0.28 Hz post-process. The IR camera was used to measure the temperature on the underside of the stainless steel

plate, and it was operated in the 100–650°C mode with an emissivity equal to that of the plate (ε = 0.97). In all these tests, the IR camera was positioned 0.648 m below the bottom surface of the plate resulting in a pixel resolution of 0.44 mm × 0.45 mm the plate surface. Plate temperature data from the IR camera was used for the inverse heat transfer calculations as described below.

Firebrand piles have been observed to accumulate on flat surfaces with external wind and remain in a pile due to the larger surrounding pile preventing them from moving (Manzello and Suzuki, 2014). To quantify the heat flux from small piles of firebrands, the firebrands in this study were placed inside a lightweight cage made of steel mesh with dimensions shown in **Figure 1**. In addition to keeping the firebrands from prematurely blowing off the plate, the cage helped the pile maintain a circular shape with diameter of 50 mm. The 6.3 mm by 6.3 mm gridding was sufficiently porous to allow wind to access the pile while still securing small firebrands.

Inverse Heat Transfer

Inverse heat transfer (IHT) analysis is the method through which the stainless steel plate temperature measurements recorded with the IR camera were used to calculate the heat flux from the firebrands onto a horizontal surface. The advantage of this method is that heat flux measurements can be resolved with the same spatial and temporal resolution as recorded by the infrared camera.

The IHT method using infrared images was originally developed by Rippe and Lattimer (2015) and relies on a thermally-thin interstitial medium (in this case the black 304 SS plate) of known optical and thermal properties between the infrared camera and the heat source. The IR camera was used to obtain a series of 2D temperature measurements of the unexposed side of the plate through time. Each pixel recorded by the camera corresponds to a small, discrete area on the plate and a known temperature. By knowing each temperature value through time and ambient conditions, an energy balance (see **Figure 2**) was conducted on every pixel to obtain a temporally-resolved 2D heat flux map.

The net heat flux into each pixel, q''_{exp}, is the combined heat flux from all modes of heat transfer on the exposed side of the plate and is determined by an energy balance on the pixel

$$q''_{exp} = q''_{stor} - \sum q''_{cond} + q''_{rad,b} + q''_{conv,b} \quad (1)$$

where q''_{stor} is rate of energy storage, q''_{cond} are the conduction fluxes into the pixel of interest from its neighbors, and $q''_{rad,b}$ and $q''_{conv,b}$ are the radiation and convection fluxes from the plate's unexposed surface. The details of how the conduction heat fluxes and the storage terms were determined can be found elsewhere (Rippe and Lattimer, 2015).

As the plate temperature increases, the actual net heat flux from the firebrand pile to the plate will decrease as the temperature difference is minimized. For this reason, it is convenient to express the measured heat transfer as the heat flux that would be experienced by a surface maintained at a standard temperature of 20°C (293K). This is also equivalent to the heat flux that would be measured with a water-cooled heat flux gauge. This heat flux at the standard temperature, q''_0, is calculated using

$$q''_0 = q''_{exp} + \varepsilon\sigma\left(T_s^4 - 293^4\right) + h_f\left(T_s - 293\right) \quad (2)$$

where h_f is the convective heat transfer coefficient of the exposed side of the plate. All heat flux values presented in this work are the heat flux at standard temperature, q''_0, as described in **Eq. 2**. The details of calculating the heat transfer coefficients on the top and bottom of the plate for the different test conditions can be found elsewhere (Bearinger et al., 2020).

The above approach was previously verified for measuring heat transfer at this scale over the range of heat fluxes expected for firebrand piles (Bearinger et al., 2020). Based on the error analysis performed in Ref. (Rippe and Lattimer, 2015), the uncertainty in the heat flux measurements is 2.6 kW/m^2.

Test Procedure

The details pertaining to each separate test will be discussed in the following sections. Unless otherwise stated, the wood used to make the firebrands was harvested from living trees in the Eastern United States. A single tree of each species provided wood for all tests to reduce variability. To make the unburned firebrands, tree branches were cut to length using a bandsaw and bark was left intact. The length tolerance for firebrands was ±0.5 mm relative to the reported lengths in **Table 1**. Due to imperfections in the natural samples, some variability existed in the diameter of the firebrands. A diameter tolerance of ±1.0 mm was specified and samples not within this window were discarded. Prior to testing, the firebrands were dried to 0% moisture content (MC) by storing them in an oven at 75°C for several days. It was confirmed that this time and temperature was sufficient to bring the samples to <0.3% MC.

Prior to each test, the metal cage shown in **Figure 1B** was centered 127 mm from leading edge of the 304 SS plate. For tests with wind, the wind tunnel was started and the wind speed inside the metal cage was verified using an Extech Hot Wire Thermo-Anemometer with 0.1 m/s resolution. A custom funnel was

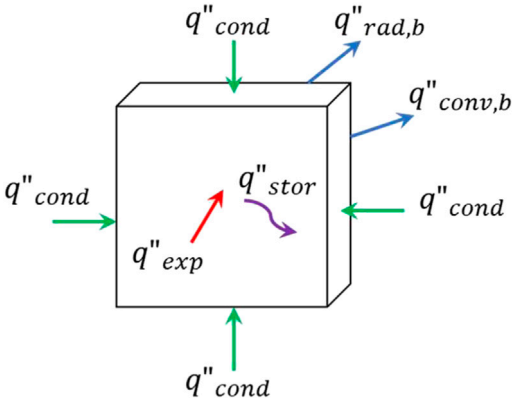

FIGURE 2 | Schematic of the energy balance on the stainless steel plate used in the inverse heat transfer analysis.

TABLE 1 | Tests used to evaluate the impact of eight factors on heat transfer from firebrand piles.

Test series name	Experiment design	Factors and levels	Wind speed (m/s)	Firebrand wood material	Firebrand sizes (L x D) (mm)
Moisture content study	Completely randomized block	0, 25%	2.0	N. Red Oak	(12.5 × 9.50)
Wood type study	Completely randomized block	Hardwood, softwood	2.0	Yellow poplar, E. White pine	(12.5 × 9.50)
Density study	Completely randomized block	540, 870 kg/m^3	2.0	Yellow poplar, N. Red Oak	(12.5 × 9.50)
Wood state study	Completely randomized block	Natural–live, Natural–dead, Artificial	2.0	N. Red Oak	(12.5 × 9.50)
Full factorial study	Full- factorial, randomized	Pile Mass: 1.5, 3.0 g	0.0 or 2.0	N. Red Oak	(12.5 × 4.75)
		Wind speed: 0.0, 2.0 m/s			(12.5 × 9.50)
		Firebrand diameter: 4.75, 9.50 mm			(50.0 × 4.75)
		Firebrand length: 12.5, 50.0 mm			(50.0 × 9.50)

placed on top of the cage to facilitate firebrand placement. Initially it was found that during tests with wind, the firebrands were blown to the trailing edge of the cage during the placement process. For this reason, a wind shield was added in front of the cage during the setup and removed at the start of testing. Data acquisition for the IR camera was started prior to the heating of the firebrand pile.

To make the firebrand pile, a carefully measured mass of unburned firebrands was heated in a wire mesh basket over a propane gas burner. Heating times and initial masses of unburned firebrands are recorded in the following sections. The initial heat time corresponded to when all the firebrands reached a state of self-sustaining flaming combustion after which the propane burner was turned off. The firebrands were allowed to flame and transition to smoldering combustion while the mass was monitored using a Sartorius FB6CCE-S scale with 0.1 g resolution. Once the total mass of the firebrands reached the desired deposited mass (approximately 60–120 s after the flames went out), the glowing firebrands were poured into the funnel and allowed to fall randomly within the cage. The funnel and wind shield were removed, and the firebrand pile burned unhindered until the peak temperature within the pile dropped below 100°C, at which point the test was ended. The firebrand piles left some residue on the plate during burning, so no more than two tests were conducted on the same plate before the plate was cleaned with acetone and repainted. No paint discoloration was observed following the firebrand pile exposures.

Design of Experiments

Experimental design was used to assess the impact of eight factors on the heat flux (response) from the firebrand piles through a series of five different studies, see **Table 1**. Using experimental design, the details of the tests that need to be performed are established so that the statistical analysis can be conducted on the data. This was done either by tests designed to evaluate main effects only (impact of a factor on the response) or assess the main effects and interactions with other main effects (impact of multiple factors on the response). Using this approach, a total of 33 tests were conducted in this study.

To assess the main effects only, the experimental design was a completely randomized block design to assess the impact of a single factor. Four separate experimental designs were performed to evaluate different factors including wood moisture content, wood type, wood density, and wood state on the heat flux from firebrand piles. In these experimental designs, all variables were kept constant except for the factor being considered. The factor had different treatment levels, which were either a high and low value or a categorical change. The goal of these tests was to determine whether these factors needed to be considered in the full-factorial design which can be time consuming if there are many factors.

To evaluate main effects and their interactions, a full-factorial design was developed based on the four factors expected to influence the heat flux from the firebrand pile. These factors included pile mass, wind speed, firebrand diameter, and firebrand length. For a full-factorial design with four factors ($n = 4$), this requires $2^n = 16$ tests without repeats. For each factor, a high and a low treatment level were chosen. These high and low levels were selected to represent the extremes that would likely be seen in a realistic wildfire scenario, but in some cases were subject to constraints of the test setup.

Moisture Content Study

To assess the impact of starting moisture content on the heat flux from firebrand piles, tests were designed with two moisture content levels (0 and 25%) as shown in **Table 2**. One replication was conducted per level for a total of four tests. Prior to heating, all the firebrands used in this study had length of 12.5 mm, diameter of 9.5 mm, and were made from live Northern Red Oak ($\rho = 870 kg/m^3$) branches. A wind speed of 2.0 m/s was used for all tests. To reduce bias, tests were run in a random order. The moisture content was calculated using

$$MC = \frac{\left(m - m_{dry}\right)}{m_{dry}} \times 100 \tag{3}$$

where m is the mass and m_{dry} is the dry mass. Initially, all firebrands were dried to 0% MC. Firebrands used for the 25% MC tests were rehydrated by storing them in an airtight container filled with damp cloth. The firebrands were turned frequently to ensure even saturation and the total mass was checked periodically until the pile reached the desired moisture content. The rehydration process typically took 24–27 h.

The test details are provided in **Table 2**. The firebrands at 25% MC had to be heated substantially longer to reach self-sustaining combustion, which was attributed to the fact that more energy

TABLE 2 | Test matrix used to assess the impact of starting moisture content factor on the heat flux from firebrand piles. Firebrand diameter 9.5 mm and length 12.5 mm with wind speed 2.0 m/s.

Test	Wood type	Moisture content level (%)	Heating time (s)	Initial firebrand count	Initial wood Mass (g)	Deposited pile Mass (g)
MC1	N. Red Oak	0	30	33	22.0	3.1
MC2	N. Red Oak	0	30	36	21.8	3.1
MC3	N. Red Oak	25	75	27	22.2	3.0
MC4	N. Red Oak	25	75	28	22.4	2.9

was required to also drive off the moisture in the wood before ignition would occur. The number of wood samples used in the testing was determined by preserving the initial mass of wood. The deposited mass is the mass of smoldering firebrands deposited onto the plate and was constant in all tests.

Wood Type Study

Differences exist in the basic cellular structure of hardwoods and softwoods. Char from wood burning is a byproduct in the decomposition of lignin and hemicellulose in the wood with approximately 45% of the lignin mass converted to char and 25% of the hemicellulose converted to char (Yang et al., 2007). Hardwood contains 18–25% lignin and 20–25% hemicellulose while softwood contains 25–30% lignin and 15–20% hemicellulose (Rowell et al., 2012). Based on average values for the lignin and hemicellulose contents, hardwood and softwood would be expected to generate approximately the same amount of char (char fractions of 0.21 and 0.22, respectively). Therefore, differences that may appear in firebrands generated by these types of wood would be attributed to their microstructure or other characteristics.

Hardwoods include many vessel elements that make the wood porous, while softwoods contain an abundance of tracheid cells with no vessels making the wood non-porous (Conners, 2015). Hardwoods come from trees that typically have broad leaves, which they typically loose during autumn, while softwoods are cone bearing trees with needle/scale-like evergreen leaves (Conners, 2015). The sapwood, which the smaller branches are primarily composed from and is on the outside of the trunk and large branches, generally has a higher moisture content in softwood vs. hardwood in living trees. The effects of this higher living tree moisture content was not explored here. Instead, assuming that both types of trees have similar moisture content, the research investigated whether firebrand piles produced from hardwood and softwood trees would result in different heat fluxes to a surface.

This experimental design was developed to have different wood type categorical levels (hardwood and softwood) with similar density. Yellow Poplar ($\rho = 548 kg/m^3$) was selected for the hardwood and Eastern White Pine ($\rho = 586 kg/m^3$) was selected for the softwood. Prior to heating, all the firebrands used in this study had a length of 12.5 mm, diameter of 9.5 mm, and were made from live branches dried to 0% MC. A wind speed of 2.0 m/s was used for all tests. As shown in **Table 3**, each level was repeated in duplicate yielding four total tests with tests run in a randomized order. The number of wood samples used in the testing was determined by preserving the initial mass of wood. The deposited mass is the mass of smoldering firebrands deposited onto the plate and was constant in all tests.

Density Study

The impact of firebrand wood density on pile heat flux has received little attention in the literature. To evaluate the impact of this parameter, tests were performed with hardwood but at different density levels using Yellow Poplar ($\rho = 548 kg/m^3$) and Northern Red Oak ($\rho = 870 kg/m^3$). As before, firebrands used in this study had length of 12.5 mm, diameter of 9.5 mm before heating, and they were made from live branches dried to 0% MC. A wind speed of 2.0 m/s was used for all tests. Each level was repeated in duplicate, yielding four total tests as shown in **Table 4** performed in randomized order. The initial wood mass and deposited pile mass were kept constant during the testing.

Wood State Study

Much of the previous work in the field of firebrand research has used dowels or other commercially-available processed woods to simulate firebrands naturally occurring in wildfires. These "artificial" firebrands typically lack bark, have very consistent sizes, and are made from wood harvested from the trunk of trees instead of the branches. It is unclear how well these artificial firebrands simulate natural results. Tao et. al. (2020) has reported some differences in heat transfer from piles made with natural and artificial firebrands. For cases using natural firebrands, a difference may also exist between firebrands made from living or dead wood.

To explore the impact of firebrand wood state factor, the experimental design included three different categorical levels (artificial, live, and dead) all of the same wood type (Northern Red Oak). Tests at each level was replicated for a total of six tests, shown in **Table 5**. The unburned live ($\rho = 870 kg/m^3$) and dead ($\rho = 664 kg/m^3$) firebrands were collected from different branches of the same Northern Red Oak tree in early autumn when it was easy to distinguish between live and dead tree limbs. The unburned artificial firebrands ($\rho = 627 kg/m^3$) were cut from commercially available Northern Red Oak dowel rods. All firebrands used in this study had length of 12.5 mm, diameter of 9.5 mm prior to heating, and were dried to 0% MC. A wind speed of 2.0 m/s was used for all tests with a randomized run order. The wood mass and applied firebrand mass were kept constant in the study.

TABLE 3 | Test matrix used to assess the impact of firebrand wood type factor on the heat flux from firebrand piles. Firebrand diameter 9.5 mm, length 12.5 mm, and MC 0% with wind speed 2.0 m/s.

Test	Wood type	Categorical level	Heating time (s)	Initial firebrand count	Initial wood Mass (g)	Deposited pile Mass (g)
W1	Yellow poplar	Hardwood	30	49	21.9	3.0
W2	Yellow poplar	Hardwood	30	50	22.1	3.0
W3	E. White pine	Softwood	30	44	22.1	3.1
W4	E. White pine	Softwood	30	45	22.1	3.1

TABLE 4 | Test matrix used to assess the impact of firebrand wood density factor on the heat flux from firebrand piles. Firebrand diameter 9.5 mm, length 12.5 mm, and MC 0% with wind speed 2.0 m/s.

Test	Wood type	Wood density level (kg/m^3)	Heating time (s)	Initial firebrand count	Initial wood Mass (g)	Deposited pile Mass (g)
W1	Yellow poplar	548	30	49	21.9	3.0
W2	Yellow poplar	548	30	50	22.1	3.0
W5	N. Red Oak	870	30	32	22.3	3.1
W6	N. Red Oak	870	30	32	22.1	3.0

TABLE 5 | Test matrix used to assess the effect of firebrand wood state on the heat transfer from firebrand piles. Firebrand diameter 9.5 mm, length 12.5 mm, and MC 0% with wind speed 2.0 m/s.

Test	Wood type	Wood state level	Heating time (s)	Initial firebrand count	Initial wood Mass (g)	Deposited pile Mass (g)
S1	N. Red Oak	Artificial	30	33	22.0	3.1
S2	N. Red Oak	Artificial	30	33	22.0	3.1
S3	N. Red Oak	Natural–Live	30	32	22.1	3.2
S4	N. Red Oak	Natural–Live	30	33	21.9	3.1
S5	N. Red Oak	Natural–Dead	30	40	22.2	3.2
S6	N. Red Oak	Natural–Dead	30	40	21.9	3.1

Full-Factorial Study

The previously described test series have examined the effect of a single factor at different levels on the heat flux from the firebrand pile. While the main effects associated with each factor are important, the interaction between factors may be significant as well and cannot be evaluated using a single factor block design. Recent studies have pointed to a complex influence of pile mass, pile bulk density, and wind speed on the heat transfer from firebrand piles (Hakes et al., 2018; Tao et al., 2020). Pile bulk density is related to pile porosity or the percentage of the pile volume occupied by gases instead of smoldering firebrands. Porosity is of particular interest due to its effect on oxygen availability and reradiation within the pile.

The porosity can be attributed to the packing density of the cylindrical firebrands which has been shown to depend on the aspect ratio ($AR = L/D$) and thus the firebrand length and diameter (Zou et al., 1997; Li et al., 2010). To capture the complexity of this interactions, the factors expected to the have the most significant impact on the heat flux from the firebrand pile (pile mass, wind speed, firebrand diameter, and firebrand length) were evaluated in a series of tests using a 2^n full-factorial experimental design. High and low levels were chosen for each factor and all possible combinations of factor levels were evaluated. The addition of a center point (combination of average levels for each factor) brought the number of tests to 17. The complete test matrix can be found in **Table 6**. All firebrands used in this study were cut from live Northern Red Oak branches and dried to 0% MC. The run order of the tests was randomized. Due to the time required to run the full-factorial test matrix, replication was not feasible.

Analysis

The data produced from the tests described were used to produce heat flux distributions from the firebrand piles with time. Additional processing was conducted on this data to reduce it in size to support determining a single heat flux level that could be used to represent the test, which is necessary for the statistical analysis. The details of the statistical analysis performed on each of the five different experimental designs is also provided below.

Heat Flux Data Processing

The infrared images from the IR Camera were used to generate high resolution maps of the heat flux through time. Each pixel corresponded to a 0.44 mm × 0.45 mm area on the underside of the 304 SS plate. Since the pile diameter was 50 mm there were ~9,900 pixels per image representing a discrete location under the

TABLE 6 | Full-factorial test matrix used to assess the effect of unburned firebrand length and diameter, pile mass, and wind speed on the heat transfer from firebrand piles from live N. Red Oak branches.

Test	Unburned firebrand length (mm)	Unburned firebrand diameter (mm)	Pile Mass (g)	Wind speed (m/s)	Heating time (s)	Initial firebrand count	Initial wood Mass (g)	Actual deposited pile Mass (g)
FF1	12.50	4.75	1.50	0.0	12	65	11.0	1.6
FF2	50.00	4.75	1.50	0.0	15	14	11.3	1.6
FF3	12.50	9.50	1.50	0.0	15	17	11.0	1.6
FF4	50.00	9.50	1.50	0.0	30	4	11.0	1.6
FF5	12.50	4.75	3.00	0.0	30	126	22.1	3.0
FF6	50.00	4.75	3.00	0.0	30	29	22.0	2.9
FF7	12.50	9.50	3.00	0.0	30	35	22.2	3.1
FF8	50.00	9.50	3.00	0.0	30	8	22.2	3.1
FF9	12.50	4.75	1.50	2.0	15	60	11.1	1.4
FF10	50.00	4.75	1.50	2.0	15	15	11.1	1.6
FF11	12.50	9.50	1.50	2.0	15	17	11.0	1.6
FF12	50.00	9.50	1.50	2.0	30	4	11.0	1.6
FF13	12.50	4.75	3.00	2.0	30	127	22.0	3.0
FF14	50.00	4.75	3.00	2.0	30	28	21.9	2.9
FF15	12.50	9.50	3.00	2.0	30	33	22.3	3.1
FF16	50.00	9.50	3.00	2.0	30	8	22.6	3.2
FF17	31.25	7.13	2.25	1.0	22.5	16	16.4	2.3

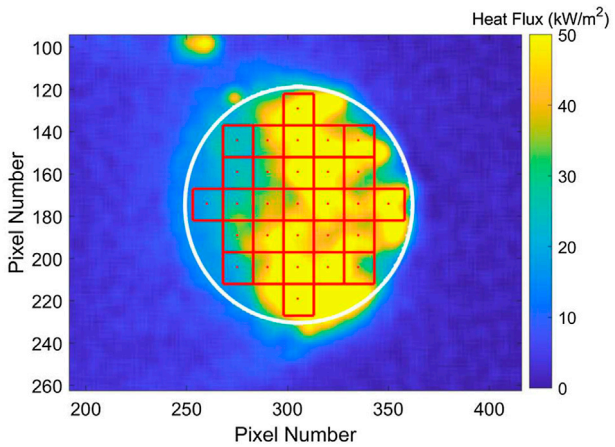

FIGURE 3 | 6.6 mm × 6.75 mm grids (shown in red) lying totally within the bounds of the 50 mm circular pile (shown in white).

pile. While this high spatial resolution is valuable for visualizing the distributed heat fluxes under the pile, it is unlikely that the ~0.5 mm length scale is relevant to ignition. High heat flux into a single 0.44 mm × 0.45 mm surface element would quickly dissipate through lateral conduction if the surrounding material were at a lower temperature. Conversely, taking the average flux under the entire pile with time would dilute higher measured values and may under-predict ignition. To remedy this length-scale issue, the pixels under each pile were divided into twenty-nine 6.6 mm × 6.75 mm (15 × 15 pixel) grids that were totally within the pile boundaries, as shown in **Figure 3**. The grid array was centered on the pile and grids lying even slightly outside the pile were not considered. This produced 29 different time-temperature heat flux plots. However, the statistical evaluation required a single heat flux value for each test (response). The determination of a single heat flux to represent a test is discussed in the Results section.

Statistical Analysis

Three different experimental designs were used in these studies: one factor with two treatment levels, one factor with three treatment levels, and full-factorial (four factors and two treatment levels). For all cases, the objective of the statistical analysis was to determine whether the factor or interaction of factors in question significantly affected the heat flux from the firebrand piles.

One Factor, Two Treatment Levels

The analysis of the experimental designs with one factor (moisture content, wood type, or density) and two different treatment levels (high and low or categorical) was conducted using one-way analysis of variance (ANOVA) to assess whether there was a statistically significant difference in the mean, μ, of the two treatment levels. Analysis was conducted using Minitab v.19 software at the 95% confidence level ($\alpha = 0.05$) and equal variance was assumed between factors. The null hypothesis, H_0, was that there was no significance between μ_1 and μ_2 and was rejected for p-values < 0.05 (i.e., 95% confidence level that the means are statistically the same). Treatments where the null hypothesis were rejected were assumed to have an effect on the heat flux from firebrand piles. The null and alternate (H_a) hypotheses are

$$H_0 : \mu_1 = \mu_2; H_a : \mu_1 \neq \mu_2 \quad (4)$$

One Factor, Three Treatment Levels

For the tests with one factor (wood state) and three treatment levels (artificial, live, dead), Fisher's Least Significant Difference

(LSD) method was chosen to conduct the pairwise comparison on the categorical treatment level means (μ_1, μ_2, μ_3) in Minitab v.19. Fisher's method is essentially a set of individual t-tests but uses the pooled standard deviation and is more powerful than conservative techniques such as Tukey's method. The Type I error rate is set for each individual contrast and does not take into account that the same data is used for multiple comparisons. A 95% confidence level was specified for each of the individual contrasts, meaning that the simultaneous confidence level for the comparison as a whole was 90.17%. The null and alternate hypotheses for experimental design with three treatment levels are

$$H_0 : \mu_1 = \mu_2 = \mu_3; H_a : At\ least\ one\ mean\ significantly\ different \tag{5}$$

Full-Factorial Design (Four Factors, Two Treatment Levels) The full-factorial design was developed to simultaneously evaluate the four independent factors (wind, pile mass, firebrand diameter, and firebrand length) and all interactions between factors with each factor at two treatment levels (a high and low value) through a series of $2^n = 16$ tests. A main effect was defined as the effect on the response (heat flux from the firebrand pile) caused by one of the four independent factors (e.g., heat flux increased with increasing wind). An interaction was defined as the impact on the response by a combination of two or more independent factors (e.g., wind and pile mass; diameter, length, and wind, etc.). Four-way analysis of variance (ANOVA) was used to assess whether each main effect or interaction had a significant effect on the pile heat transfer. For each term, the null hypothesis was that there was no effect; p-values < 0.05 indicated that the null hypothesis should be rejected, and the term significantly impacted the pile heat flux. The center point was not included in the model.

RESULTS

Select experimental data produced in this study is provided in this section along with the statistical analysis of this data. An overview of the data produced from individual tests is first provided along with an analysis to determine the appropriate response variable for the statistical analysis (i.e., a single heat flux value to represent the test). In addition, the repeatability of the test is assessed. Using this response variable, statistical analysis was performed on the different experimental designs to determine the impact of the different factors on the firebrand pile heat flux.

Data Overview

The data for the tests consisted of the average flux within each of the 29 grids at every point in time. **Figure 4** contains plots of heat flux at each grid as well as the mean heat flux for all grids with time for tests with no wind and 2.0 m/s wind speed.

The plots illustrate a trend seen in much of the data where the highest heat fluxes were measured early in the test and then the heat fluxes decreased with time as the firebrands burned out. In general, the effects of wind seen in **Figure 4** are indicative of the trends in the data collected in this study. Tests with no wind have lower heat fluxes but longer exposure durations, while the 2.0 m/s wind speed tests resulted in heat fluxes 2–3 times higher but shorter burning durations.

In the statistical analysis, only a single value for the response variable (heat flux) can be used to represent the heat flux for the firebrand pile test. Since this data will be used to assess whether a firebrand pile may cause material ignition, the selected heat flux must represent the high end of the values with space and time. For the spatial variation, a percentile approach was adopted. The 75th percentile of all of the heat flux data was selected since this heat flux would be a level that would bound 75% of all of the measured heat fluxes for a pile. An example of this is shown in **Figure 5** for the 120 s average heat flux for the same tests in **Figure 4**. The histogram represents the frequency of grids at that range of heat flux while the cumulative distribution function (CDF) represents the likelihood (percentile divided by 100) that this heat flux would occur. Since the likelihood is the percentile divided by 100, the 75th percentile would be the heat flux corresponding to a likelihood of 0.75 on the CDF line. For the data shown in **Figure 5**, the 75th percentile heat flux would be 13.8 kW/m^2 for the no wind case and 39.7 kW/m^2 for the 2.0 m/s wind case. To include time, different averaging times were considered based on averaging times used in standard material fire testing such as the cone calorimeter. The results of the different averaging times are provided in **Figure 6** for both no wind and 2.0 m/s wind speed tests in the full-factorial test matrix, where heat fluxes are the 75th percentile values for each of the averaged quantities. Based on these data, the test average is generally low while the peak values are high compared with the other averages, so these values were not used. The 120 s average heat flux represents a value between the 60 s average, which corresponds to the early time higher heat flux levels, and the longer averaging times which can be skewed low due to firebrand burnout (as seen in **Figure 4**). As a result, the response variable used in the statistical analysis was the 75th percentile value of the 120 s average heat fluxes for all grids in the test.

The repeatability of the tests was quantified through comparing results of the same test that was performed seven separate times during this study. In these tests, the pile had a mass of 3.0 g and was composed of firebrands with a diameter of 9.5 mm, length of 12.5 mm, and 0% MC. Tests were conducted with a wind speed of 2.0 m/s. The mean heat flux for all grids with time in the repeat tests is provided **Figure 7**, showing that the heat flux had a similar magnitude and trend in all tests. In addition, the 75th percentile average and peak heat fluxes are provided in **Figure 7** along with error bars corresponding to the standard deviation in the data. These results further demonstrate the similarity in results between the repeat tests. For the 120 s average heat flux, the standard deviation in the repeat test data was 3.6 kW/m^2.

Statistical Analysis of Single Factor Data

Statistical analysis was conducted to evaluate the performance of select single factors including moisture content, wood type, wood density, and wood state. The focus of this analysis was to

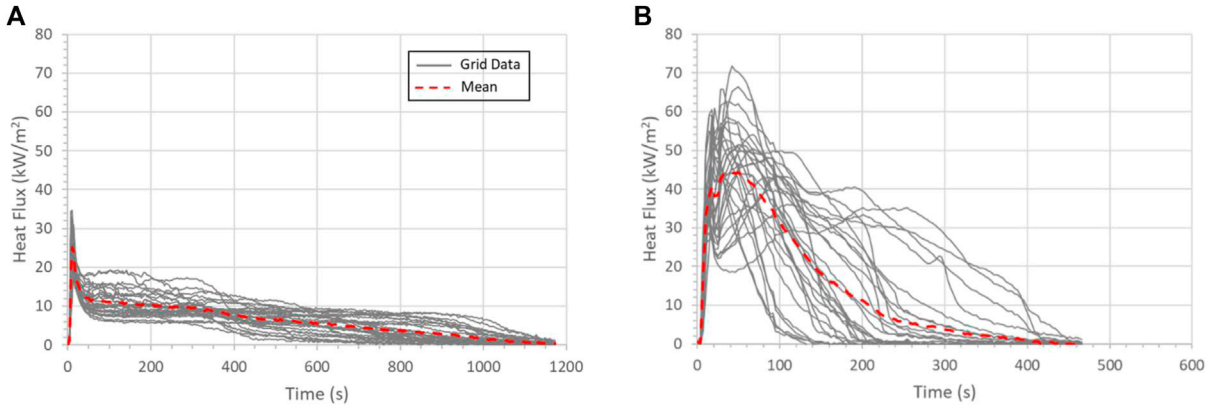

FIGURE 4 | Sample grid heat flux data with time for **(A)** FF6 with no wind and **(B)** FF14 with 2.0 m/s wind. Tests had a pile mass of 3.0 g containing firebrands with a diameter 4.75 mm, length 50 mm, and 0% MC.

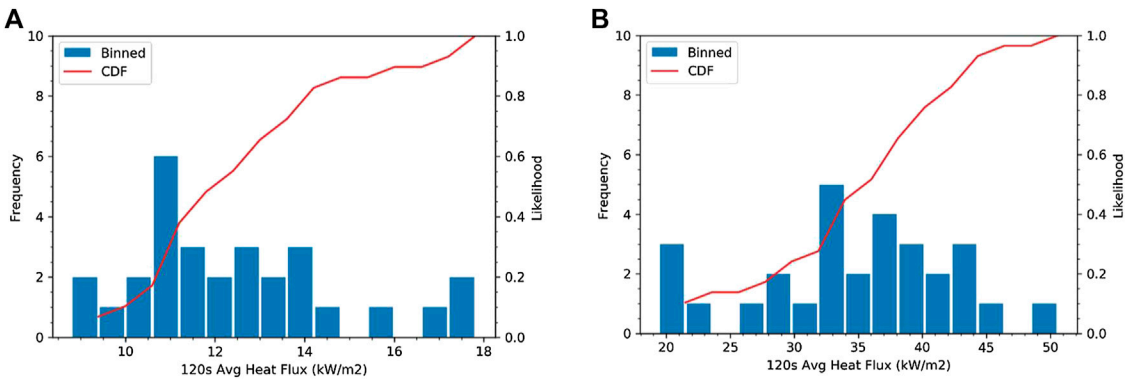

FIGURE 5 | Histogram of 120s average heat flux along with CDF for data from test **(A)** FF6 with 0 m/s wind and **(B)** FF14 with 2.0 m/s of wind. Tests had a pile mass of 3.0 g containing firebrands with a diameter 4.75 mm, length 50 mm, and 0% MC.

determine which factors had an impact on the heat flux from a firebrand pile. The results from the tests on the different factors are provided in **Figure 8**. Heat fluxes are the 75th percentile of the 120 s average heat fluxes at all grids. Each bar represents the mean from the two tests at level while the error bars correspond to the population estimated 95% confidence interval.

The impact of starting moisture content of the unburned firebrands were statistically analyzed using the one-way ANOVA with the results summarized in **Table 7** and **Figure 8A**. Piles made from firebrands with a starting moisture content of 0% were found to have a mean heat flux of 33.4 kW/m^2, while piles made from firebrands with 25% starting MC were found to have a mean heat flux of 38.8 kW/m^2 with a population estimated 95% confidence interval of ±4.76 kW/m^2. The resulting p-value of 0.075, indicates that this difference does not meet the threshold for statistical significance. As a result, the null hypothesis could not be rejected, and it was concluded that firebrand starting moisture content does not have a significant impact on firebrand pile heat flux. This result was somewhat expected since the moisture was believed to be driven off during burning to form the firebrand.

The significance of wood type (hardwood and softwood) on the heat flux from firebrand piles is summarized through the data and statistical results provided in **Table 8** and **Figure 8B**. The mean heat flux from firebrand piles made with hardwood firebrands was found to be 39.3 kW/m^2 while the mean for the piles with softwood firebrands was 45.4 kW/m^2 with a population estimated 95% confidence interval of ±15.1 kW/m^2. This higher confidence interval was due to the higher standard deviation measured in these tests. The resulting p-value of 0.346 means the null hypothesis could not be rejected. It was therefore concluded that firebrand wood type does not significantly affect heat transfer from firebrand piles.

The density study used two types of hardwood firebrands with different unburned dry densities to evaluate whether this parameter influenced heat flux from firebrand piles. A summary of the data are contained in **Figure 8C** while the statistical results are provided in **Table 9**. It was found that for low density wood (Yellow Poplar, $\rho = 548 kg/m^3$) the mean heat flux value was 39.3 kW/m^2. The high-

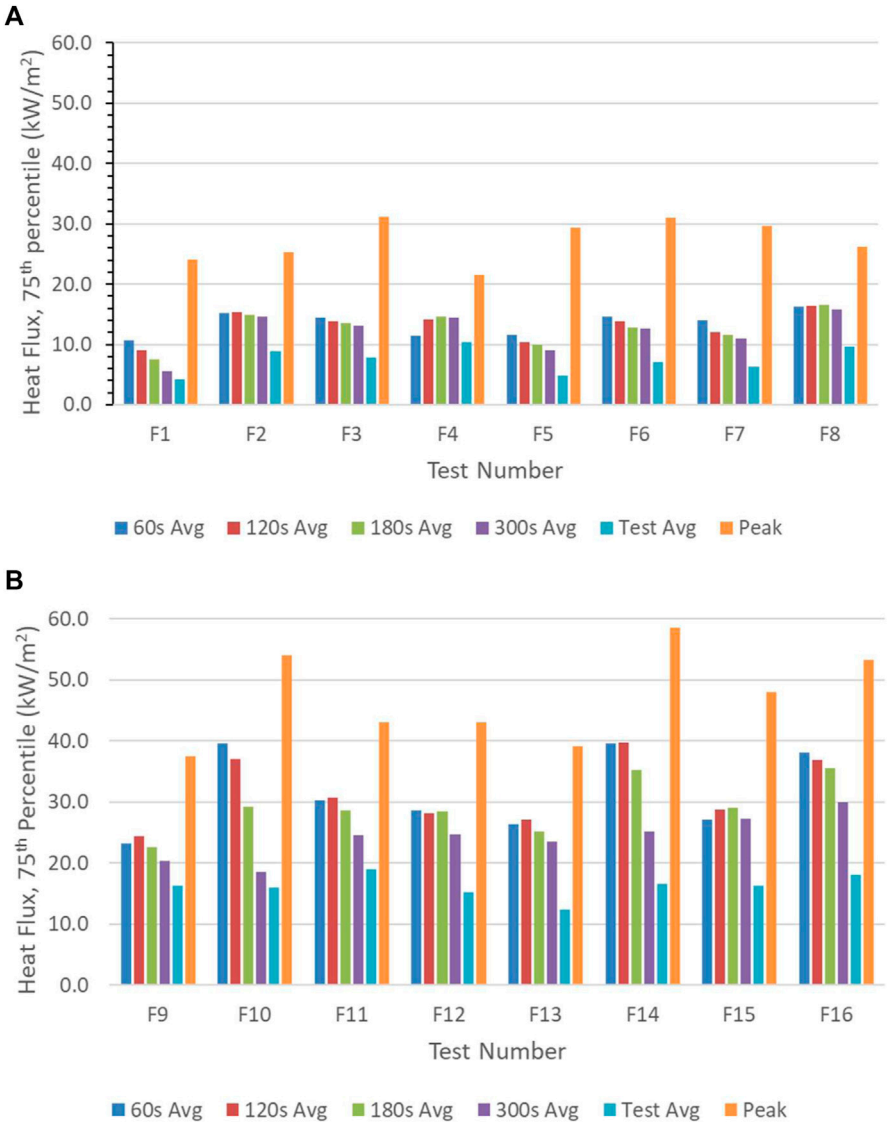

FIGURE 6 | The 75th percentile heat flux over different average times and for the peak with **(A)** a wind speed of 0 m/s and **(B)** with a 2.0 m/s wind speed for all the full-factorial tests.

density wood (N. Red Oak, $\rho = 870 kg/m^3$) had a mean heat flux of 34.33 kW/m^2 with a population estimated 95% confidence interval of ±10.44 kW/m^2. The p-value was 0.286, an order of magnitude higher than the 0.05 threshold for significance. For this reason, the null hypothesis could not be rejected, and it was concluded that firebrand wood density does not significantly affect the heat transfer from firebrand piles.

The wood state study was an experimental design with three treatment levels (live, dead, or artificial) used to assess the impact on the heat flux from firebrand piles. A summary of the data are provided in **Figure 8D** with statistical analysis results using Fisher's technique contained within **Table 10**. Fisher's technique is used in this case since there are three treatment levels. The output of Fisher's Pairwise Comparison is the ordered letter report. Treatment levels that do not share a letter have significantly different means. As seen in **Table 10**, piles made with artificial firebrands have a mean heat flux value of 48.9 kW/m^2 which is significantly different the mean value of 36.3 kW/m^2 for piles consisting of live firebrands and 35.7 kW/m^2 for piles consisting of dead firebrands. The estimated population 95% confidence interval was determined to be 7.98 kW/m^2. The ordered letter report confirms that no significant difference exists between piles made of live and dead firebrands. Fisher's method also gives the p-values for the simultaneous test of the difference in treatment level means, shown in **Table 11**. The null hypothesis for each test is that there is no significant difference between treatment means.

Statistical Analysis of Full-Factorial Data

The full-factorial experimental design was used to assess the impact of the factors and their interactions on the heat flux from

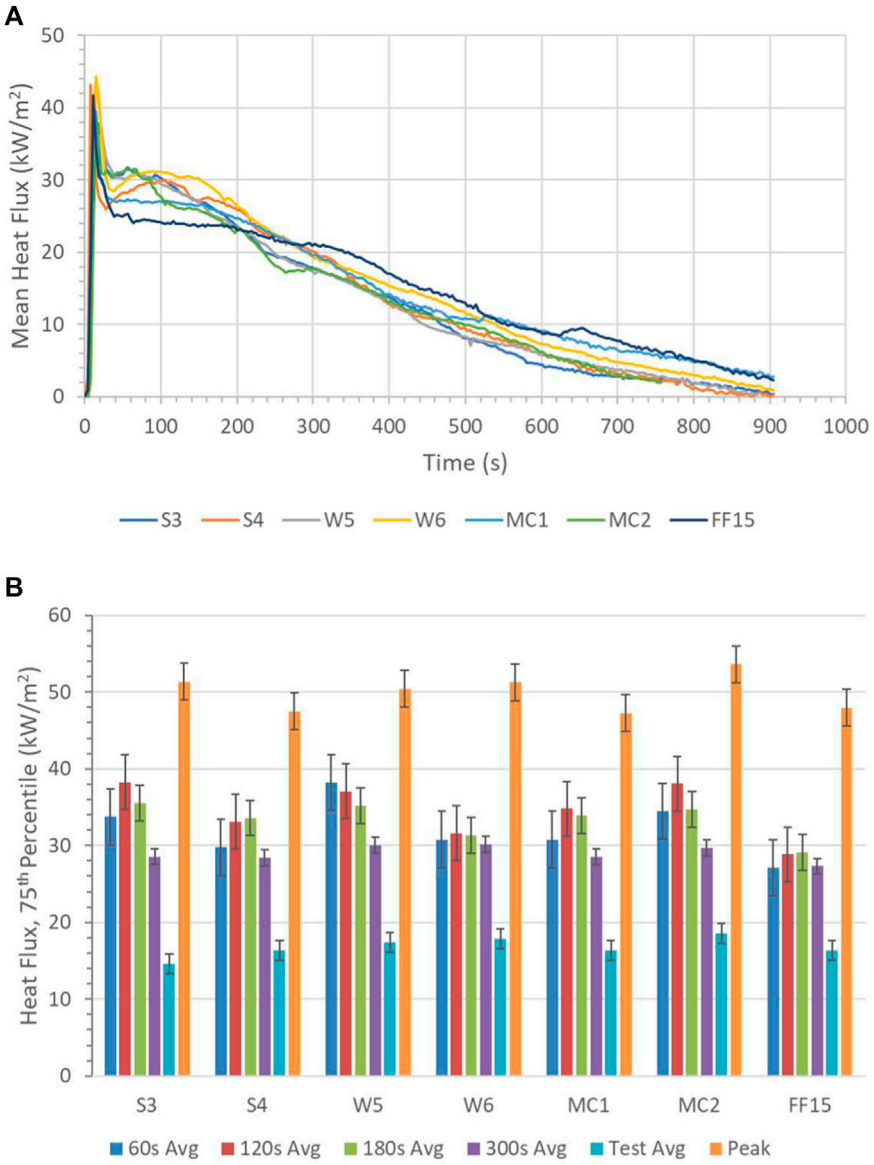

FIGURE 7 | Repeat test **(A)** mean heat flux with time and **(B)** 75th percentile average heat fluxes. Pile had a mass of 3.0 g with firebrands having a diameter of 9.5 mm, length of 12.5 mm, and 0% MC with a wind speed of 2.0 m/s.

firebrand piles. Results from the four-way ANOVA analysis on the data are shown in **Figure 9**. The Pareto chart of the standardized effects contained in **Figure 9A** illustrates the impact of each term ranked from largest to smallest with the threshold for statistical significance denoted by the red dashed line. The standardized effects are t-statistics used to test the null hypothesis that the term has no effect, with larger t-statistics corresponding to smaller p-values. The main effects are denoted by A, B, C, or D for firebrand length, firebrand diameter, pile mass, and wind, respectively. Interactions are denoted using the appropriate combination of letters. The normal plot in **Figure 9B** provides insight on the impact of the effect on the response with the red line corresponding to the response if the effect from all main effects and interactions were zero. Values positive relative to the line are effects that cause an increase in the response while negative values cause a decrease in response. The only parameter in the plot to be sufficiently far from the red line to be statistically significant is wind and since wind is on the positive side of this line increasing the wind speed is expected to increase the heat flux. From the plots in **Figure 9**, wind was determined to be the only statistically significant factor with firebrand length being the next most significant.

To improve the model, insignificant high-order interactions can be removed and the model redeveloped. In physical systems, high-order interactions consisting of three or more terms are rarely physically significant. The Pareto chart in **Figure 10A**,

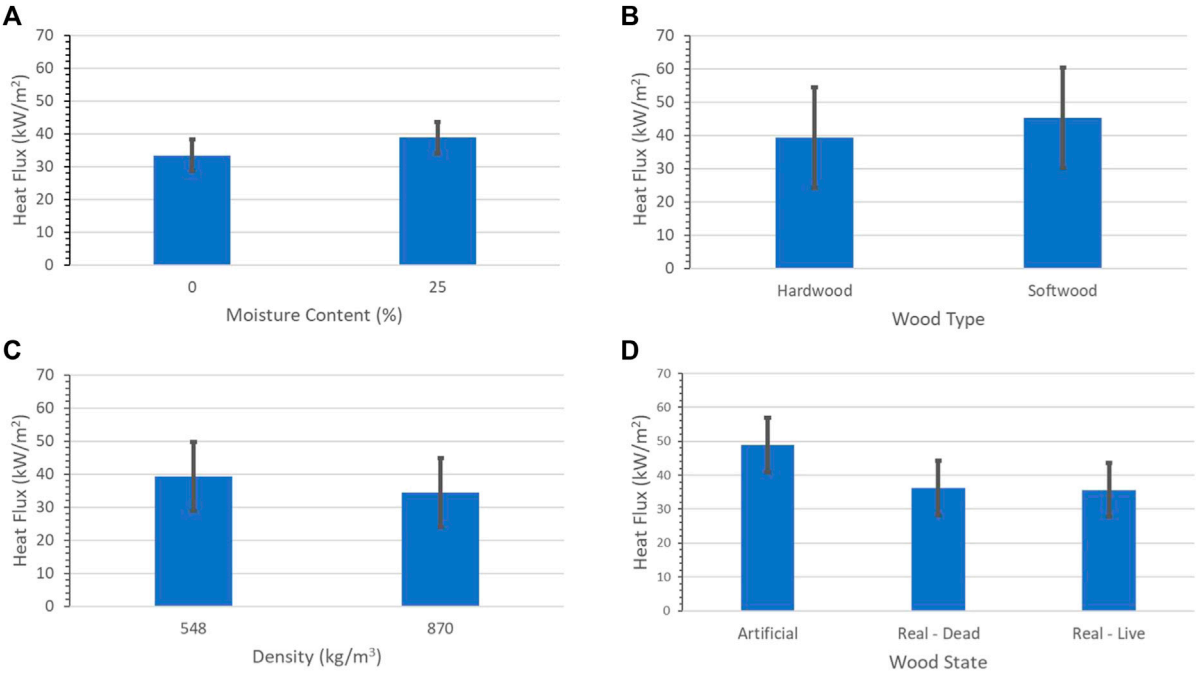

FIGURE 8 | Results from the experimental designs to evaluate the impact of single factors **(A)** moisture content, **(B)** wood type, **(C)** wood density, and **(D)** wood state. Error bars correspond to 95% confidence intervals.

TABLE 7 | Summary of the statistical analysis of the effect of starting moisture content of unburned firebrands on the heat transfer from firebrand piles.

% MC	Mean (kW/m^2)	σ(kW/m^2)	N	Hypotheses	p-value	Conclusions
0% 25%	33.4 38.8	1.93 1.07	2 2	$H_0 : \mu_1 = \mu_2$, $H_a : \mu_1 \neq \mu_2$	0.075	Fail to reject H_0. Starting moisture content does not affect heat transfer from firebrand piles

TABLE 8 | Summary of the statistical analysis of the effect of firebrand wood type on the heat transfer from firebrand piles.

Wood type	Mean (kW/m^2)	σ(kW/m^2)	N	Hypotheses	p-value	Conclusions
Hardwood Softwood	39.3 45.4	2.93 6.39	2 2	$H_0 : \mu_1 = \mu_2$, $H_a : \mu_1 \neq \mu_2$	0.346	Fail to reject H_0. Wood type does not affect heat transfer from firebrand piles

TABLE 9 | Summary of the statistical analysis of the effect of unburned firebrand dry density on the heat transfer from firebrand piles.

Wood dry density (kg/m^3)	Mean (kW/m^2)	σ(kW/m^2)	N	Hypotheses	p-value	Conclusions
548 870	39.3 34.3	2.93 3.87	2 2	$H_0 : \mu_1 = \mu_2$, $H_a : \mu_1 \neq \mu_2$	0.286	Fail to reject H_0. Wood density does not affect heat transfer from firebrand piles

shows that the fourth order interaction between length, diameter, mass, and wind (ABCD) does not appear to be important. The same is true for the length-mass-wind (ACD) and diameter-mass-wind (BCD) third order interactions. These terms were removed, and the statistical analysis was conducted again. Results are shown in **Figure 10** for the refined model with three terms now being predicted to be statistically significant: wind (D), firebrand length (A), and the length-diameter interaction (AB). The main effects of pile mass (C) and firebrand diameter (B) were found to have a statistically insignificant impact on the heat flux;

TABLE 10 | Summary of the statistical analysis of the effect of wood state on the heat flux from firebrand piles.

Wood State	Mean (kW/m^2)	σ(kW/m^2)	N	Ordered letter report	Hypotheses	Conclusions
Artificial	48.9	2.96	2	A	$H_0 : \mu_1 = \mu_2 = \mu_3 H_a$: *At least one mean significantly different*	Reject H_0. Heat transfer from piles made with artificial firebrands is significantly different from piles made from live or dead firebrands. No significant difference exists in heat transfer between piles made with live and dead firebrands
Live	36.3	3.98	2	B		
Dead	35.7	3.63	2	B		

TABLE 11 | Fisher's individual tests for difference of means from wood state statistical analysis.

Difference of treatment levels	Difference of means (kW/m^2)	Adjusted p-value	Conclusion
Dead–artificial	−12.63	0.038	Artificial and dead firebrands result in significantly different heat transfer
Live–artificial	−13.20	0.034	Artificial and live firebrands result in significantly different heat transfer
Live–dead	−0.58	0.881	No significant difference in heat transfer between live and dead firebrands

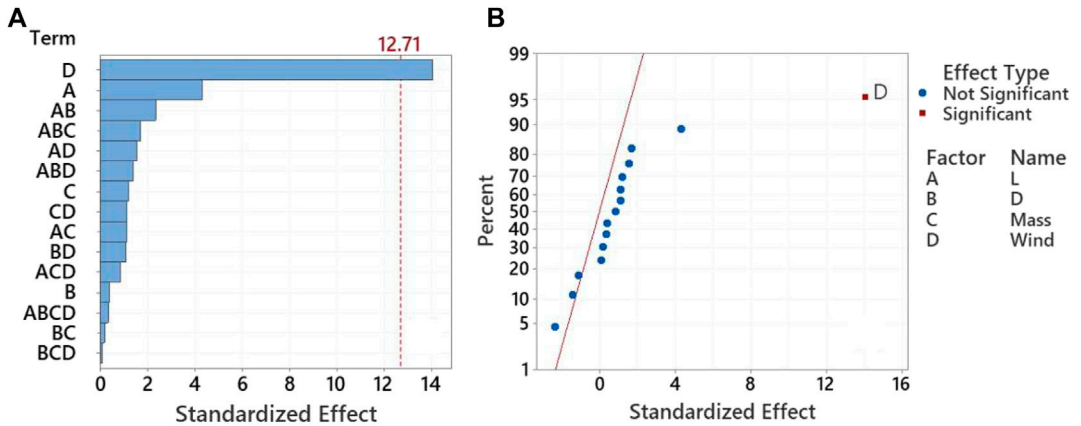

FIGURE 9 | Pareto chart **(A)** and normal plot **(B)** for the full factorial tests with all terms included.

however, firebrand length, firebrand diameter and mass (ABC) was nearly statistically significant. From the normal plot in **Figure 10B**, the wind and firebrand length are both statistically significant and an increase in the factors will result in an increase in the heat flux. The firebrand length-diameter (AB) interaction was also found to be significant but increasing this value results in a decrease in heat flux.

In addition to providing the statistical significant terms as well as their relative importance, the statistical analysis of the full-factorial data also provides a linear regression fit of the data based on the terms. The linear regression fit to predict the 75th percentile of the 120 s average heat flux is

$$\begin{aligned} q''_{120s,75\%} = &-7.87 + 0.616\,L + 3.06\,D + 5.32\,m + 2.87\,U \\ &- 0.0896\,LD - 0.185\,Lm + 0.2005\,LU - 0.973\,Dm \\ &+ 0.337\,DU + 0.999\,mU + 0.0335\,LDm - 0.0205\,LDU \end{aligned} \quad (6)$$

where L is the firebrand length (mm), D is the firebrand diameter (mm), m is the applied firebrand pile mass (g), and U is the wind speed (m/s). This equation has an R-squared value of 0.992 but is only valid over the range of the variables tested.

Firebrand Pile Heat Flux Distributions

Statistical analysis was performed using a single response value (i.e., 75th percentile of the 120 s average heat flux). As previously seen, the heat fluxes across the pile are non-uniform and change with time. To better observe these changes, heat flux distributions at different snapshots in time were created for select tests listed in **Table 12**. This table includes the factors considered in the full-factorial study as well as the firebrand aspect ratio as well as the pile porosity. The pile porosity (ratio of the volume of air in the pile to the total pile volume) was calculated using correlations from Ref. (Zou and Yu, 1996). for a loosely packed pile cylinders and is dependent only on the firebrand aspect ratio. The minimum porosity for loosely packed cylinders is 0.40 while

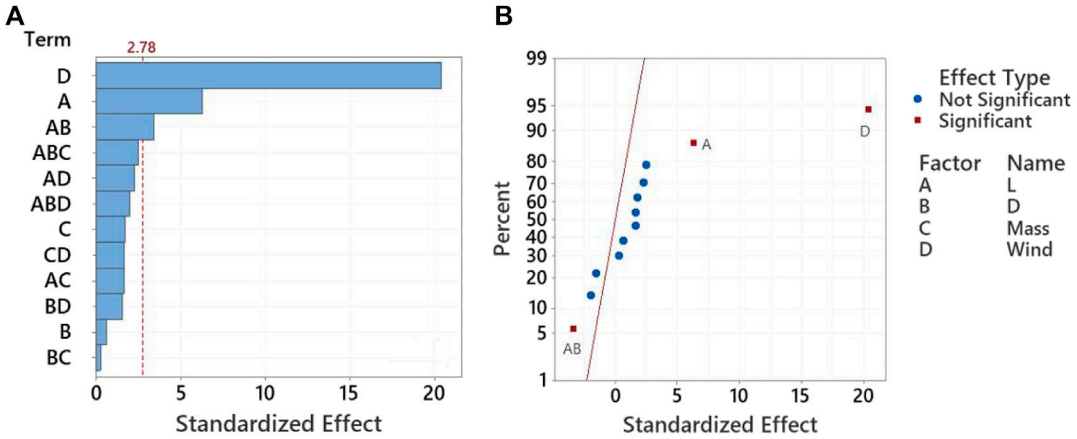

FIGURE 10 | Pareto chart **(A)** and normal plot **(B)** for the full factorial tests with ABCD, ACD, and BCD terms removed.

TABLE 12 | Tests to compare the effects of different firebrand pile parameters on the heat flux distribution with time.

Test	Firebrand diameter, *D* (mm)	Firebrand length, *L* (mm)	Firebrand aspect ratio, *AR* = *L*/*D* (– –)	Pile porosity (– –)	Pile Mass, *m* (g)	Wind speed, *U* (m/s)
FF6	4.75	50.0	10.5	0.61	3.0	0.0
FF10	4.75	50.0	10.5	0.61	1.5	2.0
FF13	4.75	12.5	2.6	0.43	3.0	2.0
FF14	4.75	50.0	10.5	0.61	3.0	2.0
FF16	9.5	50.0	5.3	0.49	3.0	2.0

the maximum porosity goes to 1.0 (all air). As seen in the table, decreasing the aspect ratio of the firebrands decreases the pile porosity resulting in less air volume in the pile.

These tests were selected to highlight the trends observed in the statistical analysis to further demonstrate the impact of these factors on the heat flux from the firebrand pile. For this, tests were selected where only one of the factors was changed and all other factors remained constant. This included the effects of wind speed (FF6 and FF14), pile mass (FF10 and FF14), firebrand length (and aspect ratio) (FF13 and FF14), and firebrand diameter (FF14 and FF16). The different heat flux distributions at different snap shots in time are provided in **Figures 11–15** with all figures having the same color scaling for heat flux magnitude. In all tests, the wind is applied on the right hand side (upstream side) of the firebrand pile.

DISCUSSION

The full-factorial study highlighted factors that were statistically important and ranked them in order of importance based on the 75th percentile 120 s average heat flux. The results from the statistical analysis were compared with the heat flux distribution data measured for the firebrand piles as different snapshots in time to further evaluate the impact of these factors.

The effects of wind speed on the heat flux can be seen through comparing the FF6 test with no wind in **Figure 11** to the FF14 test with 2.0 m/s of wind in **Figure 14**. All other factors were constant. The time data for these tests at each grid location (not shown in these figures) is also provided in **Figure 4**. In the test with no wind (**Figure 11**), the heat flux was relatively uniform over the pile and remained constant over the times shown. Tests with 2.0 m/s of wind (**Figure 14**) had a more non-uniform distribution with the highest heat fluxes on the side where the wind was applied. With time, this high heat flux region migrated from right to left which corresponded to the firebrands being consumed on the upstream side of the pile which allowed downstream firebrands to be exposed to higher wind velocities and more intense burning. Though these firebrand piles had the same mass, the one with no wind was burned for 1,170 s while the one with 2.0 m/s of wind burned for only 465 s. Clearly, wind speed has an impact on the heat flux from the firebrand pile which supports the findings of the statistical analysis as this being the most significant factor.

The impact of firebrand length on the heat flux distribution is seen by comparing Test FF13 in **Figure 13** where the length was 12.5 mm with Test FF14 in **Figure 14** where the length was 50.0 mm. This also provides a comparison of the effect of aspect ratio, which dictates the pile porosity (or volume of air within the pile). All other factors were constant. Test FF13 had an aspect ratio of 2.6 and low porosity (0.43) while Test FF14 had an aspect ratio of 10.5 and high porosity (0.61). Test FF13 (shorter length, lower aspect ratio, and lower pile porosity) had high heat fluxes at the upstream side of the firebrand pile. However, these high heat fluxes were only measured to be present along the perimeter of

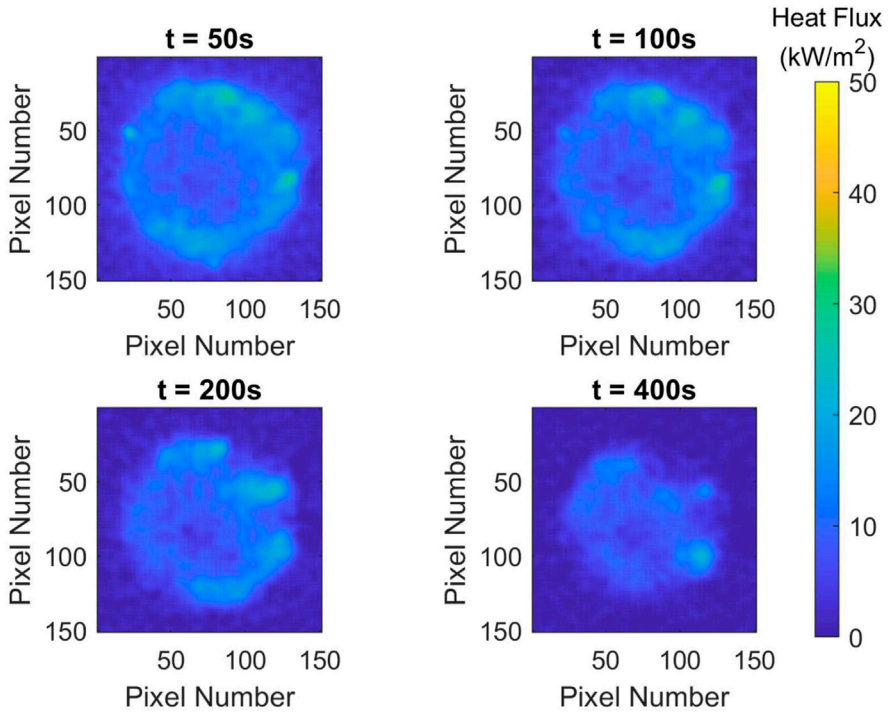

FIGURE 11 | Heat flux distribution for test FF6 at different times. Firebrands: D = 4.75 mm, L = 50.0 mm, and AR = 10.5; Pile mass of m = 3.0 g; Wind speed: U = 0.0 m/s.

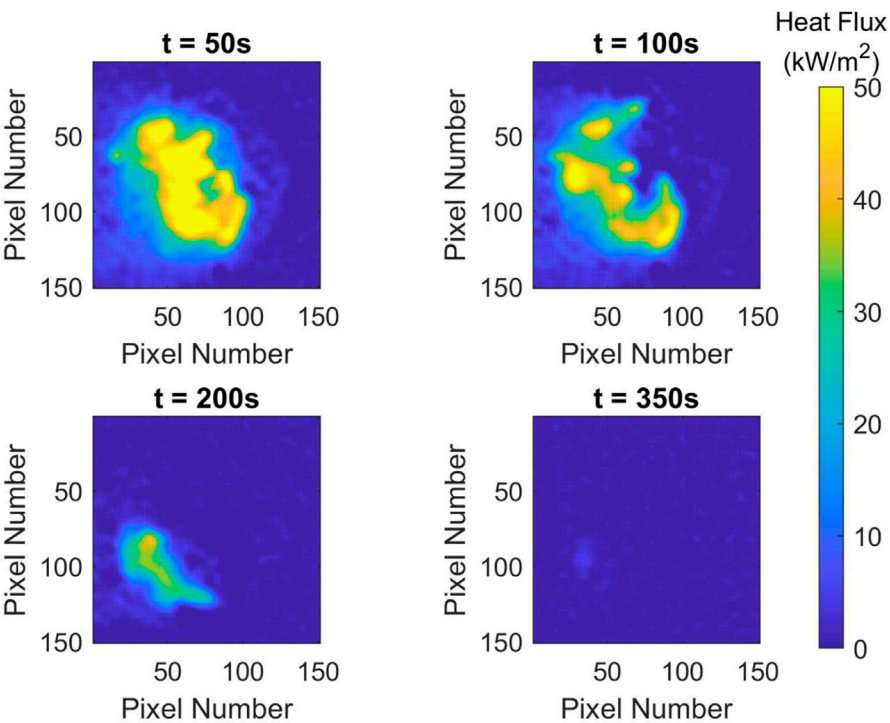

FIGURE 12 | Heat flux distribution for test FF10 at different times. Firebrands: D = 4.75 mm, L = 50.0 mm, and AR = 10.5; Pile mass of m = 1.5 g; Wind speed: U = 2.0 m/s.

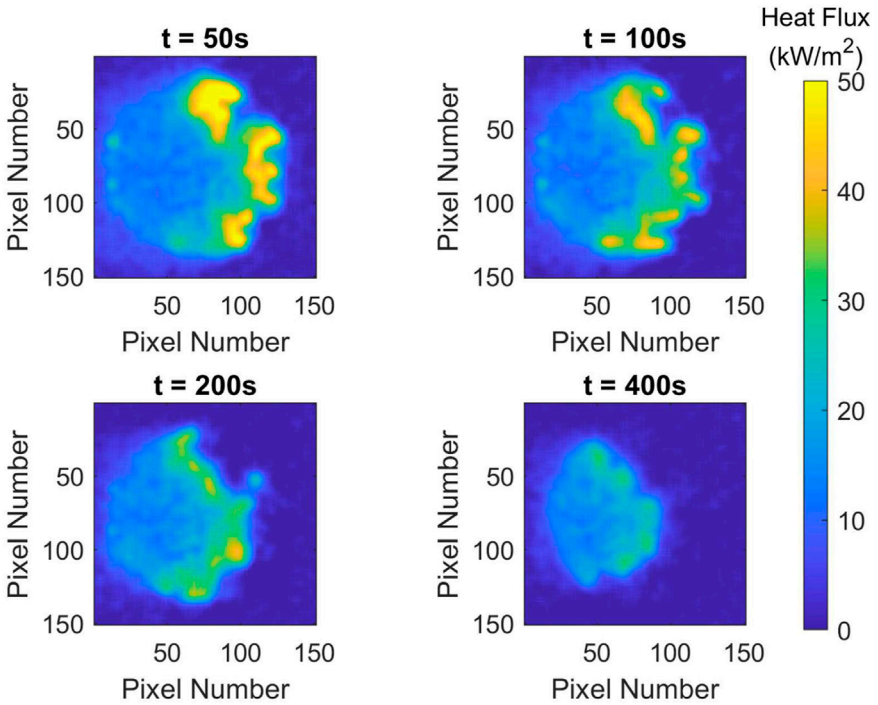

FIGURE 13 | Heat flux distribution for test FF13 at different times. Firebrands: D = 4.75 mm, L = 12.5 mm, and AR = 2.6; Pile mass of m = 3.0 g; Wind speed: U = 2.0 m/s.

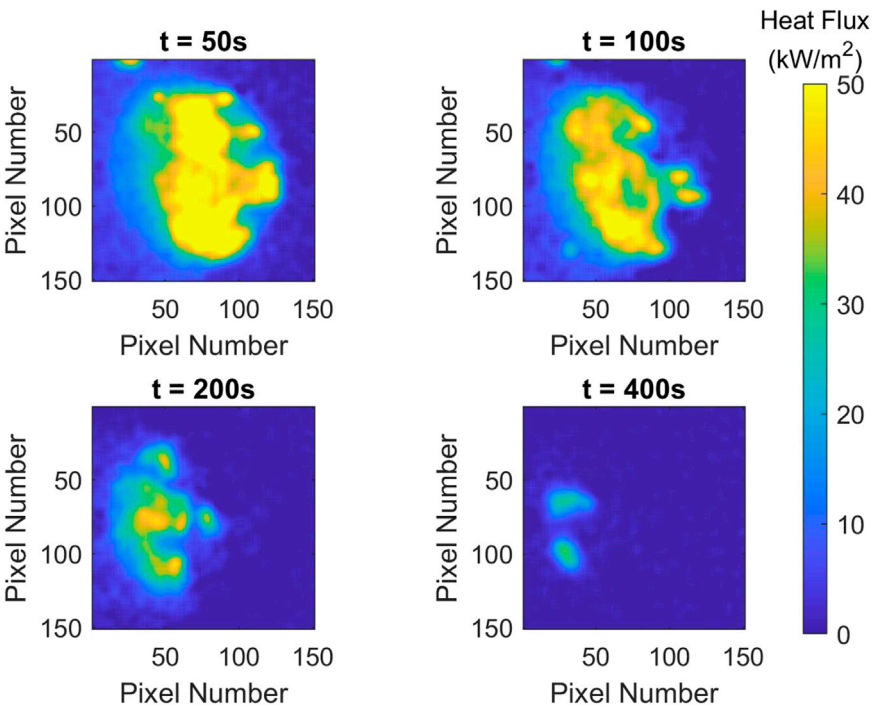

FIGURE 14 | Heat flux distributions for test FF14 at different times. Firebrands: D = 4.75 mm, L = 50.0 mm, and AR = 10.5; Pile mass of m = 3.0 g; Wind speed: U = 2.0 m/s.

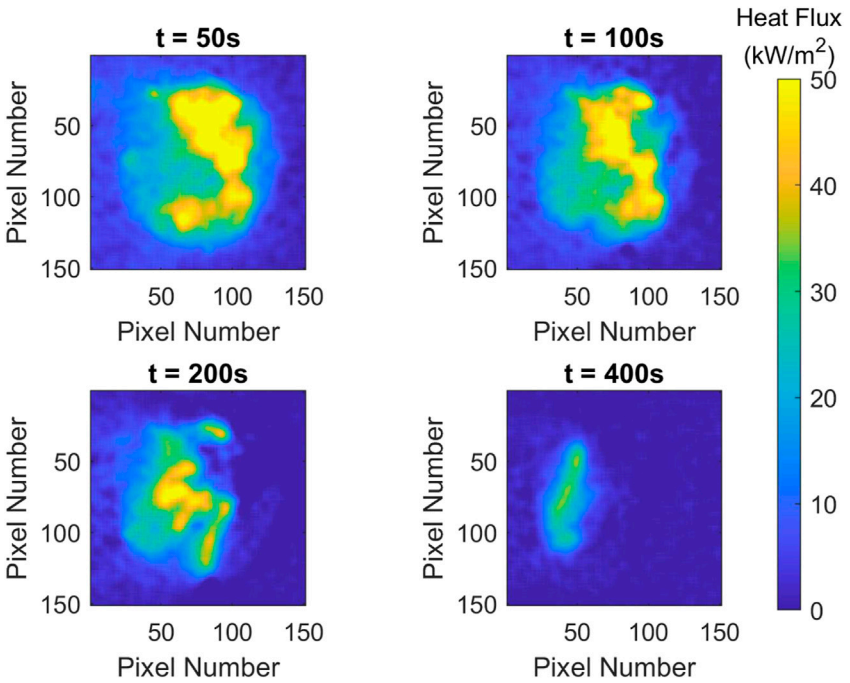

FIGURE 15 | Heat flux distribution for test FF16 at different times. Firebrands: D = 9.5 mm, L = 50.0 mm, and AR = 5.3; Pile mass of m = 3.0 g; Wind speed: U = 2.0 m/s.

the pile with low heat fluxes in the pile downstream of the where the wind was introduced. With time, the pile reduced in size as firebrands were consumed, but the highest heat fluxes always existed at the upstream perimeter with lower heat fluxes downstream. In Test FF14 (longer length, higher aspect ratio and higher porosity pile), the wind was able to penetrate into the pile more compared with Test FF14 resulting in a larger band of high heat fluxes across the upstream portion of the firebrand pile. As a result, the firebrand pile in Test FF14 (465 s) was consumed faster compared with Test FF13 (1,205 s) despite both piles having the same mass. These results confirm that firebrand length has a significant impact on the heat fluxes, which confirms the statistical analysis that had this as the second most important parameter. In addition, these tests also demonstrate the importance of aspect ratio (pile porosity) on the heat flux distribution in the pile. Aspect ratio was not explicitly identified as important in the statistical analysis. However, length times diameter was the third most important parameter and is directly related to aspect ratio in tests where the diameter is constant, $AR=(L/D)D^2$.

The impact of the firebrand diameter on the heat flux distribution is seen by comparing Test FF14 in **Figure 14** where the diameter was 4.75 mm with Test FF16 in **Figure 15** where the diameter was 9.5 mm. This also resulted in a change in the aspect ratio, with Test FF14 having an aspect ratio of 10.5 and Test FF15 having an aspect ratio of 5.3. All other factors were constant. The firebrand pile in Test FF16 (high diameter, lower aspect ratio) produced a band of high heat fluxes on the upstream side of the pile where the wind was introduced. However, this band of high heat fluxes did not cover as much of the firebrand pile as that measured in Test FF14 (lower diameter, higher aspect ratio). This was attributed to the differences in aspect ratio (pile porosity) in the two tests. Test FF16 with the higher diameter did have a longer burning duration (600 s) compared with Test FF14 with the lower diameter (465 s), which was attributed to the larger firebrand diameter taking longer to be consumed within the pile. These results support the statistical analysis in that firebrand diameter does not seem to have a significant impact on the heat flux; however, the burning duration time was affected as indicated by the times above.

The impact of the pile mass on the heat flux distribution is seen by comparing Test FF10 in **Figure 12** where the piles mass was 1.5 g with Test FF14 in **Figure 14** where the pile mass was 3.0 g. All other factors were kept constant. The heat flux distributions between these two tests with time are similar. In both tests, there was a high heat flux band on the upstream side of the pile with the heat flux band somewhat larger in Test FF14 with the larger mass compared with the Test FF10 that had the lower mass. With time, this high heat flux band migrated downstream along the pile. The burnout time of Test FF10 (350 s) with the lower mass was shorter than Test FF14 (465 s) with twice the mass; however, the difference in these burning durations is less compared to the effects of other factors on the burning duration. In review of the data, pile mass did not appear to have an impact on the heat flux level unless the number of firebrands in the pile was made small. For example, Test FF12 and Test FF16 had the same factors but different pile mass (see **Table 6**). In addition, Test FF12 had four firebrands while Test FF16 had eight firebrands. Based on the data

in **Figure 6**, Test FF16 had a higher heat fluxes compared with Test FF12. In cases with more firebrands in the pile (over 15), increasing the pile mass did not have a significant impact on the heat flux as seen in **Figure 6** for Test FF9 vs. Test FF13, Test FF10 vs. Test FF14, and Test FF11 vs. Test FF15. This indicates that number of firebrands in the pile is likely a more important factor compared with pile mass and that above a critical number of firebrands the effects of the number of firebrands on the heat flux is not significant. Based on available data, this critical value is between 4 – 8 firebrands that are 50 mm in length over the 50 mm diameter pile area. The magnitude of the heat flux will still be dependent on the firebrand size (aspect ratio and length) as well as wind speed.

Many of the results found in these tests agree well with the developing knowledge of heat transfer from individual firebrands and firebrand piles. The moisture content study showed that the moisture content of the unburned firebrands had no effect on the heat transfer from firebrand piles. The important caveat is that the firebrands in this study were heated until they reached a state of flaming combustion, likely driving off any internal moisture in the process. In a real fire scenario, branches with more moisture may be less likely to form a firebrand in the first place. Firebrands with 25% MC had to be heated 2.5 times longer than those at 0% MC to reach the same state of self-sustaining flaming. This suggests that moisture content may play an important role in the actual formation of firebrands during a wildfire scenario, but not on the burning and heat transfer from an existing firebrand.

The wood type study found that there was no significant difference in heat transfer between Yellow Poplar and E. White Pine, a hardwood and a softwood with similar densities. These results were generalized to say that the wood type does not affect the heat transfer from firebrand piles despite there being fundamental biological differences between hardwoods and softwoods. The closely related density study showed that there were also no differences in pile heat transfer based on the starting dry density of the wood used to make the firebrands.

The wood state study showed that the heat transfer was not statistically different between piles made with firebrands collected from live or dead tree branches. There was however a statistically significant difference between natural firebrands (from live or dead wood) and artificial firebrands made from dowel rods. For the limited data collected in this study, the artificial firebrands generated higher mean heat fluxes compared with the natural firebrands. A difference between artificial and natural firebrands was also reported by Tao et al. (2020), although the trend was opposite of that observed in these tests. This may be in part due to the firebrand diameters and aspect ratios not being the same in these comparison tests as well as the ability of the measurement technique being able to capture the spatial resolution. Based on the results in this study, using artificial firebrands may produce higher heat flux levels compared with natural firebrands. For cases involving safety testing of building materials, a modest overestimation of the heat flux may be desirable and artificial firebrands have the distinct advantage of consistent sizing and ample availability.

CONCLUSION

A series of tests were conducted to evaluate the impact of different firebrand pile factors on the heat flux from the pile to a flat surface. This included wood moisture content, wood type (hardwood or softwood), wood density, wood state (live, dead, or artificial), wind speed, pile mass, firebrand diameter, and firebrand length. Design of experiments was used to develop test matrices to evaluate the different factors so that statistical analysis could be performed on the results and the statistical significance of the different factors could be determined. An inverse heat transfer method was used to produce high spatial resolution heat flux data under the firebrand piles. The 75th percentile of the 120 s average flux was used to represent the heat flux from the firebrand pile and used to performed the statistical analysis.

It was found that wood moisture content, wood type, and density did not affect the heat flux. Statistically different heat fluxes were measured between natural and artificial (dowels) firebrands with higher heat fluxes from the artificial firebrands. The result suggests that artificial firebrands may be a conservative surrogate for natural firebrands. Based on a full-factorial test series, wind speed and firebrand length were found to have a statistically significant impact on heat flux while firebrand diameter and pile mass did not statistically impact the heat flux. In addition, the interaction between firebrand length and firebrand diameter (length times diameter) was also found to be statistically significant. In tests with constant diameter, the length times diameter is directly related to the firebrand aspect ratio. The aspect ratio controls the pile porosity (ratio of volume of air in the pile to pile volume). Increasing the aspect ratio (which increases the pile porosity) results in higher heat fluxes across the pile and shorter burning times (i.e., a shorter but more intense heat flux to the surface). Pile mass and firebrand diameter were observed to have an impact on burning duration, but not as significant as other effects such as decreasing the pile porosity. Lastly, reducing the number of firebrands in the pile was observed to impact the heat flux when it was decreased below a critical value. This value was not explicitly determined in these experiments but based on the available data is somewhere between 4 – 8 firebrands for firebrands 50 mm long over a 50 mm diameter region. The magnitude of the heat flux will still be dependent on the firebrand size (aspect ratio and length) as well as wind speed.

DATA AVAILABILITY STATEMENT

The raw data supporting the conclusion of this article will be made available by the authors, without undue reservation.

AUTHOR CONTRIBUTIONS

BL–data and statistical analysis writing paper, paper review EB–experiments, writing paper JH–input on experiments, paper review CR–input on experiments, paper review AK–input on experiments, paper review.

FUNDING

This research was funded by the National Institute of Standards and Technology (NIST) under contract NIST Grant No. 70NANB19H052.

ACKNOWLEDGMENTS

The authors appreciate the support of the Virginia Tech Statistics Institute (SAIG) for discussions on the statistical analysis.

REFERENCES

Bearinger, E. D., Hodges, J. L., Yang, F., Rippe, C. M., and Lattimer, B. Y. (2020). Localized Heat Transfer from Firebrands to Surfaces. *Fire Saf. J.* 120, 103037. doi:10.1016/j.firesaf.2020.103037

Brown, T., Leach, S., Wachter, B., and Gardunio, B. (2020). The Extreme 2018 Northern California Fire Season. *Bull. Am. Meteorol. Soc.* 101 (1), S1–S4. doi:10.1175/BAMS-D-19-0275.1

Cholewa, N., Summers, P. T., Feih, S., Mouritz, A. P., Lattimer, B. Y., and Case, S. W. (2016). A Technique for Coupled Thermomechanical Response Measurement Using Infrared Thermography and Digital Image Correlation (TDIC). *Exp. Mech.* 56, 145–164. doi:10.1007/s11340-015-0086-1

Conners, T. (2015). Distinguishing Softwoods from Hardwoods. *Agric. Nat. Resour. Publ.* 105, 1–5. Available at: https://uknowledge.uky.edu/anr_reports/105

Deb, P., Moradkhani, H., Abbaszadeh, P., Kiem, A. S., Engström, J., Keellings, D., et al. (2020). Causes of the Widespread 2019–2020 Australian Bushfire Season. *Earth's Futur* 8 (11), e2020EF001671. doi:10.1029/2020ef001671

Dowling, V. P. (1994). Ignition of Timber Bridges in Bushfires. *Fire Saf. J.* 22 (2), 145–168. doi:10.1016/0379-7112(94)90070-1

Filkov, A. I., Ngo, T., Matthews, S., Telfer, S., and Penman, T. D. (2020). Impact of Australia's Catastrophic 2019/20 Bushfire Season on Communities and Environment. Retrospective Analysis and Current Trends. *J. Saf. Sci. Resilience* 1 (1), 44–56. doi:10.1016/j.jnlssr.2020.06.009

Filkov, A., Kasymov, D., Zima, V., and Matvienko, O. (2016). "Experimental Investigation of Surface Litter Ignition by Bark Firebrands," in AIP Conference Proceedings, 6-9 October 2015, Tomsk, Russia, 1698, 060004.

Hakes, R. S. P., Salehizadeh, H., Weston-dawkes, M. J., and Gollner, M. J. (2018). Thermal Characterization of Firebrand Piles. *Fire Saf. J.* 104, 34–42. doi:10.1016/j.firesaf.2018.10.002

Koo, E., Pagni, P. J., Weise, D. R., and Woycheese, J. P. (2010). Firebrands and Spotting Ignition in Large-Scale Fires. *Int. J. Wildland Fire* 19 (7), 818–843. doi:10.1071/wf07119

Lagouvardos, K., Kotroni, V., Giannaros, T. M., and Dafis, S. (2019). Meteorological Conditions Conducive to the Rapid Spread of the Deadly Wildfire in Eastern attica, Greece. *Bull. Am. Meteorol. Soc.* 100 (11), 2137–2145. doi:10.1175/bams-d-18-0231.1

Li, S., Zhao, J., Lu, P., and Xie, Y. (2010). Maximum Packing Densities of Basic 3D Objects. *Chin. Sci. Bull.* 55 (2), 114–119. doi:10.1007/s11434-009-0650-0

Manzello, S. L., Cleary, T. G., Shields, J. R., Maranghides, A., Mell, W., and Yang, J. C. (2008). Experimental Investigation of Firebrands: Generation and Ignition of Fuel Beds. *Fire Saf. J.* 43 (3), 226–233. doi:10.1016/j.firesaf.2006.06.010

Manzello, S. L., Cleary, T. G., Shields, J. R., and Yang, J. C. (2006). On the Ignition of Fuel Beds by Firebrands. *Fire Mater.* 30 (1), 77–87. doi:10.1002/fam.901

Manzello, S. L., Park, S.-H., and Cleary, T. G. (2009). Investigation on the Ability of Glowing Firebrands Deposited within Crevices to Ignite Common Building Materials. *Fire Saf. J.* 44 (6), 894–900. doi:10.1016/j.firesaf.2009.05.001

Manzello, S., and Suzuki, S. (2014). Exposing Decking Assemblies to Continuous Wind-Driven Firebrand Showers. *Fire Saf. Sci.* 11, 1339–1352. doi:10.3801/iafss.fss.11-1339

Mcarthur, N. A., and Lutton, P. (1991). Ignition of Exterior Building Details in Bushfires: An Experimental Study. *Fire Mater.* 15, 59–64. doi:10.1002/fam.810150204

Mell, W., and Alexander, M. (2009). *NIST Technical Note 1635: A Case Study of a Community Affected by the Witch and Guejito Fires*. Gaithersburg, MD: National Institute of Standards and Technology.

Rippe, C. M., and Lattimer, B. Y. (2015). Full-field Surface Heat Flux Measurement Using Non-intrusive Infrared Thermography. *Fire Saf. J.* 78, 238–250. doi:10.1016/j.firesaf.2015.10.004

Rowell, R., Pettersen, R., and Tshabalala, M. (2012). *Cell Wall Chemistry*. Gaithersburg, MD: National Institute of Standards and Technology.

Santamaria, S., Kempna, K., Thomas, J. C., and Houssami, M. E. (2015). "Investigation of Structural Wood Ignition by Firebrand Accumulation," in The First International Conference on Structural Safety under Fire & Blast, Glasgow, Scotland, UK, July 2016, 1–13.

Tao, Z., Bathras, B., Kwon, B., Biallas, B., Gollner, M. J., and Yang, R. (2020). Effect of Firebrand Size and Geometry on Heating from a Smoldering Pile under Wind. *Fire Saf. J.* 120, 103031. doi:10.1016/j.firesaf.2020.103031

Theobald, D. M., and Romme, W. H. (2007). Expansion of the US Wildland-Urban Interface. *Landscape Urban Plann.* 83 (4), 340–354. doi:10.1016/j.landurbplan.2007.06.002

Turco, M., Jerez, S., Augusto, S., Tarín-Carrasco, P., Ratola, N., Jiménez-Guerrero, P., et al. (2019). Climate Drivers of the 2017 Devastating Fires in Portugal. *Sci. Rep.* 9 (1), 1–8. doi:10.1038/s41598-019-50281-2

Ward, M., Tulloch, A. I. T., Radford, J. Q., Williams, B. A., Reside, A. E., Macdonald, S. L., et al. (2020). Impact of 2019-2020 Mega-Fires on Australian Fauna Habitat. *Nat. Ecol. Evol.* 4 (10), 1321–1326. doi:10.1038/s41559-020-1251-1

Yang, H., Yan, R., Chen, H., Lee, D. H., and Zheng, C. (2007). Characteristics of Hemicellulose, Cellulose and Lignin Pyrolysis. *Fuel* 86 (12–13), 1781–1788. doi:10.1016/j.fuel.2006.12.013

Zou, R.-P., Lin, X.-Y., Yu, A.-B., and Wong, P. (1997). Packing of Cylindrical Particles with a Length Distribution. *J. Am. Ceram. Soc.* 80 (3), 646–652. doi:10.1111/j.1151-2916.1997.tb02880.x

Zou, R. P., and Yu, A. B. (1996). Evaluation of the Packing Characteristics of Mono-Sized Non-spherical Particles. *Powder Technol.* 88, 71–79. doi:10.1016/0032-5910(96)03106-3

Conflict of Interest: BL has an ownership/equity interest in Jensen Hughes. Authors JH, CR, and AK were employed by the company Jensen Hughes.

The remaining authors declare that the research was conducted in the absence of any commercial or financial relationships that could be construed as a potential conflict of interest.

frontiers in Mechanical Engineering

ORIGINAL RESEARCH
published: 22 July 2021
doi: 10.3389/fmech.2021.686638

Smoldering and Flaming of Disc Wood Particles Under External Radiation: Autoignition and Size Effect

Supan Wang[1,2], Pengfei Ding[1], Shaorun Lin[2], Junhui Gong[1] and Xinyan Huang[2]**

[1]College of Safety Science and Engineering, Nanjing Tech University, Nanjing, China, [2]Research Centre for Fire Safety Engineering, The Hong Kong Polytechnic University, Kowloon, Hong Kong

Wildfires are global issues that cause severe damages to the society and environment. Wood particles and firebrands are the most common fuels in wildfires, but the size effect on the flaming and smoldering ignitions as well as the subsequent burning behavior is still poorly understood. In this work, a well-controlled experiment was performed to investigate smoldering and flaming ignitions of stationary disc-shaped wood particles with different diameters (25–60 mm) and thicknesses (15–25 mm) under varying radiant heat flux. The ignition difficulty, in terms of the minimum heat flux, increases from smoldering ignition to piloted flaming ignition and then to flaming autoignition. As the sample thickness increases, the minimum heat flux, ignition temperature, and burning duration for flaming autoignition all increase, while the peak burning flux decreases, but they are insensitive to the sample diameter. During ignition and burning processes, the disc particle is deformed due to the interaction between chemical reactions and thermomechanical stresses, especially for smoldering. The characteristic thickness of the smoldering front on wood is also found to be 10–15 mm. This study sheds light on the size effect on the ignition of wood particles by wildfire radiation and helps understand the interaction between flaming and smoldering wildfires.

Keywords: ignition limit, minimum radiation, disc particles, smoldering fire, firebrands

OPEN ACCESS

Edited by:
Naian Liu,
University of Science and Technology of China, China

Reviewed by:
Alexander S. Rattner,
The Pennsylvania State University (PSU), United States
Patrick Jacob Shamberger,
Texas A&M University, United States

****Correspondence:***
Shaorun Lin
flynn.lin@connect.polyu.hk
Xinyan Huang
xy.huang@polyu.edu.hk

Specialty section:
This article was submitted to Thermal and Mass Transport, a section of the journal Frontiers in Mechanical Engineering

Received: *27 March 2021*
Accepted: *22 June 2021*
Published: *22 July 2021*

Citation:
Wang S, Ding P, Lin S, Gong J and Huang X (2021) Smoldering and Flaming of Disc Wood Particles Under External Radiation: Autoignition and Size Effect. Front. Mech. Eng 7:686638. doi: 10.3389/fmech.2021.686638

INTRODUCTION

Driven by the climate change, the Earth ecosystems tend to suffer more frequent wildfires and longer wildfire durations, posing severe threats to the economy, society, and environment, especially in the densely populated wildland–urban interface (WUI) (Liu et al., 2010; Moritz et al., 2014; Toledo et al., 2018; Lin et al., 2019a). Mega-scale wildfires are difficult to predict and control, and they may cause huge casualties and property loss, such as those in California, Australia, and South Europe. Because the spread of a wildfire is a result of a consecutive ignition process (Williams, 1982), it is critical to understand the ignition of wildland fuel particles to predict wildfire development and optimize the emergency response.

The ignition of wildland fuel involves complex physicochemical processes in both the solid and gas phases, and it depends on fuel properties, for example, density, type, moisture, and thermal conductivity (Simms and Law 1967; Wesson et al., 1971; Bilbao et al., 2001), and configurations, for example, size and shape (Saastamoinen et al., 2000; Momeni et al., 2013; Lin et al., 2019a). Small fuel particles, such as shrubs, twigs, bark, and litter layer, constitute a vast majority of wildland fuel loads, so the ignition of small particles is closely related to the wildfire risks and hazards (Moghtaderi et al., 1997; McAllister 2013; Finney et al., 2015; Lin et al., 2019a). The recent debate on the ignition

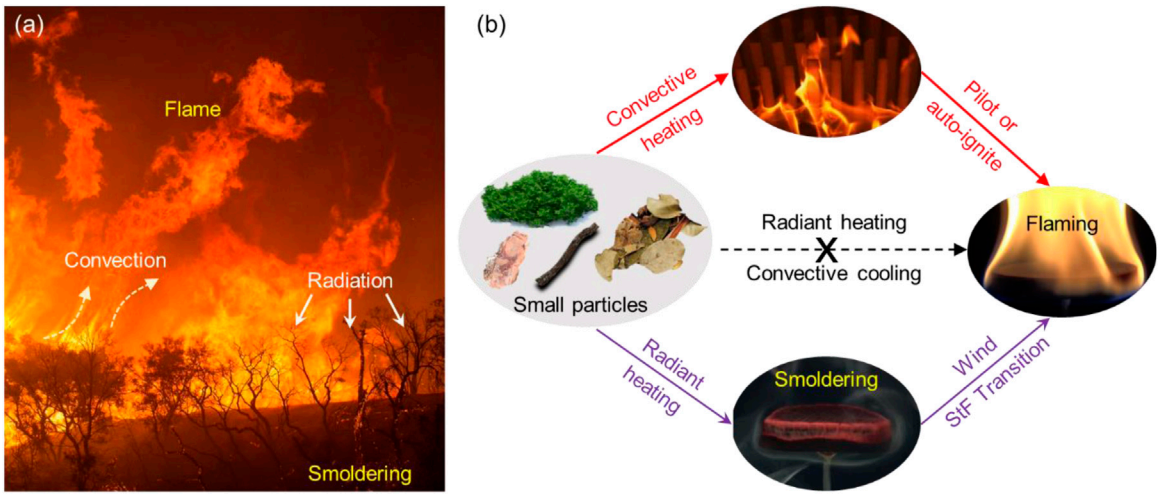

FIGURE 1 | (A) Flaming and smoldering fire of wood particles in wildfires (U.S. Forest Surveys) and **(B)** possible ignition mode of wood particles.

mechanism (Finney et al., 2013, 2015) suggested that direct flame contact played a dominant role in the flaming ignition of fine and small fuel particles, which compensated Rothermel's radiation ignition theory (Rothermel, 1972).

Almost all wildland fuels can sustain both forms of flaming and smoldering wildfires (**Figure 1A**), such as pine needle beds (Wang et al., 2017a), barks and twigs (Sullivan et al., 2018), ground litter layers (Wang et al., 2017b), and underground organic soils (Lin et al., 2019b). Flaming fire is sustained by the oxidation of pyrolysis gases in the gas phase (Quintiere, 2006). Smoldering is dominated by the char oxidation in the solid phase, so it is slow, low-temperature, flameless, and the most persistent (Rein, 2014). The ignition of smoldering does not need a pilot source, so it is also a kind of autoignition or spontaneous ignition. Both flaming and smoldering fire can transition to each other under specific conditions (Santoso et al., 2019; Huang and Gao 2020; Lin et al., 2021). As illustrated in **Figure 1B**, the flame can be piloted by direct contact with a nearby flame (Finney et al., 2015) or autoignited within the hot plume (McAllister et al., 2012; Mcallister and Finney 2017). Also, the flame can be transitioned from the smoldering fire, that is, the smoldering-to-flaming (StF) transition. Compared to piloted flaming ignition, smoldering ignition needs no pilot source. Moreover, the intensified convective cooling, which prevents the flaming ignition under radiation (Finney et al., 2013), can also facilitate and intensify smoldering by increasing the oxygen supply (Wang et al., 2016). In other words, smoldering provides an alternative shortcut for flaming ignition in the absence of direct flame contact, but it needs further verification under specific fuels and environmental conditions.

The shape of wildland fuels may be cubic, cylindrical, spherical, disc-shaped, or irregular (Paulrud and Nilsson 2004; Kuo and Hsi 2005; Lin et al., 2019a). The fuel size also has a wide range, from mm-scale fine leaves and needles (McAllister et al., 2012) to cm-scale small twigs, shrubs, and firebrands (Manzello et al., 2008; Manzello et al., 2020) to dm-scale tree trunks and to m-scale soil layers (Huang and Rein, 2017). Most research literature focused on the flaming and smoldering ignition limits of flat wood samples under external irradiation (Boonmee and Quintiere 2002; Yang et al., 2011). Nevertheless, the effects of fuel shape and size are also important. Harada (2002) pointed out that the sample thickness did not influence the flaming ignition delay time but affected the mass-loss rate. Finney et al. (2015) revealed that for the fine-sized fuel particles, the convective cooling dominated over the radiant heating, whereas the convective heating *via* contact with flames and hot gases controlled the flaming ignition. Lin et al. (2019a) showed the combined effects of fuel size and arrangement on the convective cooling and the piloted flaming ignition under external radiation. Atreya et al. (2017) also pointed out that the nominal dimensions (i.e., size and shape) have a significant effect on the pyrolysis duration and the remaining char mass. To the best of the authors' knowledge, very limited research was available on the smoldering and flaming autoignition and burning behaviors of small wildland fuel particles and the effect of particle size; thus, there is a big knowledge gap.

In this work, the smoldering ignition of disc-shaped hardwood particles is investigated with different sizes (5–60 mm) under an external radiation up to 60 kW/m^2. For comparison, the flaming autoignition experiments are also conducted. The ignition delay time, temperature, minimum heat flux, and burning rate are quantified and analyzed to provide a full picture of wildland fuel ignitability.

EXPERIMENTAL METHOD

Apparatus and Fuel Sample

The schematic diagram of the experimental setup is illustrated in **Figure 2**, and it mainly consists of a radiant panel, a sample holder, and an electric balance. The panel radiator with the dimension of 0.2 m × 0.2 m is made of several resistance heating rods that can generate a uniform radiant heat flux from 0 to 60 kW/m^2 on the top fuel surface 50 mm below. The air temperature above the wood surface is lower, so the

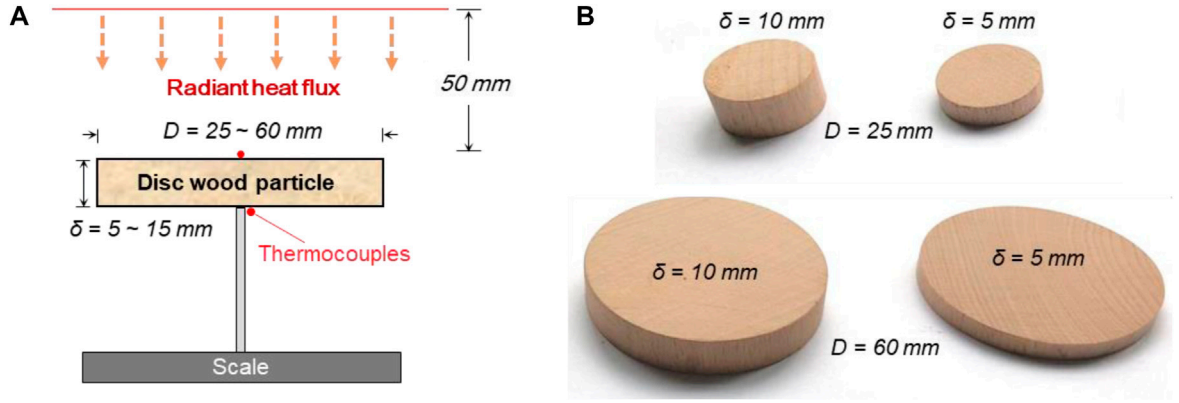

FIGURE 2 | (A) Schematic diagram of the test setup for igniting the disc-shaped wood particle under external radiation, and **(B)** photos of disc-shaped wood particles with different thicknesses and diameters.

air is responsible for cooling the wood surface. The fuel particles tested in the experiment were German beech wood. Referring to the survey of wood particle shapes and sizes in common wildlands (Manzello et al., 2008), nine disc-shaped samples with three diameters (D) of 25, 40, and 60 mm and three thicknesses (δ) of 5, 10, and 15 mm were tested. These wood samples were first oven-dried at 80°C for 8 h and then kept in a dry chamber to control the same initial condition. The initial mass of particle samples ranges from 1.6 to 25.8 g with an uncertainty of 5%, so their dry bulk density was calculated to be 621 ± 21 kg/m^3.

The wood particle was stuck to a 2-mm-thick aluminum rod using high-temperature-resistant adhesive, and then it was spaced for 5 h to form a stable connection. During the experiment, the mass evolution of the particle was measured using the electric balance (Mettler-Toledo XE10002S, resolution: 0.01 g). The upper and lower surface temperatures of the particle were measured using two thin K-type thermocouples (TCs) with a 0.5-mm bead. Because thermocouples might affect the mass measurement, the mass and temperature measurements were conducted separately in repeating tests.

Ignition Protocols

Before testing, the radiant panel was first preheated for 25 min to the prescribed heat flux which was measured and calibrated using a radiometer. Afterward, the irradiation was shielded using an insulation board that allowed the sample to be placed in the right position. Once the insulation shield was removed, the irradiation started to apply to the sample. It should be noted that no pilot source was used for flaming ignition, different from the study by Lin et al. (2019b). The whole heating and burning process was recorded using a front-view video camera (Sony FDR-AX60 at 50 fps). For any given experimental condition, the experiment was repeated 3–6 times to quantify the random uncertainty.

For the flaming autoignition, the ignition delay time ($t_{ig,f}$) could be easily quantified visually when the flame appeared. The minimum radiation for autoignition ($\dot{q}''_{min,f}$) can be obtained by decreasing the incident heat flux until no flame occurs after heating for 10 min. For the smoldering ignition, it was difficult to visually determine the onset of smoldering. Approximately, based on the threshold temperature of char oxidation (Terrei et al., 2019), the characteristic temperature of 350 ± 30°C can be defined as the threshold of smoldering. By reducing the radiation, the minimum value for smoldering ignition ($\dot{q}''_{min,sm}$) was determined when the sample had no mass loss after being fully charred.

RESULTS AND DISCUSSION

Smoldering Ignition and Burning Behaviors

Figure 3A shows an example of the smoldering ignition process and the associated burning behaviors of wood particles with the same diameter of 60 mm and two different thicknesses of 10 and 15 mm, respectively. The original videos can be found in **Supplementary Video S1, 2**. Once exposed to the irradiation, the sample was heated to release some visible smoke. The visible smoke may be the condensed water droplets (like fog) and tar droplets (the condensed pyrolysis gases with a high molecular weight) as they mix with cool air. The intensity of the smoke flow first increased, which may even form the gas jet above the sample surface, and then it gradually decreased near burnout. The flow of air streams was faster near the edge of the surface with a large curvature that can enhance convective heat transfer (Incropera and DeWitt, 1996). Moreover, due to the better oxygen supply, noticeable glowing was always first initiated at the edge, which is a widely observed phenomenon on the solid surface (Huang and Gao, 2020).

During the smoldering ignition and the burning process, complex structural behaviors of wood particles could be observed, and the deformation was more obvious for the disc sample with a larger diameter-to-thickness ratio. As shown in **Figure 3A**, there are mainly two different deformation stages:

i) Bending upward to form a bowl shape. Once exposed to the irradiation, the wood sample started to deform upward and

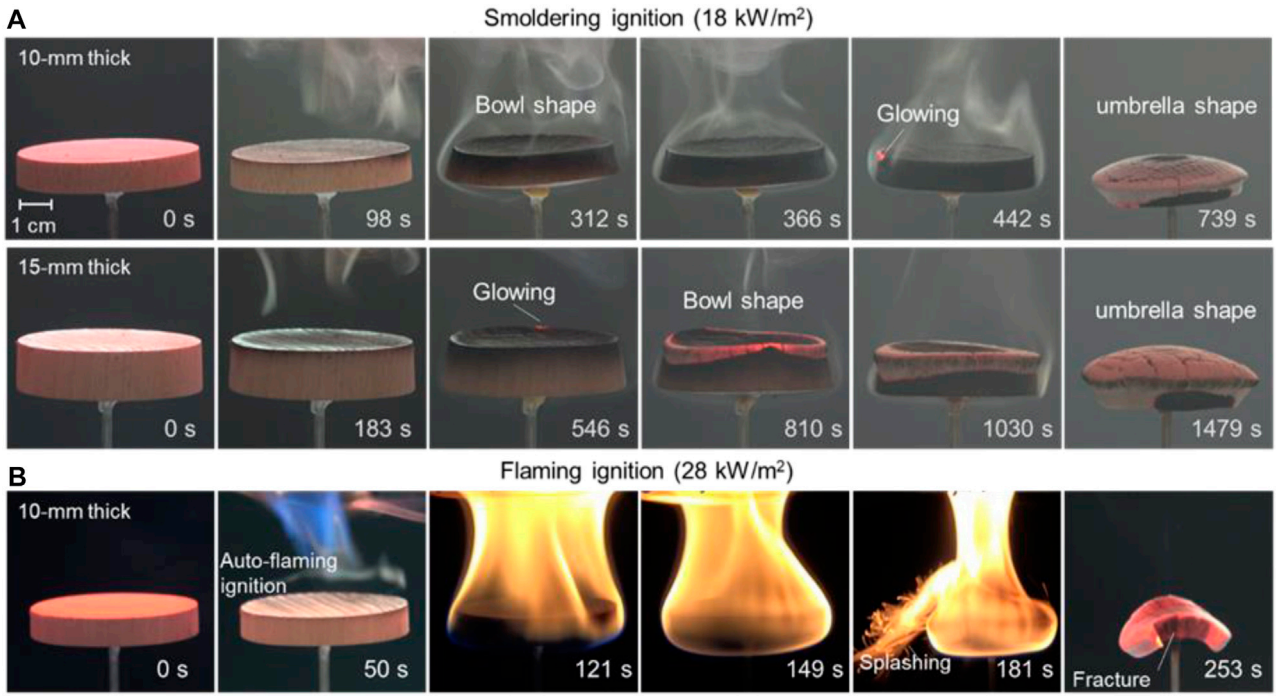

FIGURE 3 | (A) Smoldering ignition of the wood particle with a diameter of 60 mm and different thicknesses of 10 and 15 mm (Wang et al., 2021) and **(B)** flaming autoignition of the wood particle with a diameter of 60 mm and a thickness of 10 mm.

form a bowl shape. This may be caused by the shrinkage on the top surface, where there is a strong mass loss because of the drying and pyrolysis.

ii) Bending downward to form an umbrella shape. As the smoldering front approached the bottom, the sample bent back to become flat and then continued to bend downward and deformed to form an umbrella shape because of the interaction between thermal expansion and char oxidation (Wang et al., 2021).

Furthermore, a longer heating duration is required for a thicker sample to form a gas jet, as shown in **Figure 3A**. It was roughly attributed to the larger temperature gradients inside the thicker wood sample, and only the top thin layer can reach its pyrolysis temperature to release gases (Lin et al., 2019a). For the samples with thicknesses of 5 and 10 mm, the regression due to burnout on the top surface occurred after the smoldering front reached the bottom surface, whereas for the thickness of 15 mm, the regression occurred earlier. Therefore, we can presume that the characteristic thickness of the smoldering front is about 10–15 mm for this wood particle.

Flaming Autoignition and Burning Behaviors

The flaming autoignition of the wood particle was also observed as the external heat flux is larger than the critical value ($\dot{q}''_{min,f}$). **Figure 3B** shows an example of the flaming autoignition and burning processes of the large disc-shaped wood sample with a diameter of 60 mm and a thickness of 10 mm. The original video can be found in **Supplemental Video S3**. After heating for about 50 s, a blue flash could be achieved above the wood top surface. Subsequently, the flame propagated downward and covered the entire sample surface. At 253 s, the flame self-extinguished, and the wood residue was in an umbrella-shaped structure. However, the extinction of the flame is not the end of the fire; instead, it was followed by a stable smoldering in the solid phase until burnout (Lin et al., 2021). Compared with the smoldering burning of the 10-mm-thick sample in **Figure 3A**, the structure deformation and edge effect were not obvious during the flaming burning.

On the other hand, during the burning process, the macro-cracking occurred on the sample surfaces, which was widely observed in wood pyrolysis processes under the nitrogen condition (Li et al., 2017). Such cracking was due to the accumulation of internal pressure and structure failure. Moreover, the splashing phenomenon was also observed, which was a strong bright spark, like that occurs upon water dripping into boiling oil. Such a splash phenomenon might be the result of the competition of gas production and sample structural strength (see **Appendix** for more details).

The Ignition Limits of Flaming and Smoldering

By plotting the ignition time under different radiant heat fluxes, the propensity for flaming and smoldering ignition of the wood particle can be quantified. **Figure 4A** shows an example of a wood particle with a diameter of 60 mm and a thickness of 10 mm. The error bars show the standard deviations of the values measured from all repeating tests. As expected, the ignition delay time also decreases as radiant heat flux increases, the same as other

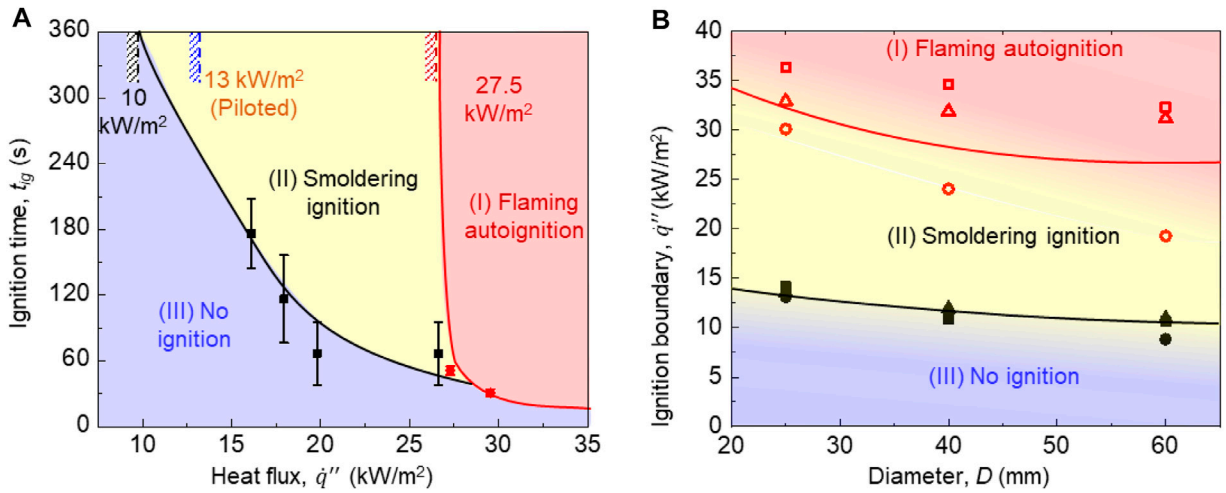

FIGURE 4 | (A) Smoldering ignition and flaming autoignition delay time of wood particles (D = 60 *mm*, δ = 10 *mm*) under different heat fluxes. **(B)** Effect of fuel size on the ignition boundary of the wood particle. The symbols of the square, triangle, and circle represent the thicknesses of 15, 10, and 5 mm, and the red and black symbols represent flaming and smoldering ignition, respectively. The striped regions represented the lowest heat fluxes or ignition boundary of smoldering ignition, piloted ignition, and autoignition, respectively.

combustibles (Rodriguez et al., 2017). More importantly, by decreasing the radiant heat flux and ignition time, the observed phenomena in the current non-piloted ignition study can be categorized into three regions: (I) flaming autoignition, (II) smoldering ignition, and (III) no ignition. A much larger heat flux is required to initiate the flaming ignition of wood particles in the absence of a pilot source than the smoldering ignition of wood particles (10 kW/m^2 vs. 28 kW/m^2), which is different from the ignition propensity of peat soil (6.5 kW/m^2 vs. 7.5 kW/m^2) (Lin et al., 2019b) with pilot source and the glowing autoignition of wood cubic samples (10 kW/m^2 vs. 18 kW/m^2) (Boonmee and Quintiere, 2002).

For comparison, the critical heat flux for the piloted ignition of wood from the study by Quintiere (2006) is also plotted in **Figure 4A**. Here, the striped regions represented the lowest heat fluxes or ignition boundaries of smoldering ignition, piloted ignition, and autoignition, respectively. The difficulty of ignition increases from smoldering to piloted flaming ignition and then to flaming autoignition in terms of the minimum heat flux. Therefore, the piloted ignition effectively lowers the flaming ignition limit and provides a shortcut to trigger a flaming fire. In real fire scenarios, the flame of burning trees can act as the heating and pilot sources, which may cause piloted flaming ignition and increase the wildfire risk.

Figure 4B further summarizes the ignition boundaries of smoldering ignition and flaming autoignition for different wood particles, where the symbols of the square, triangle, and circle represent the sample thicknesses of 15, 10, and 5 mm and the red and black symbols represent flaming and smoldering ignition, respectively. The ignition limit of flaming fire is very sensitive to the sample thickness, while the effect on smoldering ignition is negligible. For example, with the same diameter of 25 mm, as the same thickness increases from 5 to 15 mm, the critical heat flux for flaming ignition increases from 30 kW/m^2 to 37 kW/m^2. One possible reason is that for a thinner sample, both the received external radiation and the in-depth conduction are more uniform, leading to a smaller internal temperature gradient (Lin, Huang, et al., 2019). Therefore, a thicker layer below the top surface can reach pyrolysis temperature so that sufficient pyrolysis gases could be released to trigger flaming ignition. In contrast, for the sample with larger thickness, there is a large temperature gradient, and the in-depth temperature is much lower than the surface temperature. As a result, only the thin surface layer is pyrolyzing, so a larger external heat flux is required to reach the minimum fuel mass flux (Quintiere 2006) (discussed more in *Surface Temperature and Mass Loss Rate* in *Size Effect on the Flaming Burning Behaviors*). On the other hand, the minimum heat fluxes of both smoldering ignition and flaming autoignition are insensitive to the diameters, except the auto-flaming ignition of the 5-mm-thick sample, which has lower thermal resistance and is easily affected by the environmental factors.

Characteristics of Smoldering and Flaming Autoignition

Figure 5 shows an example of the measured surface temperature and mass-loss rates' time evolution for smoldering and flaming ignition of the wood particle with a thickness of 10 mm and a diameter of 60 mm. The red curves represent the flaming autoignition (28 kW/m^2), and the black curves represent the smoldering ignition (18 kW/m^2). Once exposed to the heating panel, both the surface temperature and mass loss increase remarkably with a decreasing rate. For flaming ignition, a sudden increase can be observed at the ignition moment in both surface temperature and mass flux, consistent with other research efforts (Moghtaderi et al., 1997; McAllister, 2013). For smoldering ignition, a sudden increase could also be observed in the mass flux, but it is not clear in the

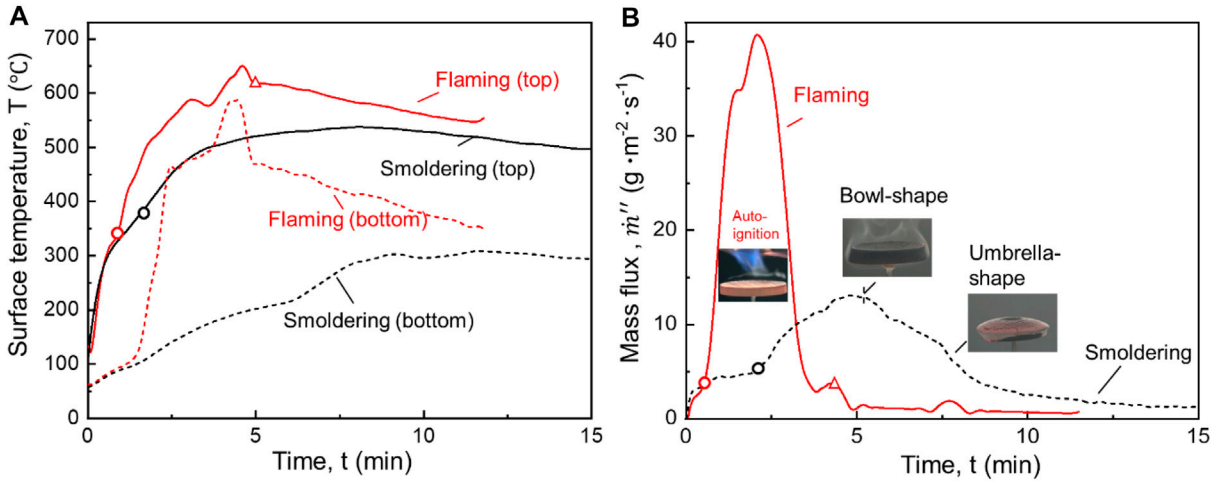

FIGURE 5 | Surface temperature **(A)** and mass loss time evolution **(B)** of the wood sample with a diameter of 60 mm and a thickness of 10 mm, where the circular symbols indicate the moment of flaming autoignition.

temperature evolution. However, the corresponding surface temperature at the smoldering ignition moment is found to be ~350°C, consistent with the findings of Terrei et al. (2019). Although the surface temperature during a flaming fire is much higher than that for a smoldering fire, their temperature difference between the top and bottom surfaces is smaller. Therefore, the thermal expansion for flaming fire is smaller than that for smoldering, as shown in **Figure 3**.

On the other hand, the mass flux for flaming is much higher than that for smoldering. For flaming burning, once the whole sample is charred, both the surface temperature and mass flux go through a sharp drop, following the self-extinction of flaming fire (Lin et al., 2021). However, the fire continues as smoldering combustion at very low mass flux, and the temperature difference keeps increasing and gradually becomes close to that of the direct smoldering ignition sample. For the flaming ignition criterion, ignition temperature (T_{ig}) is widely used, and it is very helpful in predicting the fire spread (Quintiere, 2006). If the external radiant heat flux is below the minimum value, an equilibrium between radiant heating and environmental cooling can be reached at a surface temperature below T_{ig} (Lin et al., 2019b).

Size Effect on the Flaming Burning Behaviors

Figure 6A plots the flaming ignition temperatures of wood samples with different diameters and thicknesses. It can be found that the flaming ignition temperature increases with the thickness, while it is less sensitive to the diameter. For example, for the wood particle with a diameter of 25 mm, the ignition temperature increases from 345 to 390°C as the sample thickness increases from 5 to 15 mm. Similarly, the temperature difference between the top and bottom surfaces at the ignition moment also increases with the sample thicknesses, as shown in **Figure 6B**.

A smaller temperature diffidence indicates a smaller internal temperature gradient in the direction perpendicular to the heating source, and both received external radiant heat flux and the in-depth conduction is more uniform (Lin et al., 2019a). Therefore, a thicker layer below the surface can reach the pyrolysis temperature and release combustible gases to trigger a flame. Comparatively, for the wood sample with a larger thickness, the in-depth temperature is much lower than the surface temperature, and only a very thin layer can reach the pyrolysis temperature, so a higher ignition temperature and the critical heat flux are required to reach the minimum fuel mass flux, as shown in **Figures 4B**, **6A**.

Figures 6C,D further compare the peak burning flux and flame duration of wood particles with different diameters and thicknesses. Clearly, as the thickness increases, the peak burning flux decreases while the flame duration increases. A thinner sample can burn more extensively due to a more uniform in-depth conduction so that it is easier for the whole sample to reach its pyrolysis temperature and start to burn.

Size Effect on Smoldering Burning Behaviors

Figure 7 and **Figure 8** present the thickness effect on the surface temperature and mass loss for smoldering combustion of samples with the same diameter of 60 mm. At about 35 s, the thermal energy had propagated to the lower face, and the pyrolysis gas was released. So, the small peak mass occurred at the initial heating only for the 5-mm-thick sample. Based on the characteristic temperature in TGA, the onset of "pyrolysis" and the onset of the "oxidation reaction" were determined. For sample thicknesses of 5, 10, and 15 mm, the onset of pyrolysis was at 54 ± 2, 69.5 ± 1.5, and 86 ± 4 s and the onset of the oxidation reaction was at 112 ± 5, 130.5 ± 2.5, and 143.5 ± 6.5 s, respectively. The thicker

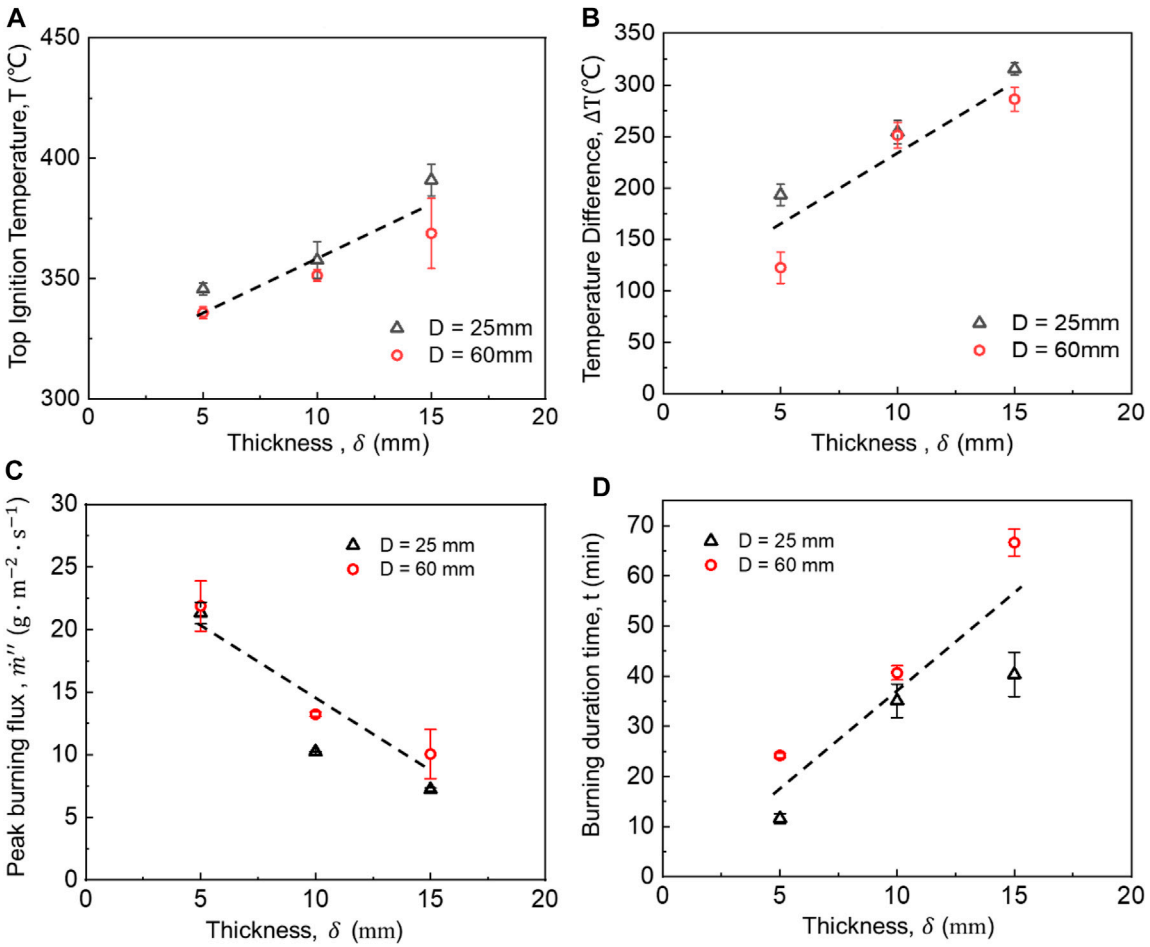

FIGURE 6 | Comparison of **(A)** autoignition fuel temperature, **(B)** temperature difference between the top and bottom surfaces at the ignition moment, **(C)** peak burning flux, and **(D)** burning duration time of flaming fire with different diameters and thicknesses.

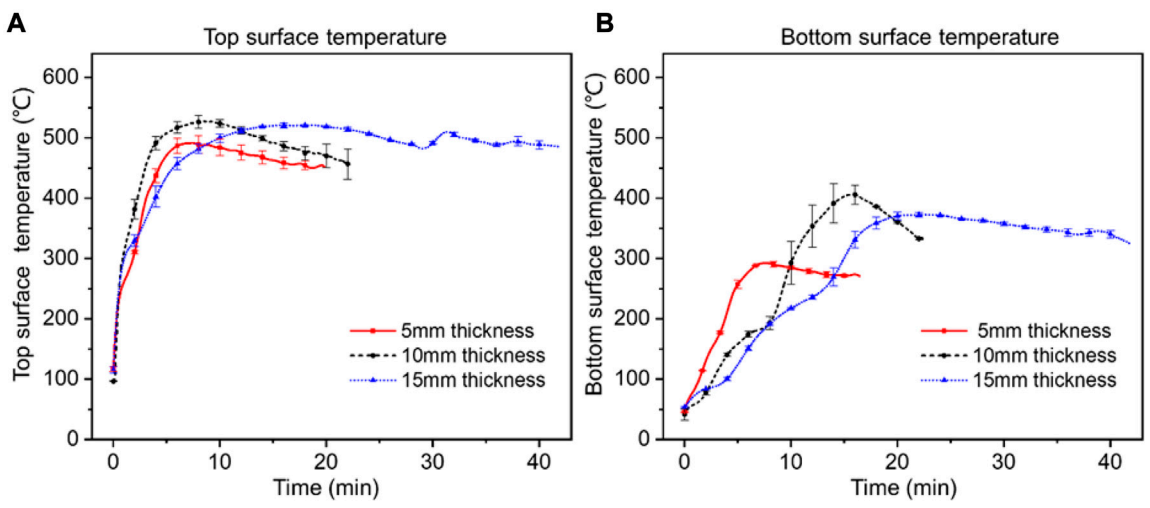

FIGURE 7 | Upper **(A)** and lower **(B)** face temperature during the smoldering ignition and burning for disc-shaped wood particles with a diameter of 60 mm, showing the thickness effect.

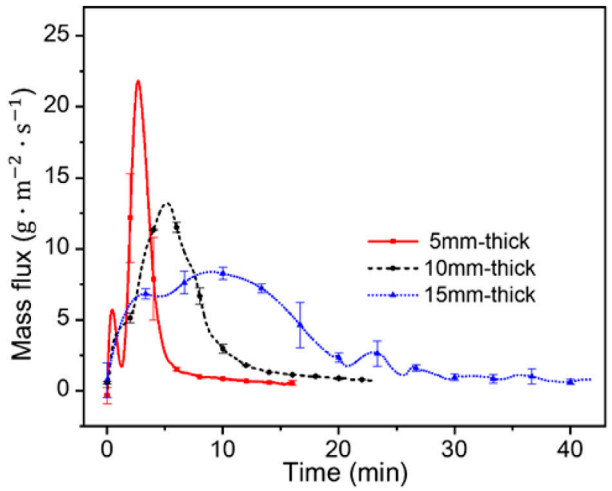

FIGURE 8 | Mass loss rate during the smoldering ignition and burning of disc-shaped wood particles with a diameter of 60 mm, showing the thickness effect.

particle has greater in-depth heat conduction, which delayed the appearance of pyrolysis and oxidation and decreased the peak reaction intensity, as indicated by the peak mass loss rate.

Due to the volume of the reaction fuel, the thickness had no obvious effect on the magnitude of upper face temperature. Conversely, the increment of thickness delayed and reduced the heating of the lower face. Also, there was one mass loss peak for $\delta < 10$ mm and two mass loss peaks for $\delta > 10$ mm. It was because the heating of the upper sample to pyrolysis of the unreacted materials is consistent with the oxidation phenomena in **Figure 2A**.

Figure 9 presents the diameter effect on the surface temperature and mass loss for smoldering combustion of 10-mm-thick samples. For the sample with the diameters of 25 and 60 mm, the onset of pyrolysis was at 62.5 ± 1.5 and 69.5 ± 1.5 s, and the onset of the oxidation reaction was at 102 ± 1 and 130.5 ± 2.5 s, respectively. Despite the same upper face temperature before 15 s, the accumulation of heat on the side surface accelerated the temperature increase of the lower face and also moved up the appearance of the smoldering onset for the sample with a diameter of 25 mm compared to that for the sample with a diameter of 60 mm. Until the onset of the oxidation of the sample with a diameter of 60 mm, its lower face temperature was higher than that of the sample with a diameter of 25 mm. Because of the difference of latent heat release, the lower face temperature of the sample with a diameter of 25 mm was lower than that of the sample with a diameter of 60 mm. The diameter had no effect on the peak temperature of the upper face temperature. There was the shoulder peak for the mass loss rate for the sample with a diameter of 25 mm, which was different from the single peak for the sample with a diameter of 60 mm. The shoulder might be attributed to the sequential oxidation reaction of both sides and the heating of the oxidation reaction for the entire sample.

Figure 10 presents the thickness and diameter effect on smoldering characteristic values for samples with a diameter of 60 mm. The increment of the size (both thickness and diameter) held the lower peak burning rate and the larger burning duration time. Thus, smoldering ignition should be significantly more sensitive to sample thickness than to sample diameter in the size range studied.

CONCLUSION

In this experimental work, we found that the ignition difficulty of the stationary disc-shaped wood particle increases from smoldering ignition to piloted flaming

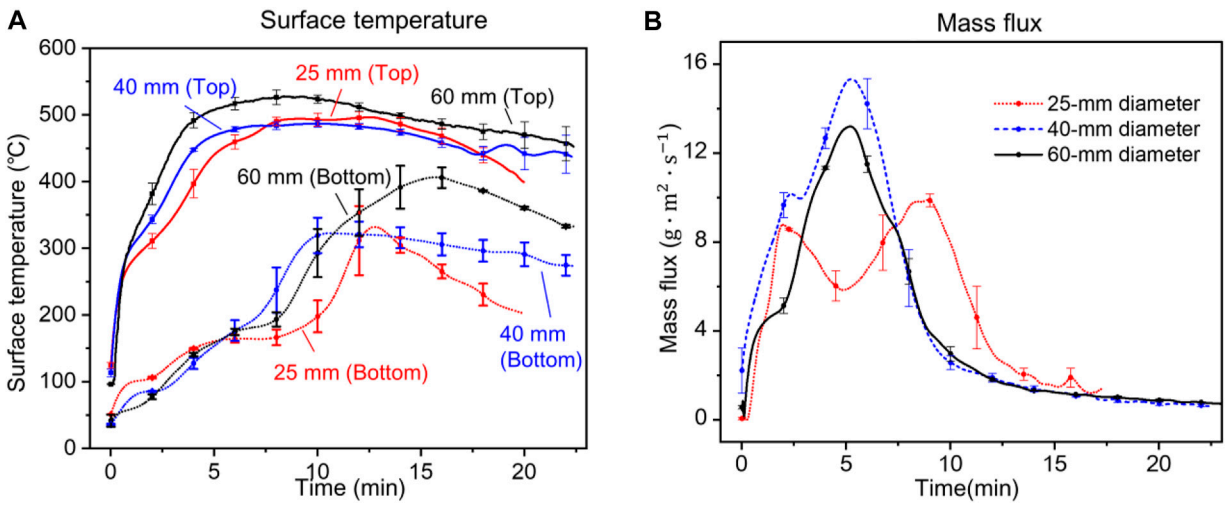

FIGURE 9 | Surface [upper (U) and lower (L)] temperature **(A)** and mass flux **(B)** vs. time: diameter effect on smoldering combustion for 10-mm-thick samples.

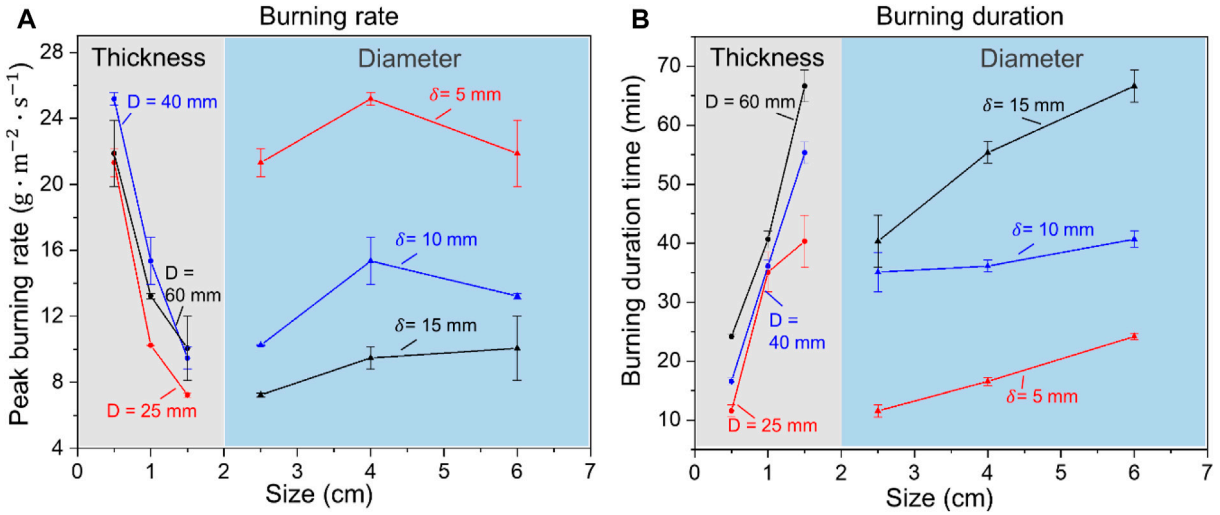

FIGURE 10 | Summarized size (thickness and diameter) effect on smoldering characteristics: **(A)** peak mass flux and **(B)** burning duration or burnout time.

ignition and then to flaming autoignition, as the required minimum heat flux approximately increases from 10 kW/m^2 to 30 kW/m^2. Compared to the smoldering ignition, the flaming autoignition is very sensitive to the fuel thickness (5–15 mm), while the effect of diameter (25–60 mm) is negligible. The ignition temperature, minimum heat flux, and burning duration of flaming all increase, while the peak burning flux decreases, as the wood thickness increases.

During the ignition and the following burning processes, the disc-shaped particle was first deformed to a bowl shape and then to an umbrella shape due to the interaction between chemical reactions and thermomechanical stresses. The characteristic thickness of the smoldering front on wood is also found to be 10–15 mm. This study helps understand the interaction between flaming and smoldering wildfires and the deformation behaviors of the wood particles in wildfires. In our future work, numerical simulations will be conducted to reproduce the deformation behaviors of wood particles and improve the up-to-date pyrolysis modeling technology.

DATA AVAILABILITY STATEMENT

The raw data supporting the conclusions of this article will be made available by the authors, without undue reservation.

AUTHOR CONTRIBUTIONS

SW: conceptualization, methodology, writing—original draft, formal analysis, and funding acquisition. PD: investigation, resources, and writing—original draft. SL: investigation, writing—review and editing, and formal analysis. JG: investigation and resources. XH: methodology, formal analysis, supervision, and writing—review and editing.

FUNDING

This work is supported by the National Natural Science Foundation of China (NSFC nos. 51706095, 51974164, and 51876183), the Natural Science Foundation of Jiangsu Province of China (Grant no. BK20171001), the HK PolyU Postdoctoral Fellowship (Grant no. P0014039) and RISUD Emerging Frontier Area (EFA) Scheme (P0013879), and the China Postdoctoral Science Foundation (Grant no. 2017M611798).

SUPPLEMENTARY MATERIAL

The Supplementary Material for this article can be found online at: https://www.frontiersin.org/articles/10.3389/fmech.2021.686638/full#supplementary-material

REFERENCES

Atreya, A., Olszewski, P., Chen, Y., and Baum, H. R. (2017). The Effect of Size, Shape and Pyrolysis Conditions on the thermal Decomposition of wood Particles and Firebrands. *Int. J. Heat Mass Transfer* 107, 319–328. doi:10.1016/j.ijheatmasstransfer.2016.11.051

Bilbao, R., Mastral, J. F., Aldea, M. E., Ceamanos, J., Betrán, M., and Lana, J. A. (2001). Experimental and Theoretical Study of the Ignition and Smoldering of wood Including Convective Effects. *Combustion and Flame*. 126, 1363–1372. doi:10.1016/S0010-2180(01)00251-6

Boonmee, N., and Quintiere, J. G. (2002). Glowing and Flaming Autoignition of wood. *Proc. Combustion Inst.* 29, 289–296. doi:10.1016/S1540-7489(02)80039-6

Finney, M. A., Cohen, J. D., Forthofer, J. M., McAllister, S. S., Gollner, M. J., Gorham, D. J., et al. (2015). Role of Buoyant Flame Dynamics in Wildfire Spread. *Proc. Natl. Acad. Sci. USA*. 112, 9833–9838. doi:10.1073/pnas.1504498112

Finney, M. A., Cohen, J. D., McAllister, S. S., and Jolly, W. M. (2013). On the Need for a Theory of Wildland Fire Spread. *Int. J. Wildland Fire*. 22 (2013), 25–36. doi:10.1071/WF11117

Harada, T. (2001). Time to Ignition, Heat Release Rate and Fire Endurance Time of wood in Cone Calorimeter Test. *Fire Mater.* 25, 161–167. doi:10.1002/fam.766

Huang, X., and Gao, J. (2021). A Review of Near-Limit Opposed Fire Spread. *Fire Saf. J.* 120, 103141. doi:10.1016/j.firesaf.2020.103141

Huang, X., and Rein, G. (2017). Downward Spread of Smouldering Peat Fire: the Role of Moisture, Density and Oxygen Supply. *Int. J. Wildland Fire*. 26, 907–918. doi:10.1071/WF16198

Incropera, F. P., and DeWitt, D. P. (1996). *Fundamentals of Heat and Mass Transfer*. John Wiley, New York. doi:10.1016/j.applthermaleng.2011.03.022

Kuo, J. T., and Hsi, C.-L. (2005). Pyrolysis and Ignition of Single Wooden Spheres Heated in High-Temperature Streams of Air. *Combustion and Flame*. 142, 401–412. doi:10.1016/j.combustflame.2005.04.002

Li, K., Hostikka, S., Dai, P., Li, Y., Zhang, H., and Ji, J. (2017). Charring Shrinkage and Cracking of Fir during Pyrolysis in an Inert Atmosphere and at Different Ambient Pressures. *Proc. Combustion Inst.* 36, 3185–3194. doi:10.1016/j.proci.2016.07.001

Lin, S., Huang, X., Gao, J., and Ji, J. (2021). Extinction of Wood Fire: A Near-Limit Blue Flame Above Hot Smoldering Surface. *Fire Technol.* doi:10.1007/s10694-021-01146-6

Lin, S., Huang, X., Urban, J., McAllister, S., and Fernandez-Pello, C. (2019a). Piloted Ignition of Cylindrical Widlland Fuels under Irradiation. *Front. Mech. Eng.* 5, 54. doi:10.3389/fmech.2019.00054

Lin, S., Sun, P., and Huang, X. (2019b). Can Peat Soil Support a Flaming Wildfire?. *Int. J. Wildland Fire*. 28, 601–613. doi:10.1071/WF19018

Liu, Y., Stanturf, J., and Goodrick, S. (2010). Trends in Global Wildfire Potential in a Changing Climate. *For. Ecol. Manage.* 259, 685–697. doi:10.1016/j.foreco.2009.09.002

Manzello, S. L., Cleary, T. G., Shields, J. R., Maranghides, A., Mell, W., and Yang, J. C. (2008). Experimental Investigation of Firebrands: Generation and Ignition of Fuel Beds. *Fire Saf. J.* 43, 226–233. doi:10.1016/j.firesaf.2006.06.010

Manzello, S. L., Suzuki, S., Gollner, M. J., and Fernandez-Pello, A. C. (2020). Role of Firebrand Combustion in Large Outdoor Fire Spread. *Prog. Energ. Combustion Sci.* 76, 100801. doi:10.1016/j.pecs.2019.100801

McAllister, S. (2013). Critical Mass Flux for Flaming Ignition of Wet wood. *Fire Saf. J.* 61, 200–206. doi:10.1016/j.firesaf.2013.09.002

Mcallister, S., and Finney, M. (2017). Autoignition of wood under Combined Convective and Radiative Heating. *Proc. Combustion Inst.* 36, 3073–3080. doi:10.1016/j.proci.2016.06.110

McAllister, S., Grenfell, I., Hadlow, a., Jolly, W. M., Finney, M., and Cohen, J. (2012). Piloted Ignition of Live forest Fuels. *Fire Saf. J.* 51, 133–142. doi:10.1016/j.firesaf.2012.04.001

Moghtaderi, B., Novozhilov, V., Fletcher, D. F., and Kent, J. H. (1997). A New Correlation for Bench-Scale Piloted Ignition Data of Wood. *Fire Saf. J.* 29, 41–59. doi:10.1016/S0379-7112(97)00004-0

Momeni, M., Yin, C., Knudsen Kær, S., and Hvid, S. L. (2013). Comprehensive Study of Ignition and Combustion of Single Wooden Particles. *Energy Fuels*. 27, 1061–1072. doi:10.1021/ef302153f

Moritz, M. A., Batllori, E., Bradstock, R. A., Gill, A. M., Handmer, J., Hessburg, P. F., et al. (2014). Learning to Coexist with Wildfire. *Nature* 515, 58–66. doi:10.1038/nature13946

Paulrud, S., and Nilsson, C. (2004). The Effects of Particle Characteristics on Emissions from Burning wood Fuel Powder. *Fuel* 83, 813–821. doi:10.1016/j.fuel.2003.10.010

Quintiere, J. G. (2006). *Fundamental of Fire Phenomena*. New York: John Wiley. doi:10.1002/0470091150

Rein, G. (2016). Smoldering Combustion. *SFPE Handbook Fire Prot. Eng.* 2014, 581–603. doi:10.1007/978-1-4939-2565-0_19

Rodriguez, A., Huang, X., Link, S., Olson, S., Ferkul, P., and Fernandez-pello, C. (2017). Piloted Ignition of Cylindrical PMMA and Wood. In 12th International Symposium on Fire Safety Science, June 17, 2017, Sweden, 36, 3073.

Rothermel, R. C. (1972). *A Mathematical Model for Predicting Fire Spread in Wildland Fuels*. Intermountain Forest & Range Experiment Station, Forest Service, U.S. Department of Agriculture, Logan, Utah.

Saastamoinen, J. J., Taipale, R., Horttanainen, M., and Sarkomaa, P. (2000). Propagation of the Ignition Front in Beds of wood Particles. *Combust. Flame*. 123, 214–226. doi:10.1016/S0010-2180(00)00144-9

Santoso, M. A., Christensen, E. G., Yang, J., and Rein, G. (2019). Review of the Transition from Smouldering to Flaming Combustion in Wildfires. *Front. Mech. Eng.* 5. 49. doi:10.3389/fmech.2019.00049

Simms, D. L., and Law, M. (1967). The Ignition of Wet and Dry wood by Radiation. *Combust. Flame* 11, 377–388. doi:10.1016/0010-2180(67)90058-2

Sullivan, A. L., Surawski, N. C., Crawford, D., Hurley, R. J., Volkova, L., Weston, C. J., et al. (2018). Effect of Woody Debris on the Rate of Spread of Surface Fires in forest Fuels in a Combustion Wind Tunnel. *For. Ecol. Manage.* 424, 236–245. doi:10.1016/j.foreco.2018.04.039

Terrei, L., Acem, Z., Georges, V., Lardet, P., Boulet, P., and Parent, G. (2019). Experimental Tools Applied to Ignition Study of spruce wood under Cone Calorimeter. *Fire Saf. J.* 108, 102845. doi:10.1016/j.firesaf.2019.102845

Toledo, T., Marom, I., Grimberg, E., and Bekhor, S. (2018). Analysis of Evacuation Behavior in a Wildfire Event. *Int. J. Disaster Risk Reduction* 31, 1366–1373. doi:10.1016/j.ijdrr.2018.03.033

Wang, H., van Eyk, P. J., Medwell, P. R., Birzer, C. H., Tian, Z. F., and Possell, M. (2016). Identification and Quantitative Analysis of Smoldering and Flaming Combustion of Radiata Pine. *Energy Fuels* 30, 7666–7677. doi:10.1021/acs.energyfuels.6b00314

Wang, H., van Eyk, P. J., Medwell, P. R., Birzer, C. H., Tian, Z. F., Possell, M., et al. (2017a). Effects of Oxygen Concentration on Radiation-Aided and Self-Sustained Smoldering Combustion of Radiata Pine. *Fire Saf. J.* 31, 427–443. doi:10.1016/j.firesaf.2006.03.006

Wang, S., Huang, X., Chen, H., and Liu, N. (2017b). Interaction between Flaming and Smouldering in Hot-Particle Ignition of forest Fuels and Effects of Moisture and Wind. *Int. J. Wildland Fire* 26, 71–81. doi:10.1071/WF16096

Wang, S., Ding, P., Lin, S., Huang, X., and Usmani, A. (2021). Deformation of wood Slice in Fire: Interactions between Heterogeneous Chemistry and Thermomechanical Stress. *Proc. Combust. Inst.* 38, 5081–5090. doi:10.1016/j.proci.2020.08.060

Wesson, H. R., Welker, J. R., and Sliepcevich, C. M. (1971). The Piloted Ignition of wood by thermal Radiation. *Combust. Flame* 16, 303–310. doi:10.1016/S0010-2180(71)80101-3

Williams, F. A. (1982). Urban and Wildland Fire Phenomenology. *Prog. Energ. Combust. Sci.* 8, 317–354. doi:10.1016/0360-1285(82)90004-1

Yang, L., Zhou, Y., Wang, Y., Dai, J., Deng, Z., and Zhou, X. (2011). Autoignition of Solid Combustibles Subjected to a Uniform Incident Heat Flux: The Effect of Distance from the Radiation Source. *Combust. Flame*. 158, 1015–1017. doi:10.1016/j.combustflame.2011.01.008

Conflict of Interest: The authors declare that the research was conducted in the absence of any commercial or financial relationships that could be construed as a potential conflict of interest.

APPENDIX

A high-speed camera was used to trace the splash phenomenon for the sample with a diameter of 60 mm and a thickness of 10 mm, and the result is shown in **Figure A1**. The original video can be found in **Supplementary Video S4**. Here, the starting point (i.e., 0 ms) was set at the moment that the record was started. The crack occurred at 72 ms on the sample surface, and splashing occurred with the tiny particles quickly flying out from the fracture at 102 ms. The splashing phenomena would be sustained for hundreds of milliseconds. During this time, there was also the dropping of the ember from the sample at 144 ms and generating many small embers nearby.

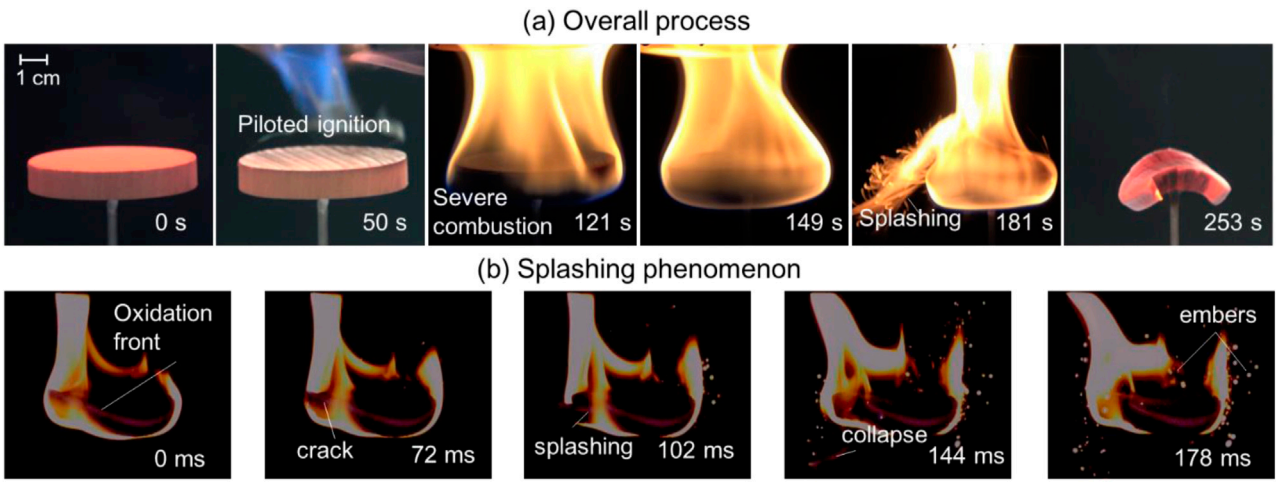

FIGURE A1 | Example of **(A)** overall flaming ignition and burning process and **(B)** splashing process is traced using a high-speed camera at 500 fps of the disc diameter of 60 mm and the disc thickness of 10 mm (**Supplementary Video S4**).

frontiers in Mechanical Engineering

ORIGINAL RESEARCH
published: 05 August 2021
doi: 10.3389/fmech.2021.653810

Sensitivities of Porous Beds and Plates to Ignition by Firebrands

Derek Bean and David L. Blunck *

Mechanical, Industrial and Manufacturing Engineering, Oregon State University, Corvallis, OR, United States

The increasing occurrence of severe wildfires, coupled with the expansion of the wildland urban interface has increased the number of structures in danger of being destroyed by wildfires. Ignition by firebrands is a significant avenue for fire spread and structure loss; thus, understanding processes and parameters that control the ignition of fuel beds by firebrands is important for reducing these losses. In this study the effect of fuel bed characteristics (i.e., particle size and porous or solid fuel bed) on ignition behavior was considered. Modelling and analysis was conducted to better understand parameters that are dominant in controlling ignition. The fuel beds, made from Douglas-fir shavings, Douglas-fir plates, or cardboard plates, were heated with a cartridge heater (i.e., surrogate firebrand) to observe ignition. Smaller particles were observed to ignite more readily in porous beds than larger particles when heat transfer from the heater is primarily through conduction. This occurs in large part due to differences in contact area between the fuel bed and the heater coupled with thermal properties of the fuel bed. As particle sizes increased, ignition was more likely to occur at extended times (>100 s) due to the increased importance of radiation heat transfer. Douglas-fir plates were primarily observed to ignite at times where conduction was the dominant mode of heat transfer (<10 s). Heat flux delivered to the fuel bed was observed to be a more accurate predictor of ignition likelihood and ignition time than heater temperatures. The characteristic ratio of transport and chemical timescales can be used, in conjunction with the measured heat flux and thermal diffusivity of the fuel beds, as a first approximation to predict ignition for the porous fuel beds. This suggests that future work focusing on these parameters may produce a general characterization of fuel bed ignition probability across fuel beds materials and morphologies.

Keywords: ignition, firebrands, wildland urban interface, wildfire, combustion

OPEN ACCESS

Edited by:
Sayaka Suzuki,
National Research Institute for Fire and Disaster, Japan

Reviewed by:
Haixiang Chen,
University of Science and Technology of China, China
Supan Wang,
Nanjing Tech University, China

***Correspondence:**
David L. Blunck
David.Blunck@oregonstate.edu

Specialty section:
This article was submitted to Thermal and Mass Transport, a section of the journal Frontiers in Mechanical Engineering

Received: *15 January 2021*
Accepted: *23 July 2021*
Published: *05 August 2021*

Citation:
Bean D and Blunck DL (2021) Sensitivities of Porous Beds and Plates to Ignition by Firebrands. Front. Mech. Eng 7:653810. doi: 10.3389/fmech.2021.653810

1 INTRODUCTION

Increasing urban expansion into the wilderness has increased the area of the wildland urban interface (WUI). The increase of the WUI, coupled with global climate change has resulted in fires of increasing severity, size, and impact to humans. For example, consider the state of California in the United States, where four of the five largest fires and three of the five most destructive fires have occurred in the past decade (Cal Fire, 2019; 2018). These fires highlight a trend in the increasing severity of wildfires. Of particular concern with the increasing severity of wildfires is the severity of fires in the WUI. The 2018 Camp fire, where residential property losses amounted to more than twice the reported costs for nationwide federal suppression efforts during the same year (U.S. Department of Interior/U.S. Department of Agriculture, F. S, 2020; California Department of Insurance, 2019), is

a stark example of how severe a fire that occurs in the WUI can be. A significant mechanism for the spread of fires into the WUI, or even within the WUI, is the ignition of fuel beds by firebrands (Mell et al., 2010; Maranghides et al., 2013). Ignition by firebrands in wildfires occurs when a hot combusting particle is generated within the fire and transported, typically by wind, to a recipient fuel bed (Koo et al., 2010). Structures in the WUI often have geometry conducive to the collection of firebrands, further increasing the risk of ignition (Suzuki and Manzello, 2020). Hence, efforts to mitigate the destruction that can be caused by fires in the WUI must consider the role of ignition by firebrands.

Three primary processes control the ignition of fuel beds by firebrands. Specifically, heat transfer between the fuel bed and the firebrand, pyrolyzate generation in the fuel bed, and the mixing of the pyrolyzates above the bed at sufficient temperatures for ignition to occur (Babrauskas, 2003). A recent review of the role of firebrands in the spread of fires by Manzello et al. (2020) identified that research into the ignition behavior of fuel beds by firebrands is critical to improving preventative measures. Work conducted by Manzello et al. (2006a, 2006b), Manzello et al. (2008) studying ignition of various fuel bed materials (e.g., cut grass and pine needle beds) concluded that the most influential factors for ignition were the number flux of firebrands to the fuel bed, the size of the firebrands, and the airflow over the fuel bed. Similar conclusions were found by Urban et al. (2019), who found that larger firebrands were more likely to ignite fuel beds (i.e., fine sawdust) across a range of fuel moisture contents. These observations illustrate the critical role of heat transfer to the fuel bed in causing ignition. What is not clear from studies such as these is how ignition behavior would change for fuel beds other than those tested, even if identical firebrands were used. Even how the size of fuel particles alter ignition is not clear. Such knowledge is needed to help transition knowledge to a variety of fuel beds that can be present near the WUI (e.g., wood shavings, needles, leaves, etc.).

Essential to understanding the ignitablility of fuel beds is understanding how the role of heat transfer and energy of a firebrand influences ignition. Hadden et al. (2011) found that as the energy content of hot metal particles increased the ignition probability increased. It was also observed that the particle energy alone is not a sufficient condition for ignition to occur and that a minimum particle temperature is required. Similarly, Zak et al. (2014) observed that the energy of a metal particle was not a sufficient parameter for ignition and minimum values for particle energy and temperature are required; the values of which are dictated by the ability of hot particles to generate sufficient amounts of hot pyrolyzates in fuel beds. Further studies by Fernandez-Pello et al. (2015) added to the understanding of these factors concluding that heat losses from the hot particle, which reduce the heat flux to the fuel bed, can have a significant impact on the ignition of fuel beds. Additional studies conducted by Urban et al. (2017), Urban et al. (2018) found that the timescale of flaming ignition can be relatively short (≤100 ms). Furthermore, smaller fuel bed particles tended to ignite at lower metal particle temperatures. A sensitivity of ignition to the chemical composition of the fuel bed was also observed. While sensitivities to fuel bed particle size, ember particle size, and ember energy have been observed, the relative effect of each parameter on ignition limits and a general application of these sensitivities across various fuel beds and embers remains elusive.

Studies evaluating the heat flux of firebrands and the critical heat flux for ignition have yielded further insights into the ignition process. Hakes et al. (2019) found that, for a single cylindrical firebrand and piles of firebrands, peak heat flux values ranged between 20 and 60 $kW\,m^{-2}$ with average heat fluxes between 12 and 25 $kW\,m^{-2}$. The mass of the firebrands or piles of firebrands had little effect on the peak heat flux but directly influenced the total energy released. Tao et al. (Tao et al., 2020) observed similar heat fluxes for various of natural and manufactured firebrands. Both Hakes et al. (2019) and Tao et al. (2020) observed that an increase in wind speed significantly increased the measured heat flux. Hernández et al. (2018) found that Monterey Pine (*Pinus radiata*) needles ignited under heat flux as low as 10 $kW\,m^{-2}$ with ignition time decreasing proportionally to the inverse square of increasing heat flux. In similar tests but with different fuels, Rivera et al. (2020) observed that critical heat fluxes for ignition were highly dependent on fuel bed properties with the critical radiative heat flux increasing as the porosity decreased. Reported critical values ranged from 6.64 to 20.85 $kW\,m^{-2}$ for Monterey Pine needles with porosities of 0.09 and 0.01, respectively. It has been observed that a variety of firebrands are capable of producing heat fluxes well above the critical heat flux values long enough for ignition in some fuels. However, upon comparing these values to other studies, ignition is not guaranteed if the critical heat flux rate and duration are met. For example, experiments conducted by Manzello et al. (2008) used firebrands similar to Hakes et al. (2019) and Tao et al. (2020) with fuels similar to Hernández et al. (2018) and Rivera et al. (2020) (e.g., wooden disks on pine needles) but did not observe ignition under conditions that would be anticipated to produce ignition. It should be noted that the studies conducted by Hernandez et al. and Rivera et al. were conducted under quiescent conditions and those by Manzello et al. between 0.5 and 1.0 $m\,s^{-1}$. Nevertheless, the reported values of firebrand heat flux at 0.5 and 1.2 $m\,s^{-1}$ conditions by Tao et al. suggest ignition is likely to occur for instances where no ignition was observed. Not observing ignition under conditions at the apparent intersection of these findings suggests that other factors may be as important as heat flux and duration of heating.

Given this background and motivation the objective of this work is to identify how the size of fuel particles influences ignition and to ascertain changes in ignition of porous and solid fuels. Time to ignition tests with a cartridge heater were conducted to elucidate this sensitivity. It is anticipated that the observations from this study will enhance the understanding of fuel bed ignition and enable more focused studies regarding additional effects of fuel bed properties on ignition.

2 METHODOLOGY

The time to ignition was measured for five different fuel bed conditions with varying surface temperatures of a resistance

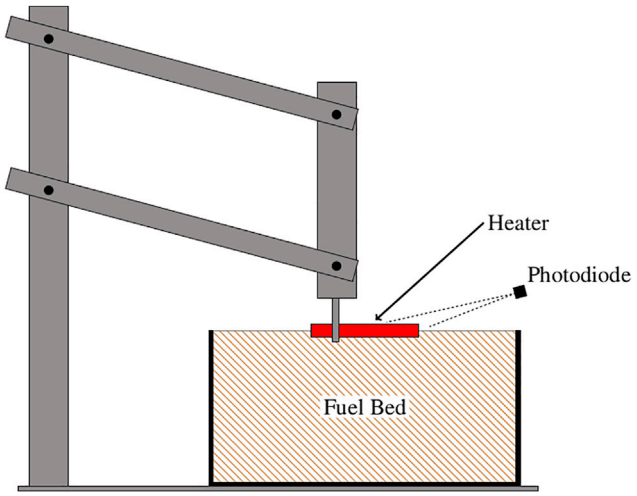

FIGURE 1 | Experimental apparatus for the ignition propensity tests. The lever arm used to lower the apparatus into the fuel bed, the fuel bed size relative to the heater, and the location of the photodiode are illustrated.

heater. The time to ignition was the metric used to evaluate the ignition propensity. The experimental apparatus, as illustrated in **Figure 1**, was designed to replicate both conduction and radiation that may occur when a firebrand lands on the fuel bed. The heater was held in place by a lever arm that, when lowered, positioned the heater at a fixed location for the duration of the test. The firebrand was represented by a 6.35 mm diameter 51 mm long cartridge heater capable of a 250 W output. The heater was inserted 3 mm into the bed (approximately half the diameter) in the porous media tests and on top of the plates for the other experiments. The temperature of the heater was continually recorded *via* a type-K thermocouple attached to the top of the heater. An important distinction between using the lever arm holder and a naturally occurring firebrand is that the location of the heater remained fixed and, for times greater than roughly 10 s, could lose contact with the fuel bed as material was lost because of pyrolysis. Thus, for the longer ignition experiments the arrangement mimicked a firebrand with a gap between it and the fuel bed, instead of a firebrand that maintained consistent contact. The rationale in using the lever arm was to ensure that the heater was placed a consistent depth within the fuel bed since sensitivities of ignition to heat source penetration depth have been observed by Wang et al. (2015). The temperature of the heater was held to within ±6% of the set point using PID control implemented in LabVIEW. Power delivery to the heater was measured at a rate of 1 kHz for all tests. Admittedly, the temperature and heat transfer from an actual firebrand to a fuel bed may vary more than that of a controlled heater, nor does the heater have a piloted ignition source. Nonetheless, trends of ignition propensity are expected to be similar between the heater and firebrands since the heat transfer rates calculated in these experiments are in the range of 1–21 kW m^{-2} which are comparable to heat flux values reported by Hakes et al. (2019) and Tao et al. (2020) for combustion of glowing firebrands on an instrumented surface. The advantage of using a heater was that it allowed sensitivities of ignition to the fuel beds and controlling processes to more readily be identified because the boundary conditions were measured, controlled, and consistent.

Wood particles and flat plates were used as the fuel bed materials. The fuel particles were Douglas-fir (*Pseudotsuga menziesii*) shavings sorted into three size classes: L_c < 1mm, 4 mm < L_c < 6 mm, and 6 mm < L_c < 12 mm to allow sensitivities of ignition to be identified. Fuel particles were generated by processing Douglas-fir lumber through a planer and then sorted by screening and/or granulating to achieve the desired size distribution. The fuels were placed in a glass container with a diameter 140 mm and a depth of 70 mm. The container was filled to the rim for the porous media tests, but the fuels were not packed. The materials used for the tests with flat plates were Douglas-fir and corrugated cardboard processed into 75 mm-by-75 mm squares. The thickness of the Douglas-fir and cardboard plates were 5 and 6 mm respectively. For plate ignition tests, the plates were stacked in the container to be level with the rim, replicating the porous media tests as close as possible.

The time to ignition was determined from the signal emitted from a BPX65 photodiode positioned to capture the lowering of the cartridge heater and the flames resulting from ignition. This measurement approach only considered flaming ignition. The time to ignition was defined as the time between the maximum light intensity gradients, which corresponds to lowering the heater onto the fuel bed and the ignition event. The photodiode was sampled at 1 kHz. Consistency in airflow, and thus oxygen availability, was achieved by maintaining the apparatus in the same orientation in a fume hood with the same airflow settings for every test. The average air velocity over the fuel bed was measured using a hot wire anemometer (TSI IFA300). Measurements were taken with the sample bowl filled with fuel particles and the heater in the lowered testing position at room temperature with the probe positioned approximately 16 mm above the fuel bed. The average air velocity over the fuel bed was 0.1 m s^{-1}.

The heat transfer to the fuel bed was estimated by applying an energy balance around the heater using the supplied (measured) power to the heater and subtracting the calculated infrared radiation losses to the surroundings. The heat flux was determined by normalizing the heat transfer to the heater by one-half of the surface area of the heater. This surface area was justified as the heater was inserted to a depth of half the diameter for each test. Heat loss to the surroundings was estimated by measuring temperatures along the length of the heater but with no fuel bed material in the apparatus. These temperature profiles were then used to estimate the heat losses to the ambient. The emissivity of the heater was taken to be 0.60 (Watlow, 2020). Heat flux values were calculated as an average for the duration of the test, and for a 200 ms window when the heater made contact with the fuel bed. These two time scales allowed differences in sensitivities between average and initial heat flux to be observed. The heat flux values provide insights into variations in the characteristic rate of heat transfer from the heater to the fuel bed for each of the materials tested. Combining the heat flux for each material with the estimated thermal

TABLE 1 | Measured $\bar{\rho}$ and estimated (k) fuel bed properties.

Material	$\bar{\rho}$ (kg m−3)	k (W m−1 K−1)
Douglas-fir plates	510	0.120
L_c < 1 mm	135	0.042
4 mm < L_c < 6 mm	69.9	0.034
6 mm < L_c < 12 mm	36.9	0.030
Cardboard plates	115	0.053

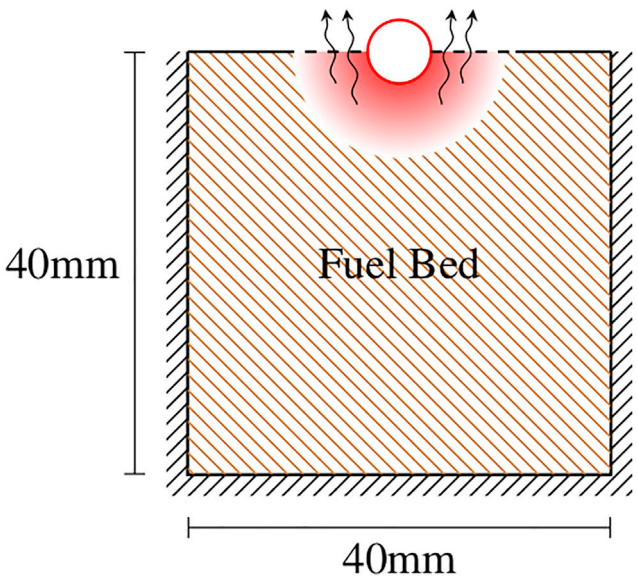

FIGURE 2 | Diagram of the computational domain where black lines indicate domain boundaries, and red lines are boundaries defined by the heater. The arrows denote flow of pyrolysis products from the fuel bed into the air above the fuel bed.

conductivity of the fuel bed enabled representative temperature distributions within the fuel bed to be determined. It is acknowledged that the processes addressed in this work are transient, thus the thermal diffusivity of the materials is applicable. However, thermal conductivity is considered here because the calculation of the thermal conductivity relies on fewer correlations and is potentially more accurate. Additionally, the thermal properties of the materials are derived from literature such that both properties are directly proportional to the experimentally obtained bulk density. Thermal conductivity of the fuel bed materials were estimated using the mean of minimum and maximum effective thermal conductivity correlations in porous media (Incropera et al., 2011). The correlation for effective thermal conductivity is shown in **Equation 1** where ϵ is defined as the proportion of volume occupied by air, as is shown in **Eq. 2**.

$$k_{eff} = \frac{1}{2}\left(\frac{1}{(1-\epsilon)/k_{solid}+\epsilon/k_{air}} + \epsilon\, k_{air} + (1-\epsilon)k_{solid}\right) \quad (1)$$

$$\epsilon = 1 - \frac{\rho_{solid}}{\rho_{bed}} \quad (2)$$

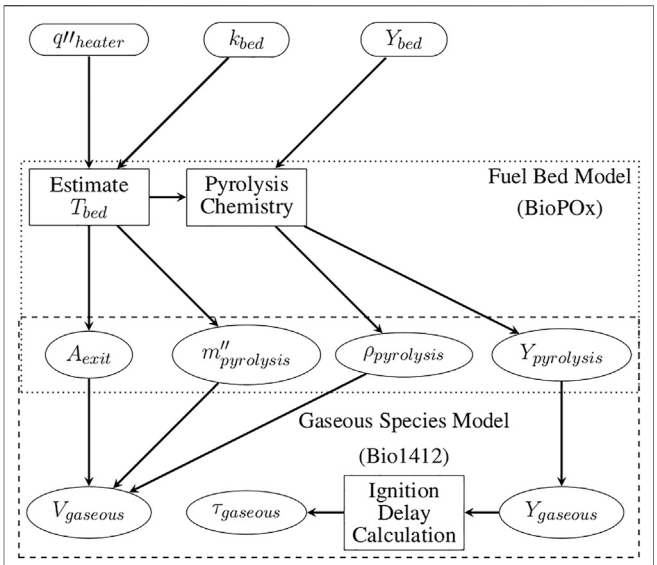

FIGURE 3 | Illustration of the model used for the estimated heater flux (q''_{heater}), thermal conductivity of the fuel bed (k_{bed}), and chemical composition of the fuel bed (Y_{bed}), (e.g., cellulose) to calculate temperature (T) and pyrolyzate distribution above the fuel bed, and determine the resulting ignition delay times(τ). Here the subscript *bed* represents the properties of the fuel bed materials and *pyrolysis* represents the pyrolysis products leaving the fuel bed and entering the air above the fuel bed. For example, $V_{pyrolysis}$ represents the velocity of pyrolysis gases leaving the fuel bed and entering the quiescent air domain.

The thermal conductivity of Douglas-fir plates and corrugated cardboard plates were obtained from literature (Forest Products Laboratory, 2010; Asdrubali et al., 2015). The bulk density of the porous material (ρ_{porous}) and the solid (ρ_{solid}) were obtained from experimental samples. **Table 1** shows the mean bulk density for each material and the corresponding estimated thermal conductivity values for the porous materials and the solid plates. The values shown in **Table 1** were used as inputs to the computational models, as discussed later.

Three simplified models were implemented to obtain further insights into the physical and chemical processes causing trends observed in the experimental ignition efforts. First, the temperature evolution of the fuel bed was modeled. Second, the time-averaged mass flux and species concentrations of the pyrolysis species leaving the fuel bed and entering the air were estimated using the calculated temperatures of the fuel bed. Third, the ignition delay times of the gaseous pyrolysis species estimated to depart the fuel bed were calculated. Time-averaged and spatially constant values were used for mass flux and mass fraction of pyrolysis products leaving the fuel bed. **Figure 2** shows the computational domain representing the fuel bed. **Figure 3** shows the data flow between the models where the rectangles indicate the implementation of a model or calculation, ellipses indicate an output of interest, and the rounded rectangles indicate an input from measurements or literature values. The dotted and dashed boxes outline which calculations pertain to each chemical mechanism used and the overlap shows the information that is transferred between the models. The fuel bed temperature was

modeled using OpenFOAM (The OpenFOAM Foundation, 2020). Modeling of the pyrolysis was conducted using Cantera (Goodwin et al., 2020) with the BioPOx mechanism (Dhahak et al., 2019). The Bio1412 mechanism (Ranzi et al., 2001, 2008) was used for gas phase species exiting the fuel bed. The Bio1412 mechanism contains 137 species and 4,533 reactions. The BioPox mechanism contains 710 species, 5,035 reactions and includes both primary pyrolysis and secondary pyrolysis. The inclusion of secondary pyrolysis is important for the combustion of products in the fuel beds studied since the particle fuel beds contain air that may affect the composition of gases as they leave the fuel bed.

Modeling of the temperature evolution of the fuel bed was implemented to represent what occurs during the experiments. The domain size for the fuel bed was 40 mm wide and 40 mm in depth and ensured that wall effects did not influence the heat transfer over the 10 s of simulations. The 10 s time limit was chosen since the majority of experimental ignitions occurred before 10 s, as explained shortly. Additionally, it was observed in experiments that the fuel bed began to lose contact with the heater beginning near 10 s, potentially reducing the applicability of the model beyond this time. All sides of the fuel bed domain were treated as insulated, aside from the heater interface. The insulated sides and bottom of the domain are representative of experimental conditions, but the insulated top surface does not account for losses due to convection or radiation from the fuel bed materials. Nonetheless the calculated temperature distribution within the fuel beds are expected to be valid because heat transfer is dominated by conduction. Reactions and mass loss are not considered in determining the temperature distributions of the fuel beds. Despite these limitations, the calculated temperature distributions provide insights into the mass of each fuel bed material that undergoes pyryolysis which in turn is used for understanding the experimental results.

Combustion of the fuel bed materials was considered in two steps. Reactions occurring within the domain of the fuel bed were characterized with the BioPOx mechanism to include both pyrolysis and gas phase reactions. Reactions occurring at the exit of the fuel bed were considered solely gas phase, thus the Bio1412 mechanism was used. Chemistry calculations for both domains were performed in Cantera. A detailed chemistry model was considered to best capture the physics of the ignition process. However, a detailed discussion of differences in chemistry leading up to ignition are beyond the scope of this work. Instead, this work focuses on qualitative insights into ignition behavior. The mass of the fuel bed undergoing pyrolysis was defined as the mass of the fuel bed material above 220°C. 220°C was selected as it corresponds to the onset of hemicellulose pyrolysis (Yang et al., 2007) and is the lowest temperature estimated for reactions to occur encapsulating the potential breakdown of all constituents. The temperature at which pyrolysis occurred was taken as the average temperature of the fuel bed material above the temperature threshold. This step was necessary since the Cantera calculations performed were 0D. This approach provided an estimate of the average mass per unit time undergoing pyrolysis reactions. The exit area of the pyrolysis products was assumed to be constant for the duration of the test and was defined by the surface area of the fuel bed adjacent to the heater above the pyrolysis temperature at 10 s. Species were anticipated to depart the fuel bed and participate in gas phase reactions if they were included in both mechanisms. The mass flux of species departing the fuel bed was defined as the mass fraction of the gas phase species in the fuel bed relative to the mass of the fuel bed undergoing pyrolysis (T > 220°C) divided by the surface area of the fuel bed above the pyrolysis temperature as shown by the dashed lines in **Figure 2**. While in a physical experiment the mass flux and exit area would vary with time, all materials were treated equally in this study for simplicity and consistency in generating and understanding trends.

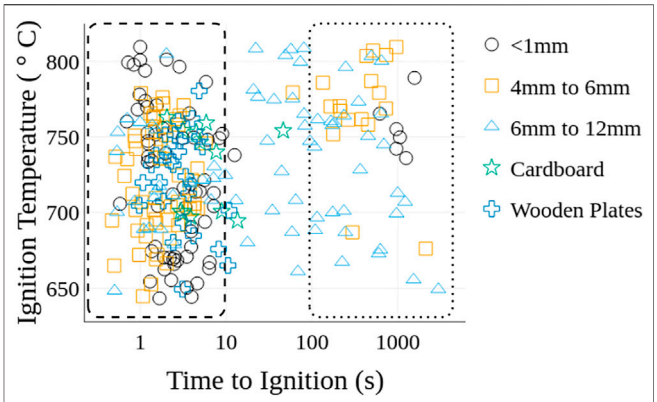

FIGURE 4 | Time to ignition and heater temperature at ignition for all fuel bed materials. The dashed and dotted boxes emphasize the two general times-scales associated with ignition.

3 RESULTS

The time required for flaming ignition to occur for the various fuel beds is shown in **Figure 4** as a function of heater set point temperature. Four observations are noted. First, the ignition times generally occurred within the first 10 s. If ignition did not occur after 10 s then it would typically take between 100 and 1000 s to ignite, if at all. Conditions where ignition did not occur are not included in **Figure 4**. A histogram of ignition times and the probability density for each material are shown in **Figure 5** to further quantify the distribution of ignition times. The probability density of the L_c < 1 mm fuel particles, Douglas-fir plates, and cardboard plates are normally distributed with centers at 2.3, 2.8, and 3.9 s. The L_c < 1 mm fuel particles have an outlier peak centered at 1,000 s. The 4 mm < L_c < 6 and 6 mm < L_c < 12 mm fuel particles are bimodal with highest density peaks at 1.7 and 113 s respectively. The secondary peaks occur at 113 s for the 4 mm < L_c < 6 mm fuel particles and 2.1 s for the 6 mm < L_c < 12 mm fuel particles. Second, the probability of ignition at extended times increased as the particle sizes increased. Specifically, the proportion of ignition events where t_{ign} < 10 s group were 90, 77, and 47% for the L_c < 1mm, 4 mm < L_c < 6 mm, and 6 mm < L_c < 12 mm particle sizes, respectively. The third observation is that ignition was not observed beyond 100 s for

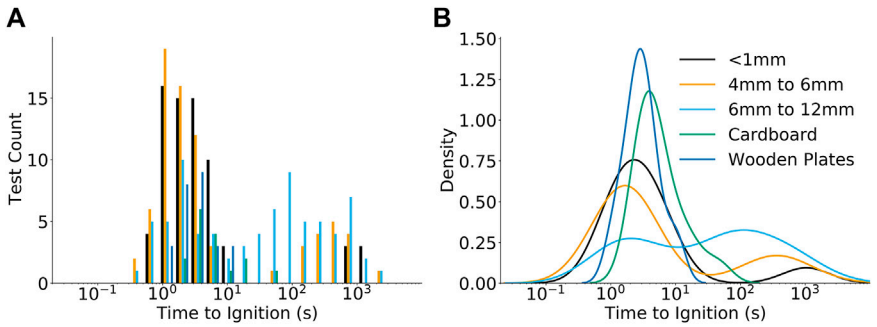

FIGURE 5 | Ignition count **(A)** and probability density **(B)** of time to ignition for the fuel bed materials tested. The dashed and dotted boxes corresponding to the two zones of ignition from **Figure 4**.

either of the solid plate fuel bed materials. Trends in ignition times for the plates were most similar to those for beds with the smallest particles. Fourth, for the ignition events that occurred within the first 10 s there is no apparent relationship between time to ignition, temperature, particle size, and fuel bed type. Additionally, the long timescales of some ignition events suggest that smoldering initiates and then transitions to flaming combustion. Since the incidence of ignition at extended times increases as the particle size increases the potential for smoldering to flaming transition is attributed to thermal and physical properties of the fuel bed. The different sensitivities of ignition just described are attributed to differences in the bulk thermal properties, the interface between the heater and fuel bed, and the global equivalence ratio of the fuel bed, as explained later.

The clustering of ignition times in either the $t_{ign} < 10$ or $100\ s < t_{ign} < 1000$ s time-scales is attributed to shifting of dominant heat transfer modes from conduction to radiation. This shift occurs because of the heater fixture apparatus and the physical properties of the fuel beds. Initially, the heater and the fuel bed are in contact. The beds with larger particles have lower bulk densities; larger fractions of the fuel bed consist of air and have less contact area between particles. As a result, the effective thermal conductivity of the fuel beds decreases as the particle size increases as is shown in **Table 1**. For a fixed heater temperature the higher effective thermal conductivity for the smaller particles would result in a higher mass of particles above the pyrolysis temperature (as supported by calculations) producing conditions more conducive to ignition. As particle sizes decrease the pyrolysis products are also in closer proximity to the heater increasing the chances of either heating or piloted ignition as the gas flows over the heater. As a result, a larger percentage of smaller particle fuel beds ignite within 10s, than the larger particle fuel beds (i.e., the second trend noted for **Figure 4**). As heating progresses, a separation between the fuel bed and heater occurred because the heater was held in a fixed location while the fuel bed height decreased because of pyrolysis. Anecdotally this separation was observed to occur after ≈10 s for the various fuel beds. This separation causes the dominant mode of heat transfer to shift from conduction to infrared radiation. This change is significant because it corresponds to ignition times to shifting from being less than 10 s to being generally greater than 100 s, as shown in **Figure 5**. In addition, the larger particles tended to be longer thin particles which, on average, have a larger view factor per volume than the smaller particles. Hence, higher energy deposition per volume occurs for the larger particles when radiation is the dominant mode of heat transfer. As a result, the larger particle fuel beds more readily receive radiation and more readily ignite for $t_{ign} > 100$ s, consistent with the trends discussed previously. The shift in dominant modes of heat transfer also causes solid plate fuel beds to not ignite after 100 s. As separation between the heater and fuel occurs and heat transfer shifts to being dominated by radiation, the higher thermal conductivity of the solid materials (i.e., $k_{solid} = 0.12\ \mathrm{W m^{-1} K^{-1}}$ vs. $k_{<1mm} \approx 0.042\ \mathrm{W m^{-1} K^{-1}}$) reduces the temperature gradients, peak temperatures, and the release of pyrolyzates.

Further analysis of the time to ignition results reaffirm the influence of the fuel bed properties and heat transfer between the heater and fuel bed. A random forest regression model was implemented using the scikit-learn python package (Pedregosa et al., 2011) to identify which parameters were most correlated to the incidence of ignition occurring at either less than or greater than 10 s. The random forest regression model builds a series of independent decision trees based on experimental variables (e.g., average heat flux, particle size, etc.) and determines from those trees which variables have the largest influence on predicting the correct outcome (i.e., flaming ignition). A model is then assembled based on the specific values of each variable that best predict the desired outcome. Of the parameters recorded or calculated from experimental results, the incidence of ignition within each of the time scales was predicted with at least a 90% certainty (out of bag and R^2 validation) when considering the estimated heat flux to the fuel bed, the fuel bed density, the power delivered to the heater at the time of heater contact, and the heater temperature. The power delivered to the heater at the time of heater contact is included as it serves as a comparison for a an initial reference of heat flux by which a comparison between ignitions that occurred in the radiation dominated mode at extended times which may bias the average heat flux values. The importance of these factors highlight the dependencies previously discussed in that the fuel bed properties and heat transfer to the fuel bed significantly influence the time-scales

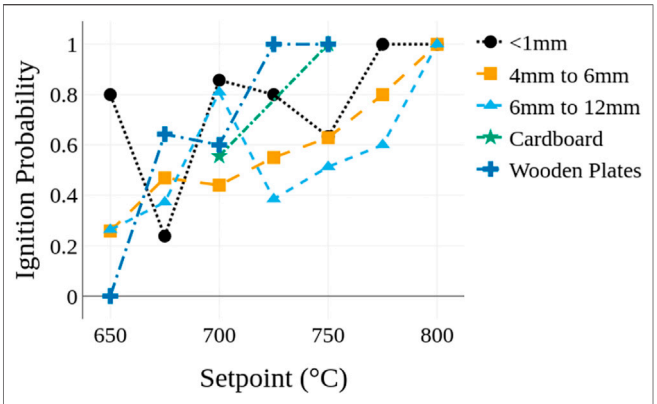

FIGURE 6 | Probability of ignition for each material as a function of heater set point temperature.

associated with ignition. Moreover, the random forest analysis highlights a potential way that ignition may be predicted with a subset of information about the fuel bed.

The results and analysis just described focus on the characteristics of igniting cases; **Figure 6** shows the probability of ignition for each of the fuel bed materials as a function of the heater temperature. The probability reported for each condition is based on the experiments being repeated at least five times. In general, the ignition probability increased as the heater temperature increased, as expected because of the higher energy deposition. It is noted that as the heater temperature increases the potential for piloted ignition of pyrolysis gases increases. However, ignition occurs both above and below the piloted ignition temperature region and there is not a significant shift in trends at higher heater temperatures. This suggests that the influence of piloted ignition on the results is less significant than the increase of heat transfer rates to the fuel beds at higher temperatures.

When considering differences in ignition between fuel bed types the fuel beds with smaller particles typically had higher ignition probabilities at a temperature than beds with larger particles. At the lower temperatures, the plates tended to have lower ignition probabilities than the porous beds, but the plates transitioned from no ignition to unity ignition probability across a narrower range of temperatures than the porous fuel beds. It is noted that significant deviations from the overall trends (i.e., decreases in ignition probability) are apparent for the L_c < 1 mm particles at 675°C and 750°C and for the 6 mm < L_c < 12 mm particles at 700°C. The cause of these deviations are unclear, but it is plausible the changes are caused by differences in ablation of the fuels and shifts in the dominant mode of heat transfer depending on the temperature.

The sensitivities in ignition probability to the fuel bed characteristics, as shown in **Figure 6**, are attributed to changes in area of the fuel bed in contact with the heater. Recall that the samples typically ignite within the first 10 s; hence conduction and the area of the fuel in contact with the heater are important in causing pyrolysis. As the particle size of the fuel bed increases fewer particles come into contact with the heater, reducing the overall contact area. Additionally, the average distance between the heater and particles not in contact with the heater increases as particle size increases due to the reduced packing density of the particles. This may result in heat transfer from infrared radiation occurring over a more distributed volume within the fuel bed. As particle sizes increase the reduction in contact area and more distributed heat flux from radiation likely decrease the temperature gradient in the fuel bed as well as the local heat flux rates immediately adjacent to the heater, ultimately resulting in lower ignition probabilities for a fixed temperature as the particle size increases.

With regards to ignition of the Douglas-fir plates, it is expected that the solid materials behave similarly to the fuel beds with large particles (i.e., lower ignition probabilities at the lower temperatures) because the contact area between Douglas-fir plates and the cylindrical heater are more likely to be similar to the 6 mm < L_c < 12 mm particles than the L_c < 1 mm particles. The Douglas-fir plates also have a much higher thermal conductivity and thermal mass than the particle fuel beds which is anticipated to result in similar temperature gradients between the largest particles and the plates. For the large particles infrared radiation to particles at greater distances from the heater, which would be occluded in the smaller particles, may act similarly to an increase in thermal conductivity and thus the similarity in ignition between the largest particles and Douglas-fir plates. The sharper transition from zero to unity ignition probability for the Douglas-fir plates is attributed to more consistent contact area between the heater and the plates from test to test. This uniformity is indicated in the narrower distribution of ignition times with only a ≈44 s difference between the shortest and longest ignition times for the Douglas-fir plates compared to ≈1550 s for the L_c < 1 mm particles. The narrower transition from non-ignition to ignition and the more consistent times to ignition of the Douglas-fir plates when compared to the particle fuel beds suggest that consistency in material properties and contact area between the heater and the fuel have a significant influence on ignition.

Similar to the time to ignition results, a random forest model was generated to gain insights into which parameters that are measured or derived are the most predictive of the occurrence of ignition of a fuel bed. The estimated heat flux to the fuel bed was the most influential parameter. With the addition of the fuel bed density, heater temperature, and heat flux at contact with the fuel bed the prediction accuracy for ignition was 80%. These values were achieved based a 50% test-train split of the entire dataset with out-of-bag and R^2 validation tests to measure predictive capabilities. The most noteworthy insight from this model is that the estimated average heat flux to the bed over the test duration has a much higher importance than the heater temperature for both porous and solid fuel beds. This is significant since the heat flux values, both upon contact and the overall average, encapsulate the effects of the heat transfer mode to the fuel bed unlike the surface temperature of the heater (or firebrand). A similar sensitivity of heat transferred to the fuel bed influencing ignition was observed by Fernandez-Pello et al. (2015).

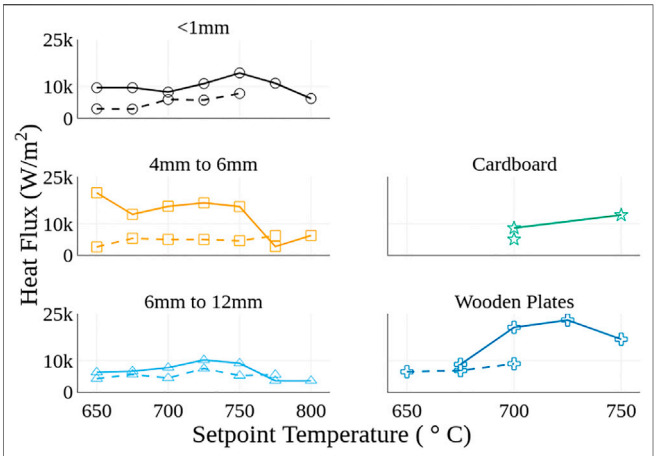

FIGURE 7 | Comparison of estimated heat flux to the fuel bed for each material: dashed lines represents the mean of non-ignition tests and solid lines represent the mean of ignition tests for each heater temperature.

Figure 7 shows the derived average heat fluxes to the fuel bed for each of the materials and heater temperatures tested. Results for igniting cases are represented by solid lines and non-igniting cases are represented with dashed lines. All the materials show two common trends except for cardboard plates, where not enough temperatures were evaluated to determine a trend. First, for tests where ignition occurred, and the heater setpoint was less than or equal to 750°C the heat flux to the fuel bed was higher than tests where ignition did not occur. Recall that the heater temperature is held constant, therefore variations in heat flux represent variations of heat transfer to the fuel. The implications of this are discussed in more detail later. Second, the heat flux values for tests where ignition occurred showed notable decreases in value for temperatures above 750°C, dropping lower than the values for the tests where ignition was not observed, in some cases.

Higher heat fluxes for the igniting cases compared to the non-igniting cases for the porous fuel beds are attributed to stochastic differences in contact area between the heater and the fuel bed particles. Seemingly, the tests with particles oriented in a manner that facilitates greater contact area have a higher heat flux due to increased conduction and are more likely to ignite. However, this assumption breaks down for high heater temperatures. At high heater temperatures (e.g., >750°C) the amount of heat transferred through infrared radiation appears be sufficient to counter differences in contact area and resulting conduction. Hence, this causes the reduction in the differences between igniting and non-igniting heat fluxes at the higher temperatures. A sensitivity to the difference between igniting and non-igniting heat fluxes is noted depending on the particle sizes. Specifically, in **Figure 7**, the 4 mm < L_c < 6 mm particles have greater differences in heat flux between the ignition and non-ignition cases when compared to the 6 mm < L_c < 12 mm and L_c < 1 mm particles. The difference between igniting and non-igniting heat fluxes is correlated to the relative size of the particles compared to the diameter of the heater. For particles much smaller than the heater (<1 mm) the random orientation of the particles would matter less than particles of similar size (4 mm < L_c < 6 mm) as the heater. A similar phenomena is anticipated for particles larger than the heater (6 mm < L_c < 12 mm), however, for the larger particles infrared radiation is anticipated to be more influential than conduction. Changes in contact between the heater and the fuel bed would then have a smaller effect on the rate of heat transfer as is shown by the spread in heat flux between ignition and non-ignition cases for the 6 mm < L_c < 12 mm particles in **Figure 7**. The 4 mm < L_c < 6 mm particles appear to represent a near critical case where the conduction is still the driving heat transfer mode but variation in contact area is high producing a larger spread in heat flux. For the wooden plates a smaller number of heater temperatures with both ignition and non ignition heat flux values is observed suggesting test to test variation in contact area is not significant enough to prevent ignition.

Results from OpenFOAM simulations of temperature profiles provide further insights into the effects of varying heat flux on ignition. **Figure 8** shows regions of the fuel bed above the pyrolysis temperature for (row I) a fixed 750°C boundary condition, (row II) a heat flux boundary condition based on the average values from ignition tests at the 750°C, and (row III) a heat flux boundary conditions based on average heat fluxes for non-ignition tests at the 750°C. Column A shows the results for the fuel bed with L_c < 1 mm, column B with a bed of 4 mm < L_c < 6 mm, and column C with a bed of 6 mm < L_c < 12 mm particles. For the constant temperature boundary shown in row I, the region of the fuel bed above the pyrolysis temperature increases as particle sizes increase from left to right. Note, however, that the mass of the fuel bed material above the pyrolysis temperature decreases from left to right due to the decreasing density and thermal conductivity of the fuel bed as particle sizes increases. Specifically, the estimated mass of the fuel bed above the temperature for the onset of pyrolysis is 2.79, 1.59, and 1.55 μg for columns (A), (B), and (C), respectively. As a result, it is expected that the fuel bed with the smallest particles would release the most pyrolzates.

Perhaps surprising, is the difference in area at elevated temperatures between columns A and B in row II. Recall from **Figure 6** that at this heater temperature (750°C) the particles with L_c < 1 mm (i.e., column A), and the 4 mm < L_c < 6 mm (i.e., column B) have nearly identical ignition probabilities; however, the calculated average temperatures and region undergoing pyrolysis are notably different (e.g., 175°C). More importantly, a 30% mass increase in pyrolyzates occurs from L_c < 1–4 mm < L_c < 6 mm conditions. The corresponding ignition delay time, calculated using mass of pyrolyzates released and the average temperature of the pyrolysis region, was 0.5 s for the L_c < 1 mm gaseous products compared to 0.06 s for the 4 mm < L_c < 6 mm products. The differences in ignition delay time results from differences in the average fuel bed temperature and in the global equivalence ratio as pyrolyzates are released. Physically, these ignition delay times correspond to the characteristics of the pyrolyzates exiting the fuel bed. The differences in ignition delay time would suggest that the particles with 4 mm < L_c < 6 mm would ignite more readily, counter to the measured similar ignition probability. Note, however, that the calculated velocity of the gaseous products also varies, specifically $4.3 \cdot 10^{-3}$ m s^{-1} for

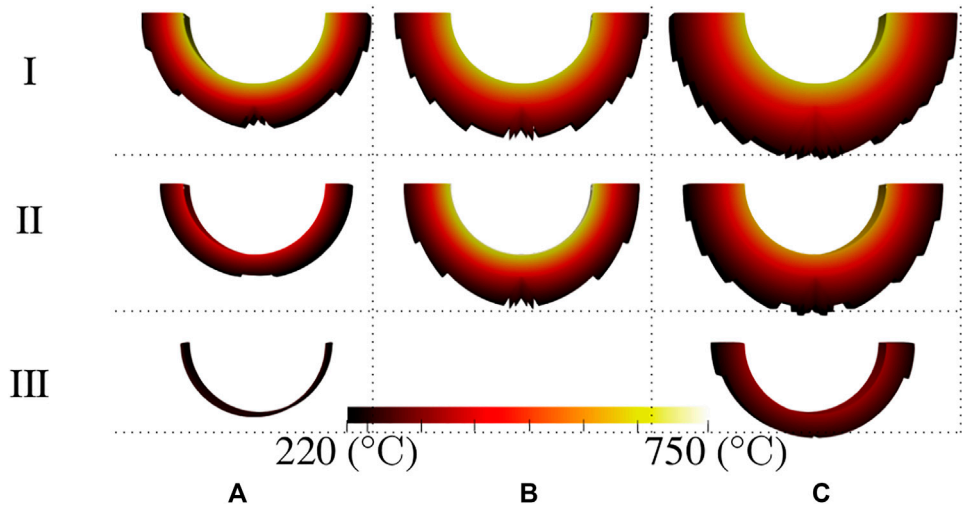

FIGURE 8 | Calculated region of fuel bed above the pyrolysis temperature 10 s after heater contact for a fixed 750°C boundary (I), ignition event heat flux (II), and non-ignition test event flux (III) for L_c < 1 mm **(A)**, 4 mm < L_c < 6 mm **(B)**, and 6 mm < L_c < 12 mm particles **(C)**.

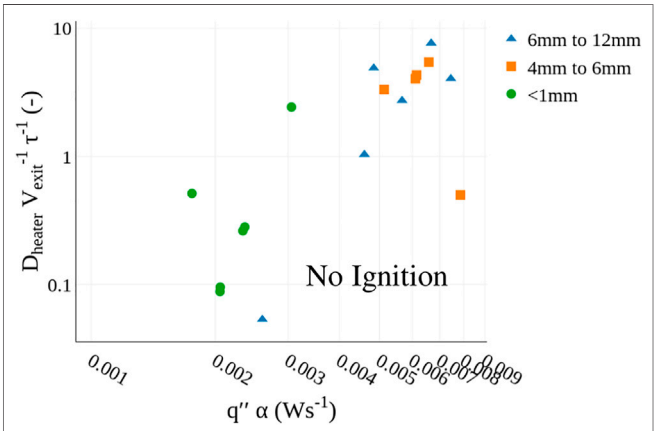

FIGURE 9 | Comparison of non-dimensional chemical and flow timescale (for the igniting cases) as a function of heat flux time and thermal diffusivity. Conditions where ignition and non-ignition are anticipated are highlighted.

the L_c < 1 mm fuel compared to $2.6 \cdot 10^{-2}$ m s^{-1} for the 4 mm < L_c < 6 mm fuel bed. In short, consideration of both the ignition delay time and exit velocity of the gases maybe needed to more completely capture ignition probabilities.

The Damkohler number (*Da*), which represents the ratio of the transport to chemical times-scales, has been used previously to consider ignition behavior (Dai et al., 2013), and is now considered to help evaluate ignition behavior. In this work, the ratio of the heater diameter D normalized by the product of the exit velocity (V_{exit}) and ignition delay time (τ) were considered, to create a Damkohler number of ignition for porous beds. This analysis results in the non-dimensional values of 2.42, 4.04, and 7.66 for the smallest to largest particles (respectively) for the results just described in the previous paragraph. Note that the smaller the (*Da*) the smaller the transport time (relative to chemical time-scale) and the less time that a parcel of reactants is near the high temperatures of the heater. In its limit, rectants may diffuse/advect away from the fuel prior to ignition.

To further explore the potential role of using a (*Da*) to characterize ignition propensity or porous, **Figure 9** shows the (*Da*) number for the gaseous products at the exit of the fuel bed for each particle size and heater set point. Data from the plates is excluded, as the supporting calculations were beyond the scope of the work. The abscissa is plotted relative to the average heat flux to the fuel bed multiplied by the thermal diffusivity of the fuel bed. These values were selected to include the influence of heat flux and thermal properties of the fuel beds in the characterization of ignition. Effectively, the chemical properties of the fuel bed and transport behavior are captured in the *Da* analysis and thermal properties are included in the heat flux and thermal diffusivity. The lower right area of the plot, labelled No Ignition, represents values estimated to be less conducive to ignition (i.e., longer ignition delay times) than those observed to produce ignition in experiments. The region where ignition is expected contains the remainder of the plot and represents values estimated to equally or more conducive to ignition (i.e., higher heat fluxes and shorter ignition delay times) than those observed in experiments. The relative similarity trends in ignition behavior when considering the (*Da*) indicate that considering the local transport conditions may be important to predicting ignition, in addition to considering the local heat flux and release of pyrolyzates.

4 SUMMARY AND CONCLUSION

Flaming ignition tests have been conducted for porous Douglas-fir beds, Douglas-fir plates, and cardboard plates. A cylindrical cartridge heater was used as a firebrand surrogate. Heater

temperature and electrical power to the heater were collected throughout each test. The derived heat flux to the fuel bed was within the range reported in literature of heat fluxes delivered by firebrands. The time to ignition and probablity of ignition were used to evaluate the ignition propensity for the various fuel beds and heater temperatures. A simplified heat transfer, pyrolysis, and ignition delay model was developed and used to provide further insights into the physical processes associated with ignition. The specific conclusions from this work are as follows.

1. Smaller particles ignite more readily in porous beds than larger particles when heat transfer from the heater is primarily through conduction. This was evident by higher ignition probabilities, in general, of the smaller particles for a fixed heater temperature. As particle sizes increase radiant heat transfer becomes more important and fuel beds with larger particles were more likely than smaller particles to ignite at extended times (>100 s) due to the increased importance of radiant ignition.
2. Douglas-fir plates ignite at times where conduction is the dominant mode of heat transfer (<10 s) due to the higher thermal conductivity of the solid plates. The ignition probability of plates was the most similar to the larger particle, in particular at lower heater temperatures, due to dispersed heating of the porous fuel bed through radiation and the increased thermal conductivity of the plates creating similar temperature profiles. The rise in ignition probability over a smaller heater temperature range time with temperature results from more consistent contact between the heater and plate surface.
3. Heat flux delivered to the fuel bed, when compared to heater temperature, is more indicative of ignition likelihood and ignition time for porous fuel beds. Heat flux is a more significant predictor of ignition because it captures differences in heat transfer modes and particle contact that heater temperature values do not. While this finding is not new, what is novel is that the mixed mode of heating (conduction and radiation) has a significant impact on the flaming ignition of fuel beds.
4. Consideration of the transport characteristics of pyrolyzate gases near the high temperature source can be important for more fully predicting ignition propensity. A *Da* of ignition, in relation to the measured heat flux and thermal diffusivity of the fuel beds, is a promising relationship for predicting ignition for the porous fuel beds.

Further work is needed to verify that the *Da* may be used to predict ignition for solid surfaces and for porous fuel beds with varying chemical compositions. If proven valid, the (*Da*), measured/predicted heat fluxes, and fuel bed properties may be used to help predict ignition of fuel beds both in and out of the WUI, ultimately helping to increase the effectiveness of fire prevention and suppression efforts.

DATA AVAILABILITY STATEMENT

The raw data supporting the conclusions of this article will be made available by the authors, without undue reservation.

AUTHOR CONTRIBUTIONS

All authors listed have made a substantial, direct and intellectual contribution to the work, and approved it for publication.

FUNDING

This research was supported by NIST under grant 70NANB19H164.

ACKNOWLEDGMENTS

The authors would like to thank Ryan Diltz and Cailin Moore for their assistance in conducting the time to ignition tests.

REFERENCES

Asdrubali, F., Pisello, A., Alessandro, F., Bianchi, F., Cornicchia, M., and Fabiani, C. (2015). Innovative Cardboard Based Panels with Recycled Materials from the Packaging Industry: Thermal and Acoustic Performance Analysis. *Energ. Proced.* 78, 321–326.

Babrauskas, V. (2003). *Ignition Handbook*. Issaquah, WA: Fire Science Publishers.

Cal Fire (2019). *Top 20 Largest California Wildfires*. Sacramento, CA.

Cal Fire (2018). *Top 20 Most Destructive California Wildfires*. Sacramento, CA.

California Department of Insurance (2019). *Wildfire Insurance Losses from November 2018 Blazes Top $12 Billion*. Sacramento, CA.

Dai, J., Delichatsios, M. A., Yang, L., and Zhang, J. (2013). Piloted Ignition and Extinction for Solid Fuels. *Proc. Combustion Inst.* 34, 2487–2495. doi:10.1016/j.proci.2012.07.021

Dhahak, A., Bounaceur, R., Le Dreff-Lorimier, C., Schmidt, G., Trouve, G., and Battin-Leclerc, F. (2019). Development of a Detailed Kinetic Model for the Combustion of Biomass. *Fuel* 242, 756–774. doi:10.1016/j.fuel.2019.01.093

Fernandez-Pello, A. C., Lautenberger, C., Rich, D., Zak, C., Urban, J., Hadden, R., et al. (2015). Spot Fire Ignition of Natural Fuel Beds by Hot Metal Particles, Embers, and Sparks. *Combustion Sci. Technology* 187, 269–295. doi:10.1080/00102202.2014.973953

Forest Products Laboratory (2010). Wood Handbook-Wood as an Engineering Material. *Tech. Rep.*. Madison, WI: U.S. Department of Agriculture.

Goodwin, D. G., Speth, R. L., and Moffat, H. K. (2020). An Object-Oriented Software Toolkit for Chemical Kinetics, Thermodynamics, and Transport Processes. *Cantera*. doi:10.5281/zenodo.1174508

Hadden, R. M., Scott, S., Lautenberger, C., and Fernandez-Pello, C. C. (2011). Ignition of Combustible Fuel Beds by Hot Particles: An Experimental and Theoretical Study. *Fire Technology* 47, 341–355. doi:10.1007/s10694-010-0181-x

Hakes, R. S., Salehizadeh, H., Weston-Dawkes, M. J., and Gollner, M. J. (2019). Thermal Characterization of Firebrand Piles. *Fire Saf. J.* 104, 34–42. doi:10.1016/j.firesaf.2018.10.002

Hernández, N., Fuentes, A., Consalvi, J. L., and Elicer-Cortés, J. C. (2018). Spontaneous Ignition of Wildland Fuel by Idealized Firebrands. *Exp. Therm. Fluid Sci.* 95, 88–95. doi:10.1016/j.expthermflusci.2018.01.037

Incropera, F., Dewitt, D., Bergman, T., and Lavine, A. (2011). *Fundamentals of Heat and Mass Transfer*. 7 edn. Hoboken, NJ: Wiley.

Koo, E., Pagni, P. J., Weise, D. R., and Woycheese, J. P. (2010). Firebrands and Spotting Ignition in Large-Scale Fires. *Int. J. Wildland Fire* 19, 818.

Manzello, S. L., Cleary, T. G., Shields, J. R., Maranghides, A., Mell, W., and Yang, J. C. (2008). Experimental Investigation of Firebrands: Generation and Ignition of Fuel Beds. *Fire Saf. J.* 43, 226–233. doi:10.1016/j.firesaf.2006.06.010

Manzello, S. L., Cleary, T. G., Shields, J. R., and Yang, J. C. (2006a). Ignition of Mulch and Grasses by Firebrands in Wildlandurban Interface Fires. *Int. J. Wildland Fire* 15, 427–431. doi:10.1071/WF06031

Manzello, S. L., Cleary, T. G., Shields, J. R., and Yang, J. C. (2006b). On the Ignition of Fuel Beds by Firebrands. *Fire Mater.* 30, 77–87. doi:10.1002/fam.901

Manzello, S. L., Suzuki, S., Gollner, M. J., and Fernandez-Pello, A. C. (2020). Role of Firebrand Combustion in Large Outdoor Fire Spread. *Prog. Energ. Combustion Sci.* 76, 100801. doi:10.1016/j.pecs.2019.100801

Maranghides, A., McNamara, D., Mell, W., Trook, J., and Toman, B. (2013). *NIST Technocal Note 1796: A Case Study of a Community Affected by the Witch and Guejito Fires Report: #2 – Evaluating the Effects of Hazard Mitigation Actions on Structure Ignitions*. Tech. Rep. 1796. Washington, D.C: U.S. Department of Commerce, National Institute of Standards and Technology. doi:10.6028/NIST.TN.1796

Mell, W. E., Manzello, S. L., Maranghides, A., Butry, D., and Rehm, R. G. (2010). The Wildland - Urban Interface Fire Problem - Current Approaches and Research Needs. *Int. J. Wildland Fire* 19, 238. doi:10.1071/wf07131

Pedregosa, F., Varoquaux, G., Gramfort, A., Michel, V., Thirion, B., Grisel, O., et al. (2011). Scikit-learn: Machine Learning in Python. *J. Machine Learn. Res.* 12, 2825–2830.

Ranzi, E., Cuoci, A., Faravelli, T., Frassoldati, A., Migliavacca, G., Pierucci, S., et al. (2008). Chemical Kinetics of Biomass Pyrolysis. *Energy and Fuels* 22, 4292–4300. doi:10.1021/ef800551t

Ranzi, E., Dente, M., Goldaniga, A., Bozzano, G., and Faravelli, T. (2001). Lumping Procedures in Detailed Kinetic Modeling of Gasification, Pyrolysis, Partial Oxidation and Combustion of Hydrocarbon Mixtures. *Prog. Energ. Combustion Sci.* 27, 99–139. doi:10.1016/S0360-1285(00)00013-7

Rivera, J., Hernández, N., Consalvi, J. L., Reszka, P., Contreras, J., and Fuentes, A. (2020). Ignition of Wildland Fuels by Idealized Firebrands. *Fire Saf. J.* doi:10.1016/j.firesaf.2020.103036

Suzuki, S., and Manzello, S. L. (2020). Role of Accumulation for Ignition of Fuel Beds by Firebrands. *Appl. Energ. Combustion Sci.* 1-4, 100002.

Tao, Z., Bathras, B., Kwon, B., Biallas, B., and Gollner, M. J. (2020). Effect of Firebrand Size and Geometry on Heating from a Smoldering Pile under Wind. *Fire Saf. J.* 103031. doi:10.1016/j.firesaf.2020.103031

The OpenFOAM Foundation (2020). *OpenFOAM*. London, United Kingdom.

Urban, J. L., Song, J., Santamaria, S., and Fernandez-Pello, C. (2019). Ignition of a Spot Smolder in a Moist Fuel Bed by a Firebrand. *Fire Saf. J.* 108, 102833. doi:10.1016/j.firesaf.2019.102833

Urban, J. L., Zak, C. D., and Fernandez-Pello, C. (2018). Spot Fire Ignition of Natural Fuels by Hot Aluminum Particles. *Fire Technology* 54, 797–808. doi:10.1007/s10694-018-0712-4

Urban, J. L., Zak, C. D., Song, J., and Fernandez-Pello, C. (2017). Smoldering Spot Ignition of Natural Fuels by a Hot Metal Particle. *Proc. Combustion Inst.* 36, 3211–3218. doi:10.1016/j.proci.2016.09.014

U.S. Department of Interior/U.S. Department of Agriculture, F. S. (2020). Federal Firefighting Costs (Suppression Only).

Wang, S., Chen, H., and Liu, N. (2015). Ignition of Expandable Polystyrene Foam by a Hot Particle: An Experimental and Numerical Study. *J. Hazard. Mater.* 283, 536–543. doi:10.1016/j.jhazmat.2014.09.033

Watlow (2020). *Heat Loss Factors and Graphs*. St. Louis, MO.

Yang, H., Yan, R., Chen, H., Lee, D. H., and Zheng, C. (2007). Characteristics of Hemicellulose, Cellulose and Lignin Pyrolysis. *Fuel* 86, 1781–1788. doi:10.1016/j.fuel.2006.12.013

Zak, C. D., Urban, J. L., and Fernandez-Pello, C. (2014). Characterizing the Flaming Ignition of Cellulose Fuel Beds by Hot Steel Spheres. *Combustion Sci. Technology* 186, 1618–1631. doi:10.1080/00102202.2014.935612

Conflict of Interest: The authors declare that the research was conducted in the absence of any commercial or financial relationships that could be construed as a potential conflict of interest.

frontiers in Mechanical Engineering

ORIGINAL RESEARCH
published: 16 December 2021
doi: 10.3389/fmech.2021.650580

Coupled Assessment of Fire Behavior and Firebrand Dynamics

*Jan C. Thomas[1], Eric V. Mueller[1], Michael R. Gallagher[2], Kenneth L. Clark[2], Nicholas Skowronski[3], Albert Simeoni[4] and Rory M. Hadden[1]**

[1]School of Engineering, University of Edinburgh, Edinburgh, United Kingdom, [2]Northern Research Station, USDA Forest Service, New Lisbon, NJ, United States, [3]Northern Research Station, USDA Forest Service, Morgantown, WV, United States, [4]Department of Fire Protection Engineering, Worcester Polytechnic Institute, Worcester, MA, United States

The hazards associated with firebrands have been well documented. However, there exist few studies that allow for the hazard from a given fire to be quantified. To develop predictive tools to evaluate this hazard, it is necessary to understand the conditions that govern firebrand generation and those that affect firebrand deposition. A method is presented that allows for time-resolved measurements of fire behavior to be related to the dynamics of firebrand deposition. Firebrand dynamics were recorded in three fires undertaken in two different ecosystems. Fire intensity is shown to drive firebrand generation and firebrand deposition—higher global fire intensities resulting in the deposition of more, larger firebrands at a given distance from the fire front. Local firebrand dynamics are also shown to dominate the temporal firebrand deposition with periods of high fire intensity within a fire resulting in firebrand shower at deposition sites at times commensurate with firebrand transport. For the range of conditions studied, firebrand deposition can be expected up to 200 m ahead of the fire line based on extrapolation from the measurements.

Keywords: wildland–urban interface (WUI), prescribed fire, firebrand flux, firebrand deposition, firebrand generation, fire behavior, firebrands

OPEN ACCESS

Edited by:
Domingos Xavier Viegas, University of Coimbra, Portugal

Reviewed by:
Miguel Almeida, Associação para o Desenvolvimento da Aerodinâmica Industrial, Portugal
Wei Tang, National Institute for Occupational Safety and Health (NIOSH), United States

****Correspondence:***
Rory M. Hadden
r.hadden@ed.ac.uk

Specialty section:
This article was submitted to Thermal and Mass Transport, a section of the journal Frontiers in Mechanical Engineering

Received: *07 January 2021*
Accepted: *17 November 2021*
Published: *16 December 2021*

Citation:
Thomas JC, Mueller EV, Gallagher MR, Clark KL, Skowronski N, Simeoni A and Hadden RM (2021) Coupled Assessment of Fire Behavior and Firebrand Dynamics. Front. Mech. Eng 7:650580. doi: 10.3389/fmech.2021.650580

1 INTRODUCTION

The hazards associated with firebrands as the leading cause of structure ignitions in fires at the wildland–urban interface and as a fire spread vector are well documented (Caton et al., 2017; Hakes et al., 2017; Manzello et al., 2020)). In addition to predicting the hazard associated with the ignition of structures, better understanding of firebrand dynamics will aid the planning and execution of prescribed fires by allowing improved estimates of firebrand travel distances and ignition potential, allowing the firebrand hazard to be managed more effectively. Despite a large number of studies in recent years aimed at reproducing firebrand exposures for material testing (Manzello et al., 2008; Manzello and Suzuki, 2013; Thomas et al., 2018), identifying the ignition hazard posed by firebrands and firebrand accumulations (Manzello et al., 2017; Fernandez-Pello, 2017; Matvienko et al., 2018; Hakes et al., 2019), and the development of numerical models (Wadhwani et al., 2017), there exists very little information on firebrand exposures from wildland fires which captures the link between the dynamic quantities of firebrand deposition and fire behavior.

The primary sources of firebrand deposition data are generally associated with investigations carried out after large fires of special interest (Maranghides and Mell, 2011), or measurements of firebrand deposition after prescribed fires (El Houssami et al., 2016a; Filkov et al., 2017; Thomas et al., 2017). Such approaches have been limited in allowing the firebrand hazard to be quantified in terms of an integrated firebrand deposition and particle size distributions only.

To provide robust assessments of the hazard associated with firebrands, it is necessary to expand this approach to allow for the time-resolved firebrand exposure to be related to the fire behavior and the firebrand sources. This requires simultaneous measurements of the temporal dynamics of firebrand deposition and fire behavior and detailed quantification of the firebrand source.

1.1 Defining the Firebrand Hazard

The firebrand hazard is defined by the number, mass, geometry, and energy content of the firebrands landing in an area. In addition, the reaction condition (or temperature) of the firebrands is significant in determining whether the firebrands can result in the ignition of a substrate directly or by the formation of a smoldering accumulation. Such accumulations have been shown to be a leading cause of the ignition of structures (Manzello et al., 2020). Of particular significance in this context are the mass and time-resolved firebrand deposition. The hazard is defined explicitly to be independent of the conditions when the firebrand lands, e.g., fuel bed and environmental properties which may lead to ignition.

Quantification of the firebrands alone is therefore insufficient. It is essential to link them to the extrinsic factors such as the fuels (vegetative or structural) that are present; the ambient meteorological conditions, particularly the local wind field, to assess travel distances of the firebrands; and finally the fire behavior as this will influence the generation, injection height, and buoyant flow available. High temporal and spatial resolution measurements of these quantities are therefore needed to contextualize the firebrand hazard arising from a fire.

1.1.1 Generation of Firebrands

In the natural environment, firebrands primarily originate from bark fragments, branches, twigs, and foliage. The mechanisms of firebrand generation are not well understood; however, this logically requires the separation of the material from a parent body (plant, litter layer) due to combined thermal and mechanical forces (Barr and Ezekoye, 2013). The magnitude of these forces will be strongly dependent on the fire behavior (e.g., thermal environment and fire-induced flows) and the fuel present (e.g., structure and propensity to fragment). The fire dynamics will also determine the plume characteristics, which in turn will influence the transport of the firebrands.

1.1.2 Transport of Firebrands

The transport of firebrands depends on multiple factors including the plume injection into the atmosphere as determined by the heat release rate of the fire, atmospheric turbulence, the generation height of the firebrand as determined by the fuel structures, the shape of the particles, and the thermal and reaction conditions of the particles. This problem has been extensively studied (Tarifa et al., 1965; Woycheese et al., 1999; Koo et al., 2010); however, to be of use, their proposed methods require detailed fire behavior and firebrand characteristics.

1.1.3 Deposition of Firebrands

The deposition of firebrands is governed by the aerodynamic properties (shape, size, and mass) of the firebrands; the temperature evolution of the firebrands, including the combustion processes; and the local flow conditions downwind of the fire front. Very short-range firebrands are deposited close to the fire front, locally enhancing the fire spread rate. Longer range firebrand deposition, which may occur hundreds of meters or kilometers distant from the fire front, is influenced by the fire-induced flows which can act over these distances (Mueller et al., 2017), flow obstructions, and the wind profile (Heilman et al., 2019; Clark et al., 2020).

1.1.4 Condition of Firebrands

The condition of firebrands upon deposition (hot, cold, reacting) will depend on the fire behavior, the firebrand material, and the flow conditions. The vegetation characteristics, transport time, and velocity will also determine whether the firebrand is capable of sustaining combustion throughout its trajectory (Tarifa et al., 1965; Woycheese et al., 1999). The fire intensity and residence time will impact the heating and degradation of vegetation (Tarifa et al., 1965) during the generation and initial lofting processes. Few quantitative assessments of the thermal condition of firebrands have been made (Maranghides and Mell, 2011; Filkov et al., 2017); however, these have lacked contextualization with detailed fire behavior data.

1.2 Measuring the Firebrand Hazard

There have been a limited number of studies in which the firebrand generation and deposition have been related to fire behavior (El Houssami et al., 2016b; Thomas et al., 2017); however, these have not resolved the temporal dynamics of firebrand deposition and have presented only integral measurements of firebrand deposition and firebrand mass.

To provide data necessary to evaluate the hazard posed by firebrand deposition, an experimental methodology must allow determination of the following:

- the total and time-resolved firebrand deposition and firebrand characteristics (e.g., size and temperature) as a function of fire intensity and fuel type;
- the time-resolved firebrand deposition and relationship to fire behavior; and
- the firebrand deposition as a function of distance from the fire line.

Measurement of the time-resolved firebrand deposition from well-described real fires is essential in order to generate the data required to understand the risks posed by firebrands, for example, spot fires or structure ignitions, to develop appropriate test methods to evaluate risk, assess mitigation strategies, and develop predictive tools.

2 METHODS

Three large-scale fire experiments were conducted to allow the measurement of time-resolved firebrand deposition dynamics while varying fire intensity, environmental conditions, and fuel types. Detailed measurements to quantify the fuels, time-

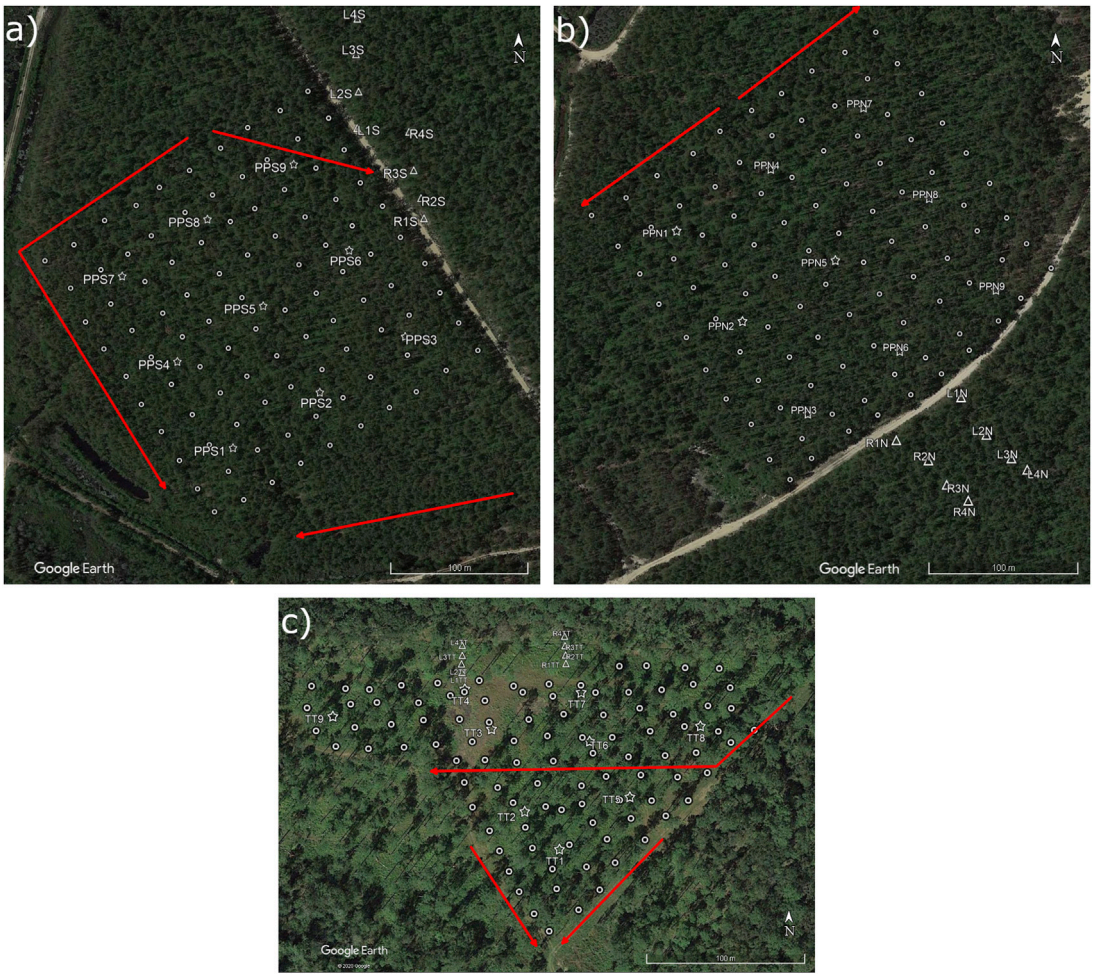

FIGURE 1 | Site layout for 2017 experimental burns. **(A)** PPS, **(B)** PPN, and **(C)** TT. Circles: FireTrackers, Stars: Understory towers. Triangles: Firebrand Collection Sites. Sonic anemometers were located at R1S, R4S, R1N, L2N, R2TT, and L2TT. Ignition lines are marked with red arrows. The arrows show the direction of the ignitions, but it should be noted that these did not occur simultaneously in PPS and TT.

dependent fire behavior, and firebrand dynamics were made as described in the following sections.

2.1 Site Descriptions

Two experiments were conducted at sites in the New Jersey Conservation Foundation Franklin Parker Preserve, within the New Jersey Pinelands National Reserve. The first unit was burned on the evening of March 6, 2017 (PPS), while the second unit was burned on the morning of March 23, 2017 (PPN). Both units were dominated by pitch pine (*Pinus rigida* Mill.), and neither unit had burned or been managed since a major wildfire in the spring of 1954. A square area within each unit measuring 250 m × 250 m was instrumented within each approximately 7-ha plot. PPN and PPS were both approximately flat with no significant topographical features within the area of interest. The pitch pine-dominated vegetation and previous prescribed fires in the surrounding landscape are described in the literature (El Houssami et al., 2016a; Filkov et al., 2017; Simeoni et al., 2017; Thomas et al., 2017; Mueller et al., 2018).

The third experiment was undertaken at the Tall Timbers Research Station & Land Conservancy in southern Georgia (TT). This site covered an area of approximately 3 ha and was burned on April 21, 2017. Prior management of this stand included a prescribed fire approximately one year prior to the current study. The forest overstory in this stand was composed of a monoculture of longleaf pine (*Pinus taeda*), while the understory was composed primarily of sweet gum (*Liquidambar styraciflua*), wiregrass (*Aristida stricta*), various southern shrub form oaks (*Quercus* spp.), and other forbs typical of the longleaf–wiregrass ecosystem. There were no significant topological features in the plot with the instrumented region of interest being approximately flat.

The ignition of each burn unit was undertaken to direct firebrands toward the collection sites. Ignition lines are shown in **Figure 1**. PPS was initially ignited along the northwest edge, turning through 90° and continuing along the southwest edge using a drip torch; later, a line was ignited moving approximately east to west; a final ignition line was made moving southeast

toward the end of the fire. In the PPN fire, two drip torches were used to ignite a line perpendicular to the prevailing wind one moving northeast and the other southwest. Ignition of the TT fire was by vehicular mounted torch. Two lines were ignited initially: one moving southeast and the other southwest; later, a line was ignited moving approximately east to west through the unit. It is recognized that ignition may have an impact on firebrand generation, and this was controlled in PPS. Unfortunately, conditions at PPS and TT resulted in more complex behaviors which could not be assessed in the current work.

2.2 Fire Behavior Measurements

Fire behavior was characterized by measurement of the rate of spread, the fire line intensity, and the sub-canopy fire–induced flows.

2.2.1 Spread Rate and Fire Front Position

The progression of the fire front was tracked using a regular array of FireTrackers at ground level. These sensors consisted of individual Arduino Feather® –based data loggers with thermocouple amplifiers and GPS antennas in order to establish a consistent time stamp and location for all sensors. Temperature was measured using 1.5-mm-diameter K-type thermocouples, and data were logged at a frequency of 2 Hz. FireTrackers were buried such that the tip of the thermocouple protruded through the surface fuels. Sensors were placed at a nominal spacing of 25 m for the PPS (n = 92 successfully recorded) and PPN burns (n = 88), and 20 m for the TT burn (n = 91).

Fire arrival at a FireTracker was determined by a temperature rise of greater than 2°C·s^{-1}. Arrival times were linearly interpolated onto a 5m × 5m grid, and the inverse of the gradient was used to calculate spread rate vectors. These were smoothed with a box filter, owing to regions of complex fire line interactions resulting in spuriously large values of spread. For each point, the filter takes the average of the nearest surrounding grid points (i.e., over a 10 m × 10 m area).

Nine 6.5-m tall understory towers, placed in a regular grid, were used to measure the vertical profile of gas temperature at the locations identified in **Figure 1**. Temperatures were measured at twelve vertical positions, with spacing of 0.5 m starting at 1.0 m from the ground. Probes were glass-insulated K-type thermocouples, with bead size of 1.2 ± 0.1 mm diameter. Data were recorded at 2 Hz on Arduino Feather® data logger units with thermocouple amplifiers. The flame height was estimated as the highest position at which a temperature of 300°C was recorded.

2.2.2 Fire Line Intensity

The fire line intensity was determined by using two methods: 1) based on fuel consumption and spread rate as described in **Eq. 1**, where χ is the combustion efficiency (assumed to be unity), Δh_c is the heat of combustion (18.7 MJ·kg^{-1}), Δm is the fuel consumed, and R is the spread rate (Byram, 1959); 2) based on local flame length as described in **Eq. 2**, where L is the flame length (assumed to be equal to flame height) (Alexander, 1982):

$$I = \chi \Delta h_c \Delta m R \tag{1}$$

$$I = 259.833 L^{2.174}. \tag{2}$$

2.2.3 Wind Speed and Direction

Wind speed and direction were measured 10 m above ground level using a sonic anemometer (RM 80001V, R. M. Young, Inc.) and wind vane (05013-5, R.M. Young Co., Traverse City, MI, United States). This "control tower" measurement was located on the western edge of PPN and 0.89 km from PPS. Wind speed was measured with a precision of ±0.3 m·s^{-1} and a directional precision of ±3°. Ambient wind and temperature for the TT fire were recorded at 10 Hz with a sonic anemometer (RM 80001V, R. M. Young, Inc.) 350 m upwind of the burn unit in an area of open vegetation and canopy conditions. Additionally, wind speed and direction were measured at a height of 3 m with two sonic anemometers (RM 80001V, R. M. Young, Inc., 1 Hz) placed at selected firebrand collection sites, in order to monitor the conditions at the point of deposition (**Figure 1**).

2.3 Firebrand Measurement Techniques

2.3.1 Firebrand Generation

Previously, studies (El Houssami et al., 2016a; Thomas et al., 2017) demonstrated that firebrand generation in this ecosystem is dominated by bark flakes originating from tree boles. Consequently, in this work, it is assumed that all firebrands are generated by bark flakes. The total number of firebrands produced per tree, F, can be calculated from the following ratio:

$$F = \frac{\Delta r C_f h_s}{\tau A_f}, \tag{3}$$

where Δr is the radius reduction calculated from the circumference reduction, C_f is the post-fire perimeter, h_s is the scorch height, τ is the characteristic thickness of a bark firebrand slice, and A_f is the area of a firebrand. The following assumptions are made in the application of this method:

- Trees are cylindrical with no taper.
- Firebrand generation is constant around the trunk and extends from ground level to the scorch height.
- An average virgin bark flake is cuboidal with area, A_f, and thickness, τ.
- The trunk only loses volume due to detachment of bark flakes as a first-order approximation.

The total number of firebrands produced is calculated using the following equation:

$$F_T = F \times SDI \times A_b, \tag{4}$$

where F_T is the total number of firebrands produced in the burn unit, SDI is the stand density index (trees·ha^{-1}), and A_b is the area of the burn unit (m^2).

Two or three trees were measured in the vicinity of each understory tower before and after the fires (depending on their proximity to the tower). A total of 25 measurements were made at PPN and 18 at PPS. Measurements of tree circumference were

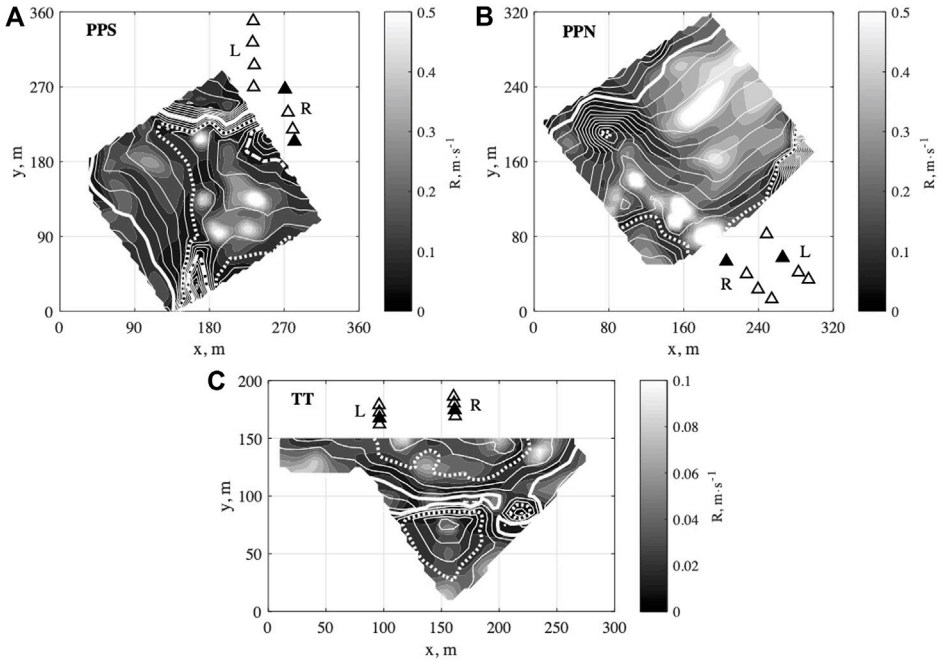

FIGURE 2 | Maps of fire spread rate for the three experiments: **(A)** PPS, **(B)** PPN, and **(C)** TT. Grayscale shading corresponds to the spread rate. White contours are isochrones of fire position, shown in minutes from ignition for every **(A)** 2 min (bold line: 30 min; dotted line: 40 min; dashed line: 50 min), **(B)** 1 min (bold line: 6 min; dotted line: 16 min), and **(C)** 6 min (solid line: 12 min; dotted line: 30 min). Firebrand collection sites are shown as triangles, with black triangles indicating the sites which included sonic anemometers.

made a breast height before and after the fire. For improved measurement accuracy, the tree circumference was divided into eight segments which were measured individually (El Houssami et al., 2016a). When calculating the mass and total number of firebrands, the mass of a firebrand $m_f = 0.016$ g and a value of 2,750 trees ha^{-1} are used (McCormick and Jones, 1973).

2.3.2 Firebrand Collection

Firebrands were collected following the established methods (Thomas et al., 2017), with the aim of assessing the temporal and spatial distribution dynamics of deposition. Firebrands were collected at eight firebrand collection sites (FCSs) in each fire. These were arranged in two transects (left and right) outside the burn unit with a nominal separation of 50 m between transects and 25 m between FCSs along a transect. The position of the FCSs is shown in **Figure 1**. Each FCS comprised fifteen, 0.22-m-diameter water-filled cans randomly distributed within a 3-m^2-area, resulting in a total collection area at each FCS of 0.57 m^2. Following an experiment, the number of firebrands and the distribution of their projected areas were measured for each can using image analysis, with a minimum detection threshold of 7.5×10^{-6} (Thomas et al., 2017).

Measurement of the time-dependent firebrand deposition was taken by correlating the arrival time as measured by a video camera facing one can at each FCS. These time-stamped data allowed firebrand deposition to be correlation to fire behavior measurements.

Analysis of the total firebrand deposition employed the following assumptions:

- Firebrands are deposited downwind of the fire and can be deposited inside and outside the burn area.
- Firebrands deposition inside the burn unit is constant.
- Firebrands travel in the direction of the ambient wind.
- The wind was ideally aligned with the burn unit and FCSs for the duration of the experiment.
- Outside deposition occurs in an area that has the same width as the burn unit (i.e., no lateral deposition occurs).

The validity of these assumptions is not known; however, in the absence of more detailed information, they are required to interpret the firebrand deposition. It is hoped that further work will allow improvements of these assumptions.

Furthermore, firebrand deposition is represented by a piecewise function:

$$f''(x) = \begin{cases} c, & -d \le x \le 0 \\ g(x), & x > 0, \end{cases} \tag{5}$$

where x is the distance from the primary ignition line which is located at $-d$, that is, d is the distance from the ignition line to the downwind edge of the burn unit (250 m in PPN and PPS). The firebrand deposition inside the burn unit is assumed to be constant, c, and g is the function representing the deposition of the firebrands outside the burn unit. The value of c is not measured in this work. Firebrand deposition data from all FCSs are evaluated against separation distance ($x > 0$) from the burn unit (measured in line with ambient wind direction). Finally, the function f'' can be integrated over the area of deposition to give f,

TABLE 1 | Plot average (±1 SD) spread rate and fire line intensity (as calculated using **Eq. 1** (Fuel consumed) and **Eq. 2** (Flame length)). The measurements made using the flame length technique are presented as an average and with the range of calculated values in [ ].

Burn	Rate of spread (m s^{-1})	Fire line intensity (kW $\cdot m^{-1}$)	
		Fuel consumed	Flame length
PPS	0.142 ± 0.093	4,200 ± 3,200	1,420 [260—5,291]±1786
PPN	0.257 ± 0.155	10800 ± 7,000	7,572 [260–15 204]
TT	0.035 ± 0.017	700 ± 600	< 230

and the total number of firebrands deposited inside and outside the burn unit.

3 RESULTS AND DISCUSSION

Results pertaining to the fire behavior measurements are presented first before introducing the results from the firebrand generation, deposition, and characterization studies. Finally, the time-dependent firebrand deposition results are presented before a brief discussion contextualizing the total firebrand generation and deposition measurements.

3.1 Fire Behavior Measurements

The fire behaviors observed in the three experiments are discussed later. Details of the surface and canopy fuel loads, and fuel moisture content are given in the **Supplementary Material**.

3.1.1 Spread Rate

Maps of fire spread for all three fires are shown in **Figure 2**, and average spread rates are given in **Table 1**. Animated flame spread maps for PPN and PPS are given in the **Supplementary Material** (PPN_spread.mp4 and PPS_spread.mp4, respectively).

PPN had the highest spread rate, with the highest local values of spread rate occurring between 7–9 min and 14–16 min after ignition. This was followed by PPS, which, although having a lower overall spread rate, had moments of locally high spread rates between 40 and 46 min after ignition. TT had a significantly lower spread rate than the pitch pine ecosystem, with a mean value which is nearly an order of magnitude less than that of PPN and PPS (**Table 1**). This is potentially due to a combination of lower fuel load; the prevalence of live, rather than dormant, shrubs; and a higher relative humidity. The measurements of fire front position indicate that ignition patterns (PPS and TT) and features such as local spotting and fuel discontinuity (PPN) have a significant effect on the fire development.

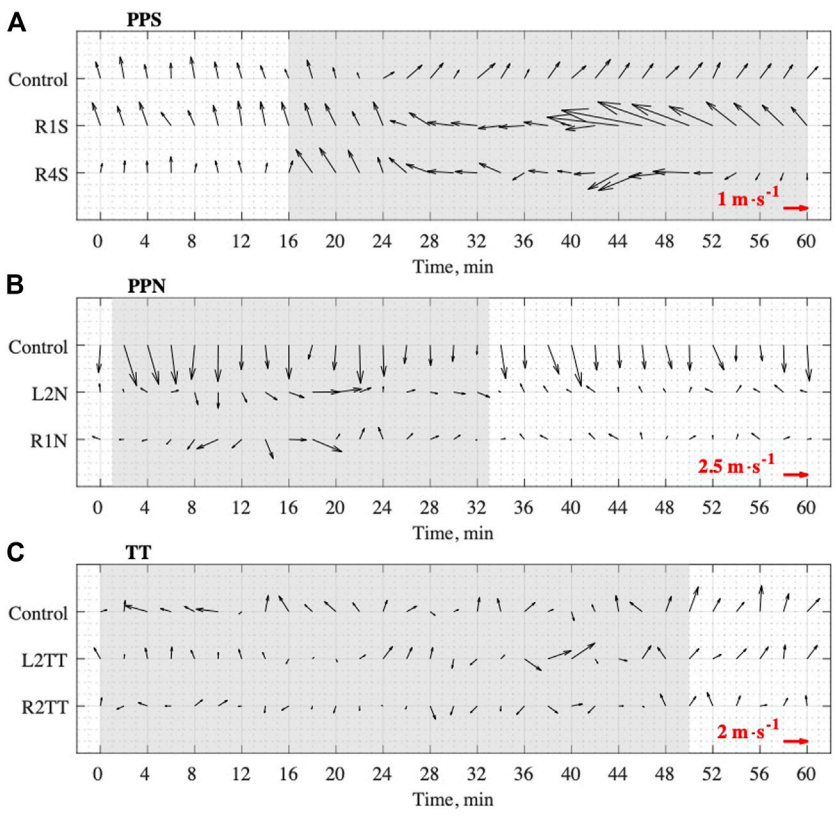

FIGURE 3 | Wind characterization for three burns: **(A)** PPS, **(B)** PPN, and **(C)** TT. Each one showing a control location (10 m AGL) and two local measurements at the specified FCS (3 m AGL). Shaded areas correspond to the time of fire spread within the instrumented blocks (**Figure 2**). The vectors represent a 2-min average of the horizontal wind, and time is in minutes from ignition. Note that vector scales are not the same for each figure (reference scales are given in the lower left).

TABLE 2 | Measurements required for the calculation of the firebrand generation for PPN and PPS.

	PPN	PPS
Scorch height (m)	5.19	4.23
Radius reduction (m)	$6.37 \times 10^{-3} \pm 4.21 \times 10^{-3}$	$2.74 \times 10^{-3} \pm 2.39 \times 10^{-3}$
Number of firebrands per tree -	30 000	12 000
Firebrand mass per tree (kg)	4.8	1.9
Total number of firebrands -	500×10^6	182×10^6
Total mass of firebrands (kg)	81 000	29 000

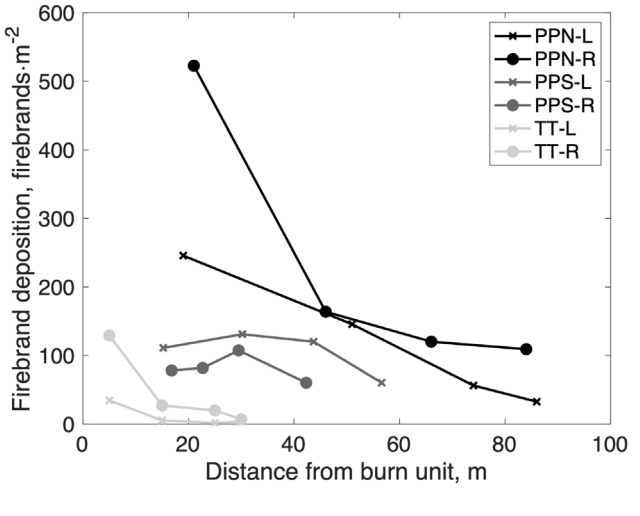

FIGURE 4 | Total firebrand deposition as a function of distance from the edge of the burn unit. L and R indicate the left and right FCS transects of each burn unit.

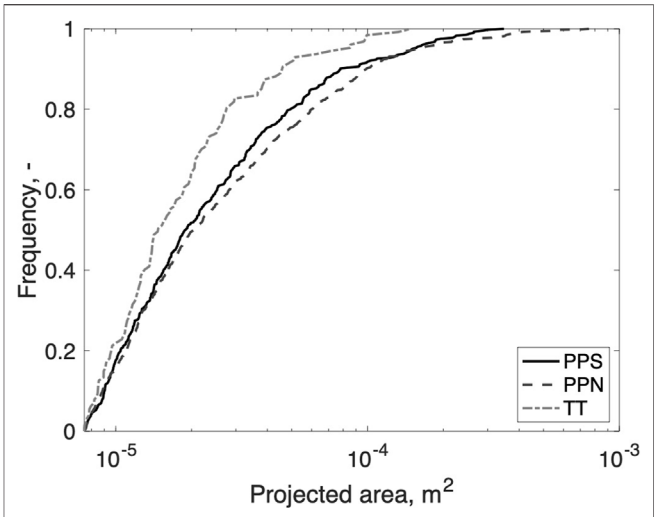

FIGURE 5 | Cumulative distribution of firebrand area for PPN (n = 767), PPS (n = 404), and TT (n = 128) (n is the number of firebrands collected). To allow comparison between sites, only particles with projected areas greater than 75 mm^2 are included in this analysis.

3.1.2 Fire Line Intensity

The average fire line intensities for each site, using both the fuel consumption and flame height methods, are listed in **Table 1**. Both estimation techniques show the same trends between the fires, although the flame length correlation consistently produces a lower value of intensity than the fuel consumption technique. The nature of this discrepancy is likely due to the assumption that flame length is equal to flame height, which is only approximated, as well as due to local variations in fuel consumption.

Comparing the tabulated values to previous work in similar fuels (Mueller et al., 2017; Thomas et al., 2017), PPN falls in the range of a high intensity surface fire with local crown involvement, PPS in a moderate to high intensity surface fire, and TT in a low intensity surface fire. In addition, temperature measurements 1 m above ground level did not exceed 300°C during the TT experiment. Low intensity is attributed to low ambient wind, and the presence is live foliage.

3.1.3 Wind Speed and Direction

Time histories of both the ambient wind (control tower) and winds at the firebrand collection sites are shown in **Figure 3**. For the PPS burn, winds averaged 0.8 ± 0.4 $m{\cdot}s^{-1}$ at the control tower for the 60-min period following ignition. The dominant direction was south/south to southeast at ignition, but this shifted to southwest around 24 min after ignition, aiding the coalescing of the secondary and tertiary ignition lines into a head fire. The local winds at the collection sites agreed with the ambient winds during the early stages of the fire, with site L1S having higher values due to its location on a road, as opposed to L4S which was placed within the stand opposite to the burn unit (**Figure 1**). Around 24 min after ignition, these sites experienced an increasing east wind, which may be attributed to the onset of a fire-induced indraft; however, the strongest influence is seen closer to the 45-min mark. Around this time, values exceed those of the ambient wind, reaching a maximum of 5.2 $m{\cdot}s^{-1}$ at L1S and 3.6 $m{\cdot}s^{-1}$ at L4S.

Ambient winds were nearly four times stronger for the PPN burn, averaging 3.1 ± 1.5 $m{\cdot}s^{-1}$ for the 33-min period containing fire spread in the instrumented block. The direction was relatively steady from the north, resulting in a slight swinging of the fireline from the southwest–northeast ignition line to a more east–west front. In this case, local winds at the collection sites were initially light but grew stronger and diverted from their ambient direction 8 min after ignition as the fire approached the sites and began to experience some local periods of high intensity (**Figure 2**).

For the TT fire, ambient winds were moderate, falling between PPS and PPN at an average of 1.4 ± 0.8 $m{\cdot}s^{-1}$ for the 50-min following ignition. However, the direction fluctuated more over the course of the burn, covering at least a 90° range between an east and west wind in the first 30 min of the burn. Local winds at the collection sites also fluctuated significantly, masking a clear influence of the fire. However, a slight increase in the wind at L2 around the 36–40 min mark to an average of 2.1 $m{\cdot}s^{-1}$ (exceeding concurrent ambient wind by a factor of ~1.7) does coincide with the arrival of the fire in this region (**Figure 2**).

The aforementioned features reveal the complexity of flow patterns which can impact firebrand deposition. While the ambient winds above the canopy certainly impact the tilt of the

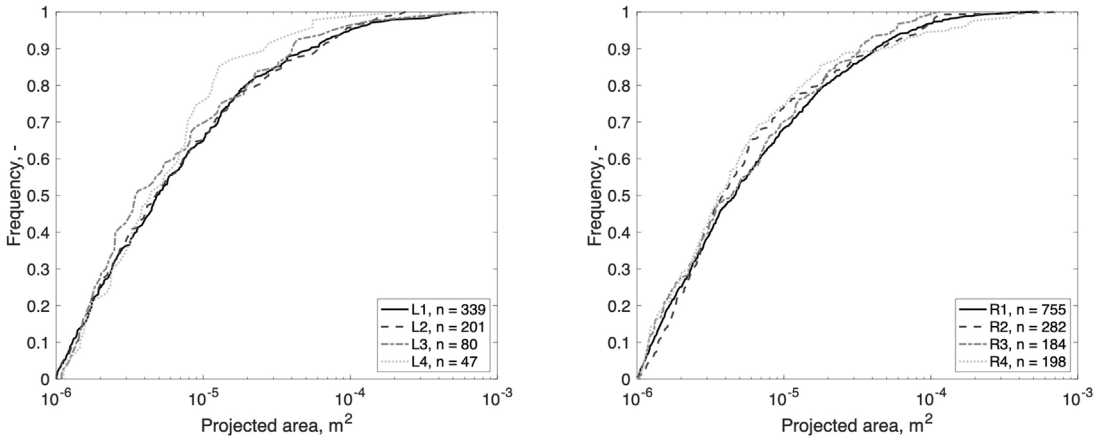

FIGURE 6 | Cumulative distribution of projected area for the left **(left)** and right **(right)** transects of FCS in PPN. Particles with a projected area greater than 1 mm^2 are included in this analysis. *n* is the number of firebrands collected.

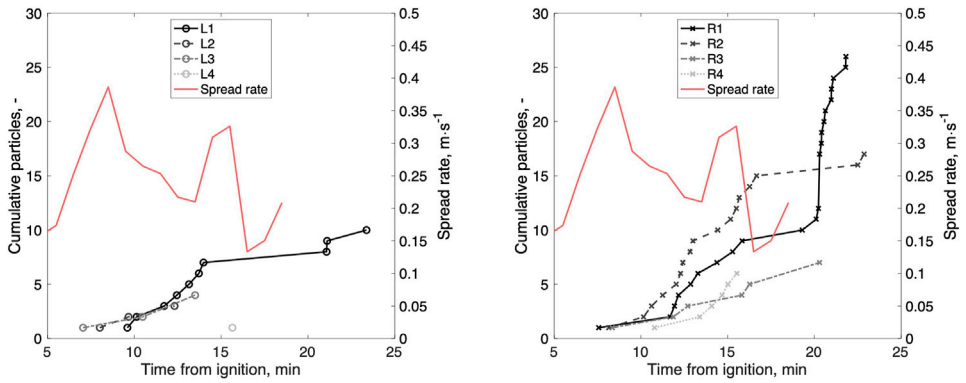

FIGURE 7 | Firebrand collection in one can at each FCS in the left **(left)** and right **(right)** transects at PPN and the spread rate. Note that firebrand deposition continued for a period of 5 min after the fire had reached the end of the burn unit.

plume and the initial trajectory of firebrands. Close to the surface, in the lee of the plume, entrainment tends to draw air back into the plume, which can explain the fact that many firebrands are observed to land moving in a direction toward the fire. Using **Figure 3**, measuring in the direction of the prevailing ambient wind, a clear influence of the fire can be seen as much as 100 m away from the front in PPS and 200 m in PPN (note that the location of the fire in PPS is more ambiguous due to the multiple ignitions, but the strong acceleration in surface winds is assumed to correspond to the period of high fire intensity in the southeast region of the plot). Therefore, understanding the role of fire intensity in the firebrand problem is important not only for generation but also for quantifying the strength of the indraft and its impact on firebrand trajectories.

3.2 Firebrand Generation

Firebrand generation was measured in the PPN and PPS fires only. Pre- and post-fire measurements of tree circumference revealed an average change in radius of $\Delta r = 6.37 \times 10^{-3} \pm 4.21 \times 10^{-3}$ m for PPN ($n = 25$) and $\Delta r = 2.74 \times 10^{-3} \pm 2.39 \times 10^{-3}$ m for PPS (n = 18). The uncertainty in the measurements is expressed as the standard deviation.

To apply **Eq. 3**, data from previous measurements of bark firebrands in the same ecosystem (Thomas et al., 2017) give values of $\tau = 1.14$ mm and $A_f = 6.72 \times 10^{-5}$ m^2. Scorch heights in PPN and PPS were measured as part of a burn severity assessment with an average scorch height of $h_s = 5.19$ and $h_s = 5.23$ m, respectively.

Using these values, the number and mass of firebrands generated per tree and the total number and mass of firebrands can be calculated. These data are shown in **Table 2**. The larger reduction in the diameter of tree boles and the larger number of firebrands in PPN compared to PPS indicate that fire intensity is a driver of firebrand generation.

3.3 Firebrand Deposition

The firebrand deposition density, calculated from the total number of firebrands collected divided by the total collection area, is shown in **Figure 4** for each transect in the three fires. Separation distances between FCSs to the burn unit were measured along the direction of the prevailing ambient wind. In all cases, a general decreasing trend in firebrand deposition is observed with increasing distance from the edge of the burn unit. These data suggest a positive relationship

TABLE 3 | Assessment of regression models for the total firebrand deposition. Results provide peak deposition, maximum deposition distance, and the total amount of particles deposited. Comparison to total production is included.

	Regression model		
$g(x)$	$ax + b$	ax^b	ae^{bx}
A	−4.8313	7,909	651.6
B	444.5	−1.022	−0.028
R^2	0.668	0.6745	0.7104
Peak deposition (firebrands·m^{-2})	445	7,909	652
Max. firebrand deposition distance (m)	92	6,520	231
Firebrands deposited outside (×10^6)	5	8	6
Firebrands deposited inside (×10^6)	69	1,200	100
Total firebrand deposition (×10^6)	74	1,208	106
Firebrand deposition outside (%)	7	1	6

between firebrand deposition and fire intensity; however, the different fuels at TT preclude a definitive conclusion. The non-monotonic relationship observed for PPS, where the FCSs are not parallel to the prevailing wind, indicates that there is a relationship between ambient wind and firebrand deposition.

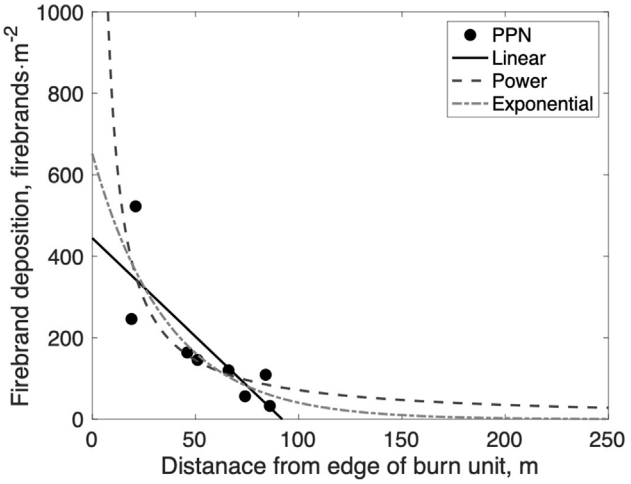

FIGURE 8 | Total firebrand deposition as a function of distance from the edge of the burn unit, m, and the regression analysis for linear, power law, and exponential equations fit to the data.

3.4 Firebrand Characteristics

The cumulative distribution functions (CDFs) of the projected area for the firebrands collected in each fire are shown in **Figure 5**. Approximately 80% of particles in PPN and PPS and 90% of particles in TT have an area less than 1×10^{-4} m^2. The size distribution from TT is skewed to significantly smaller projected areas than PPN and PPS. PPN has the largest number of larger particles suggesting that there is a relationship between fire behavior and size distribution of firebrands deposited. However, it is not possible to say whether this is due to the generation of larger firebrands or the enhanced ability of the plume to transport larger particles. These data are in line with previous studies (El Houssami et al., 2016a; Filkov et al., 2017; Thomas et al., 2017; Zen et al., 2021) which are similarly skewed with a large number of small particles.

The distribution of particles in the individual collection sites for PPN is presented in **Figure 6**. Only data for PPN are presented because this fire had a simple linear ignition which resulted in a relatively steady head fire across the unit. The ignition patterns for PPS and TT were more complex, and the collection sites were less well aligned to the prevailing wind, which means that this analysis cannot be reliably used in these cases.

The analysis of PPN indicates that while the number of particles may show an inverse relationship with distance, there is no such trend with particle projected area. This highlights the complexity of the deposition process and indicates the local flow conditions to be dominant over particle characteristics. Analysis following the approaches developed by Tachikawa (Holmes et al., 2006) has been proposed; however, previous studies did not show expected trends Manzello and Suzuki (2013).

3.5 Time-Dependent Firebrand Deposition

Given the previously established dependence of the firebrand deposition on global fire behavior, the variation in firebrand deposition throughout the duration of the fire was explored. This allows for changes in fire intensity and firebrand deposition dynamics to be explored. Using the data for PPN in which the ignition pattern and wind are best aligned with the FCS (and thereby allowing the most straightforward comparison), the cumulative, time-dependent deposition in one collection can at each FCS is shown in **Figure 7** and in the **Supplementary Material** PPN_spread.mp4. Periods of high rates of fire spread are shown between 7 and 9 min and 14 and 16 min after ignition, as discussed previously.

The first particles arrived approximately 7 min after ignition at FCS L3, a linear distance of approximately 225 m from the fire front. This highlights the complexity of deposition patterns and suggests that the particle trajectories are affected by the fire-induced wind and local flow obstructions. After approximately 11.5 min, the firebrand deposition becomes more rapid at all collection sites. At this time, the fire was approximately 100 m distant from the FCS. This period of rapid firebrand deposition occurs until approximately 16.5 min and was followed by a period of approximately 2.5–3 min of no firebrand deposition. Between 20 and 21.5 min, there was another period of rapid firebrand deposition.

Linking the rate of spread and deposition data indicates that the typical travel time for a firebrand is between 4.5 and 7.5 min for the first period of high spread rate and 6.5–7 min for the second period corresponding to travel distances of approximately 100 m and 50 m, respectively. The resulting average firebrand velocities are less than the upper limit of the above canopy wind speed, lending credibility to this assessment. However, before drawing firm conclusions on this issue, further information on the firebrand generation and trajectories is required.

3.6 Total Firebrand Deposition

Three regression models were considered to represent the relationship, $g(x)$, that defines the firebrand deposition outside the burn area: linear, power, and exponential. The results of fitting these functions to the data are presented in **Table 3**; **Figure 8**. For the power law and exponential models, the maximum deposition distance was estimated when the deposition reaches 1 firebrand m^{-2}. Integrating the functions allows the total quantity of firebrands

deposited to be estimated. The linear and exponential models suggest that 74 and 106 million firebrands are deposited, respectively. This compares to the estimated 500 million firebrands being generated (**Table 2**). Assuming constant firebrand deposition within the fire, between 6 and 7% of firebrands land outside the burn unit. The higher generation of firebrands compared to the deposition outside the burn unit suggests that either a large proportion of firebrands are not lofted from the fire front or are consumed in the plume.

Clearly, there are significant uncertainties embedded in these approaches and their physical interpretation. Although statistically there are insufficient data to reject any of the proposed deposition models, it is unlikely that a power law can explain the deposition relationship—it is undefined at the fire front ($x = 0$), and the asymptotic behavior approaching a nonzero deposition rate at distances greater than 150 m seems unlikely to be true. However, the order of magnitude agreement between the independent calculations of firebrands generated and firebrands deposited gives confidence in the method and suggests that refinement in the measurements and increased data collection will yield improved predictive relationships.

4 CONCLUSIONS

The hazard associated with firebrand exposure is a complex coupling of fire behavior, fuels, and environmental factors. The results in this study demonstrate that firebrand generation and deposition are strongly coupled to fire behavior, and therefore, to adequately assess the hazard, it is necessary to provide context with fire behavior measurements. A method to provide such coupled measurements has been designed, and it is demonstrated to provide the required measurements.

By measuring detailed fire behavior (spread rate and intensity), with both spatial and temporal resolution, it has been possible to obtain insights into the relationship between firebrand generation, transport, and deposition in a system dominated by bark firebrands.

The following general observations can be made:

- A regular array of temperature measurements overlaid with an array of flame height measurements allows time-resolved fire behavior to be calculated.
- The firebrand generation can be evaluated using measurements of tree characteristics and fire severity assessments.
- Firebrand generation is a function of the fuel characteristics and the fire intensity.
- Higher fire intensities resulted in higher firebrand generation and, on average, higher firebrand deposition rates and larger firebrand projected areas, as observed between different fires and within the same fire;
- It is possible to link the temporal dynamics of firebrand deposition to fire behavior;
- Firebrand deposition is not adequately predicted by the mean wind vector and analysis of the local flow dynamics, and fire-induced flow reversal is required.
- Total firebrand deposition decreases as a function of distance from the fire line possibly following an exponential decay.

The data also point toward an influence of fire return interval in determining the firebrand hazard. Two fires that were undertaken in areas that had not been burned for more than 50 years (PPS and PPN) resulted in a larger firebrand generation than the areas which had been burned more recently (TT). This suggests that fire return interval may also be important in determining the firebrand hazard.

Factors which require further consideration to improve the assessments made here include time-resolved measurements of firebrand generation to evaluate the rate, temporal, and spatial distribution of firebrand generation relative to the fire front; firebrand trajectory to evaluate the travel distance and velocities including within and above canopy turbulence measurements, the reaction dynamics of firebrands during transport, and the temperature evolution of firebrands during transport and upon deposition.

Nevertheless, the results of this study demonstrate that it is possible to assess the relationship between fire behavior and the firebrand hazard and present an experimental design for doing so. However, clearly, this methodology must be adopted widely to gather sufficient data across a wider range of fire behaviors and fuel types to generate datasets appropriate for the development of predictive tools.

DATA AVAILABILITY STATEMENT

The raw data supporting the conclusion of this article will be made available by the authors, without undue reservation.

AUTHOR CONTRIBUTIONS

JT, EM, MG, KC, NS, AS, and RH developed the experimental methods. JT, EM, MG, KC, NS, and RH collected the data and conducted the experiments. JT, EM, and RH led the preparation of the manuscript with input from MG, KC, and NS.

FUNDING

The authors are thankful for funding for this work that was provided by the Joint Fire Science Program (15-1-04-55) and the Strategic Environmental Research and Development Program (RC-2641).

ACKNOWLEDGMENTS

The authors wish to thank the New Jersey Conservation Foundation and the Tall Timbers Research Station (particularly Kevin Hiers) for facilitating the experimental fires. The support of the New Jersey Forest Fire Service in managing the fires and the experimental objectives is gratefully acknowledged.

SUPPLEMENTARY MATERIAL

The Supplementary Material for this article can be found online at: https://www.frontiersin.org/articles/10.3389/fmech.2021.650580/full#supplementary-material

REFERENCES

Alexander, M. E. (1982). Calculating and Interpreting forest Fire Intensities. *Can. J. Bot.* 60, 349–357. doi:10.1139/b82-048

Barr, B. W., and Ezekoye, O. A. (2013). Thermo-mechanical Modeling of Firebrand Breakage on a Fractal Tree. *Proc. Combustion Inst.* 34, 2649–2656. doi:10.1016/J.PROCI.2012.07.066

Byram, G. M. (1959). "Combustion of forest Fuels," in *Forest Fire: Control and Use*. Editor K. P. Davis (New York: McGraw-Hill).

Caton, S. E., Hakes, R. S. P., Gorham, D. J., Zhou, A., and Gollner, M. J. (2017). Review of Pathways for Building Fire Spread in the Wildland Urban Interface Part I: Exposure Conditions. *Fire Technol.* 53, 429–473. doi:10.1007/s10694-016-0589-z

Clark, K. L., Heilman, W. E., Skowronski, N. S., Gallagher, M. R., Mueller, E., Hadden, R. M., et al. (2020). Fire Behavior, Fuel Consumption, and Turbulence and Energy Exchange during Prescribed Fires in Pitch pine Forests. *Atmosphere* 11, 242. doi:10.3390/atmos11030242

El Houssami, M., Mueller, E., Filkov, A., Thomas, J. C., Skowronski, N., Gallagher, M. R., et al. (2016a). Experimental Procedures Characterising Firebrand Generation in Wildland Fires. *Fire Technol.* 52, 731–751. doi:10.1007/s10694-015-0492-z

Fernandez-Pello, A. C. (2017). Wildland Fire Spot Ignition by sparks and Firebrands. *Fire Saf. J.* 91, 2–10. doi:10.1016/J.FIRESAF.2017.04.040

Filkov, A., Prohanov, S., Mueller, E., Kasymov, D., Martynov, P., Houssami, M. E., et al. (2017). Investigation of Firebrand Production during Prescribed Fires Conducted in a pine forest. *Proc. Combustion Inst.* 36, 3263–3270. doi:10.1016/J.PROCI.2016.06.125

Hakes, R. S. P., Caton, S. E., Gorham, D. J., and Gollner, M. J. (2017). A Review of Pathways for Building Fire Spread in the Wildland Urban Interface Part Ii: Response of Components and Systems and Mitigation Strategies in the united states. *Fire Technol.* 53, 475–515. doi:10.1007/s10694-016-0601-7

Hakes, R. S. P., Salehizadeh, H., Weston-Dawkes, M. J., and Gollner, M. J. (2019). Thermal Characterization of Firebrand Piles. *Fire Saf. J.* 104, 34–42. doi:10.1016/J.FIRESAF.2018.10.002

Heilman, W. E., Clements, C. B., Zhong, S., Clark, K. L., and Bian, X. (2019). Atmospheric Turbulence. in *Encyclopedia of Wildfires and Wildland-Urban Interface (WUI) Fires* (Springer).

Holmes, J. D., Baker, C. J., and Tamura, Y. (2006). Tachikawa Number: A Proposal. *J. Wind Eng. Ind. Aerodynamics* 94, 41–47. doi:10.1016/j.jweia.2005.10.004

Houssami, M. E., Thomas, J. C., Lamorlette, A., Morvan, D., Chaos, M., Hadden, R., et al. (2016b). Experimental and Numerical Studies Characterizing the Burning Dynamics of Wildland Fuels. *Combustion and Flame* 168, 113–126. doi:10.1016/j.combustflame.2016.04.004

Koo, E., Pagni, P. J., Weise, D. R., and Woycheese, J. P. (2010). Firebrands and Spotting Ignition in Large-Scale Fires. *Int. J. Wildland Fire* 19, 818–843. doi:10.1071/WF07119

Manzello, S. L., Shields, J. R., Cleary, T. G., Maranghides, A., Mell, W. E., Yang, J. C., et al. (2008). On the Development and Characterization of a Firebrand Generator. *Fire Saf. J.* 43, 258–268. doi:10.1016/j.firesaf.2007.10.001

Manzello, S. L., and Suzuki, S. (2013). Experimentally Simulating Wind Driven Firebrand Showers in Wildland-Urban Interface (Wui) Fires: Overview of the Nist Firebrand Generator (Nist Dragon) Technology. *Proced. Eng.* 62, 91–102. doi:10.1016/J.PROENG.2013.08.047

Manzello, S. L., Suzuki, S., Gollner, M. J., and Fernandez-Pello, A. C. (2020). Role of Firebrand Combustion in Large Outdoor Fire Spread. *Prog. Energ. Combustion Sci.* 76, 100801. doi:10.1016/j.pecs.2019.100801

Manzello, S. L., Suzuki, S., and Nii, D. (2017). Full-scale Experimental Investigation to Quantify Building Component Ignition Vulnerability from Mulch Beds Attacked by Firebrand Showers. *Fire Technol.* 53, 535–551. doi:10.1007/s10694-015-0537-3

Maranghides, A., and Mell, W. (2011). A Case Study of a Community Affected by the Witch and Guejito Wildland Fires. *Fire Technol.* 47, 379–420. doi:10.1007/s10694-010-0164-y

Matvienko, O. V., Kasymov, D. P., Filkov, A. I., Daneyko, O. I., and Gorbatov, D. A. (2018). Simulation of Fuel Bed Ignition by Wildland Firebrands. *Int. J. Wildland Fire* 27, 550–561. doi:10.1071/wf17083

McCormick, J., and Jones, L. (1973). The Pine Barrens: Vegetation Geography. *Tech. Rep.* doi:10.7282/T3GX49DC

Mueller, E. V., Skowronski, N., Clark, K., Gallagher, M., Kremens, R., Thomas, J. C., et al. (2017). Utilization of Remote Sensing Techniques for the Quantification of Fire Behavior in Two pine Stands. *Fire Saf. J.* 91, 845–854. doi:10.1016/j.firesaf.2017.03.076

Mueller, E. V., Skowronski, N., Thomas, J. C., Clark, K., Gallagher, M. R., Hadden, R., et al. (2018). Local Measurements of Wildland Fire Dynamics in a Field-Scale experiment. *Combustion and Flame* 194, 452–463. doi:10.1016/J.COMBUSTFLAME.2018.05.028

Simeoni, A., Owens, Z. C., Christiansen, E. W., Kemal, A., Gallagher, M., Clark, K. L., et al. (2017). A Preliminary Study of Wildland Fire Pattern Indicator Reliability Following an Experimental Fire. *J. Fire Sci.* 35, 359–378. doi:10.1177/0734904117720674

Tarifa, C. S., Notario, P. P. d., and Moreno, F. G. (1965). On the Flight Paths and Lifetimes of Burning Particles of wood. *Symp. (International) Combustion* 10, 1021–1037. doi:10.1016/s0082-0784(65)80244-2

Thomas, J. C., et. al., V. E., and Hadden, R. M. (2018). Estimating Net Heat Flux from Surrogate Firebrand Accumulations Using an Inverse Heat Transfer Approach. *Adv. For. fire Res.* 2017, 769–779. doi:10.14195/978-989-26-16-506_84

Thomas, J. C., Mueller, E. V., Santamaria, S., Gallagher, M., El Houssami, M., Filkov, A., et al. (2017). Investigation of Firebrand Generation from an Experimental Fire: Development of a Reliable Data Collection Methodology. *Fire Saf. J.* 91, 864–871. doi:10.1016/j.firesaf.2017.04.002

Wadhwani, R., Sutherland, D., Ooi, A., Moinuddin, K., and Thorpe, G. (2017). Verification of a Lagrangian Particle Model for Short-Range Firebrand Transport. *Fire Saf. J.* 91, 776–783. doi:10.1016/j.firesaf.2017.03.019

Woycheese, J. P., Pagni, P. J., and Liepmann, D. (1999). Brand Propagation from Large-Scale Fires. *J. Fire Prot. Eng.* 10, 32–44. doi:10.1177/104239159901000203

Zen, S., Thomas, J. C., Mueller, E. V., Dhurandher, B., Gallagher, M. R., Skowronski, N., et al. (2021). Development of a Field Deployable Firebrand Flux and Condition Measurement System. *Fire Technol* 57, 1401–1424. doi:10.1007/s10694-020-01074-x

Conflict of Interest: The authors declare that the research was conducted in the absence of any commercial or financial relationships that could be construed as a potential conflict of interest.

Advantages of publishing in Frontiers

OPEN ACCESS
Articles are free to read for greatest visibility and readership

FAST PUBLICATION
Around 90 days from submission to decision

HIGH QUALITY PEER-REVIEW
Rigorous, collaborative, and constructive peer-review

TRANSPARENT PEER-REVIEW
Editors and reviewers acknowledged by name on published articles

Frontiers
Avenue du Tribunal-Fédéral 34
1005 Lausanne | Switzerland

Visit us: www.frontiersin.org
Contact us: frontiersin.org/about/contact

REPRODUCIBILITY OF RESEARCH
Support open data and methods to enhance research reproducibility

DIGITAL PUBLISHING
Articles designed for optimal readership across devices

FOLLOW US
@frontiersin

IMPACT METRICS
Advanced article metrics track visibility across digital media

EXTENSIVE PROMOTION
Marketing and promotion of impactful research

LOOP RESEARCH NETWORK
Our network increases your article's readership